

<https://doi.org/10.15388/vu.thesis.920>

<https://orcid.org/0000-0003-4775-0071>

VILNIUS UNIVERSITY  
CENTER FOR PHYSICAL SCIENCES AND TECHNOLOGY

Rokas Silkinis

# *Ab Initio* Optical Lineshape Modeling of Deep-Level Point Defects in Semiconductors

**DOCTORAL DISSERTATION**

Natural Sciences,  
Physics (N 002)

VILNIUS 2026

The dissertation was prepared between 2020 and 2025 at the Center for Physical Sciences and Technology (FTMC).

**Academic Supervisor:**

**Dr. Lukas Razinkovas** (Center for Physical Sciences and Technology, Natural Sciences, Physics – N 002).

**Former Academic Supervisor (in memoriam):**

**Prof. Dr. Audrius Alkauskas** (supervised from 2020 to 2023).

Dissertation Defense Panel:

**Chairman:**

**Prof. Dr. Darius Abramavičius** (Vilnius University, Natural Sciences, Physics – N 002).

**Members:**

**Prof. Dr. Ramūnas Aleksiejūnas** (Vilnius University, Natural Sciences, Physics – N 002),

**Dr. Marius Franckevičius** (Center for Physical Sciences and Technology, Natural Sciences, Physics – N 002),

**Assoc. Prof. Dr. Andrius Gelžinis** (Vilnius University, Natural Sciences, Physics – N 002),

**Dr. Ronald Ulbricht** (Max Planck Institute for Polymer Research, Natural Sciences, Physics – N 002).

The dissertation shall be defended at a public meeting of the Dissertation Defense Panel at 14:00 on 26<sup>th</sup> May 2026 in meeting room D401 of the Center for Physical Sciences and Technology.

Address: Saulėtekio al. 3, LT-10257 Vilnius, Lietuva

Phone: +370 645 15550

E-mail: office@ftmc.lt

<https://doi.org/10.15388/vu.thesis.920>

<https://orcid.org/0000-0003-4775-0071>

VILNIAUS UNIVERSITETAS  
FIZINIŲ IR TECHNOLOGIJOS MOKSLŲ CENTRAS

Rokas Silkinis

# Giliųjų taškinių defektų puslaidininkiuose optinių linijų modeliavimas *ab initio* metodais

**DAKTARO DISERTACIJA**

Gamtos mokslai,  
Fizika (N 002)

VILNIUS 2026

Disertacija rengta 2020–2025 metais Fizinių ir technologijos mokslų centre (FTMC).

**Mokslinis vadovas:**

**dr. Lukas Razinkovas** (Fizinių ir technologijos mokslų centras, gamtos mokslai, fizika – N 002).

**Buvęs mokslinis vadovas (in memoriam):**

**prof. dr. Audrius Alkauskas** (vadovavo nuo 2020 iki 2023).

Gynimo taryba:

**Pirmininkas:**

**prof. dr. Darius Abramavičius** (Vilniaus universitetas, gamtos mokslai, fizika – N 002).

**Nariai:**

**prof. dr. Ramūnas Aleksiejūnas** (Vilniaus universitetas, gamtos mokslai, fizika – N 002),

**dr. Marius Franckevičius** (Fizinių ir technologijos mokslų centras, gamtos mokslai, fizika – N 002),

**doc. dr. Andrius Gelžinis** (Vilniaus universitetas, gamtos mokslai, fizika – N 002),

**dr. Ronald Ulbricht** (Makso Planko polimerų tyrimų institutas, gamtos mokslai, fizika – N 002).

Disertacija ginama viešame Gynimo tarybos posėdyje 2026 m. gegužės mėn. 26 d. 14 val. 00 min. Fizinių ir technologijos mokslų centro D401 posėdžių salėje.

Adresas: Saulėtekio al. 3, LT-10257 Vilnius, Lietuva

Tel.: +370 645 15550

El. paštas: office@ftmc.lt

# Acknowledgements

First and foremost, I would like to acknowledge our late supervisor, Dr. Audrius Alkauskas, who set me on this path when I first met him as an undergraduate student. I sometimes joke that over the course of his brilliant career, he forgot more physics than I will ever learn. We miss you dearly.

I am deeply grateful to my current supervisor, Dr. Lukas Razinkovas, a former student of Audrius, who took up the mantle of supervision during challenging times for our group. His guidance and patience have been invaluable.

I also thank the past and present members of our *Puntukas* group—Dr. Vytautas Žalandauskas, Dr. Mažena Mackoit-Sinkevičienė, and Dr. Marek Maciaszek—for the years of shared work and countless discussions, both scientific and otherwise.

To our colleagues abroad—Dr. Marianne Etzelmüller Bathen, Dr. Lasse Vines, and Dr. Christopher Linderälv—thank you for the insightful weekly discussions and the delightful encounters at conferences over the years.

Finally, my deepest gratitude goes to my parents, Neringa and Aurelijus, and to my life partner, Aistė, for their encouragement in “whatever it is I do”, and for their love, patience, and unwavering support throughout every stage of this journey.



# Table of contents

<b>List of tables</b>	<b>xi</b>
<b>List of figures</b>	<b>xiv</b>
<b>List of acronyms</b>	<b>xv</b>
<b>Introduction</b>	<b>17</b>
The goal of the thesis . . . . .	19
Tasks of the thesis . . . . .	19
The relevance and novelty of the work . . . . .	20
Relevance . . . . .	20
Novelty . . . . .	20
Statements to be defended . . . . .	21
Structure of the thesis . . . . .	21
Author contribution . . . . .	22
Publications . . . . .	22
Conferences . . . . .	23
<b>1 Theoretical and methodological framework</b>	<b>25</b>
1.1 The many-body problem . . . . .	25
1.2 Crude adiabatic approximation . . . . .	26
1.3 Density functional theory . . . . .	29
1.3.1 Hohenberg–Kohn theorems . . . . .	30
1.3.2 Kohn–Sham formalism . . . . .	32
1.3.3 Exchange–correlation functionals . . . . .	34
1.3.4 Practical implementation . . . . .	37
1.4 Vibrational properties of solids . . . . .	41
1.4.1 Adiabatic potential energy surface . . . . .	42
1.4.2 Harmonic approximation . . . . .	43
1.4.3 Vibrations in the classical description . . . . .	44
1.4.4 Normal modes and phonons . . . . .	45
1.4.5 Defect vibrational modes . . . . .	47
1.5 Electronic degeneracy and vibronic interactions . . . . .	48
1.5.1 Vibronic states and the Jahn–Teller Hamiltonian . . . . .	49
1.5.2 Solving the Jahn–Teller problem . . . . .	51
1.5.3 Extraction of Jahn–Teller parameters from DFT . . . . .	54
1.5.4 Few-mode approximation . . . . .	56
1.6 Optical spectra . . . . .	57
1.6.1 Transitions between non-degenerate states . . . . .	58

1.6.2	Lineshapes for $A$ to $E$ transitions . . . . .	61
1.7	Embedding methodology . . . . .	61
1.8	Computational details . . . . .	63
<b>2</b>	<b>Application of different exchange–correlation functionals: NV<sup>−</sup> center in diamond</b>	<b>65</b>
2.1	Introduction . . . . .	65
2.2	Computational details . . . . .	67
2.3	Results and discussion . . . . .	68
2.3.1	Lattice parameters of diamond . . . . .	68
2.3.2	Vibrational properties of diamond . . . . .	69
2.3.3	Zero-phonon line energy . . . . .	71
2.3.4	Electron–phonon interaction . . . . .	72
2.3.5	Luminescence lineshape . . . . .	75
2.4	Summary and conclusions . . . . .	79
<b>3</b>	<b>Correlated electronic states: G-center in silicon</b>	<b>81</b>
3.1	Introduction . . . . .	81
3.2	Computational details . . . . .	84
3.3	Results and discussion . . . . .	86
3.3.1	Lattice parameters of silicon . . . . .	86
3.3.2	Vibrational properties of silicon . . . . .	87
3.3.3	Zero-phonon line energy . . . . .	88
3.3.4	Vibrational structure . . . . .	89
3.3.5	Electron–phonon interaction and luminescence line- shape . . . . .	91
3.4	Summary and conclusions . . . . .	94
<b>4</b>	<b>Weakly bound exciton-like electronic states: C-center in silicon</b>	<b>95</b>
4.1	Introduction . . . . .	95
4.2	Computational details . . . . .	97
4.2.1	Thermodynamic quantities . . . . .	99
4.3	Results and discussion . . . . .	100
4.3.1	Thermodynamic properties . . . . .	100
4.3.2	Vibrational structure . . . . .	102
4.3.3	Electron–phonon interaction . . . . .	105
4.3.4	Optical lineshapes . . . . .	106
4.4	Summary and conclusions . . . . .	115
<b>5</b>	<b>Electronic degeneracy: NiV<sup>−</sup> center in diamond</b>	<b>117</b>
5.1	Introduction . . . . .	117
5.2	Computational details . . . . .	119

5.3	Results and discussion . . . . .	121
5.3.1	Spectral functions of electron–phonon interaction .	121
5.3.2	Optical spectral functions . . . . .	123
5.3.3	Luminescence lineshape . . . . .	126
5.4	Summary and conclusions . . . . .	129
<b>References</b>		<b>131</b>
<b>Santrauka</b>		<b>147</b>
	Įvadas . . . . .	147
	Darbo tikslas . . . . .	149
	Darbo uždaviniai . . . . .	149
	Darbo aktualumas ir naujumas . . . . .	150
	Ginamieji teiginiai . . . . .	151
	Darbo struktūra . . . . .	151
	Autoriaus indėlis . . . . .	152
1	Teorinis ir metodologinis pagrindas . . . . .	155
1.1	Daugiadalelis uždavinys . . . . .	155
1.2	Adiabatinė aproksimacija . . . . .	155
1.3	Tankio funkcionalo teorija . . . . .	156
1.4	Kietųjų kūnų virpesinės savybės . . . . .	159
1.5	Elektroninis išsigimimas ir vibroninės sąveikos . . .	162
1.6	Optiniai spektrai . . . . .	166
1.7	Įterpimo metodologija . . . . .	168
1.8	Skaičiavimų detalės . . . . .	168
2	Skirtingų tankio funkcionalų taikymas: $NV^-$ centras deimante . . . . .	170
2.1	Rezultatai . . . . .	170
3	Koreliuotos elektroninės būsenos: G-centras silicyje . . . .	176
3.1	Rezultatai . . . . .	176
4	Silpnai susietos eksitoninės sužadintos elektroninės būsenos: C-centras silicyje . . . . .	181
4.1	Rezultatai . . . . .	181
5	Elektroninis išsigimimas: $NiV^-$ centras deimante . . . . .	186
5.1	Rezultatai . . . . .	186
<b>Curriculum vitae</b>		<b>191</b>
<b>Gyvenimo aprašymas</b>		<b>192</b>



# List of tables

2.1	Lattice constants and band gaps of bulk diamond . . . . .	68
2.2	Longitudinal optical phonon frequencies at high-symmetry reciprocal lattice points of bulk diamond . . . . .	70
2.3	Zero-phonon line energies of the $NV^-$ center in diamond .	72
2.4	Huang–Rhys factors for the luminescence of the $NV^-$ center in diamond . . . . .	75
3.1	Lattice constants and band gaps of bulk silicon . . . . .	86
3.2	Longitudinal optical phonon frequencies at high-symmetry reciprocal lattice points of bulk silicon . . . . .	88
3.3	Zero-phonon line energies of the G-center in silicon . . . .	89
4.1	Formation energies of neutral $C_i$ , $O_i$ , and C-center defects in silicon, and the binding energy of the C-center . . . . .	100
4.2	Charge-state transition levels for the $C_i$ and C-center defects in silicon . . . . .	101
S1	Deimanto gardelės konstantos ir draustinės juostos tarpai	171
S2	Deimanto išilginių optinių fononų dažniai aukštos simetrijos atvirkštinės gardelės taškuose . . . . .	172
S3	$NV^-$ centro deimante befononinės linijos energijos vertės	172
S4	$NV^-$ centro deimante liuminescencijos proceso Huang–Rhys faktoriai . . . . .	174
S5	Slicio gardelės konstantos ir draustinės juostos tarpai . .	177
S6	Silicio išilginių optinių fononų dažniai aukštos simetrijos atvirkštinės gardelės taškuose . . . . .	177
S7	G-centro silicyje befononinės linijos energijos vertės . . .	178
S8	Neutralių $C_i$ , $O_i$ ir C-centro defektų silicyje formavimosi energijos ir C-centro surišimo energija . . . . .	182
S9	$C_i$ ir C-centro silicyje krūvio būsenų perėjimo lygmenys .	182



# List of figures

1.1	Representation of the supercell approach . . . . .	41
1.2	Illustration of the embedding methodology . . . . .	62
2.1	Structure of the $NV^-$ center in diamond . . . . .	66
2.2	Phonon dispersion relations of bulk diamond . . . . .	70
2.3	Partial spectral functions of electron–phonon coupling for the luminescence of the $NV^-$ center in diamond . . . . .	73
2.4	Spectral functions of electron–phonon coupling for the luminescence of the $NV^-$ center in diamond . . . . .	74
2.5	Luminescence lineshapes of the $NV^-$ center in diamond . . . . .	76
2.6	Convergence of the luminescence lineshape of the $NV^-$ center in diamond with respect to supercell size . . . . .	77
3.1	Structure of the G-center in silicon . . . . .	82
3.2	Phonon dispersion relations of bulk silicon . . . . .	87
3.3	Vibrational structure of the ground state of the G-center in silicon . . . . .	90
3.4	Luminescence lineshapes of the G-center in silicon . . . . .	92
4.1	Structure of the C-center in silicon . . . . .	96
4.2	Formation energies of the $C_i$ , $O_i$ , and C-center defects in silicon as a function of the Fermi level . . . . .	102
4.3	Vibrational structure of the ground state of the C-center in silicon . . . . .	103
4.4	Illustrations of the localized vibrational modes of the ground state of the C-center in silicon . . . . .	105
4.5	Vibrational structure of the positively charged state of the C-center in silicon . . . . .	106
4.6	Luminescence lineshape of the C-center in silicon . . . . .	107
4.7	Convergence of the luminescence lineshape of the C-center in silicon with respect to supercell size . . . . .	109
4.8	Comparison of the luminescence lineshapes of the C-center in silicon obtained using SCAN and PBE functionals . . . . .	110
4.9	Comparison of the luminescence lineshapes of the C-center in silicon obtained using two approximations ( $ P\rangle$ and $ T\rangle$ ) to the excited state . . . . .	111
4.10	Comparison of the luminescence lineshapes of the C-center in silicon obtained using two approximations ( $ P\rangle$ and $ M\rangle$ ) to the excited state . . . . .	112

4.11	Comparison of absorption and luminescence lineshapes of the C-center in silicon . . . . .	113
5.1	Structure of the NiV <sup>-</sup> center in diamond . . . . .	118
5.2	Spectral functions of electron–phonon coupling for the luminescence of the NiV <sup>-</sup> center in diamond . . . . .	122
5.3	Convergence of the effective linear Jahn–Teller coupling spectral density for the luminescence of the NiV <sup>-</sup> center in diamond with respect to the number of effective modes . . . . .	124
5.4	Optical spectral functions for the luminescence of the NiV <sup>-</sup> center in diamond . . . . .	125
5.5	Comparison of the luminescence lineshapes of the NiV <sup>-</sup> center in diamond obtained using different theories . . . . .	127
5.6	Convergence of the luminescence lineshape of the NiV <sup>-</sup> center in diamond with respect to the number of effective modes and the size of the phonon basis . . . . .	128
S1	Deimanto fononų dispersijos kreivės . . . . .	171
S2	NV <sup>-</sup> centro deimante liuminescencijos proceso elektron-fononinės sąveikos dalinės spektrinės funkcijos . . . . .	173
S3	NV <sup>-</sup> centro deimante liuminescencijos proceso elektron-fononinės sąveikos spektrinė funkcija . . . . .	174
S4	NV <sup>-</sup> centro deimante liuminescencijos linija . . . . .	175
S5	Silicio fononų dispersijos kreivės . . . . .	178
S6	G-centro silicyje pagrindinės būsenos virpesinė struktūra . . . . .	179
S7	G-centro silicyje liuminescencijos linijos . . . . .	180
S8	C-centro silicyje pagrindinės būsenos virpesinė struktūra . . . . .	183
S9	C-centro silicyje liuminescencijos linija . . . . .	184
S10	C-centro silicyje liuminescencijos linijų, suskaičiuotų su PBE ir SCAN funkcionalais, palyginimas . . . . .	185
S11	NiV <sup>-</sup> centro deimante liuminescencijos proceso elektron-fononinės sąveikos spektrinės funkcijos . . . . .	187
S12	NiV <sup>-</sup> centro deimante liuminescencijos proceso optinės spektrinės funkcijos . . . . .	188
S13	NiV <sup>-</sup> centro deimante liuminescencijos linijų palyginimas . . . . .	189

# List of acronyms

APES	adiabatic potential energy surface
BZ	Brillouin zone
CBM	conduction band minimum
CTL	charge-state transition level
DFT	density functional theory
DJT	dynamical Jahn–Teller
DOS	density of states
DWF	Debye–Waller factor
GGA	generalized gradient approximation
HF	Hartree–Fock
HK	Hohenberg–Kohn
HR	Huang–Rhys
HSE	Heyd–Scuseria–Ernzerhof
HWHM	half-width at half maximum
INS	inelastic neutron scattering
IPR	inverse participation ratio
IXS	inelastic X-ray scattering
JT	Jahn–Teller
KS	Kohn–Sham
LDA	local-density approximation
LO	longitudinal optical
PAW	projector-augmented wave
PBE	Perdew–Burke–Ernzerhof
PES	potential energy surface
PSB	phonon sideband
r <sup>2</sup> SCAN	re-regularized SCAN

rSCAN	regularized SCAN
SCAN	strongly constrained and appropriately normed
$\Delta$ SCF	$\Delta$ self-consistent field
UEG	uniform electron gas
VASP	Vienna Ab initio Simulation Package
VBM	valence band maximum
XC	exchange–correlation
ZPL	zero-phonon line

# Introduction

Point defects, atomic-scale imperfections such as vacancies, interstitials, or substitutional impurities, are disruptions of the otherwise periodic lattice structure of a crystal. From a technological standpoint, these defects are generally categorized into two classes: shallow and deep-level. Shallow impurities, which can be thermally ionized, enable controlled doping and device functionality. In contrast, deep-level defects, with ionization energies exceeding thermal energies, have traditionally been regarded as detrimental due to carrier trapping [1] and non-radiative recombination [2].

However, in recent decades, certain deep-level point defects have emerged as promising candidates for solid-state quantum technologies. Localized electronic states deep within the band gap give rise to spectroscopically stable and narrow optical transitions, enabling single-photon emission. These defects can also host controllable spin states with long coherence times, sometimes even under ambient conditions. Together, these properties form the basis for applications in quantum communication, sensing, and information processing.

A canonical example is the negatively charged nitrogen-vacancy (NV<sup>-</sup>) center in diamond [3], which exhibits spin coherence times exceeding milliseconds at room temperature [4–6], making it a leading platform for quantum sensing applications [7–12]. Likewise, various defects in silicon have been shown to emit in the telecom wavelength range [13–20], offering compatibility with existing fiber-optic infrastructure and positioning silicon as a promising host material for single-photon sources for quantum communication [21]. These and other point defects across different materials are also being actively explored as potential platforms for quantum computing [22–24].

The search for point defects with desirable properties for quantum technologies requires a systematic exploration of the immense landscape defined by possible defect configurations and host materials [25]. To navigate this complexity, it is essential to reliably determine the electronic, vibronic, magnetic, and optical signatures associated with each system, as these underpin their potential utility in quantum technologies. While experimental techniques are indispensable, they often fall short of providing a complete understanding of the atomic-scale structure and optoelectronic behavior of such systems. In this context, *ab initio*<sup>1</sup>

---

<sup>1</sup>In Latin, *ab initio* means “from the beginning”. In a scientific context, it refers to calculations based solely on fundamental physical laws, without empirical parameters or external input.

computational methods, such as density functional theory (DFT), offer a theoretical approach for exploring defect properties that are difficult to observe directly through experiments.

DFT enables quantum-mechanical modeling of many-electron molecular systems and provides predictive insight into their structural, vibrational, and electronic properties. At its core, DFT reformulates the electronic many-body Schrödinger equation as a problem of determining the ground-state electron density, from which all relevant observables can, in principle, be obtained [26, 27]. This reformulation is accomplished through the use of *functionals*—mathematical objects that map a function to a scalar quantity. In the context of DFT, the input to the functional typically depends on the electron density of the system, its higher-order terms, and possibly other quantities, while the output is a scalar quantity such as the total energy of the system.

Despite its widespread success, DFT is not without limitations. A fundamental challenge lies in the fact that the exact form of the exchange–correlation functional, an essential component governing electron–electron interactions, remains unknown. In this thesis, the novel class of SCAN functionals [28–30] is employed as a promising alternative for modeling point-defect systems, as it provides a balance of computational efficiency and predictive accuracy. Its performance is benchmarked for the NV<sup>−</sup> center in diamond against experimental data and other widely used alternatives: the PBE functional [31] and the more computationally demanding HSE06 hybrid functional [32], often regarded as the “gold standard” for defect calculations. While this benchmarking is not the primary contribution of the thesis, it provides a consistent reference point for the more advanced methodological developments that follow.

Point defects in semiconductors exhibit a wide range of electronic and vibronic behavior that extends well beyond what can be described by standard ground-state DFT. In many technologically relevant defects, the properties of interest are influenced by excited electronic states and their interactions with lattice vibrations, which is the main focus of this thesis. In some cases, excited states are statically correlated and cannot be captured using a mean-field approach, requiring approximations or more advanced methods to understand their energetics and electron–phonon interactions [33–35]. In other systems, optical excitation gives rise to weakly bound exciton-like excited states [36], whose electron–hole binding is not reliably captured within standard DFT-based approaches. Additionally, in many key defect centers, electronic states are intimately linked to lattice motion. This results in complex non-adiabatic phenomena, such as the dynamical Jahn–Teller effect, in which the electronic states are dynamically coupled to the vibrational motion [37–39].

By combining *ab initio* DFT calculations with tailored methodolo-

gies and controlled approximations for excited-state, excitonic, and non-adiabatic phenomena, along with vibrational mode analysis and advanced lineshape modeling frameworks, this work aims to provide predictive insights into the optical behavior of selected defect centers in technologically relevant materials— namely, diamond and silicon.

## **The goal of the thesis**

The main goal of this thesis is to investigate and advance the use of density functional theory methods for modeling electron–phonon interactions and optical lineshapes associated with deep-level point defects in semiconductors. Particular emphasis is placed on challenging cases, including:

- correlated excited states,
- weakly bound exciton-like excited states, and
- systems exhibiting significant non-adiabatic Jahn–Teller interactions.

## **Tasks of the thesis**

To achieve the goal of this thesis, the following tasks were set:

- (1) Assess the effectiveness of the SCAN family of functionals in describing the structural and vibrational properties of point defects in diamond and silicon.
- (2) Evaluate the effectiveness of the harmonic approximation and approximate methods for correlated excited states in reproducing the luminescence lineshape of the G-center in silicon.
- (3) Benchmark approximate optical lineshape modeling strategies for the C-center defect in silicon, where the optical transition involves a weakly bound exciton-like excited state.
- (4) Model the luminescence lineshape of the negatively charged split nickel-vacancy defect in diamond, which exhibits prominent non-adiabatic Jahn–Teller interactions, using a novel multimode Jahn–Teller computational methodology.

## The relevance and novelty of the work

This thesis is situated at the intersection of computational materials science and the rapidly evolving field of quantum technologies. The significance of this research is summarized below.

### Relevance

Driven by significant global interest in establishing reliable architectures for quantum communication, sensing, and computing, deep-level point defects in semiconductors have emerged as a promising platform for such technologies. Given the vast search space of potential defect configurations and host materials, the identification and characterization of these systems presents a complex challenge that necessitates reliable *ab initio* methods. This work contributes to the development and application of theoretical frameworks designed to characterize the optical signatures of these defects.

### Novelty

- A primary novelty of this work is the systematic application of a sophisticated embedding methodology to multiple color centers. By modeling systems effectively encompassing tens of thousands of atoms, this methodology enables the calculation of high-resolution optical lineshapes.
- This research applies and evaluates computational strategies for electronic configurations that remain challenging for standard density functional theory, specifically addressing static electron correlation and weakly bound exciton-like states.
- This thesis provides the first fully *ab initio*, multimode dynamical Jahn–Teller simulation of a spectroscopic signal for a color center, specifically the  $\text{NiV}^-$  center in diamond. By explicitly solving the vibronic Hamiltonian, this approach successfully captures the extended phonon sideband that standard adiabatic methods fail to reproduce.

## Statements to be defended

- (I) The luminescence lineshape of the G-center defect in silicon could only be partially reproduced using the approximate spin projection method to model the multi-Slater-determinant nature of the excited state. Differences between theory and experiment may arise from either a limited approximation of static correlation in the excited state or from anharmonic effects in the ionic potential that are not captured by the harmonic framework.
- (II) The experimental luminescence lineshape of the C-center defect in silicon, arising from an optical transition involving a weakly bound exciton-like excited state, is accurately reproduced by approximating the ionic potential energy surface of the neutral excitonic configuration with that of the positively charged (ionized) defect.
- (III) The close agreement between the luminescence lineshape predicted from dynamical Jahn–Teller theory and the experimental spectrum provides strong evidence that the 1.40 eV center in diamond originates from the negatively charged split nickel-vacancy defect. This result underscores the decisive role of Jahn–Teller-active vibrational modes in determining the optical lineshape and demonstrates the effectiveness of advanced computational approaches for modeling optical properties in complex systems with multiple Jahn–Teller-active frequencies.

## Structure of the thesis

The thesis consists of five principal chapters. Chapter 1 introduces the theoretical background and methodological framework, including a brief overview on density functional theory, the description of vibrational dynamics, electron–phonon coupling, the Jahn–Teller effect, and the computational approaches employed. Chapters 2–5 present the results obtained for four representative point-defect systems. Chapter 2 focuses on the  $\text{NV}^-$  center in diamond and benchmarks different exchange–correlation functionals. Chapter 3 analyzes the G-center in silicon, whose excited state exhibits pronounced static electron correlation. Chapter 4 investigates the C-center in silicon, which displays luminescence arising from a weakly bound exciton-like excited state. Finally, Chapter 5 examines the  $\text{NiV}^-$  center in diamond as a prototypical Jahn–Teller-active defect, combining adiabatic and dynamical vibronic modeling to describe its emission properties.

## Author contribution

During their doctoral studies, the author contributed to four scientific publications and delivered eight conference presentations (five of which were international), consisting of two oral and six poster presentations. The specific contributions to the publications are detailed below:

- Publication (P1): The author performed optical lineshape calculations for the  $NV^-$  center in diamond using various density functionals and conducted vertical excitation energy calculations for all color centers investigated in the study. Additionally, the author contributed to the critical revision of the manuscript. These results form the basis of Chapter 2.
- Publication (P2): The author was the lead contributor, performing the majority of the numerical calculations for bulk diamond and the  $NiV^-$  center. Utilizing the multi-mode Jahn–Teller computational methodology, the author analyzed the resulting data and interpreted the findings. Furthermore, in collaboration with the supervisor, the author took the primary role in drafting and revising the manuscript. These results form the basis of Chapter 5.
- Publication (P3): The author served as the lead contributor, performing the majority of numerical calculations for silicon, including various impurities and defects, and analyzed the associated data. The author also held the primary responsibility for drafting the manuscript and managing the revision process. These results form the basis of Chapter 4.
- Publication (P4): The author contributed the emission lineshape calculations for two configurations of the divacancy in silicon carbide and participated in the critical revision of the manuscript. The results from this publication are not included in this thesis.

## Publications

- (P1) M. Maciaszek, V. Žalandauskas, R. Silkinis, A. Alkauskas, and L. Razinkovas, *The application of the SCAN density functional to color centers in diamond*, J. Chem. Phys. **159**, 084708 (2023).
- (P2) R. Silkinis, V. Žalandauskas, G. Thiering, A. Gali, C. G. Van de Walle, A. Alkauskas, and L. Razinkovas, *Optical lineshapes for orbital singlet to doublet transitions in a dynamical Jahn–Teller system: The  $NiV^-$  center in diamond*, Phys. Rev. B **110**, 075303 (2024).

- (P3) R. Silkinis, M. Maciaszek, V. Žalandauskas, M. E. Bathen, L. Vines, A. Alkauskas, and L. Razinkovas, *Optical lineshapes of the C-center in silicon from ab initio calculations: Interplay of localized modes and bulk phonons*, Phys. Rev. B **111**, 125136 (2025).
- (P4) V. Žalandauskas, R. Silkinis, L. Vines, L. Razinkovas, and M. E. Bathen, *Theory of the divacancy in 4H-SiC: Impact of Jahn–Teller effect on optical properties*, npj Comput. Mater. **11**, 155 (2025).

## Conferences

- (C1) R. Silkinis, L. Razinkovas, and A. Alkauskas, *Modeling semiconductor alloys using special quasi-random structures*, 10th conference of FTMC doctoral students and young researchers “FizTeCh2020”, 2020-10-23, Vilnius, Lithuania. Poster presentation.
- (C2) R. Silkinis, L. Razinkovas, and A. Alkauskas, *Theoretical modeling of luminescence lineshape in silicon due to a carbon-carbon pair complex*, 65th international scientific conference for students of physics and natural sciences “Open Readings 2022”, 2022-03-15, Vilnius, Lithuania. Poster presentation.
- (C3) R. Silkinis, L. Razinkovas, and A. Alkauskas, *Theoretical modeling of luminescence lineshape in silicon due to a carbon-carbon pair complex*, International conference “Defects in solids for quantum technologies” (DSQT), 2022-06-15, Stockholm, Sweden. Poster presentation.
- (C4) R. Silkinis, L. Razinkovas, V. Žalandauskas, and A. Alkauskas, *Luminescence lineshape of the G-center in silicon from ab-initio calculations*, 12th conference of FTMC doctoral students and young researchers “FizTeCh2022”, 2022-10-19, Vilnius, Lithuania. Oral presentation.
- (C5) R. Silkinis, M. E. Bathen, A. Alkauskas, and L. Razinkovas, *Theoretical modeling of vibrationally resolved optical lineshapes of a carbon-oxygen pair defect in silicon*, International conference “Humboldt Kolleg on Synthetic Quantum Matter”, 2023-07-03, Vilnius, Lithuania. Poster presentation.
- (C6) R. Silkinis, M. E. Bathen, A. Alkauskas, and L. Razinkovas, *Theoretical modeling of vibrationally resolved optical lineshapes of a carbon-oxygen pair defect in silicon*, 32nd International Conference on Defects in Semiconductors (ICDS), 2023-09-11, Rehoboth Beach, Delaware, USA. Poster presentation.

- (C7) R. Silkinis, M. Maciaszek, V. Žalandauskas, M. E. Bathen, L. Vines, A. Alkauskas, and L. Razinkovas, *Theoretical modeling of vibrationally resolved optical lineshapes of a carbon-oxygen pair defect in silicon*, 13th conference of FTMC doctoral students and young researchers “FizTeCh2023”, 2023-10-19, Vilnius, Lithuania. Oral presentation.
- (C8) R. Silkinis, M. Maciaszek, V. Žalandauskas, M. E. Bathen, L. Vines, A. Alkauskas, and L. Razinkovas, *Theoretical modeling of vibrationally resolved optical lineshapes of a carbon-oxygen pair defect in silicon*, International conference “Defects in solids for quantum technologies” (DSQT), 2024-06-11, Budapest, Hungary. Poster presentation.

# 1. Theoretical and methodological framework

## 1.1. The many-body problem

At the most fundamental level, the behavior of matter and light is governed by the principles of quantum mechanics. For isolated, non-relativistic systems, the starting point is the time-independent Schrödinger equation:

$$\hat{H}|\Psi\rangle = E|\Psi\rangle. \quad (1.1)$$

Here,  $\hat{H}$  is the Hamiltonian operator of the system,  $|\Psi\rangle$  is the state vector, and  $E$  is the total energy of the system. In principle, all measurable physical properties, such as electronic structure, optical response, and thermodynamic characteristics, can be derived from the system's state vector  $|\Psi\rangle$ , obtained by solving this equation. However, for many-body systems composed of interacting electrons and nuclei (as is the case in semiconductors), the complexity of the problem increases rapidly, rendering exact solutions intractable for all but the simplest systems.

In the context of molecular or condensed-phase systems, the time-independent Schrödinger equation can be written more explicitly as

$$\hat{H}(\mathbf{r}, \mathbf{R})\Psi_t(\mathbf{r}, \mathbf{R}) = E_t\Psi_t(\mathbf{r}, \mathbf{R}), \quad (1.2)$$

where  $\mathbf{r} \equiv \{\mathbf{r}_1, \mathbf{r}_2, \dots, \mathbf{r}_{N_e}\}$  and  $\mathbf{R} \equiv \{\mathbf{R}_1, \mathbf{R}_2, \dots, \mathbf{R}_{N_n}\}$  denote the positions of the  $N_e$  electrons and  $N_n$  nuclei, respectively.<sup>2</sup> The eigenfunction  $\Psi_t(\mathbf{r}, \mathbf{R})$  is the wave function of the  $t$ -th quantum state of the system, with total energy  $E_t$ , and incorporates both electronic and nuclear degrees of freedom. The total Hamiltonian  $\hat{H}(\mathbf{r}, \mathbf{R})$  includes all kinetic and potential energy contributions and is given by

$$\hat{H}(\mathbf{r}, \mathbf{R}) = \hat{T}_e + \hat{T}_n + \hat{V}_{ee}(\mathbf{r}) + \hat{V}_{en}(\mathbf{r}, \mathbf{R}) + \hat{V}_{nn}(\mathbf{R}). \quad (1.3)$$

Using Hartree atomic units ( $\hbar = m_e = e = 4\pi\epsilon_0 = 1$ ), the electronic and nuclear kinetic energy operators are

$$\hat{T}_e = -\frac{1}{2} \sum_i^{N_e} \frac{\partial^2}{\partial \mathbf{r}_i^2} = \sum_i^{N_e} \hat{T}_{e_i}, \quad \hat{T}_{e_i} \equiv -\frac{1}{2} \frac{\partial^2}{\partial \mathbf{r}_i^2}, \quad (1.4)$$

---

<sup>2</sup>The spin degrees of freedom  $\boldsymbol{\sigma} \equiv \{\sigma_1, \sigma_2, \dots, \sigma_{N_e}\}$  can be included by extending the electronic coordinate vector  $\mathbf{r} \equiv \{\mathbf{r}_1, \mathbf{r}_2, \dots, \mathbf{r}_{N_e}\}$  to  $\mathbf{x} \equiv \{\mathbf{x}_1, \mathbf{x}_2, \dots, \mathbf{x}_{N_e}\}$ , where each  $\mathbf{x}_i = (\mathbf{r}_i, \sigma_i)$  combines the spatial and spin coordinates of the  $i$ -th electron.

$$\hat{T}_n = -\frac{1}{2} \sum_{\alpha}^{N_n} \frac{1}{M_{\alpha}} \frac{\partial^2}{\partial \mathbf{R}_{\alpha}^2} = \sum_{\alpha}^{N_n} \hat{T}_{n\alpha}, \quad \hat{T}_{n\alpha} \equiv -\frac{1}{2M_{\alpha}} \frac{\partial^2}{\partial \mathbf{R}_{\alpha}^2}, \quad (1.5)$$

where

$$\frac{\partial}{\partial \mathbf{a}} \equiv \begin{bmatrix} \frac{\partial}{\partial a_1} \\ \frac{\partial}{\partial a_2} \\ \vdots \\ \frac{\partial}{\partial a_n} \end{bmatrix}, \quad \frac{\partial^2}{\partial \mathbf{a}^2} \equiv \sum_{i=1}^n \frac{\partial^2}{\partial a_i^2},$$

and  $M_{\alpha}$  is the mass of nucleus  $\alpha$ . The potential energy terms for electron–electron, electron–nucleus, and nucleus–nucleus Coulomb interactions are given by<sup>3</sup>

$$\hat{V}_{ee}(\mathbf{r}) = \sum_i^{N_e} \sum_{j>i}^{N_e} \frac{1}{|\mathbf{r}_i - \mathbf{r}_j|}, \quad (1.6)$$

$$\hat{V}_{en}(\mathbf{r}, \mathbf{R}) = - \sum_i^{N_e} \sum_{\alpha}^{N_n} \frac{Z_{\alpha}}{|\mathbf{r}_i - \mathbf{R}_{\alpha}|}, \quad (1.7)$$

$$\hat{V}_{nn}(\mathbf{R}) = \sum_{\alpha}^{N_n} \sum_{\beta>\alpha}^{N_n} \frac{Z_{\alpha} Z_{\beta}}{|\mathbf{R}_{\alpha} - \mathbf{R}_{\beta}|}, \quad (1.8)$$

where  $Z_{\alpha}$  is the atomic number of nucleus  $\alpha$ .

As noted earlier, the many-body nature of Eq. (1.2) renders direct solutions infeasible for systems of realistic size. However, by introducing a series of physically motivated approximations (Sec. 1.2) and employing the density functional theory formalism (Sec. 1.3), one can obtain tractable solutions that provide quantitatively meaningful insights into the properties of real materials.

## 1.2. Crude adiabatic approximation

In general, the Schrödinger equation (1.2) cannot be solved exactly, because the total Hamiltonian  $\hat{H}(\mathbf{r}, \mathbf{R})$  does not allow for a complete separation of the electronic and nuclear variables. This is due to the coupling term  $\hat{V}_{en}(\mathbf{r}, \mathbf{R})$ , which depends simultaneously on both electronic and nuclear coordinates and is the source of the complexity of the many-body problem.

Progress can be made by considering the electron-dependent potential

$$\hat{V}_e(\mathbf{r}, \mathbf{R}) = \hat{V}_{ee}(\mathbf{r}) + \hat{V}_{en}(\mathbf{r}, \mathbf{R}) \quad (1.9)$$

---

<sup>3</sup>Both electrons and nuclei are treated as point-like charged particles.

and expanding it in a Taylor series around a reference nuclear configuration  $\mathbf{R}^{(0)} \equiv \{\mathbf{R}_1^{(0)}, \mathbf{R}_2^{(0)}, \dots, \mathbf{R}_{N_n}^{(0)}\}$ :

$$\begin{aligned} \hat{V}_e(\mathbf{r}, \mathbf{R}) &= \underbrace{\hat{V}_e(\mathbf{r}; \mathbf{R}^{(0)})}_{\hat{V}_{ee}(\mathbf{r}) + \hat{V}_{en}(\mathbf{r}; \mathbf{R}^{(0)})} \\ &+ \sum_{\alpha}^{N_n} \sum_{i \in \{x, y, z\}} \left( \frac{\partial \hat{V}_e}{\partial \mathbf{R}_{\alpha i}} \right)_{\mathbf{R}^{(0)}} \mathbf{u}_{\alpha i} \\ &+ \frac{1}{2} \sum_{\alpha, \beta}^{N_n} \sum_{i, j \in \{x, y, z\}} \left( \frac{\partial^2 \hat{V}_e}{\partial \mathbf{R}_{\alpha i} \partial \mathbf{R}_{\beta j}} \right)_{\mathbf{R}^{(0)}} \mathbf{u}_{\alpha i} \mathbf{u}_{\beta j} \\ &+ O(\mathbf{u}^3), \end{aligned} \quad (1.10)$$

where  $\mathbf{u}_{\alpha} = \mathbf{R}_{\alpha} - \mathbf{R}_{\alpha}^{(0)}$  is the displacement of nucleus  $\alpha$  from its equilibrium position  $\mathbf{R}_{\alpha}^{(0)}$  and  $\mathbf{u} \equiv \{\mathbf{u}_1, \mathbf{u}_2, \dots, \mathbf{u}_{N_n}\}$ . The displacement-dependent terms are collected into  $\Delta \hat{V}_e(\mathbf{r}, \mathbf{R})$ .

Substituting this expansion into Eq. (1.3) and regrouping terms gives

$$\begin{aligned} \hat{H}(\mathbf{r}, \mathbf{R}) &= \hat{T}_e + \hat{T}_n + \hat{V}_e(\mathbf{r}; \mathbf{R}^{(0)}) + \Delta \hat{V}_e(\mathbf{r}, \mathbf{R}) + \hat{V}_{nn}(\mathbf{R}) \\ &= \underbrace{\hat{T}_e + \hat{V}_e(\mathbf{r}; \mathbf{R}^{(0)})}_{\hat{H}_e(\mathbf{r}, \mathbf{R})} + \Delta \hat{V}_e(\mathbf{r}, \mathbf{R}) + \hat{T}_n + \hat{V}_{nn}(\mathbf{R}). \end{aligned} \quad (1.11)$$

The *electronic* Hamiltonian is therefore defined as

$$\hat{H}_e(\mathbf{r}, \mathbf{R}) = \underbrace{\hat{T}_e + \hat{V}_e(\mathbf{r}; \mathbf{R}^{(0)})}_{\hat{H}_e(\mathbf{r}; \mathbf{R}^{(0)})} + \Delta \hat{V}_e(\mathbf{r}, \mathbf{R}), \quad (1.12)$$

with the nuclear kinetic energy  $\hat{T}_n$  and nucleus–nucleus repulsion  $\hat{V}_{nn}(\mathbf{R})$  treated separately, since they depend only on the nuclear coordinates.

In the *crude adiabatic approximation* [40], which is a specific variant within the broader class of adiabatic approximations,<sup>4</sup> the displacement-

---

<sup>4</sup>The term *adiabatic* in the *adiabatic approximation* refers to the separation of electronic and nuclear timescales: nuclei move much more slowly than electrons, allowing the electronic subsystem to remain in its instantaneous eigenstate as long as the nuclear configuration changes gradually and a finite energy gap separates it from nearby states. In the crude adiabatic approximation, this leads to the so-called *frozen nuclei* picture: the electronic structure is solved for fixed nuclear positions, effectively treating the nuclei as static parameters during the electronic problem.

dependent term  $\Delta\hat{V}_e(\mathbf{r}, \mathbf{R})$  in Eq. (1.12) is neglected.<sup>5</sup> The electronic Hamiltonian is then approximated by its *static* counterpart

$$\hat{H}_e(\mathbf{r}; \mathbf{R}^{(0)}) = \hat{T}_e + \hat{V}_e(\mathbf{r}; \mathbf{R}^{(0)}), \quad (1.13)$$

which defines the *electronic* Schrödinger equation:

$$\left[ \hat{T}_e + \hat{V}_e(\mathbf{r}; \mathbf{R}^{(0)}) \right] \psi_s(\mathbf{r}; \mathbf{R}^{(0)}) = \varepsilon_s(\mathbf{R}^{(0)}) \psi_s(\mathbf{r}; \mathbf{R}^{(0)}). \quad (1.14)$$

Here,  $\varepsilon_s(\mathbf{R}^{(0)})$  is the  $s$ -th eigenvalue, depending parametrically on the reference nuclear configuration  $\mathbf{R}^{(0)}$ . This equation is called *static* because it neglects nuclear dynamics. The corresponding *static* eigenfunctions  $\psi_s(\mathbf{r}; \mathbf{R}^{(0)})$  form a complete orthonormal set, which can be used to expand the total electron–nuclear wave function:

$$\Psi_t(\mathbf{r}, \mathbf{R}) = \sum_k \psi_k(\mathbf{r}; \mathbf{R}^{(0)}) \chi_{kt}(\mathbf{R}). \quad (1.15)$$

At this stage,  $\chi_{kt}(\mathbf{R})$  serves as the  $k$ -th expansion coefficient that is itself a function of the nuclear coordinates  $\mathbf{R}$ .

Substituting the ansatz from Eq. (1.15) and the full Hamiltonian of Eq. (1.11) into Eq. (1.2) leads to a set of coupled equations:

$$\begin{aligned} & \left[ \hat{T}_n + \hat{V}_{nn}(\mathbf{R}) \right] \chi_{st}(\mathbf{R}) + \sum_k \left\langle \psi_s(\mathbf{r}; \mathbf{R}^{(0)}) \left| \Delta\hat{V}_e(\mathbf{r}, \mathbf{R}) \right| \psi_k(\mathbf{r}; \mathbf{R}^{(0)}) \right\rangle_{\mathbf{r}} \chi_{kt}(\mathbf{R}) \\ & = \left[ E_{st} - \varepsilon_s(\mathbf{R}^{(0)}) \right] \chi_{st}(\mathbf{R}), \end{aligned} \quad (1.16)$$

where

$$\left\langle y \left| \hat{A} \right| x \right\rangle_{\mathbf{r}} \equiv \int y^* \hat{A} x \, d\mathbf{r}_1 \dots d\mathbf{r}_{N_e}, \quad \mathbf{r} \equiv \{\mathbf{r}_1, \mathbf{r}_2, \dots, \mathbf{r}_{N_e}\}.$$

If the off-diagonal matrix elements of  $\Delta\hat{V}_e(\mathbf{r}, \mathbf{R})$  are neglected,

$$\left\langle \psi_s(\mathbf{r}; \mathbf{R}^{(0)}) \left| \Delta\hat{V}_e(\mathbf{r}, \mathbf{R}) \right| \psi_k(\mathbf{r}; \mathbf{R}^{(0)}) \right\rangle_{\mathbf{r}} = 0 \quad \text{for } k \neq s, \quad (1.17)$$

then it can be shown that the total wave function simplifies to the adiabatic form:

$$\Psi_{st}(\mathbf{r}, \mathbf{R}) = \psi_s(\mathbf{r}; \mathbf{R}^{(0)}) \chi_{st}(\mathbf{R}), \quad (1.18)$$

---

<sup>5</sup>More refined adiabatic approximations, such as the Born–Oppenheimer and Born–Huang schemes, retain the displacement-dependent term  $\Delta\hat{V}_e(\mathbf{r}, \mathbf{R})$ . As a result, the corresponding electronic wave functions depend explicitly on the nuclear coordinates and are referred to as *dynamical*, in contrast to the *static* wave functions used in the crude adiabatic approximation.

where the expansion coefficients  $\chi_{st}(\mathbf{R})$  are obtained by solving the *nuclear* Schrödinger equation:

$$\begin{aligned} & \left[ \hat{T}_n + \hat{V}_{nn}(\mathbf{R}) + \left\langle \psi_s(\mathbf{r}; \mathbf{R}^{(0)}) \left| \Delta \hat{V}_e(\mathbf{r}, \mathbf{R}) \right| \psi_s(\mathbf{r}; \mathbf{R}^{(0)}) \right\rangle_{\mathbf{r}} \right] \chi_{st}(\mathbf{R}) \\ & = \left[ E_{st} - \varepsilon_s(\mathbf{R}^{(0)}) \right] \chi_{st}(\mathbf{R}). \end{aligned} \quad (1.19)$$

It follows that the coefficients  $\chi_{st}(\mathbf{R})$  represent *vibrational* wave functions associated with the *electronic* wave function  $\psi_s(\mathbf{r}; \mathbf{R}^{(0)})$ . The total wave function  $\Psi_{st}(\mathbf{r}, \mathbf{R})$  is thus referred to as *vibronic*, comprising an electronic and a vibrational component.

Even after applying the crude adiabatic approximation and formally separating electronic and nuclear degrees of freedom, solving the resulting electronic and nuclear Schrödinger equations [Eqs. (1.14) and (1.19)] remains a highly complex task, feasible only for the simplest systems. Fortunately, a computational framework exists that enables efficient and accurate treatment of systems containing up to several thousand atoms. This framework is the subject of the following section.

### 1.3. Density functional theory

After applying the crude adiabatic approximation, the first step is to solve the eigenvalue problem defined in Eq. (1.14). In general, the static electronic Hamiltonian  $\hat{H}_e(\mathbf{r}; \mathbf{R}^{(0)})$  appearing in Eq. (1.14) can be written as

$$\hat{H}_e(\mathbf{r}; \mathbf{R}^{(0)}) = \hat{T}_e + \hat{V}_{ee}(\mathbf{r}) + \underbrace{\sum_i^{N_e} v(\mathbf{r}_i; \mathbf{R}^{(0)})}_{\hat{V}_{en}(\mathbf{r}; \mathbf{R}^{(0)})}, \quad (1.20)$$

where  $v(\mathbf{r}_i; \mathbf{R}^{(0)})$  is the external potential acting on the  $i$ -th electron, evaluated at a fixed nuclear configuration  $\mathbf{R}^{(0)}$ . For isolated molecular systems, this external potential corresponds to the interaction between the  $i$ -th electron and the nuclei [Eq. (1.7)]:

$$v(\mathbf{r}_i; \mathbf{R}^{(0)}) = - \sum_{\alpha}^{N_n} \frac{Z_{\alpha}}{|\mathbf{r}_i - \mathbf{R}_{\alpha}^{(0)}|}. \quad (1.21)$$

Despite the adiabatic decoupling, the many-body electronic problem posed by Eq. (1.14) remains computationally intractable for systems of realistic size due to the electron–electron interaction term  $\hat{V}_{ee}(\mathbf{r})$ . Rather than attempting to solve for the many-electron wave function, which depends on  $3N_e$  spatial variables (plus spin), density functional theory (DFT) offers an alternative formulation of the quantum many-electron

problem based solely on the electron density  $\rho(\bar{\mathbf{r}})$ , a function of only three spatial coordinates  $\bar{\mathbf{r}} = (x, y, z)$ , regardless of the number of electrons.

Physically, the electron density  $\rho(\bar{\mathbf{r}})$  gives the average number of electrons contained in an infinitesimal volume element centered at position  $\bar{\mathbf{r}}$ . It is formally<sup>6</sup> defined as

$$\begin{aligned} \rho(\bar{\mathbf{r}}) &\equiv \langle \psi | \hat{\rho}(\bar{\mathbf{r}}) | \psi \rangle = \left\langle \psi \left| \sum_i^{N_e} \delta(\bar{\mathbf{r}} - \mathbf{r}_i) \right| \psi \right\rangle_{\mathbf{r}} \\ &= N_e \int |\psi(\bar{\mathbf{r}}, \mathbf{r}_2, \dots, \mathbf{r}_{N_e})|^2 d^3\mathbf{r}_2 \dots d^3\mathbf{r}_{N_e}, \end{aligned} \quad (1.22)$$

where  $\hat{\rho}(\bar{\mathbf{r}})$  is the electron density operator, and  $\psi$  is the many-body electronic wave function obtained from Eq. (1.14). The prefactor  $N_e$  reflects the indistinguishability of electrons, ensuring that each of the  $N_e$  identical integrals contributes equally to the total density.

Traditional wave function-based methods determine the ground-state energy by minimizing the expectation value of the static electronic Hamiltonian  $\hat{H}_e$  with respect to the many-body electronic wave function  $\psi$ :

$$E_0 = \min_{\psi} \langle \psi | \hat{H}_e | \psi \rangle. \quad (1.23)$$

However, a central insight of DFT is that the ground-state energy and, in principle, all ground-state observables can be expressed as functionals of the ground-state electron density alone, thereby bypassing the need to compute the many-body wave function. This foundational idea is rigorously established by two theorems, which are introduced in the following section.

### 1.3.1. Hohenberg–Kohn theorems

Formulated by Pierre Hohenberg and Walter Kohn in 1964 [26], the Hohenberg–Kohn (HK) theorems provide the theoretical foundation for DFT. These theorems establish a rigorous relationship between the ground-state electron density  $\rho_0(\bar{\mathbf{r}})$  and all ground-state properties of an interacting many-electron system. The original formulation applies to systems with a non-degenerate ground state and in the absence of a vector potential (i.e., magnetic fields), although subsequent generalizations have extended their applicability [41–43].

**First Hohenberg–Kohn theorem.** *For any system of interacting electrons in an external potential  $v(\bar{\mathbf{r}})$ , the ground-state electron density  $\rho_0(\bar{\mathbf{r}})$*

---

<sup>6</sup>The spin degrees of freedom are not explicitly included. In general, the electron density is obtained by integrating Eq. (1.22) over all spatial *and* spin degrees of freedom.

uniquely determines the external potential, up to an additive constant. As a result, the full many-electron Hamiltonian, ground-state wave function, and all ground-state observables are unique functionals of  $\rho_0(\bar{\mathbf{r}})$ .

This theorem establishes that the ground-state density  $\rho_0(\bar{\mathbf{r}})$  encodes, in principle, all information necessary to determine the ground-state properties of the system. In particular, the ground-state wave function  $\psi_0$  and the ground-state energy  $E_0$  can be expressed as unique functionals of  $\rho_0(\bar{\mathbf{r}})$ . Using Eq. (1.20), this leads to the following expression for the ground-state energy:

$$\begin{aligned} E_0 = E[\rho_0] &= \left\langle \underbrace{\psi[\rho_0]}_{\psi_0} \left| \hat{T}_e + \hat{V}_{ee}(\mathbf{r}) + \sum_i^{N_e} v(\mathbf{r}_i; \mathbf{R}^{(0)}) \right| \psi[\rho_0] \right\rangle_{\mathbf{r}} \\ &= F[\rho_0] + \int v(\bar{\mathbf{r}})\rho_0(\bar{\mathbf{r}}) d^3\bar{\mathbf{r}}. \end{aligned} \quad (1.24)$$

In this expression, the total energy is separated into two contributions: the first term,  $F[\rho_0]$ , is a *universal functional* that accounts for the kinetic energy of the electrons and the electron–electron interaction, while the second term represents the interaction with the external potential  $v(\bar{\mathbf{r}}) \equiv v(\bar{\mathbf{r}}; \mathbf{R}^{(0)})$ . More generally, this expression can be written for an arbitrary electron density  $\rho(\bar{\mathbf{r}})$  as

$$E[\rho] = \underbrace{\left\langle \psi[\rho] \left| \hat{T}_e + \hat{V}_{ee}(\mathbf{r}) \right| \psi[\rho] \right\rangle_{\mathbf{r}}}_{F[\rho]} + \int v(\bar{\mathbf{r}})\rho(\bar{\mathbf{r}}) d^3\bar{\mathbf{r}}. \quad (1.25)$$

The universal functional  $F[\rho]$  is so named because it is independent of the external potential and applies to all systems of interacting electrons. It encapsulates the internal energy contributions arising from the kinetic energy and the electron–electron interaction.

**Second Hohenberg–Kohn theorem.** *The energy functional  $E[\rho]$  attains its minimum value if and only if the input density  $\rho(\bar{\mathbf{r}})$  is equal to the true ground-state density  $\rho_0(\bar{\mathbf{r}})$ . That is,*

$$E_0 = \min_{\rho} E[\rho] \iff \rho(\bar{\mathbf{r}}) = \rho_0(\bar{\mathbf{r}}). \quad (1.26)$$

This theorem introduces a variational principle for DFT: if the exact form of the universal functional  $F[\rho]$  were known, the ground-state density  $\rho_0(\bar{\mathbf{r}})$  and corresponding ground-state energy  $E_0$  could be obtained by minimizing the total energy functional  $E[\rho]$  with respect to all physically

admissible densities. Once the ground-state density is determined, all other ground-state properties can, in principle, be derived from it.

However, the exact form of  $F[\rho]$  is unknown, representing the central challenge of practical DFT. Consequently, computational implementations rely on approximate forms of  $F[\rho]$ . Common choices include the local-density approximation (LDA), generalized gradient approximations (GGAs), meta-GGA functionals, and hybrid functionals, each offering a different trade-off between computational efficiency and physical accuracy. These approximations are briefly reviewed in Sec. 1.3.3.

### 1.3.2. Kohn–Sham formalism

While the HK theorems establish that the ground-state electron density uniquely determines all ground-state properties of an interacting many-electron system, they do not provide a practical method for computing this density. To address this limitation, Walter Kohn and Le Jeu Sham proposed in 1965 an auxiliary system of non-interacting electrons that reproduces the exact ground-state electron density of the fully interacting system [27]. This conceptual reformulation leads to a set of self-consistent single-particle equations, known as the Kohn–Sham (KS) equations, which resemble the conventional Schrödinger equation but incorporate electron–electron interactions via an effective potential. The KS formalism enables efficient numerical solutions while retaining the essential physics of the interacting system, and it forms the foundation of nearly all practical implementations of DFT.

In the KS framework, the electron density is constructed from a set of fictitious non-interacting single-particle orbitals,

$$\left\{ \phi_1^{\text{KS}}(\mathbf{r}_1), \phi_2^{\text{KS}}(\mathbf{r}_2), \dots, \phi_{N_e}^{\text{KS}}(\mathbf{r}_{N_e}) \right\}, \quad (1.27)$$

commonly referred to as KS orbitals. These orbitals form an antisymmetric many-electron wave function  $\psi_{\text{KS}}(\mathbf{r})$ , expressed as a single<sup>7</sup> Slater determinant:

$$\begin{aligned} \psi_{\text{KS}}(\mathbf{r}) &= \frac{1}{\sqrt{N_e!}} \left| \phi_1^{\text{KS}} \phi_2^{\text{KS}} \dots \phi_{N_e}^{\text{KS}} \right\rangle \\ &\equiv \frac{1}{\sqrt{N_e!}} \det \begin{pmatrix} \phi_1^{\text{KS}}(\mathbf{r}_1) & \phi_2^{\text{KS}}(\mathbf{r}_1) & \dots & \phi_{N_e}^{\text{KS}}(\mathbf{r}_1) \\ \phi_1^{\text{KS}}(\mathbf{r}_2) & \phi_2^{\text{KS}}(\mathbf{r}_2) & \dots & \phi_{N_e}^{\text{KS}}(\mathbf{r}_2) \\ \vdots & \vdots & \ddots & \vdots \\ \phi_1^{\text{KS}}(\mathbf{r}_{N_e}) & \phi_2^{\text{KS}}(\mathbf{r}_{N_e}) & \dots & \phi_{N_e}^{\text{KS}}(\mathbf{r}_{N_e}) \end{pmatrix}. \end{aligned} \quad (1.28)$$

---

<sup>7</sup>In general, not every electron density  $\rho(\bar{\mathbf{r}})$  can be expressed via a single Slater determinant.

Although the KS wave function  $\psi_{\text{KS}}(\mathbf{r})$  does not represent the true wave function of the interacting system, it is constructed to reproduce the exact ground-state electron density:

$$\begin{aligned}\rho(\bar{\mathbf{r}}) &= \langle \psi_{\text{KS}}(\mathbf{r}) | \hat{\rho}(\bar{\mathbf{r}}) | \psi_{\text{KS}}(\mathbf{r}) \rangle_{\mathbf{r}} \\ &= \sum_i^{N_e} \left| \phi_i^{\text{KS}}(\bar{\mathbf{r}}) \right|^2,\end{aligned}\tag{1.29}$$

where  $\hat{\rho}(\bar{\mathbf{r}})$  is the electron density operator defined in Eq. (1.22).

The central idea proposed by Kohn and Sham was to decompose the universal functional  $F[\rho]$  from Eq. (1.25) into three components:

$$F[\rho] = T_s[\rho] + E_{\text{H}}[\rho] + E_{\text{XC}}[\rho],\tag{1.30}$$

where  $T_s[\rho]$  is the kinetic energy functional of non-interacting electrons, defined as

$$T_s[\rho] = -\frac{1}{2} \sum_i^{N_e} \left\langle \phi_i^{\text{KS}}(\bar{\mathbf{r}}) \left| \frac{\partial^2}{\partial \bar{\mathbf{r}}^2} \right| \phi_i^{\text{KS}}(\bar{\mathbf{r}}) \right\rangle_{\bar{\mathbf{r}}}.\tag{1.31}$$

The second term,  $E_{\text{H}}[\rho]$ , is the classical electrostatic (Hartree) energy of the electron density with itself:

$$E_{\text{H}}[\rho] = \frac{1}{2} \iint \frac{\rho(\bar{\mathbf{r}})\rho(\bar{\mathbf{r}}')}{|\bar{\mathbf{r}}' - \bar{\mathbf{r}}|} d^3\bar{\mathbf{r}} d^3\bar{\mathbf{r}}'.\tag{1.32}$$

The third and final term is the exchange–correlation (XC) energy functional  $E_{\text{XC}}[\rho]$ , defined implicitly as

$$E_{\text{XC}}[\rho] = T_e[\rho] - T_s[\rho] + V_{\text{ee}}[\rho] - E_{\text{H}}[\rho],\tag{1.33}$$

where  $T_e[\rho]$  is the true kinetic energy of the interacting electrons, and  $\hat{V}_{\text{ee}}[\rho]$  is the full electron–electron interaction energy. Thus,  $E_{\text{XC}}[\rho]$  captures all non-classical contributions to the total energy, including exchange, correlation, and the correction to the kinetic energy due to the interactions.

The KS equations are obtained by minimizing the total energy functional  $E[\rho]$  from Eq. (1.25), using the decomposition of  $F[\rho]$  in Eq. (1.30), with respect to a set of orthogonal orbitals. This yields a set of single-particle Schrödinger-like equations:

$$\left[ -\frac{1}{2} \frac{\partial^2}{\partial \bar{\mathbf{r}}^2} + v_{\text{eff}}(\bar{\mathbf{r}}) \right] \phi_i^{\text{KS}}(\bar{\mathbf{r}}) = \varepsilon_i^{\text{KS}} \phi_i^{\text{KS}}(\bar{\mathbf{r}}), \quad i = 1, \dots, N_e,\tag{1.34}$$

where the effective KS potential  $v_{\text{eff}}(\bar{\mathbf{r}})$  is given by

$$v_{\text{eff}}(\bar{\mathbf{r}}) = v(\bar{\mathbf{r}}) + \int \frac{\rho(\bar{\mathbf{r}}')}{|\bar{\mathbf{r}} - \bar{\mathbf{r}}'|} d^3\bar{\mathbf{r}}' + v_{\text{XC}}(\bar{\mathbf{r}}),\tag{1.35}$$

with  $v(\bar{\mathbf{r}})$  being the external potential due to the nuclei [Eq. (1.21)], and  $v_{\text{XC}}(\bar{\mathbf{r}}) = \delta E_{\text{XC}}[\rho]/\delta\rho(\bar{\mathbf{r}})$  the XC potential. This last term is the only component of the effective potential that is not known exactly and must be approximated in practice.

Because the effective potential  $v_{\text{eff}}(\bar{\mathbf{r}})$  depends on the electron density  $\rho(\bar{\mathbf{r}})$ , which itself is constructed from the KS orbitals, the equations in (1.34) must be solved self-consistently. The typical procedure involves:

1. Choosing an initial guess for  $\rho(\bar{\mathbf{r}})$  or for the KS orbitals.
2. Constructing  $v_{\text{eff}}(\bar{\mathbf{r}})$ .
3. Solving the KS equations (1.34) to obtain new orbitals.
4. Recomputing  $\rho(\bar{\mathbf{r}})$  from the new orbitals.
5. Repeating steps 2–4 until convergence is reached.

It is important to emphasize that DFT is formally exact: if the exact XC functional  $E_{\text{XC}}[\rho]$  were known, minimizing the energy functional would yield the exact ground-state electron density and energy. In practice, however, the exact form of  $E_{\text{XC}}[\rho]$  is unknown, and this remains the central challenge of DFT. The next section introduces several commonly used approximations to  $E_{\text{XC}}[\rho]$ . Another key limitation is that, within the Kohn–Sham formalism, the electron density is constrained to originate from an auxiliary system of non-interacting electrons described by a single Slater determinant, making it challenging to treat states that are inherently multi-determinant.

### 1.3.3. Exchange–correlation functionals

As was mentioned previously, the XC energy functional  $E_{\text{XC}}[\rho]$  lies at the core of DFT, capturing the many-body effects of electron exchange and correlation. Since its exact form is unknown, practical DFT relies on a hierarchy of approximations, often organized according to “Jacob’s ladder” [44], a conceptual framework in which successive rungs represent classes of functionals with increasing complexity and accuracy. Each level incorporates additional information about the electron density, such as gradients or kinetic energy density, and offers different trade-offs between accuracy and computational cost. The following subsections provide a brief overview of the most commonly used functional classes.

#### Local-density approximation

The local-density approximation (LDA), first introduced by Kohn and Sham [27], is the simplest non-trivial approximation to the XC functional

and constitutes the first rung of Jacob’s ladder. It is based on the uniform electron gas (UEG) model and assumes that the XC energy at a point in space depends only on the local electron density:

$$E_{\text{XC}}^{\text{LDA}}[\rho] = \int \rho(\bar{\mathbf{r}}) \varepsilon_{\text{XC}}^{\text{UEG}}(\rho(\bar{\mathbf{r}})) d^3\bar{\mathbf{r}}, \quad (1.36)$$

where  $\varepsilon_{\text{XC}}^{\text{UEG}}(\rho(\bar{\mathbf{r}}))$  is the exchange–correlation energy per particle of UEG with density  $\rho(\bar{\mathbf{r}})$ . Despite its simplicity, LDA often yields accurate structural properties for systems with slowly varying electron densities, such as bulk metals and semiconductors. However, it performs poorly for binding energies, chemical reaction barriers, and electronic band gaps [45, 46].

### Generalized gradient approximation

The generalized gradient approximation (GGA) improves upon LDA and constitutes the second rung of Jacob’s ladder [47, 48]. Unlike LDA, which depends only on the local density, GGA also incorporates the density gradient  $\nabla\rho(\bar{\mathbf{r}})$  to account for spatial inhomogeneity:

$$E_{\text{XC}}^{\text{GGA}}[\rho] = \int \rho(\bar{\mathbf{r}}) \varepsilon_{\text{XC}}^{\text{GGA}}(\rho(\bar{\mathbf{r}}), \nabla\rho(\bar{\mathbf{r}})) d^3\bar{\mathbf{r}}. \quad (1.37)$$

By including gradient corrections, GGA functionals better capture density variations. They generally improve equilibrium geometries, cohesive energies, and atomization energies compared to LDA. However, they still suffer from self-interaction errors, systematically underestimate band gaps, and in some cases overcorrect LDA, leading to underbinding.

The most widely used GGA functional is the non-empirical Perdew–Burke–Ernzerhof (PBE) [31], which has become the standard in solid-state physics owing to its balance of accuracy and computational efficiency.

### Meta-GGA functionals

Meta-GGA functionals [49, 50] form the third rung on Jacob’s ladder and introduce additional complexity by incorporating the kinetic energy density  $\tau(\bar{\mathbf{r}})$ :

$$\tau(\bar{\mathbf{r}}) = \frac{1}{2} \sum_i^{N_e} \left| \nabla \phi_i^{\text{KS}}(\bar{\mathbf{r}}) \right|^2, \quad (1.38)$$

where  $\phi_i^{\text{KS}}(\bar{\mathbf{r}})$  are the Kohn–Sham orbitals defined in Eq. (1.27). The general form of a meta-GGA functional is

$$E_{\text{XC}}^{\text{mGGA}}[\rho] = \int \rho(\bar{\mathbf{r}}) \varepsilon_{\text{XC}}^{\text{mGGA}}(\rho(\bar{\mathbf{r}}), \nabla\rho(\bar{\mathbf{r}}), \tau(\bar{\mathbf{r}})) d^3\bar{\mathbf{r}}. \quad (1.39)$$

By including  $\tau(\bar{\mathbf{r}})$ , meta-GGA functionals capture additional non-local effects while avoiding the full computational cost of hybrid or orbital-dependent functionals. They satisfy more exact physical constraints than LDA or GGA and generally provide improved accuracy across a broader range of systems, particularly in describing the lattice parameters and energetics of solids [51].

A prominent example is the strongly constrained and appropriately normed (SCAN) meta-GGA functional [28], which was constructed to satisfy all 17 known exact physical constraints applicable to semilocal functionals. While SCAN significantly improves the description of lattice properties and partially mitigates the band gap underestimation inherent to GGA functionals, it is known to suffer from numerical instabilities, particularly in self-consistent all-electron calculations. To address these issues, the regularized SCAN (rSCAN) [29] functional was introduced; however, this regularization led to a loss of transferability in certain properties, such as atomization energies [52]. This necessitated the development of the re-regularized SCAN (r<sup>2</sup>SCAN) [30] functional. By combining numerical efficiency with the restoration of exact constraint adherence, r<sup>2</sup>SCAN yields consistent performance across diverse systems.

## Hybrid functionals

Hybrid functionals [53] represent the fourth rung of Jacob’s ladder and extend beyond semilocal approximations by incorporating a fraction of exact exchange from Hartree–Fock (HF) theory into the XC functional. In their general form, hybrid functionals are written as

$$E_{\text{XC}}^{\text{hybrid}}(\alpha) = \alpha E_{\text{X}}^{\text{HF}} + (1 - \alpha) E_{\text{X}}^{\text{DFT}} + E_{\text{C}}^{\text{DFT}}, \quad (1.40)$$

where  $E_{\text{X}}^{\text{HF}}$  is the exact non-local HF exchange energy evaluated from Kohn–Sham orbitals,  $E_{\text{X}}^{\text{DFT}}$  and  $E_{\text{C}}^{\text{DFT}}$  are the exchange and correlation contributions from a semilocal functional (typically GGA), and  $\alpha$  is the mixing parameter that determines the fraction of exact exchange.

By partially correcting the self-interaction error inherent in semilocal functionals, hybrid functionals significantly improve the accuracy of electronic structure predictions, particularly for band gaps, defect levels, and reaction barriers. Their main limitation, however, lies in the substantially increased computational cost, since the evaluation of non-local exchange integrals scales poorly with system size, making such calculations especially demanding for extended systems.

To mitigate this, Heyd, Scuseria, and Ernzerhof (HSE) introduced the screened hybrid functional HSE06 [32], which modifies the Coulomb operator used in the exchange interaction. The bare Coulomb potential is

separated into short-range (SR) and long-range (LR) components using the error function  $\text{erf}(z)$  and complementary error function  $\text{erfc}(z)$ :

$$\frac{1}{r_{ij}} = \underbrace{\frac{\text{erfc}(\omega r_{ij})}{r_{ij}}}_{\text{SR}} + \underbrace{\frac{\text{erf}(\omega r_{ij})}{r_{ij}}}_{\text{LR}}, \quad (1.41)$$

where  $r_{ij} = |\mathbf{r}_i - \mathbf{r}_j|$  is the distance between two electrons at positions  $\mathbf{r}_i$  and  $\mathbf{r}_j$ , and  $\omega$  is the screening parameter controlling the range separation. The SR term, which decays rapidly with distance, is treated with exact HF exchange, while the LR part is described at the semilocal DFT level. In HSE06, the hybrid XC functional in Eq. (1.40) therefore takes the form

$$E_{\text{XC}}^{\text{HSE}}(\alpha, \omega) = \alpha E_{\text{X}}^{\text{HF,SR}}(\omega) + (1 - \alpha) E_{\text{X}}^{\text{DFT,SR}}(\omega) + E_{\text{X}}^{\text{DFT,LR}}(\omega) + E_{\text{C}}^{\text{DFT}}, \quad (1.42)$$

where only the SR part of the exchange is mixed with HF exchange. The standard HSE06 functional uses  $\alpha = 0.25$  and  $\omega = 0.2 \text{ \AA}^{-1}$  [32].

This range separation offers several advantages. By confining the expensive HF exchange to SR interactions, the computational cost is significantly reduced compared to unscreened hybrids such as PBE0 [54], while much of the accuracy is retained. At the same time, the treatment of LR exchange at the semilocal level mitigates artificial delocalization of states in extended systems, improving the description of solids and defect levels.

Despite these improvements, HSE06 calculations remain substantially more computationally demanding than those based on LDA, GGA, or meta-GGA functionals. The high cost restricts their applicability in large supercell calculations and high-throughput studies, even though they provide superior accuracy for band gaps, defect levels, and excitation energies. Consequently, HSE06 is often regarded as the “gold standard” for solid-state and defect studies, offering excellent accuracy but at a computational expense that frequently necessitates the use of more approximate functionals for large-scale vibrational or electron-phonon calculations.

### 1.3.4. Practical implementation

While the choice of XC functional determines the theoretical accuracy of a DFT calculation, its practical realization requires several additional considerations. These include the choice of basis set, the treatment of core electrons, and the modeling of extended systems. In the context of solid-state systems such as semiconductors, efficient and accurate

computational methods have been developed to translate the formalism of Kohn–Sham DFT into scalable algorithms suitable for modern high-performance computing architectures.

A number of software packages implement DFT for both finite and extended systems. Widely used frameworks include the **Vienna Ab initio Simulation Package** (VASP) [55, 56], **Quantum ESPRESSO** [57, 58], **ABINIT** [59], and **CASTEP** [60], among others. These codes differ in their internal implementations, supported XC functionals, and pseudopotential formats, but all are grounded in the same fundamental principles of DFT. The present work employs VASP, a plane-wave-based code well-suited for periodic systems and large-scale defect supercells. The specific computational parameters used in this study are described in the final section of this chapter (Sec. 1.8) and in the respective results chapters.

The following subsections outline the core elements of the practical implementation of Kohn–Sham DFT for periodic solids: the plane-wave basis set, the use of pseudopotentials to simplify the treatment of core electrons, and the supercell approach employed to model isolated defects in a crystalline host.

## Plane waves

In periodic solids, the translational symmetry of the crystal lattice allows the application of Bloch’s theorem, which states that the solutions of the Schrödinger equation in a periodic potential can be expressed as plane waves modulated by lattice-periodic functions [61]. Within DFT, each single-particle KS orbital  $\phi^{\text{KS}}(\bar{\mathbf{r}})$  [Eq. (1.27)] takes the form

$$\phi_{n\mathbf{k}}^{\text{KS}}(\bar{\mathbf{r}}) = \exp(i\mathbf{k}\bar{\mathbf{r}})u_{n\mathbf{k}}(\bar{\mathbf{r}}), \quad (1.43)$$

where  $u_{n\mathbf{k}}(\bar{\mathbf{r}})$  is a lattice-periodic function,  $\mathbf{k}$  is an electron wave vector from the first Brillouin zone (BZ), and  $n$  is the band index. The periodic component can be expanded as a Fourier series:

$$u_{n\mathbf{k}}(\bar{\mathbf{r}}) = \sum_{\mathbf{G}} C_{n\mathbf{k}}(\mathbf{G}) \exp(i\mathbf{G}\bar{\mathbf{r}}), \quad (1.44)$$

where the summation runs over all reciprocal lattice vectors  $\mathbf{G}$ , and  $C_{n\mathbf{k}}(\mathbf{G})$  are the expansion coefficients. Substituting this expansion yields the full KS orbital in terms of plane waves:

$$\phi_{n\mathbf{k}}^{\text{KS}}(\bar{\mathbf{r}}) = \sum_{\mathbf{G}} C_{n\mathbf{k}}(\mathbf{G}) \exp[i(\mathbf{k} + \mathbf{G})\bar{\mathbf{r}}]. \quad (1.45)$$

In practice, this expansion is truncated using a kinetic energy cutoff  $E_{\text{cut}}$ , such that only plane waves satisfying

$$\frac{1}{2}|\mathbf{k} + \mathbf{G}|^2 \leq E_{\text{cut}} \quad (1.46)$$

are included. The cutoff energy is a key convergence parameter that must be tested to ensure that total energies and derived properties are adequately described.

Many physical quantities, such as total energy, charge density, or the density of states, require integration over the BZ:

$$\langle A \rangle = \frac{1}{\Omega_{\text{BZ}}} \int_{\text{BZ}} A(\mathbf{k}) \, d^3\mathbf{k}, \quad (1.47)$$

where  $\Omega_{\text{BZ}}$  is the volume of the BZ. In practice, this integral is replaced by a discrete weighted sum over a finite set of  $\mathbf{k}$ -points:

$$\langle A \rangle \approx \sum_{\mathbf{k}} w_{\mathbf{k}} A(\mathbf{k}), \quad (1.48)$$

where  $w_{\mathbf{k}}$  are the weights associated with each sampled point. A widely adopted method for generating such grids is the Monkhorst–Pack scheme, which produces uniform, symmetry-respecting meshes in the BZ [62]. The density of the  $\mathbf{k}$ -point mesh must be systematically tested to ensure convergence of calculated properties.

The plane-wave basis set is particularly well-suited for periodic systems because of its orthogonality, completeness, and systematic convergence with respect to the cutoff energy. However, the large number of plane waves required, especially near atomic nuclei, renders calculations prohibitively expensive if all electrons are treated explicitly. This motivates the use of pseudopotentials, which replace the all-electron problem with an effective potential that reproduces valence electron behavior while simplifying the treatment of tightly bound core electrons.

## Pseudopotentials

In all-electron calculations, the presence of tightly bound core electrons gives rise to rapid oscillations of the wave functions near the nuclei. Resolving these oscillations accurately requires an extremely large number of plane waves, rendering such calculations computationally prohibitive. Pseudopotentials provide an effective solution by replacing the strong Coulomb potential of the nucleus and core electrons with a smoother effective potential that acts only on valence electrons. In this approach, the chemically inert core electrons are frozen, while the valence electrons, responsible for bonding and electronic properties, are described explicitly.

Several types of pseudopotentials are widely used. Norm-conserving pseudopotentials [63] enforce exact conservation of the norm of the all-electron and pseudo wave functions outside a chosen cutoff radius, ensuring transferable scattering properties but often requiring relatively high plane-wave cutoffs. Ultrasoft pseudopotentials [64] relax the norm-conservation condition, yielding much “softer” pseudo wave functions and significantly reducing the required basis size.

An alternative approach, and the one employed in this thesis, is the projector-augmented wave (PAW) method [65], as implemented in VASP. The PAW method combines the efficiency of pseudopotentials with the accuracy of all-electron methods. It introduces a linear transformation  $\mathcal{T}$  that relates a “soft” pseudo wave function  $\psi_{\text{PS}}$  to the corresponding all-electron<sup>8</sup> wave function  $\psi_{\text{AE}}$ :

$$\begin{aligned} |\psi_{\text{PS}}\rangle &= \mathcal{T}|\psi_{\text{AE}}\rangle, \\ &= \left[ \hat{I} + \sum_m (|\phi_m\rangle - |\phi'_m\rangle)\langle p_m| \right] |\psi_{\text{AE}}\rangle \end{aligned} \quad (1.49)$$

where  $\hat{I}$  is the identity operator,  $\phi_m$  are atom-centered all-electron partial waves,  $\phi'_m$  are the corresponding smooth pseudo partial waves, and  $p_m$  are localized projector functions. Within each augmentation sphere surrounding an atom, the true nodal structure of the wave function is fully reconstructed from the smooth pseudo wave function using this transformation. Outside the spheres, the pseudo and all-electron wave functions coincide.

The PAW method thus retains all-electron accuracy while dramatically reducing the plane-wave cutoff required for convergence. This makes it particularly effective for systems containing transition metals or heavy elements, where core electrons are tightly localized. At the same time, the method remains systematically improvable and free from many of the transferability issues that affect traditional pseudopotentials.

## Supercell approach

In defect modeling, the supercell approach is a widely used technique to represent an isolated defect within a periodic solid. A supercell is constructed by repeating either the primitive or conventional unit cell of the host crystal to form a larger simulation cell, into which a defect is introduced. When combined with periodic boundary conditions,

---

<sup>8</sup>Note that the “all-electron” wave function  $\psi_{\text{AE}}$  is a Kohn–Sham single-particle wave function, and should not be confused with the many-electron wave function introduced earlier.

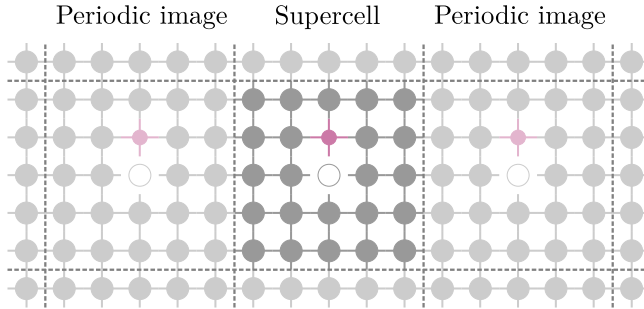


**Figure 1.1.** Schematic illustration of the supercell approach for a point defect in solid, with supercell boundaries shown as dashed lines

this effectively models an infinite crystal containing a periodic array of identical defects, as illustrated in Fig. 1.1.

Although conceptually straightforward, this periodic repetition introduces finite-size effects, which arise from spurious interactions between a defect and its periodic images. These effects influence calculated total energies, electronic structure, and vibrational properties, and must be carefully assessed by performing convergence tests with respect to supercell size.

This self-interaction issue is especially pronounced for charged defects. In such cases, the periodic repetition of charged supercells leads to artificial electrostatic interactions that do not exist in the dilute-defect limit. Correction schemes, such as that proposed by Freysoldt *et al.* [66], are commonly applied to eliminate the dominant spurious contributions and yield quantitatively reliable defect formation energies and charge-state transition levels.

Another important finite-size effect concerns nuclear relaxation. In the supercell method, relaxation of nuclear positions is confined to the volume of the simulation cell. As a result, displacement fields cannot extend beyond the supercell boundaries, and almost no relaxation occurs at positions midway between a defect and its periodic image. In reality, relaxation patterns around defects may be long-ranged, and this behavior is not always captured within finite supercells. This limitation is further addressed in Sec. 1.7.

## 1.4. Vibrational properties of solids

In the previous sections, the many-body problem was introduced, and the crude adiabatic approximation was used to separate the electronic and nuclear degrees of freedom. While the preceding discussion focused

on solving the electronic problem in Eq. (1.14), the focus here shifts to the nuclear problem in Eq. (1.19), which governs the dynamics of ions in the crystal lattice.<sup>9</sup> In practice, the most relevant processes involve vibrations of ions around their equilibrium positions, which determine the vibrational structure of solids.

### 1.4.1. Adiabatic potential energy surface

The electronic Schrödinger equation can, in principle, be solved for any fixed configuration of the nuclei. However, when investigating vibrational properties, the primary interest lies in the dynamics of nuclei near the equilibrium geometry  $\mathbf{R}^{(0)}$ , corresponding to the minimum of the adiabatic potential energy surface (APES),  $E_{\text{APES}}(\mathbf{R})$ . The procedure of locating this minimum is known as *ionic relaxation*, during which the forces on the nuclei are minimized.

Within DFT, the APES is given by

$$E_{\text{APES}}(\mathbf{R}) = \varepsilon_s(\mathbf{R}) + \hat{V}_{\text{nn}}(\mathbf{R}), \quad (1.50)$$

where  $\varepsilon_s(\mathbf{R})$  is the electronic energy of state  $\psi_s(\mathbf{r}; \mathbf{R})$  [Eq. (1.14)] and  $\hat{V}_{\text{nn}}(\mathbf{R})$  is the nucleus–nucleus Coulomb repulsion [Eq. (1.8)].

The forces on the nuclei follow from the gradient of the APES. Using the Hellmann–Feynman theorem [67], the force on nucleus  $\alpha$  is

$$\begin{aligned} \mathbf{F}_\alpha(\mathbf{R}) &= -\frac{\partial E_{\text{APES}}(\mathbf{R})}{\partial \mathbf{R}_\alpha} \\ &= -\left\langle \psi_s(\mathbf{r}; \mathbf{R}) \left| \frac{\partial \hat{V}_{\text{en}}(\mathbf{r}; \mathbf{R})}{\partial \mathbf{R}_\alpha} \right| \psi_s(\mathbf{r}; \mathbf{R}) \right\rangle_{\mathbf{r}} - \frac{\partial \hat{V}_{\text{nn}}(\mathbf{R})}{\partial \mathbf{R}_\alpha}. \end{aligned} \quad (1.51)$$

Expressed in terms of the electron density  $\rho(\bar{\mathbf{r}})$ , this becomes

$$\mathbf{F}_\alpha(\mathbf{R}) = -\int \rho(\bar{\mathbf{r}}) \frac{\partial \hat{V}_{\text{en}}(\bar{\mathbf{r}}; \mathbf{R})}{\partial \mathbf{R}_\alpha} d^3\bar{\mathbf{r}} - \frac{\partial \hat{V}_{\text{nn}}(\mathbf{R})}{\partial \mathbf{R}_\alpha}. \quad (1.52)$$

Thus, the forces depend explicitly on the electron density  $\rho(\bar{\mathbf{r}})$ , which is directly accessible within DFT. The nuclear kinetic energy operator  $\hat{T}_{\text{n}}$  [Eq. (1.5)] has no explicit dependence on  $\mathbf{R}$  and therefore does not contribute to the static force.

---

<sup>9</sup>In this work, unless stated otherwise, the terms “nucleus” and “ion” are used interchangeably, even though they are not strictly identical. In condensed matter physics, “ion” typically means “nucleus + frozen core electrons”.

### 1.4.2. Harmonic approximation

To describe nuclear vibrations, the APES is expanded in a Taylor series around the equilibrium configuration  $\mathbf{R}^{(0)}$ , analogous to the expansion of  $\hat{V}_e(\mathbf{r}, \mathbf{R})$  in Eq. (1.10):

$$\begin{aligned}
 E_{\text{APES}}(\mathbf{R}) &= E_{\text{APES}}\left(\mathbf{R}^{(0)}\right) \\
 &+ \sum_{\alpha}^{N_n} \sum_{i \in \{x,y,z\}} \left( \frac{\partial E_{\text{APES}}}{\partial \mathbf{R}_{\alpha_i}} \right)_{\mathbf{R}^{(0)}} \mathbf{u}_{\alpha_i} \\
 &+ \frac{1}{2} \sum_{\alpha, \beta}^{N_n} \sum_{i, j \in \{x,y,z\}} \left( \frac{\partial^2 E_{\text{APES}}}{\partial \mathbf{R}_{\alpha_i} \partial \mathbf{R}_{\beta_j}} \right)_{\mathbf{R}^{(0)}} \mathbf{u}_{\alpha_i} \mathbf{u}_{\beta_j} \\
 &+ O(\mathbf{u}^3),
 \end{aligned} \tag{1.53}$$

where  $\mathbf{u}_{\alpha} = \mathbf{R}_{\alpha} - \mathbf{R}_{\alpha}^{(0)}$  are displacements from equilibrium. The first term,  $E_{\text{APES}}(\mathbf{R}^{(0)})$ , is a constant reference point. The second (linear) term vanishes because the forces are zero at equilibrium, leaving the quadratic term:

$$\begin{aligned}
 E_{\text{APES}}(\mathbf{R}) &\approx \frac{1}{2} \sum_{\alpha, \beta}^{N_n} \sum_{i, j \in \{x,y,z\}} \left( \frac{\partial^2 E_{\text{APES}}}{\partial \mathbf{R}_{\alpha_i} \partial \mathbf{R}_{\beta_j}} \right)_{\mathbf{R}^{(0)}} \mathbf{u}_{\alpha_i} \mathbf{u}_{\beta_j} \\
 &= \frac{1}{2} \sum_{\alpha, \beta}^{N_n} \sum_{i, j \in \{x,y,z\}} \Phi_{\alpha_i \beta_j} \mathbf{u}_{\alpha_i} \mathbf{u}_{\beta_j},
 \end{aligned} \tag{1.54}$$

with the elements of the *force-constant (Hessian) matrix*  $\Phi$  defined as

$$\Phi_{\alpha_i \beta_j} \equiv \left( \frac{\partial^2 E_{\text{APES}}}{\partial \mathbf{R}_{\alpha_i} \partial \mathbf{R}_{\beta_j}} \right)_{\mathbf{R}^{(0)}}. \tag{1.55}$$

Each sub-block  $\Phi_{\alpha\beta}$  is a  $3 \times 3$  matrix,

$$\Phi_{\alpha\beta} \equiv \begin{pmatrix} \Phi_{\alpha_x \beta_x} & \Phi_{\alpha_x \beta_y} & \Phi_{\alpha_x \beta_z} \\ \Phi_{\alpha_y \beta_x} & \Phi_{\alpha_y \beta_y} & \Phi_{\alpha_y \beta_z} \\ \Phi_{\alpha_z \beta_x} & \Phi_{\alpha_z \beta_y} & \Phi_{\alpha_z \beta_z} \end{pmatrix}, \tag{1.56}$$

where  $\Phi_{\alpha_i \beta_j}$  is the force acting on nucleus  $\alpha$  along Cartesian direction  $i$  when nucleus  $\beta$  is displaced from its equilibrium position by a unit vector along Cartesian direction  $j$ .

Neglecting *anharmonic*, higher-order terms in the expansion ( $\mathbf{u}^3, \mathbf{u}^4, \dots$ ), the nuclear Hamiltonian becomes

$$\hat{H}_n(\mathbf{R}) = \hat{T}_n + \frac{1}{2} \sum_{\alpha, \beta}^{N_n} \mathbf{u}_{\alpha}^{\top} \Phi_{\alpha\beta} \mathbf{u}_{\beta}, \tag{1.57}$$

where

$$\mathbf{u}_\alpha^\top = [\mathbf{u}_{\alpha_x} \quad \mathbf{u}_{\alpha_y} \quad \mathbf{u}_{\alpha_z}]$$

denotes the transpose of the displacement column vector of nucleus  $\alpha$ . This Hamiltonian represents the *harmonic* approximation of the general nuclear Hamiltonian introduced in Eq. (1.19); it is obtained by expanding the APES about the equilibrium geometry  $\mathbf{R}^{(0)}$  and truncating at the second order.

In this formulation, the system is composed of a set of *coupled* harmonic oscillators. A direct solution is difficult because the nuclear coordinates are coupled through the off-diagonal Hessian elements. However, a transformation to the *normal-mode* basis diagonalizes both the kinetic and potential energy operators, yielding a set of *independent* oscillators—the *phonon modes* of the crystal.

### 1.4.3. Vibrations in the classical description

In the harmonic approximation, the potential energy of the lattice is expressed in terms of the force-constant matrix  $\Phi$ , which couples the displacements of different nuclei. For a crystal containing  $N_{\text{cells}}$  unit cells, each labeled by a tuple  $m \equiv (m_1, m_2, m_3)$  and associated with a Bravais lattice vector  $\mathbf{l}_m = m_1 \mathbf{a}_1 + m_2 \mathbf{a}_2 + m_3 \mathbf{a}_3$  (where  $\mathbf{a}_i$  are the primitive lattice vectors), and hosting  $\sigma$  nuclei per unit cell (so that  $N_n = \sigma N_{\text{cells}}$ ), the displacement of nucleus  $\alpha \in \{1, 2, \dots, \sigma\}$  in unit cell  $m \in \{1, 2, \dots, N_{\text{cells}}\}$  is denoted as  $\mathbf{u}_{m_\alpha}(t)$ . The classical equations of motion are

$$M_\alpha \ddot{\mathbf{u}}_{m_\alpha}(t) = - \sum_n^{N_{\text{cells}}} \sum_\beta^\sigma \Phi_{m_\alpha n_\beta} \mathbf{u}_{n_\beta}(t), \quad (1.58)$$

which represents a system of  $3\sigma N_{\text{cells}} = 3N_n$  coupled second-order differential equations.

Because of the translational symmetry of the lattice, the displacements can be expressed as collective plane-wave oscillations, analogous to Bloch's theorem [61]. The solutions of Eq. (1.58) can thus be written as

$$\begin{aligned} \mathbf{u}_{m_\alpha}(t, \mathbf{q}) &= \frac{1}{\sqrt{N_{\text{cells}} M_\alpha}} e_\alpha(\mathbf{q}) A_{\mathbf{q}}(t) \exp(i\mathbf{q}\mathbf{l}_m), \\ A_{\mathbf{q}}(t) &= A_{\mathbf{q}} \exp(-i\omega_{\mathbf{q}} t), \end{aligned} \quad (1.59)$$

where  $\mathbf{q}$  is the vibrational wave vector in the first Brillouin zone,  $\omega_{\mathbf{q}}$  is the angular frequency,  $e_\alpha(\mathbf{q})$  is the *polarization vector* of nucleus  $\alpha$ ,  $A_{\mathbf{q}}(t)$  is the (mass-weighted) *normal coordinate* with dimension  $[A_{\mathbf{q}}(t)] = \text{M}^{1/2}\text{L}$ , and  $\exp(i\mathbf{q}\mathbf{l}_m)$  is the Bloch factor.

Substituting Eq. (1.59) into Eq. (1.58) gives

$$\omega_{\mathbf{q}}^2 \mathbf{e}_{\alpha}(\mathbf{q}) = \sum_{\beta}^{\sigma} \mathbf{D}_{\alpha\beta}(\mathbf{q}) \mathbf{e}_{\beta}(\mathbf{q}), \quad (1.60)$$

where the *dynamical matrix*  $\mathbf{D}(\mathbf{q})$  is constructed from the force constants:

$$\mathbf{D}_{\alpha\beta}(\mathbf{q}) = \sum_n^{N_{\text{cells}}} \frac{\Phi_{m_{\alpha}n_{\beta}}}{\sqrt{M_{\alpha}M_{\beta}}} \exp[i\mathbf{q}(\mathbf{l}_n - \mathbf{l}_m)]. \quad (1.61)$$

The matrix  $\mathbf{D}(\mathbf{q})$  is Hermitian and of size  $3\sigma \times 3\sigma$ , much smaller than the full Hessian  $\Phi$ . Consequently, Eq. (1.60) reduces the problem to finding  $3\sigma$  real eigenvalues  $\omega_{\mathbf{q}\lambda}$  and generally complex<sup>10</sup> eigenvectors  $\mathbf{e}_{\alpha\lambda}(\mathbf{q})$  for each  $\mathbf{q}$ , instead of solving  $3\sigma N_{\text{cells}}$  equations as in Eq. (1.58).<sup>11</sup> Here  $\lambda \in \{1, 2, \dots, 3\sigma\}$  labels the *vibrational branches*. To obtain the full vibrational spectrum, Eq. (1.60) is solved for all  $\mathbf{q}$ -points in the first Brillouin zone, whose number equals the number of unit cells  $N_{\text{cells}}$  in the crystal [68].

#### 1.4.4. Normal modes and phonons

The solution in Eq. (1.59) describes the vibration of nucleus  $\alpha$  in unit cell  $m$  for branch  $\lambda$  at wave vector  $\mathbf{q}$ . Any vibrational motion of nucleus  $\alpha$  can be expressed as a superposition of such harmonic vibrations:

$$\mathbf{u}_{m_{\alpha}}(t) = \sum_{\mathbf{q}}^{N_{\text{cells}}} \sum_{\lambda}^{3\sigma} \frac{1}{\sqrt{N_{\text{cells}}M_{\alpha}}} \mathbf{e}_{\alpha\lambda}(\mathbf{q}) A_{\mathbf{q}\lambda}(t) \exp(i\mathbf{q}\mathbf{l}_m), \quad (1.62)$$

$$A_{\mathbf{q}\lambda}(t) = A_{\mathbf{q}\lambda} \exp(-i\omega_{\mathbf{q}\lambda}t).$$

Each pair  $(\mathbf{q}, \lambda)$  defines a *normal mode* of lattice vibration. A normal mode is not the motion of a single nucleus but a collective pattern of displacements<sup>12</sup> across the entire lattice:

$$\mathbf{u}_{m_{\alpha}}^{(\mathbf{q}, \lambda)}(t) = \frac{1}{\sqrt{N_{\text{cells}}M_{\alpha}}} \mathbf{e}_{\alpha\lambda}(\mathbf{q}) A_{\mathbf{q}\lambda}(t) \exp(i\mathbf{q}\mathbf{l}_m). \quad (1.63)$$

<sup>10</sup>Complex polarization vectors describe elliptically polarized nuclear motions. At the  $\Gamma$ -point ( $\mathbf{q} = \mathbf{0}$ ), however, the dynamical matrix  $\mathbf{D}(\mathbf{q})$  becomes real, and consequently the polarization vectors  $\mathbf{e}_{\alpha\lambda}(\mathbf{q})$  are real as well.

<sup>11</sup>This “reduction” is possible because the elements of the force-constant matrix  $\Phi$  depend only on the relative unit cell index  $(n - m)$ , ensured by the translational symmetry of the crystal lattice.

<sup>12</sup>Strictly speaking, the physically observable displacements correspond to the real component of Eq. (1.63).

- The polarization vector  $\mathbf{e}_{\alpha\lambda}(\mathbf{q})$  is generally complex and dimensionless, defining the relative motion of nucleus  $\alpha$  within the unit cell. It satisfies the following conditions [69]:

$$\begin{aligned}\sum_{\alpha}^{\sigma} \mathbf{e}_{\alpha\lambda}(\mathbf{q}) \mathbf{e}_{\alpha\lambda'}^*(\mathbf{q}) &= \delta_{\lambda\lambda'}, \\ \sum_{\lambda}^{3\sigma} e_{\alpha\gamma\lambda}(\mathbf{q}) e_{\beta\gamma'\lambda}^*(\mathbf{q}) &= \delta_{\alpha\beta} \delta_{\gamma\gamma'}, \\ \mathbf{e}_{\alpha\lambda}(\mathbf{q}) &= \mathbf{e}_{\alpha\lambda}^*(-\mathbf{q}), \\ \mathbf{e}_{\alpha\lambda}(\mathbf{q} + \mathbf{q}') &= \mathbf{e}_{\alpha\lambda}(\mathbf{q}), \quad \mathbf{q}' \in \mathbf{G}.\end{aligned}$$

- The normal coordinate  $A_{\mathbf{q}\lambda}(t)$  is a mass-weighted amplitude of mode  $(\mathbf{q}, \lambda)$ , oscillating harmonically with frequency  $\omega_{\mathbf{q}\lambda}$ .
- The Bloch factor  $\exp(i\mathbf{q}\mathbf{l}_m)$  ensures that the displacement pattern is periodically reproduced across the lattice with the correct phase relation between unit cells.

Thus, a normal mode  $(\mathbf{q}, \lambda)$  corresponds to the complete set of displacements  $\{\mathbf{u}_{m\alpha}^{(\mathbf{q},\lambda)}(t)\}$ , with  $m\alpha \in \{1, \dots, N_n\}$ . The ensemble of all such modes constitutes a complete basis for representing any possible harmonic lattice vibration.

Using these definitions,<sup>13</sup> the harmonic nuclear Hamiltonian (1.57) can be expressed in terms of the normal coordinates  $A_{\mathbf{q}\lambda}(t)$ :

$$\hat{H}_n = \frac{1}{2} \sum_{\mathbf{q}}^{N_{\text{cells}}} \sum_{\lambda}^{3\sigma} \left[ \dot{A}_{\mathbf{q}\lambda}(t) \dot{A}_{\mathbf{q}\lambda}^*(t) + \omega_{\mathbf{q}\lambda}^2 A_{\mathbf{q}\lambda}(t) A_{\mathbf{q}\lambda}^*(t) \right]. \quad (1.64)$$

Introducing real generalized coordinates

$$Q_{\mathbf{q}\lambda}(t) = \frac{1}{\sqrt{2}} (A_{\mathbf{q}\lambda}(t) + A_{\mathbf{q}\lambda}^*(t)), \quad (1.65)$$

the Hamiltonian becomes

$$\hat{H}_n = \frac{1}{2} \sum_{\mathbf{q}}^{N_{\text{cells}}} \sum_{\lambda}^{3\sigma} \left[ \dot{Q}_{\mathbf{q}\lambda}^2(t) + \omega_{\mathbf{q}\lambda}^2 Q_{\mathbf{q}\lambda}^2(t) \right]. \quad (1.66)$$

---

<sup>13</sup>The derivation employs the symmetry and normalization properties of the dynamical matrix  $\mathbf{D}(\mathbf{q})$  and the polarization vectors  $\mathbf{e}_{\alpha\lambda}(\mathbf{q})$ .

This transformation diagonalizes both the kinetic and potential energy terms, revealing that the set  $\mathbf{Q} \equiv \{Q_{\mathbf{q}\lambda}\}$  constitutes a basis of *mass-weighted normal coordinates*, each describing an *independent* harmonic oscillator.

The vibrational eigenfunctions of the Schrödinger equation corresponding to the Hamiltonian (1.66) can be written as products of one-dimensional harmonic oscillator eigenfunctions:

$$\chi(\mathbf{Q}) = \prod_k^{3N_n} \chi_k(Q_k), \quad m_k \in \{0, 1, 2, \dots\}, \quad (1.67)$$

where  $k \equiv (\mathbf{q}, \lambda)$  labels a normal mode,  $\chi_k(Q_k)$  is the eigenfunction of a one-dimensional harmonic oscillator with frequency  $\omega_k$ , and  $m_k$  is the vibrational quantum number specifying the excitation level of mode  $k$ . The complete vibrational state of the lattice is thus characterized by the set  $\{m_k\}$  and can be represented by a Fock state vector  $|m_1, m_2, \dots, m_{3N_n}\rangle$ .

In the quantum-mechanical description (and in Hartree atomic units, where  $\hbar = 1$ ), each harmonic oscillator has energy eigenvalues

$$\epsilon_k = \omega_k \left(m_k + \frac{1}{2}\right), \quad m_k \in \{0, 1, 2, \dots\}. \quad (1.68)$$

The quantum of energy  $\omega_k$  associated with mode  $k$  defines a *phonon*. When the oscillator is in its  $m_k$ -th state, the mode  $k$  contains  $m_k$  phonons, i.e.,  $m_k$  quanta of lattice vibration  $k$ .

### 1.4.5. Defect vibrational modes

The quantization of lattice vibrations into phonons, introduced in the previous section, assumes perfect translational symmetry of the crystal. The presence of a point defect breaks this symmetry and modifies the phonon spectrum. Although spatially confined, a defect can alter the vibrational properties of nearby nuclei and lead to distinct types of vibrational modes, generally classified into three categories [70, 71]:

1. Bulk-like modes—spatially extended, closely resemble vibrations in the pristine lattice.
2. Localized modes—confined to the vicinity of the defect, typically appearing outside the bulk phonon energy spectrum.
3. Quasi-localized (resonant) modes—hybrid modes lying within the bulk phonon energy spectrum, resulting from coupling between extended phonons and defect-induced distortions.

To quantify localization, mass-weighted polarization vectors  $\sqrt{M_\alpha}\mathbf{e}_\alpha(k)$  are used. The total contribution of nucleus  $\alpha \in \{1, \dots, N_n\}$  to phonon mode  $k \in \{1, \dots, 3N_n\}$  is given by [70]

$$w_\alpha(k) = M_\alpha |\mathbf{e}_\alpha(k)|^2, \quad (1.69)$$

which is proportional to the kinetic energy of nucleus  $\alpha$ .

Using these contribution quantities, the inverse participation ratio (IPR) is defined as [70, 71]

$$\text{IPR}_k = \frac{\left[ \sum_{\alpha}^{N_n} w_\alpha(k) \right]^2}{\sum_{\alpha}^{N_n} [w_\alpha(k)]^2}. \quad (1.70)$$

The  $\text{IPR}_k$  represents the effective number of nuclei participating in vibrational mode  $k$ . If only one nucleus contributes,  $\text{IPR}_k = 1$ . If all  $N_n$  nuclei contribute equally,  $\text{IPR}_k = N_n$ . For partial localization involving  $P < N_n$  nuclei,  $\text{IPR}_k \approx P$ . A truly localized mode is characterized by an IPR that remains constant as the supercell size increases [71].

In defect calculations employing periodic supercells (Sec. 1.3.4), the IPR is evaluated over the nuclei contained in the supercell. A complementary dimensionless quantity, the *localization ratio*, is defined as [71]

$$\beta_k = \frac{N_n}{\text{IPR}_k}. \quad (1.71)$$

A larger  $\beta_k$  indicates stronger localization and, consequently, a smaller spatial extent of the defect-induced vibrational mode.

## 1.5. Electronic degeneracy and vibronic interactions

Electronic degeneracy is a characteristic feature of point defects in solids, especially those with high-symmetry atomic arrangements. The most common case is an orbital doublet, conventionally denoted as  $E$ , which appears, for example, in trigonal or tetrahedral environments. Such degeneracies give rise to non-adiabatic interactions between electronic states and symmetry-lowering vibrational modes, a phenomenon known as the Jahn–Teller (JT) effect [72–75].

In the adiabatic picture discussed in Sec. 1.2, the nuclear dynamics are described as motion on a single potential energy surface (PES). When an electronic state is orbitally degenerate, however, coupling to vibrational modes of appropriate symmetry invalidates this adiabatic separation: nuclear motion can “mix” different components of the electronic multiplet,

and the PES develops a multidimensional structure with several minima. The JT effect is therefore inherently vibronic, involving the simultaneous treatment of electronic and vibrational degrees of freedom.

If the electron–phonon coupling is strong, the electronic degeneracy is lifted statically and the system distorts to a symmetry-broken geometrical configuration. If the coupling is weak or moderate, the electronic degeneracy is preserved on average, but the vibronic states differ fundamentally from those of the simple adiabatic framework. This regime is referred to as the dynamical Jahn–Teller (DJT) effect [74, 76]. The DJT effect modifies effective low-energy Hamiltonians, such as spin–orbit and Zeeman interactions [76, 77], and has important consequences for the spectroscopic signatures of point defects.

The canonical model is the  $E \otimes e$  problem, in which a doubly degenerate orbital couples to a doubly degenerate vibrational mode of  $e$ -symmetry. Longuet-Higgins *et al.* [74] showed that optical transitions involving such states exhibit characteristic double-peaked vibronic sidebands. Later, O’Brien [78, 79] extended the theory by demonstrating that for strong vibronic couplings the problem can often be mapped onto effective single-mode Hamiltonians, whereas weak and intermediate couplings require multimode treatments [80, 81]. More recently, Razinkovas *et al.* [39] developed a methodology to construct the full  $E \otimes (e \oplus e \oplus \dots)$  Hamiltonian from DFT calculations, enabling realistic modeling of defect centers where many vibrational modes contribute to the JT effect. Their work highlighted the limitations of the single-mode approximation and the adiabatic Huang–Rhys (HR) model in describing optical lineshapes when the final state is a degenerate JT-active state. They applied this methodology to the absorption spectrum of the negatively charged nitrogen-vacancy ( $\text{NV}^-$ ) center in diamond. In this case, however, the JT coupling was relatively minor compared with the contribution from symmetry-preserving, JT-inactive modes. While the theory successfully reproduced the weight distribution in the absorption lineshape, the DJT effect did not produce prominent features associated with the JT-active modes. In Chapter 5 of this thesis, a system is addressed where JT coupling plays a more significant role than the contributions from JT-inactive modes.

### 1.5.1. Vibronic states and the Jahn–Teller Hamiltonian

For a non-degenerate electronic state, the vibronic wave function factorizes into independent electronic and vibrational components [Eqs. (1.18) and (1.67)]:

$$\Psi_{pr}(\mathbf{r}, \mathbf{R}) = \chi_p^a(\mathbf{Q}_a) \chi_r^e(\mathbf{Q}_e) \psi_A(\mathbf{r}; \mathbf{R}^{(0)}), \quad (1.72)$$

where  $\psi_A(\mathbf{r}; \mathbf{R}^{(0)})$  is the static electronic wave function [the solution of Eq. (1.14)], while  $\chi_p^a(\mathbf{Q}_a)$  and  $\chi_r^e(\mathbf{Q}_e)$  are vibrational eigenfunctions associated with symmetry-preserving ( $a$ ) and symmetry-breaking ( $e$ ) mass-weighted normal coordinates,  $\mathbf{Q}_a$  and  $\mathbf{Q}_e$ , respectively. The indices  $p$  and  $r$  enumerate the excitation levels of the corresponding harmonic oscillators. In this representation, the electronic wave function  $\psi_A(\mathbf{r}; \mathbf{R}^{(0)})$  depends only on the electronic degrees of freedom and remains decoupled from the vibrational dynamics.

In an  $E \otimes (e \oplus e \oplus \dots)$  system, the Hamiltonian describing the JT interaction commutes with the Hamiltonian associated with symmetry-preserving  $a$ -type modes. This allows the harmonic phonon states  $|\chi_p^a\rangle$  to be treated separately, while the JT-active subsystem involves the  $e$ -symmetry vibrational coordinates coupled to the degenerate electronic doublet  $\{|E_x\rangle, |E_y\rangle\}$ .

For this JT-active subsystem, the degeneracy of the electronic doublet necessitates the inclusion of electron–phonon coupling terms that mix the two components through nuclear displacements, that are absent in Eq. (1.19). The general vibronic wave function can therefore be expressed as [75]

$$\begin{aligned}\Psi_{st}(\mathbf{r}, \mathbf{R}) &= \chi_s^a(\mathbf{Q}_a)\Phi_t(\mathbf{r}, \mathbf{R}), \\ \Phi_t(\mathbf{r}, \mathbf{R}) &= \chi_t^{e_x}(\mathbf{Q}_e)\psi_{E_x}(\mathbf{r}; \mathbf{R}^{(0)}) + \chi_t^{e_y}(\mathbf{Q}_e)\psi_{E_y}(\mathbf{r}; \mathbf{R}^{(0)}),\end{aligned}\tag{1.73}$$

where  $\chi_t^{e\gamma}(\mathbf{Q}_e)$  ( $\gamma \in \{x, y\}$ ) are vibrational coefficients obtained by solving the JT problem, and the quantum number  $t$  enumerates the vibronic excitations of the coupled system.

The vibronic Hamiltonian describing the *linear* JT interaction between the orbital doublet and the  $e$ -symmetry vibrational modes can be written in operator form<sup>14</sup> as [75]

$$\hat{H} = \hat{H}_0 + \hat{H}_{\text{JT}}.\tag{1.74}$$

In the basis of electronic states  $\{|E_x\rangle, |E_y\rangle\}$ , which transform as Cartesian  $x$  and  $y$  vectors under point group operations, the zero-order term

---

<sup>14</sup>From this point onward, Dirac notation is adopted. Hamiltonians are expressed as operators acting on abstract basis kets, such as  $|E_\gamma\rangle$  for the orbital doublet and phonon Fock states for vibrational excitations, rather than directly on coordinate-space wave functions.

corresponds to harmonic vibrational motion [Eq. (1.66)]:

$$\begin{aligned}\hat{H}_0 &= \frac{1}{2} \sum_k^{N_e} \sum_{\gamma \in \{x,y\}} (P_{k\gamma}^2 + \omega_k^2 Q_{k\gamma}^2) \hat{I} \\ &= \sum_k^{N_e} \sum_{\gamma \in \{x,y\}} \omega_k \left( \hat{a}_{k\gamma}^\dagger \hat{a}_{k\gamma} + \frac{1}{2} \right) \hat{I},\end{aligned}\quad (1.75)$$

where  $P_{k\gamma} = -i \partial / \partial Q_{k\gamma}$  is the conjugate momentum of coordinate  $Q_{k\gamma}$ ,  $\omega_k$  is the angular frequency of mode  $k$ , with  $k$  running over all  $N_e$  pairs of degenerate  $e$ -symmetry vibrations, and  $\hat{I}$  is the two-dimensional identity operator acting in the orbital subspace. The phonon creation and annihilation operators are defined as

$$\hat{a}_{k\gamma}^\dagger = \sqrt{\frac{\omega_k}{2}} \left( Q_{k\gamma} - i \frac{P_{k\gamma}}{\omega_k} \right), \quad \hat{a}_{k\gamma} = \sqrt{\frac{\omega_k}{2}} \left( Q_{k\gamma} + i \frac{P_{k\gamma}}{\omega_k} \right), \quad (1.76)$$

where  $\gamma \in \{x, y\}$  distinguishes the two orthogonal components of each  $e$ -symmetry doublet. The basis is chosen such that both the electronic and vibrational states transform as Cartesian  $x$  and  $y$  vectors under point group operations.

The linear JT coupling term is expressed as [39, 75, 77, 79]

$$\begin{aligned}\hat{H}_{\text{JT}} &= \sum_k^{N_e} \sum_{\gamma \in \{x,y\}} V_k Q_{k\gamma} \hat{C}_{E\gamma} \\ &= \sum_k^{N_e} \sum_{\gamma \in \{x,y\}} \frac{V_k}{\sqrt{2}\omega_k} \left( \hat{a}_{k\gamma}^\dagger + \hat{a}_{k\gamma} \right) \hat{C}_{E\gamma},\end{aligned}\quad (1.77)$$

where  $V_k$  are the *vibronic coupling coefficients* and  $\hat{C}_{E\gamma}$  are Clebsch–Gordan coefficient matrices. In the chosen Cartesian representation, these are

$$\hat{C}_{E_x} = \frac{1}{\sqrt{2}} \begin{pmatrix} 0 & 1 \\ 1 & 0 \end{pmatrix}, \quad \hat{C}_{E_y} = \frac{1}{\sqrt{2}} \begin{pmatrix} 1 & 0 \\ 0 & -1 \end{pmatrix}. \quad (1.78)$$

### 1.5.2. Solving the Jahn–Teller problem

The solution of the DJT problem outlined above consists of three essential steps. First, the harmonic vibrational states are computed within the framework of the zero-order Hamiltonian in Eq. (1.75). Second, the matrix elements corresponding to the linear JT coupling [Eq. (1.77)] are evaluated within the basis of these vibrational states, employing a basis cutoff of  $N_{\text{ex}}$  total phonon excitations to maintain computational

tractability while retaining accuracy. Finally, the complete Hamiltonian in Eq. (1.74) is diagonalized to obtain the fully coupled vibronic states.

Even with a modest excitation cutoff  $N_{\text{ex}}$ , the numerical problem quickly becomes intractable when the number of vibrational modes exceeds a few. However, the linear JT Hamiltonian  $\hat{H}_{\text{JT}}$  possesses an additional continuous SU(2) symmetry, which can be exploited to reduce the computational cost [39, 74, 79].

The zero-order Hamiltonian  $\hat{H}_0$  commutes with both the generator of SU(2) rotations in the orbital subspace,

$$\hat{J}_{\text{el}} = \frac{1}{2}\hat{\sigma}_y = \frac{i}{2} \begin{pmatrix} 0 & -1 \\ 1 & 0 \end{pmatrix}, \quad (1.79)$$

and the generator that induces rotations in the subspace of degenerate normal coordinates,

$$\hat{J}_{\text{ph}} = \sum_k^{N_e} \hat{L}_{z,k} \hat{I}, \quad (1.80)$$

where

$$\hat{L}_{z,k} = Q_{kx}P_{ky} - Q_{ky}P_{kx} = -i \left( \hat{a}_{kx}^\dagger \hat{a}_{ky} - \hat{a}_{ky}^\dagger \hat{a}_{kx} \right) \quad (1.81)$$

represents the angular momentum operator associated with the degenerate vibrational doublet  $\{Q_{kx}, Q_{ky}\}$ . Therefore, the eigenstates of  $\hat{H}_0$  can be chosen to be simultaneous eigenstates of both  $\hat{J}_{\text{el}}$  and  $\hat{J}_{\text{ph}}$ .

The linear JT coupling Hamiltonian in Eq. (1.77) does not commute individually with  $\hat{J}_{\text{el}}$  or  $\hat{J}_{\text{ph}}$ , but it does commute with their sum [74]:

$$\hat{J} = \hat{J}_{\text{el}} + \hat{J}_{\text{ph}}. \quad (1.82)$$

This symmetry allows the zero-order basis to be labeled by the eigenvalues of  $\hat{J}$ . States with different total angular quantum numbers  $j$  are not coupled by  $\hat{H}_{\text{JT}}$ , as  $\hat{J}$  is a constant of motion.

We now seek states that are simultaneous eigenstates of  $\hat{H}_0$ ,  $\hat{J}_{\text{el}}$ , and  $\hat{J}_{\text{ph}}$ . The orbital eigenstates of  $\hat{J}_{\text{el}}$  are

$$|E_{\pm}\rangle = \frac{1}{\sqrt{2}}(|E_x\rangle \pm i|E_y\rangle), \quad (1.83)$$

with eigenvalues  $J_{\text{el}} = \pm\frac{1}{2}$ . These states transform as the spherical harmonics  $Y_{1,\pm 1}$ . Knowing that  $J_{\text{el}} = j_{\text{el}}$ , the corresponding quantum number  $j_{\text{el}} = \pm\frac{1}{2}$  is referred to as the *electronic pseudospin*. Since  $\hat{H}_0$  does not mix different electronic components,  $|E_{\pm}\rangle$  are also eigenstates of  $\hat{H}_0$ .

The phonon eigenstates of  $\hat{J}_{\text{ph}}$  correspond to *circular phonons*, described in the second-quantization formalism by [39]

$$\hat{a}_{k\pm} = \frac{1}{\sqrt{2}}(\hat{a}_{kx} \mp i\hat{a}_{ky}), \quad (1.84)$$

with right- and left-handed phonon number operators given by

$$\hat{n}_{k\pm} = \hat{a}_{k\pm}^\dagger \hat{a}_{k\pm}. \quad (1.85)$$

The total phonon angular momentum operator then becomes

$$\hat{J}_{\text{ph}} = \sum_k^{N_e} (\hat{n}_{k+} - \hat{n}_{k-}) \hat{I}, \quad (1.86)$$

and the zero-order Hamiltonian can be rewritten as

$$\hat{H}_0 = \sum_k^{N_e} \omega_k (\hat{n}_{k+} + \hat{n}_{k-} + 1) \hat{I}. \quad (1.87)$$

Comparing Eqs. (1.86) and (1.87) shows that the common eigenfunctions of  $\hat{H}_0$  and  $\hat{J}_{\text{ph}}$  can be labeled by two quantum numbers for each pair  $k$  of degenerate  $e$ -symmetry phonons:

- $n_k = n_{k+} + n_{k-}$ : the total number of phonons of pair  $k$ ,
- $l_k = n_{k+} - n_{k-}$ : the angular momentum quantum number of phonons of pair  $k$ .

Since  $n_{k+}$  and  $n_{k-}$  are integers, for a fixed  $n_k$ , the allowed  $l_k$  values are  $l_k = n_k, n_k - 2, n_k - 4, \dots, -n_k$ .

The common eigenstates of  $\hat{H}_0$ ,  $\hat{J}_{\text{el}}$ , and  $\hat{J}_{\text{ph}}$  can therefore be written as  $|n_1 l_1 \dots n_{N_e} l_{N_e}; E_+\rangle$  and  $|n_1 l_1 \dots n_{N_e} l_{N_e}; E_-\rangle$ . Because these are also eigenstates of  $\hat{J} = \hat{J}_{\text{el}} + \hat{J}_{\text{ph}}$ , each state can be labeled by the conserved quantum number

$$j = j_{\text{el}} + \sum_k^{N_e} l_k. \quad (1.88)$$

The key advantage of this representation is that the  $\hat{H}_{\text{JT}}$  matrix can be constructed and diagonalized independently for each value of  $j$ , reducing the original large matrix problem into several smaller, tractable subspaces.

In this new basis of electronic orbitals and circular phonons, the linear JT coupling Hamiltonian becomes [39]

$$\hat{H}_{\text{JT}} = \sum_k^{N_e} K_k \omega_k \begin{pmatrix} 0 & \hat{a}_{k+} + \hat{a}_{k-}^\dagger \\ \hat{a}_{k-} + \hat{a}_{k+}^\dagger & 0 \end{pmatrix}, \quad (1.89)$$

where

$$K_k = \frac{V_k}{\sqrt{2\omega_k^3}} \quad (1.90)$$

are the *dimensionless vibronic coupling constants* for each pair  $k$  of degenerate  $e$ -phonons. Using these expressions and performing some algebra, the matrix elements of  $\hat{H}_{\text{JT}}$  in the new basis are [39]

$$\begin{aligned} & \langle n'_1 l'_1, \dots, n'_{N_e} l'_{N_e}; E_- | \hat{H}_{\text{JT}} | n'_1 l'_1, \dots, n'_{N_e} l'_{N_e}; E_+ \rangle \\ &= \sqrt{2} \sum_k^{N_e} K_k \omega_k \delta_{l'_k, l_k + 1} \left[ \prod_{j \neq k} \delta_{n'_j, n_j} \delta_{l'_j, l_j} \right] \\ & \times \left[ \sqrt{\frac{n_k - l_k}{2}} \delta_{n'_k, n_k - 1} + \sqrt{\frac{n_k + l_k + 2}{2}} \delta_{n'_k, n_k + 1} \right]. \end{aligned} \quad (1.91)$$

The zero-order Hamiltonian  $\hat{H}_0$  is diagonal in both the orbital and vibrational degrees of freedom, with matrix elements

$$\begin{aligned} & \langle n_1 l_1, \dots, n_{N_e} l_{N_e}; E_{\pm} | \hat{H}_0 | n_1 l_1, \dots, n_{N_e} l_{N_e}; E_{\pm} \rangle \\ &= \sum_k^{N_e} \omega_k (n_k + 1). \end{aligned} \quad (1.92)$$

Eqs. (1.91) and (1.92) constitute the final working expressions used in the numerical solution of the vibronic Hamiltonian [Eq. (1.74)].

### 1.5.3. Extraction of Jahn–Teller parameters from DFT

Thus far, we have examined the formal structure of the  $E \otimes (e \oplus e \oplus \dots)$  JT problem. However, we have not yet discussed how the vibrational frequencies and normal modes entering the zero-order Hamiltonian  $\hat{H}_0$  [Eq. (1.75)] are obtained from practical DFT calculations, nor how the vibronic coupling constants  $K_k$  in Eq. (1.90) are determined.

The zero-order adiabatic Hamiltonian  $\hat{H}_0$  is obtained by suppressing all non-adiabatic effects associated with the degeneracy of the electronic states. In practice, this can be achieved by modeling an ensemble that equally occupies both components of the degenerate electronic doublet. This ensemble is represented by the density matrix

$$\hat{\rho} = \frac{1}{2} (|E_x\rangle\langle E_x| + |E_y\rangle\langle E_y|). \quad (1.93)$$

The expectation value of any symmetrized operator  $\hat{O}_{\Gamma\gamma}$ , where  $\Gamma$  denotes the irreducible representation and  $\gamma$  labels its row, is given by

$$\langle \hat{O}_{\Gamma\gamma} \rangle = \text{Tr}(\hat{\rho} \hat{O}_{\Gamma\gamma}). \quad (1.94)$$

This expectation value vanishes unless  $\Gamma$  corresponds to the totally symmetric representation, which is invariant under all point group operations of the electronic states. Since the orbital operators of the JT interaction (e.g.,  $\hat{C}_x$  and  $\hat{C}_y$ ) transform according to nontrivial irreducible representations, the linear JT term  $\hat{H}_{\text{JT}}$  and all higher-order coupling terms vanish for the ensemble described by Eq. (1.93) [82].

In practical DFT calculations, this suppression is implemented by constraining the Kohn–Sham single-particle orbital occupations to fractional values. Here, an electronic configuration refers to the specific assignment of electrons to the available set of single-particle orbitals. For an orbital doublet state, such as the  $|^3E\rangle$  state of the negatively charged nitrogen-vacancy ( $\text{NV}^-$ ) center in diamond shown in Fig. 2.1c, multiple single-determinant configurations can be constructed, such as  $a_1 e_x^2 e_y$  and  $a_1 e_x e_y^2$ . Individually, each of these configurations represents a single component of the doublet that would typically lead to a symmetry-breaking structural distortion.

Fractional occupancies involve a computational scheme where electrons are distributed non-integrally and equally across the degenerate orbitals—for example, by assigning 1.5 electrons to both  $e_x$  and  $e_y$  orbitals. This technique effectively models the system according to the ensemble density matrix of Eq. (1.93), representing an average over the degenerate electronic components. By occupying these orbitals fractionally, the system is prevented from undergoing a Jahn–Teller distortion and instead retains its highest geometric symmetry. Under these conditions, the PES becomes harmonic, allowing for the application of the methodology in Sec. 1.4.4 to compute the harmonic vibrational states that define the zero-order Hamiltonian  $\hat{H}_0$ .

To determine the linear JT coupling constants  $K_k$  for each  $e$ -symmetry vibrational doublet  $k$ , the procedure described in Ref. [39] was followed. In standard DFT calculations, ions are treated as classical, stationary point charges, implying the absence of nuclear kinetic energy. Consequently, the effective total Hamiltonian of the JT-active system corresponds entirely to the potential energy, which, using Eqs. (1.75) and (1.77), can be expressed as

$$\hat{U} = \sum_k^{N_e} \left[ \frac{1}{2} \omega_k (Q_{kx}^2 + Q_{ky}^2) \hat{I} + \sqrt{2\omega_k^3} K_k \begin{pmatrix} Q_{ky} & Q_{kx} \\ Q_{kx} & -Q_{ky} \end{pmatrix} \right]. \quad (1.95)$$

Diagonalization of the electronic subspace yields two PESs,

$$U_{\pm} = \sum_k^{N_e} \frac{1}{2} \omega_k (Q_{kx}^2 + Q_{ky}^2) \pm 2 \left[ \sum_{k,k'}^{N_e} \sqrt{\omega_k^3 \omega_{k'}^3} K_k K_{k'} (Q_{kx} Q_{k'x} + Q_{ky} Q_{k'y}) \right]^{1/2}. \quad (1.96)$$

In practice, ionic relaxation in DFT follows the lower branch,  $U_-$ . The minimum of this surface occurs at  $\Delta \mathbf{Q}_{\text{JT}}$ , which quantifies the relaxation amplitude between the high-symmetry, fractional-occupation configuration and the relaxed, symmetry-broken configuration, obtained from calculations where the orbital occupation is constrained to represent a single component of the degenerate electronic subspace. This displacement is projected onto each degenerate pair  $k$  of vibrational modes, with the projection defined as [75]

$$\Delta Q_k^2 = (\Delta Q_{kx})^2 + (\Delta Q_{ky})^2 = \frac{2K_k^2}{\omega_k}. \quad (1.97)$$

Here,  $\Delta Q_{k\gamma}$  represents the mass-weighted displacement along the  $\gamma \in \{x, y\}$  component of the  $k$ -th vibrational doublet. Equation (1.97) thus enables estimation of the vibronic coupling constants  $K_k$  through the relation

$$K_k^2 = \frac{\omega_k (\Delta Q_k)^2}{2}. \quad (1.98)$$

This expression is analogous to the definition of the Huang–Rhys (HR) factor introduced later in Eq. (1.108), except that here  $\Delta Q_k$  does not connect the minima of APESs corresponding to different electronic states. Instead, it quantifies the symmetry-breaking distortion between the high-symmetry ensemble configuration and the JT-distorted minimum within the same electronic manifold.

#### 1.5.4. Few-mode approximation

Even with the simplifications introduced in Sec. 1.5.2, diagonalizing the vibronic Hamiltonian in Eq. (1.74) remains computationally demanding because a realistic supercell contains hundreds or even thousands of pairs of  $e$ -symmetry vibrational modes. To make the numerical problem computationally tractable, additional approximations are required. In this work, we employ the few-mode approach proposed in Ref. [39], which replaces the full set of symmetry-breaking modes with a smaller number of effective modes that reproduce the essential vibronic coupling features.

Analogous to the treatment of HR coupling in Sec. 1.6.1, we first define the spectral density of JT coupling as

$$K^2(\omega) = \sum_k^{N_e} K_k^2 \delta(\omega - \omega_k), \quad (1.99)$$

where  $K_k$  is the dimensionless vibronic coupling strength [Eq. (1.90)] for each symmetry-breaking vibrational mode pair  $k \in \{1, \dots, N_e\}$ , and  $\omega_k$  is its frequency. Due to the discrete nature of this spectral function, the Dirac  $\delta$ -functions are replaced with Gaussians of finite width, as detailed at the end of Sec. 1.6.1. The resulting broadened function is primarily used to visualize how the JT coupling is distributed across the vibrational spectrum, identifying which phonon energy ranges are most influential in the symmetry-breaking process.

This continuous distribution, constructed from the discrete function in Eq. (1.99), is then approximated by an effective counterpart composed of a sum of a limited number,  $N_{\text{eff}}$ , of Gaussian-broadened modes:

$$K_{\text{eff}}^2(\omega) = \sum_k^{N_{\text{eff}}} \bar{K}_k^2 g_\sigma(\omega - \bar{\omega}_k), \quad (1.100)$$

where  $g_\sigma(\omega - \bar{\omega}_k)$  is a normalized Gaussian of width (standard deviation)  $\sigma$ , centered at the effective frequency  $\bar{\omega}_k$ . Each term represents an effective symmetry-breaking vibrational mode pair characterized by an average frequency  $\bar{\omega}_k$  and an effective coupling strength  $\bar{K}_k$ . The parameters  $\bar{K}_k$ ,  $\bar{\omega}_k$ , and  $\sigma$  are optimized so that  $K_{\text{eff}}^2(\omega)$  accurately reproduces the original broadened coupling density  $K^2(\omega)$ . Within this framework, Eq. (1.100) serves as a diagnostic tool to evaluate how well the reduced set of effective modes approximates the original spectral density.

The ultimate goal of this procedure is to obtain the discrete set of dimensionless vibronic coupling constants defined in Eq. (1.90), which are essential for constructing the matrix elements of the linear JT Hamiltonian as given in Eq. (1.91). By reducing the number of active pairs of  $e$ -symmetry vibrational modes to a small, manageable set  $N_{\text{eff}} \ll N_e$ , this few-mode approximation makes the numerical diagonalization of the vibronic Hamiltonian [Eq. (1.74)] feasible while retaining the essential physics of the JT interaction. To ensure the reliability of the resulting vibronic spectral functions, convergence is verified with respect to the number of effective mode pairs  $N_{\text{eff}}$ .

## 1.6. Optical spectra

Optical transitions in semiconductor defects correspond to electronic excitations or relaxations induced by the absorption or emission of a

photon, accompanied by changes in the nuclear configuration of the lattice. Such transitions occur between the PESs of different electronic states and are therefore inherently coupled to lattice vibrations. The resulting optical lineshape reflects the overlap between vibrational states of the initial and final electronic manifolds, incorporating both the zero-phonon line (ZPL), corresponding to a purely electronic transition without phonon involvement, and the accompanying phonon sideband (PSB) arising from phonon-assisted processes. This optical signal provides direct insight into the strength and character of electron–phonon coupling in the defect system.

In the adiabatic approximation, and at  $T = 0\text{ K}$ , the *normalized lineshape*  $L(\omega)$  of a luminescence or absorption spectrum is given by [39, 71]

$$L(\omega) = C\omega^\kappa A(\omega), \quad (1.101)$$

where  $C$  is a normalization constant,  $A(\omega)$  is the *optical spectral function*, and  $\kappa$  depends on the optical process:  $\kappa = 3$  for luminescence and  $\kappa = 1$  for absorption. The function  $A(\omega)$  contains all information about the transition amplitudes between vibrational states of different electronic manifolds.

### 1.6.1. Transitions between non-degenerate states

When no electronic degeneracy is present, the optical spectral function  $A(\omega)$  is expressed as [71]

$$A(\omega) = \sum_m |\langle \chi_{0,i} | \chi_{m,f} \rangle|^2 \delta(E_{\text{ZPL}} \mp [\epsilon_{m,f} - \epsilon_{0,f}] - \omega), \quad (1.102)$$

where  $E_{\text{ZPL}}$  is the ZPL energy of the optical transition,  $|\chi_{0,i}\rangle$  and  $|\chi_{m,f}\rangle$  are vibrational eigenstates of the initial and final electronic states, respectively, and  $\epsilon_{m,f}$  is the energy of the  $m$ -th vibrational level in the final state relative to its APES minimum [Eq. (1.68)]. The minus and plus signs correspond to luminescence and absorption, respectively.

Evaluating the overlap integrals  $\langle \chi_{0,i} | \chi_{m,f} \rangle$  in Eq. (1.102) is computationally demanding due to the large number of vibrational modes in realistic defect systems. Moreover, an electronic transition alters the shape of the APES, leading to differences in both the vibrational frequencies and polarization vectors of the two electronic states. To make the calculation tractable, the *equal-mode approximation* is commonly adopted [39, 83]. This approximation assumes that the vibrational modes are identical for the initial and final electronic states. Typically, the phonon modes of the final electronic state are employed—ground-state modes for luminescence and excited-state modes for absorption [39, 71].

Under this approximation, the *generating function method* introduced by Lax [84], and by Kubo and Toyozawa [85] provides an efficient way to compute  $A(\omega)$ . The optical spectral function is obtained from the generating function  $G(t)$  via a Fourier transform:

$$A(\omega) = \frac{1}{2\pi} \int_{-\infty}^{\infty} G(t) \exp[-i(E_{\text{ZPL}} - \omega)t] \exp(-\gamma|t|) dt, \quad (1.103)$$

where the phenomenological broadening factor  $\exp(-\gamma|t|)$  accounts for both homogeneous (lifetime-related) and inhomogeneous (environment-related) broadening of the ZPL that are not captured within the zero-temperature regime. In practice, the broadening parameter  $\gamma$  is adjusted to reproduce the experimental linewidth.

Within the equal-mode approximation, the generating function takes the form [82]

$$G(t) = \exp \left[ - \sum_k^{3N_n} S_k (1 - \exp(\pm i\omega_k t)) \right], \quad (1.104)$$

where the plus sign applies to luminescence and the minus sign to absorption. Here,  $S_k$  is the partial Huang–Rhys (HR) factor associated with phonon mode  $k$ , and  $\omega_k$  is its frequency. The total HR factor is

$$S_{\text{tot}} = \sum_k^{3N_n} S_k, \quad (1.105)$$

which characterizes the overall strength of electron–phonon coupling and thus the vibrational structure of the optical transition.

Neglecting the prefactor  $\omega^3$  in Eq. (1.101) and assuming identical vibrational modes for the two electronic states, the relative weight of the ZPL is given by [71, 83, 84]

$$w_{\text{ZPL}} = e^{-S_{\text{tot}}}, \quad (1.106)$$

known as the Debye–Waller factor (DWF). It represents the ratio of the integrated ZPL intensity to the total intensity of the spectrum. Since  $w_{\text{ZPL}}$  can be measured experimentally, it provides an estimate of the effective HR factor through

$$\tilde{S}_{\text{tot}} = -\ln(w_{\text{ZPL}}), \quad (1.107)$$

where the tilde distinguishes this quantity from the theoretical  $S_{\text{tot}}$  defined in Eq. (1.105). The two differ slightly due to the assumptions above, but both quantify the coupling strength between electronic and vibrational degrees of freedom.

Each partial HR factor quantifies the average number of phonons of mode  $k$  involved in the optical transition<sup>15</sup> and is defined as [86]

$$S_k = \frac{\omega_k (\Delta Q_k)^2}{2}, \quad (1.108)$$

where  $\Delta Q_k$  is the mass-weighted nuclear displacement along phonon mode  $k$  between the equilibrium geometries of the two electronic states, induced by the optical transition. It is obtained as the projection of the total mass-weighted nuclear displacement vector  $\boldsymbol{\xi}$  onto the total normalized phonon eigenvector  $\mathbf{e}(k)$ :

$$\Delta Q_k = \sum_{\alpha}^{N_n} \mathbf{e}_{\alpha}(k) \boldsymbol{\xi}_{\alpha}, \quad (1.109)$$

$$\boldsymbol{\xi}_{\alpha} = \sqrt{M_{\alpha}} \Delta \mathbf{R}_{\alpha}, \quad (1.110)$$

where  $\mathbf{e}_{\alpha}(k)$  is the polarization vector of nucleus  $\alpha$  for vibrational mode  $k$ ,  $\boldsymbol{\xi}_{\alpha}$  is the mass-weighted displacement of nucleus  $\alpha$  with atomic mass  $M_{\alpha}$ , and  $\Delta \mathbf{R}_{\alpha}$  is the Cartesian displacement of nucleus  $\alpha$  between the two electronic states.

To account for the continuum of vibrational modes contributing to the electron–phonon interaction, the *spectral density of electron–phonon coupling* (also known as the *spectral function*) is defined as [71]

$$S(\omega) \equiv \sum_k^{3N_n} S_k \delta(\omega_k - \omega), \quad (1.111)$$

allowing the generating function in Eq. (1.104) to be rewritten in integral form:

$$G(t) = \exp \left[ -S_{\text{tot}} + \int S(\omega) \exp(\pm i\omega t) d\omega \right]. \quad (1.112)$$

To achieve realistic spectral resolution, the Dirac  $\delta$ -functions in Eq. (1.111) are replaced with finite-width smoothing kernels selected according to the localization properties of the vibrational modes. For bulk-like and quasi-localized modes, Gaussian broadening is typically applied to produce a smooth PSB, whereas for strongly localized modes, a Lorentzian profile is often preferred, with the half-width at half maximum (HWHM) chosen to capture narrow vibrational features in the optical spectrum.

---

<sup>15</sup>For non-degenerate case, *vibronic* coupling is negligible, and only symmetry-preserving vibrational modes contribute to the electron–phonon interaction.

### 1.6.2. Lineshapes for $A$ to $E$ transitions

For an optical transition in which the final electronic state is degenerate, such as  $A \rightarrow E$ , the situation differs from the non-degenerate case. Here, symmetry-breaking ( $e$ -symmetry) vibrational modes participate in the electron–phonon interaction in addition to the symmetry-preserving ( $a$ -symmetry) modes. Accordingly, the optical spectral function  $A(\omega)$  in Eq. (1.101) is expressed as a convolution of the spectral function contributions from the two symmetry classes [39]:

$$A(\omega) = \int A_a(\omega - \omega') A_e(\omega') d\omega', \quad (1.113)$$

where  $A_a(\omega)$  denotes the contribution from symmetry-preserving phonons, as defined in Eq. (1.102), and  $A_e(\omega)$  accounts for the contribution from symmetry-breaking phonons, given by [82]

$$A_e(\omega) = \sum_m \left[ \left| \langle \chi_{0,i}^e | \chi_{m,f}^{e_x} \rangle \right|^2 + \left| \langle \chi_{0,i}^e | \chi_{m,f}^{e_y} \rangle \right|^2 \right] \times \delta(\mp[\epsilon_{m,f}^e - \epsilon_{0,f}^e] - \omega), \quad (1.114)$$

where  $|\chi_{m,f}^{e_x}\rangle$  and  $|\chi_{m,f}^{e_y}\rangle$  are the vibrational eigenstates associated with the two components of the degenerate electronic doublet  $\{|E_x\rangle, |E_y\rangle\}$ . The minus and plus signs correspond to luminescence and absorption, respectively.

## 1.7. Embedding methodology

Accurate modeling of vibrational properties in point-defect systems is often hindered by *finite-size effects* in periodic supercell calculations, particularly when the supercell contains fewer than about 1000 atoms. Under such conditions, the use of periodic boundary conditions artificially increases the defect concentration and suppresses long-wavelength acoustic phonons. Furthermore, the limited number of atoms in the supercell leads to a discrete and sparse sampling of the vibrational spectrum, reducing the resolution of the calculated electron–phonon coupling data. To overcome these limitations, an embedding methodology is employed [39, 71]. This approach constructs large Hessian matrices [Eq. (1.56)] by combining force-constant data obtained from smaller, computationally feasible supercells. It exploits the short-range nature of interatomic force constants, enabling the vibrational properties of a much larger effective supercell to be approximated by embedding information from both defect-containing and pristine bulk environments.

The force-constant embedding procedure, illustrated schematically in Fig. 1.2, follows the criteria below:

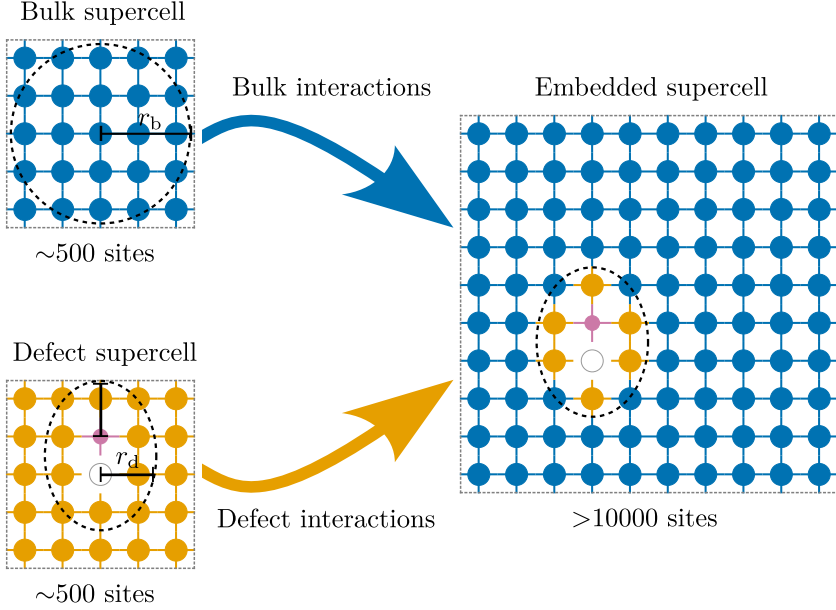


**Figure 1.2.** Schematic illustration of the force-constant matrix embedding methodology for a point defect in solid

- For atoms pairs separated by a distance smaller than the bulk cutoff radius  $r_b$ , the corresponding elements from the bulk Hessian matrix are used; otherwise, they are set to zero.
- For atom pairs located within a defect cutoff radius  $r_d$  from each defect center, the corresponding elements from the defect-containing Hessian matrix are used.

This hybrid force-constant matrix preserves the local defect-induced modifications near the defect site while maintaining accurate long-range acoustic behavior characteristic of the bulk crystal.

A related complication arises when evaluating the structural relaxation profile associated with an optical transition. In small supercells, long-wavelength components of the nuclear displacement vector  $\Delta\mathbf{R}_\alpha$  [Eqs. (1.109) and (1.110)] are artificially suppressed, which leads to an underestimation of the total lattice relaxation. To recover the correct displacement in the dilute-defect limit, the mass-weighted normal-mode displacements  $\Delta Q_k$  are computed for each vibrational mode  $k$  of the embedded supercell using the harmonic approximation and force-

displacement relationship:

$$\Delta Q_k = \frac{1}{\omega_k^2} \sum_{\alpha}^{N_n} \frac{\mathbf{F}_{\alpha}}{\sqrt{M_{\alpha}}} \mathbf{e}_{\alpha}(k), \quad (1.115)$$

were  $\mathbf{F}_{\alpha}$  is the force acting on nucleus  $\alpha$  in the final electronic state, while the nuclear geometry is fixed at the equilibrium configuration of the initial state. The eigenvectors  $\mathbf{e}_{\alpha}(k)$  are the polarization vectors obtained from the embedded supercell calculation.

Because the atomic forces converge rapidly with increasing supercell size, the combination of the embedding approach and the force-projection method allows an accurate reconstruction of the relaxation profile and the associated electron–phonon coupling parameters, particularly for low-frequency, long-wavelength modes. As a result, this methodology provides a robust framework for computing high-resolution optical lineshapes of point defects entirely from first principles.

## 1.8. Computational details

All DFT calculations presented in this thesis were performed using VASP [55, 56]. Spin polarization was included in all defect calculations. The interaction between valence electrons and atomic cores was described using the PAW method [65].

Defect modeling was performed using periodic supercells constructed from conventional cubic unit cells of the host material. Phonon calculations were carried out using the finite-displacement method, as implemented in the `phonopy` software package [87, 88].

Several XC functionals were employed throughout the thesis, including PBE [31], SCAN [28], rSCAN [29], r<sup>2</sup>SCAN [30], and HSE06 [32] functionals. The specific choice of functionals and any additional computational parameters are detailed in the respective chapters.

Unless otherwise noted, excited electronic states were modeled using the  $\Delta$  self-consistent field ( $\Delta$ SCF) method [46, 89, 90], in which an electron was promoted from an occupied localized orbital to a different unoccupied orbital. The detailed orbital configurations and symmetry considerations for the ground and excited states are provided in the corresponding chapters, as these vary across different defect systems.

High-resolution vibrational structure calculations were performed using the embedding methodology [39, 71] described in Sec. 1.7. This approach reduces the finite-sized effects inherent to supercell-based simulations and enables accurate modeling of the APES and the vibrational structure of the defect in the dilute limit. It was employed to compute

spectral functions and optical lineshapes from first-principles electron-phonon coupling data.

As noted in Ref. [39], the choice of phonon modes used in the calculations depends on the specific optical process under consideration. For luminescence, it is most appropriate to use the vibrational modes and frequencies of the ground state, whereas absorption processes are more accurately described using the vibrational characteristics of the excited state.

To facilitate a meaningful comparison between theoretical and experimental optical lineshapes, all calculated spectra were aligned relative to the experimental ZPL energy. Additionally, the experimental spectra were rescaled so that their PSB features aligned with those of the theoretical spectra. This rescaling was necessary due to common limitations in experimental measurements: the ZPL intensity is often clipped, and the PSB may be incompletely recorded, especially in its low-intensity tail. As a result, proper normalization of the experimental spectrum is typically not feasible.

# 2. Application of different exchange–correlation functionals: $NV^-$ center in diamond

## 2.1. Introduction

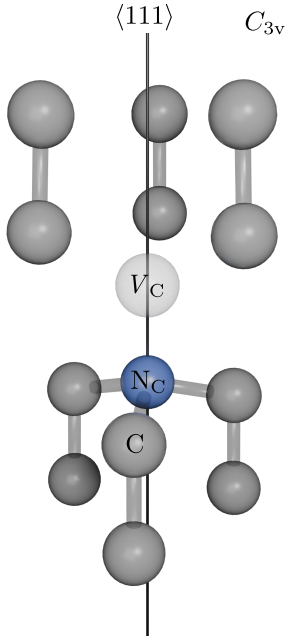
Diamond is a wide-band-gap semiconductor with a band gap of approximately 5.5 eV, which makes it transparent across the visible spectrum. Any coloration observed in diamond originates from point defects that introduce localized electronic states within the band gap.

Nitrogen, the most common impurity in diamond, typically forms isolated substitutional defects or more complex aggregates. Under conditions of radiation damage [91] or ion implantation [92], followed by thermal annealing, carbon vacancies ( $V_C$ ) become mobile and can be captured by substitutional nitrogen ( $N_C$ ) atoms, forming negatively charged nitrogen-vacancy ( $NV^-$ ) centers. These defects are stable in nitrogen-rich single-crystalline and nanocrystalline diamond and remain robust well above room temperature [4–6].

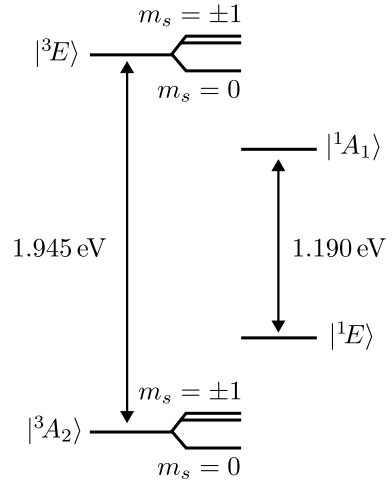
Among all known point defects in diamond, the  $NV^-$  center is one of the most thoroughly investigated [3]. It is a paramagnetic [93] point defect consisting of a  $N_C$  atom adjacent to a  $V_C$ , with its symmetry axis oriented along the  $\langle 111 \rangle$  crystallographic direction. This configuration gives rise to  $C_{3v}$  point group symmetry [94, 95], as illustrated in Fig. 2.1a.

The most prominent optical feature of the  $NV^-$  center is a strong absorption line at 1.945 eV (637 nm), which produces a sharp zero-phonon line (ZPL) and a broad phonon sideband (PSB) in the luminescence spectrum [91, 94]. The relative intensity of the ZPL, quantified by the Debye–Waller factor (DWF), is about 3.2% [71] at low temperature, indicating moderate electron–phonon coupling. These spectral features arise from radiative transitions between the spin-triplet excited state  $|^3E\rangle$  and the spin-triplet ground state  $|^3A_2\rangle$  [93, 96–99], as shown in Fig. 2.1b. In addition to this radiative channel, non-radiative intersystem crossing occurs through intermediate spin-singlet states  $|^1A_1\rangle$  and  $|^1E\rangle$ . This process gives rise to a secondary emission channel with a ZPL at 1.190 eV (1042 nm) [100] and enables spin-dependent optical transitions [3, 101].

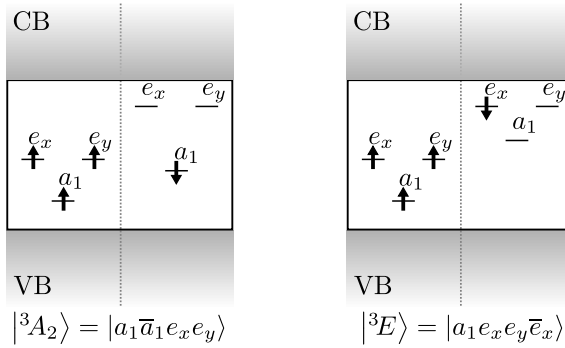
Over the past several decades, the  $NV^-$  center has attracted significant attention due to its potential in quantum technologies. Its long spin coherence time [4–6] and spin-dependent fluorescence [3, 101] make it a leading candidate for quantum sensing [7–12] and quantum computing [23, 24] applications.



(a) Atomic structure representation



(b) Energy-level diagram



(c) Representations of the Kohn–Sham electronic configurations of the spin-triplet ground state  $|{}^3A_2\rangle$  and the spin-triplet excited state  $|{}^3E\rangle$

**Figure 2.1.** The  $NV^-$  center in diamond

In this chapter, the SCAN family of functionals [28–30] is benchmarked for both the bulk properties of diamond and the defect-related properties of the  $\text{NV}^-$  center. The goal is to assess their accuracy relative to the widely used PBE and HSE06 functionals. While PBE is computationally efficient, its accuracy is limited. In contrast, HSE06 is considerably more accurate and often regarded as the “gold standard”, but its computational cost restricts its use in large-scale studies, particularly those involving vibrational properties and electron–phonon coupling, which are the central focus of this thesis. Benchmarking these exchange–correlation functionals on a well-characterized defect such as  $\text{NV}^-$  provides a reference for evaluating their reliability when modeling vibrational and optical properties of other, less-studied centers examined in later chapters. The present comparison includes key bulk quantities, such as the lattice constant, band gap, and phonon spectrum of diamond, as well as defect-related quantities, including the ZPL, electron–phonon coupling strength, and resulting luminescence lineshape of the  $\text{NV}^-$  center.

The results summarized in this chapter are based on the study by Maciaszek *et al.* [102], in which the author of this thesis was a co-author. Although not the main subject of this work, this benchmarking study provides a methodological foundation for the modeling of the electron–phonon interactions in the defect systems analyzed in the subsequent chapters.

## 2.2. Computational details

The calculations presented in this chapter follow the general methodology outlined in Sec. 1.8. The properties of diamond and the  $\text{NV}^-$  center were modeled using a 512-site cubic supercell, obtained by repeating the conventional cubic diamond unit cell (containing eight atoms) in a  $4 \times 4 \times 4$  arrangement. A plane-wave energy cutoff of 600 eV was used, and Brillouin-zone sampling was restricted to the  $\Gamma$ -point. Five exchange–correlation functionals were employed: PBE [31], SCAN [28], rSCAN [29],  $r^2$ SCAN [30], and HSE06 [32].

The spin-triplet excited state  $|^3E\rangle$  was modeled using the  $\Delta$ SCF method [46, 89, 90] by promoting an electron in the spin-minority channel from the occupied, localized  $a_1$  orbital to one of the unoccupied, degenerate  $e$ -type orbitals. This produces single-determinant state described as  $|^3E\rangle = |a_1 e_x e_y \bar{e}_x\rangle$ , where the overbar denotes spin-down orientation. The corresponding Kohn–Sham configurations for the ground-state  $|^3A_2\rangle = |a_1 \bar{a}_1 e_x e_y\rangle$  and excited-state  $|^3E\rangle$  are illustrated in Fig. 2.1c.

Phonon dispersion relations for bulk diamond and the vibrational properties of the  $\text{NV}^-$  center were obtained using the finite-displacement

**Table 2.1.** Calculated lattice constants  $a$  (in Å) and band gaps  $E_g$  (in eV) of bulk diamond, obtained using multiple density functionals. Experimental low-temperature values are taken from Ref. [103]. For comparison, the zero-point-corrected experimental lattice constant reported in Ref. [104] is also included. Values in parentheses indicate the relative deviations from the experimental reference.

	$a$	$E_g$
PBE	3.572 (+0.48 %)	4.12 (−25 %)
SCAN	3.554 (−0.03 %)	4.56 (−17 %)
rSCAN	3.556 (+0.03 %)	4.38 (−20 %)
r <sup>2</sup> SCAN	3.561 (+0.17 %)	4.33 (−21 %)
HSE06	3.546 (−0.25 %)	5.34 (−3 %)
Expt.	3.567 <sup>a</sup> 3.555 <sup>b</sup>	5.48 <sup>a</sup>

<sup>a</sup>Ref. [103]    <sup>b</sup>Ref. [104]

method [87, 88] with atomic displacements of 0.01 Å.

To achieve a detailed description of the vibrational structure and the corresponding luminescence lineshape of the NV<sup>−</sup> center, the embedding methodology [39, 71] described in Sec. 1.7 was employed. This approach effectively extended the supercell size to  $20 \times 20 \times 20$  (64 000 atomic sites) for PBE and HSE06 functionals, and  $18 \times 18 \times 18$  (46 656 atomic sites) for the SCAN family of functionals. For a smooth representation of the electron–phonon coupling data and the resulting luminescence lineshapes, the Dirac  $\delta$ -functions in Eq. (1.111) were approximated by Gaussians with linearly varying standard deviations  $\sigma$ , decreasing from 3.5 meV near the ZPL to 1.5 meV at the low-energy tail of the spectrum. Finally, the ZPL broadening in the calculated luminescence spectra was modeled using the phenomenological parameter  $\gamma = 0.3$  meV introduced in Eq. (1.103).

## 2.3. Results and discussion

### 2.3.1. Lattice parameters of diamond

To begin, the lattice constant  $a$  and band gap  $E_g$  of bulk diamond were calculated using the XC functionals introduced above. The results, together with the experimental low-temperature reference values from Ref. [103], are summarized in Table 2.1.

Relative to the experimental lattice constant  $a = 3.567$  Å [103], PBE appears to yield the closest match, predicting  $a = 3.572$  Å, a deviation

of  $+0.005 \text{ \AA}$  ( $+0.14 \%$ ). However, experimental lattice parameters include the effect of zero-point vibrational expansion. After correcting for this anharmonic contribution, the equilibrium lattice constant becomes  $3.555 \text{ \AA}$  [104]. Compared with this corrected reference, the SCAN family provides the best agreement, with values of  $3.554 \text{ \AA}$  ( $-0.001 \text{ \AA}$ ,  $-0.03 \%$ ) for SCAN,  $3.556 \text{ \AA}$  ( $+0.001 \text{ \AA}$ ,  $+0.03 \%$ ) for rSCAN, and  $3.561 \text{ \AA}$  ( $+0.006 \text{ \AA}$ ,  $+0.17 \%$ ) for r<sup>2</sup>SCAN. In comparison, PBE overestimates the corrected value, yielding  $3.572 \text{ \AA}$  ( $+0.017 \text{ \AA}$ ,  $+0.48 \%$ ), while HSE06 slightly underestimates, producing  $3.546 \text{ \AA}$  ( $-0.009 \text{ \AA}$ ,  $-0.25 \%$ ).

For the band gap, HSE06 shows the best agreement with experimental value of  $E_g = 5.48 \text{ eV}$  [103], predicting  $E_g = 5.34 \text{ eV}$  ( $-0.14 \text{ eV}$ ,  $-3 \%$ ). PBE underestimates the gap substantially, yielding  $4.12 \text{ eV}$  ( $-1.36 \text{ eV}$ ,  $-25 \%$ ), a common shortcoming of semilocal functionals. SCAN improves upon PBE, predicting  $4.56 \text{ eV}$  ( $-0.92 \text{ eV}$ ,  $-17 \%$ ), while rSCAN and r<sup>2</sup>SCAN provide slightly smaller corrections, with values of  $4.38 \text{ eV}$  ( $-1.10 \text{ eV}$ ,  $-20 \%$ ) and  $4.33 \text{ eV}$  ( $-1.15 \text{ eV}$ ,  $-21 \%$ ), respectively.

### 2.3.2. Vibrational properties of diamond

After establishing the structural and electronic properties of bulk diamond, the next step is to assess the description of lattice dynamics, since accurate phonon frequencies are essential for modeling electron-phonon coupling and optical spectra of point defect systems.

Figure 2.2 shows the phonon dispersion relations of bulk diamond calculated with PBE, r<sup>2</sup>SCAN, and HSE06 functionals, compared with experimental room-temperature inelastic neutron scattering (INS) and inelastic X-ray scattering (IXS) data [105]. The corresponding longitudinal optical (LO) phonon frequencies at selected high-symmetry points are listed in Table 2.2.

All functionals reproduce the qualitative shape of the phonon dispersion but differ systematically in their absolute values. Regarding the upper optical phonon branches, PBE clearly underestimates frequencies, reflecting its tendency to soften the lattice. Conversely, HSE06 systematically overestimates them, indicating a slightly stiffer bonding environment. The SCAN functionals yield intermediate values; specifically, r<sup>2</sup>SCAN (the only member of the SCAN family included in Fig. 2.2) provides the best overall agreement with experimental data.

It is important to note that while DFT is a 0 K theory, the reported experimental data used for comparison were obtained at room temperature [105]. In covalent crystals, increasing temperature typically induces a slight softening of phonon modes due to thermal expansion and anharmonic phonon-phonon interactions [106, 107]. However, diamond possesses an exceptionally high Debye temperature ( $T_D \approx 2200 \text{ K}$ )—a pa-

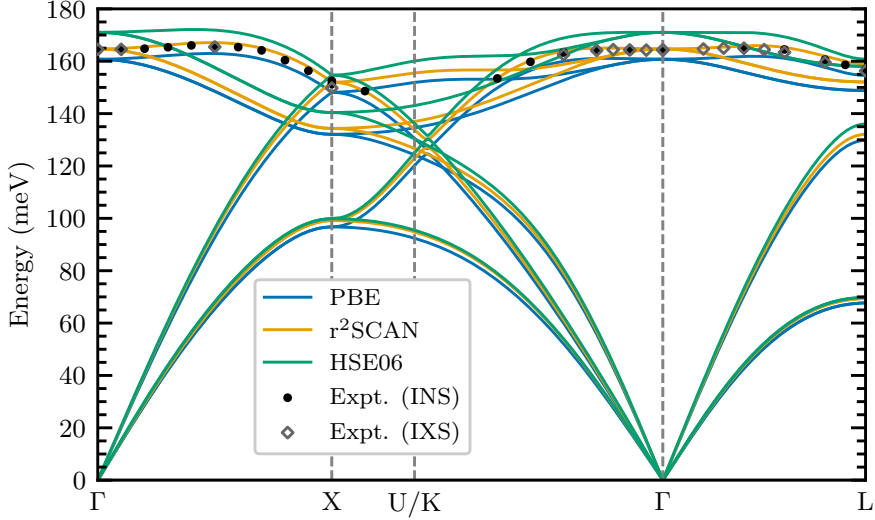


**Figure 2.2.** Calculated phonon dispersion relations of bulk diamond using PBE,  $r^2$ SCAN, and HSE06 functionals. Experimental room-temperature values from INS and IXS measurements are taken from Ref. [105].

**Table 2.2.** Calculated longitudinal optical (LO) phonon frequencies  $\omega$  (in meV) at high-symmetry points in the Brillouin zone of the reciprocal lattice of bulk diamond, obtained using multiple density functionals. Experimental room-temperature values from INS and IXS measurements are taken from Ref. [105]. Only the frequencies of the highest-lying LO branches are reported. Values in parentheses indicate the relative deviations from the experimental reference.

	$\omega(\Gamma)$	$\omega(X)$	$\omega(L)$
PBE	160.7 (-2.01 %) (-2.31 %)	148.1 (-2.12 %) (-1.13 %)	154.6 (-1.53 %) (-1.09 %)
SCAN	167.0 (+1.83 %) (+1.52 %)	153.2 (+1.26 %) (+2.27 %)	160.4 (+2.17 %) (+2.62 %)
$r^2$ SCAN	165.0 (+0.61 %) (+0.30 %)	152.5 (+0.79 %) (+1.80 %)	159.6 (+1.66 %) (+2.11 %)
$r^2$ SCAN	164.7 (+0.43 %) (+0.12 %)	152.0 (+0.46 %) (+1.47 %)	159.0 (+1.27 %) (+1.73 %)
HSE06	171.0 (+4.27 %) (+3.95 %)	154.7 (+2.25 %) (+3.27 %)	160.8 (+2.42 %) (+2.88 %)
Expt. (INS)	164.0	151.3	157.0
Expt. (IXS)	164.5	149.8	156.3

parameter representing the temperature above which all vibrational modes in a crystal are excited and classical thermal effects become significant. Since room temperature is much lower than  $T_D$ , the thermal shifts in diamond are minimal. Consequently, the theoretical results remain a reliable basis for evaluating different exchange–correlation functionals against the measured dispersion.

In summary, comparing the phonon dispersion results with those of the lattice constants presented earlier, it can be seen that the SCAN family of functionals produces results that fall between those of PBE and HSE06. Bulk diamond is “softer” in PBE, resulting in a slightly larger lattice constant and lower phonon frequencies. Conversely, diamond is “harder” in HSE06, giving rise to a smaller lattice constant and correspondingly higher phonon frequencies.

### 2.3.3. Zero-phonon line energy

Building on the benchmark of bulk diamond properties presented in previous sections, this section addresses the first property of the  $NV^-$  center in diamond: the zero-phonon line. The ZPL serves as a key benchmark for evaluating the accuracy of an XC functional in describing both the electronic and lattice-relaxation contributions to the defect excitation energy. It represents the energy difference between the lowest vibrational levels of the ground and excited electronic states and appears experimentally as a sharp Lorentzian peak in the luminescence or absorption spectrum.

Table 2.3 lists the calculated  $E_{ZPL}$  values for the  $|^3A_2\rangle \leftrightarrow |^3E\rangle$  optical transition of the  $NV^-$  center and their relative deviations from the experimental reference of 1.945 eV [3]. Among the tested functionals, HSE06 gives the best quantitative agreement, overestimating the ZPL by only +0.057 eV (+2.9%). All semilocal functionals underestimate the ZPL, with PBE showing the largest deviation (−0.253 eV, −13.0%). SCAN reduces this error substantially (−0.078 eV, −4.0%), providing a good balance between accuracy and computational cost. The regularized versions of SCAN yield slightly larger deviations, with rSCAN and r<sup>2</sup>SCAN underestimating the ZPL by −0.133 eV (−6.8%) and −0.139 eV (−7.1%), respectively.

Overall, HSE06 delivers the highest accuracy in reproducing the experimental ZPL of the  $NV^-$  center, while SCAN offers a computationally efficient alternative with significantly better performance than PBE. The rSCAN and r<sup>2</sup>SCAN functionals achieve intermediate accuracy, maintaining reasonable agreement with experiment.

**Table 2.3.** Calculated ZPL energies  $E_{\text{ZPL}}$  (in eV) for the  $|^3A_2\rangle \leftrightarrow |^3E\rangle$  optical transition of the  $\text{NV}^-$  center in diamond, obtained using multiple density functionals. The experimental reference value is taken from Ref. [3]. Values in parentheses indicate the relative deviations from the experimental reference.

	$E_{\text{ZPL}}$
PBE	1.692 (−13.0 %)
SCAN	1.867 (−4.0 %)
rSCAN	1.812 (−6.8 %)
r <sup>2</sup> SCAN	1.806 (−7.1 %)
HSE06	2.002 (+2.9 %)
Expt.	1.945

### 2.3.4. Electron–phonon interaction

The next benchmark concerns the description of electron–phonon coupling at the  $\text{NV}^-$  center and its influence on the luminescence lineshape of the  $|^3E\rangle \rightarrow |^3A_2\rangle$  optical transition. The contribution of  $e$ -symmetry phonons was included within the adiabatic Huang–Rhys (HR) framework introduced in Sec. 1.6.1, which provides an adequate approximation for transitions from the Jahn–Teller-active excited state to the non-degenerate ground state [39]. All calculations employed the embedding methodology [39, 71] introduced in Sec. 1.7, enabling accurate treatment of the dilute-defect limit. For PBE and HSE06, vibrational data were taken from Ref. [39] using supercells of size  $20 \times 20 \times 20$  (64 000 atomic sites). For the SCAN family of functionals, slightly smaller supercells of  $18 \times 18 \times 18$  (46 656 atomic sites) were used. Smooth spectral functions were obtained by applying the broadening parameters described in Sec. 2.2.

In the HR formalism, electron–phonon coupling is characterized by the spectral function  $S(\hbar\omega)$  [Eq. (1.111)], which quantifies the coupling strength as a function of phonon energy.<sup>16</sup> Specifically,  $S(\hbar\omega) d\hbar\omega$  gives the average number of phonons emitted during a single optical transition within the interval  $[\hbar\omega, \hbar\omega + d\hbar\omega]$ . Figure 2.3 shows the calculated partial spectral functions for (a)  $a_1$ -symmetry and (b)  $e$ -symmetry vibrational modes. The total spectral function, obtained by summing both symmetry contributions, is shown in Fig. 2.4.

Notably, HSE06 predicts stronger coupling to  $a_1$ -symmetry modes, particularly near 65 meV, corresponding to a defect-induced quasi-localized vibrational resonance [39, 71] that lies within the host-lattice phonon band, up to about 167 meV. Additional features occur at higher energies:

<sup>16</sup>From this point onward, Hartree atomic units are replaced by SI units.

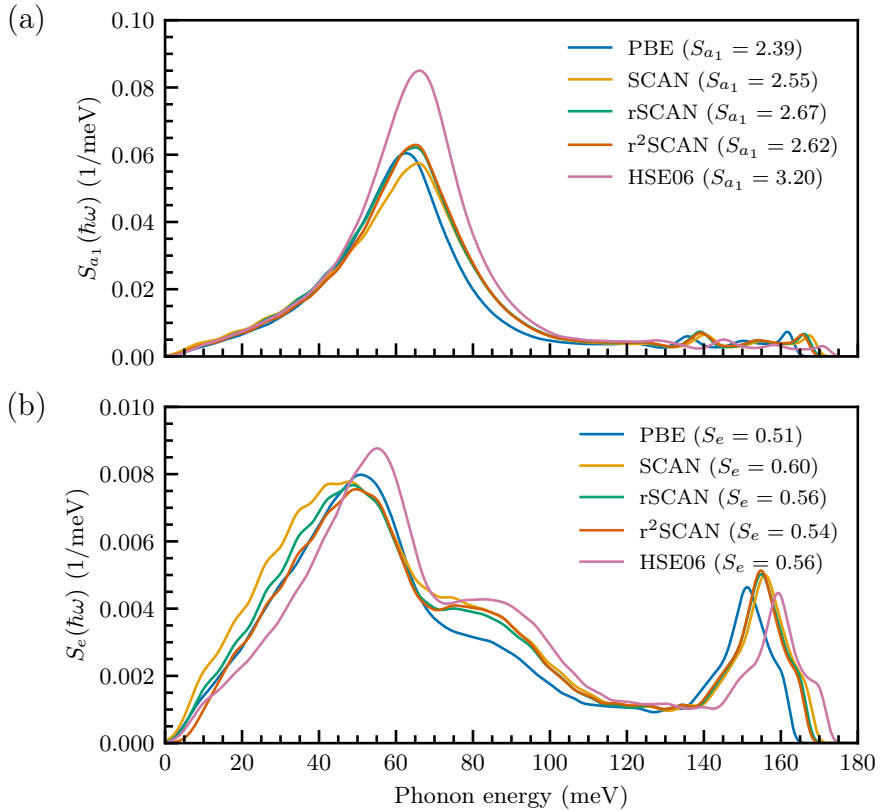


**Figure 2.3.** Calculated partial spectral functions of electron–phonon coupling for the luminescence of the  $\text{NV}^-$  center in diamond, obtained using multiple functionals. Panel (a) shows the spectral density  $S_{a_1}(\hbar\omega)$  associated with  $a_1$ -symmetry modes, while panel (b) presents the spectral density  $S_e(\hbar\omega)$  corresponding to  $e$ -symmetry modes.

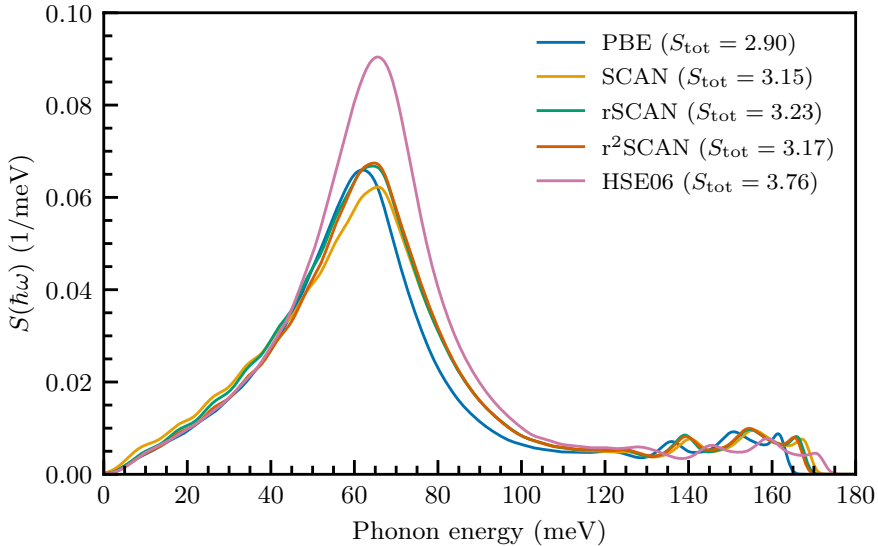


**Figure 2.4.** Calculated spectral functions of electron–phonon coupling  $S(\hbar\omega)$  for the luminescence of the  $\text{NV}^-$  center in diamond, obtained using multiple functionals

for the SCAN family, peaks near 139 meV and 167 meV; for PBE, these features are shifted to slightly lower energies at 136 meV and 162 meV; while for HSE06, they are found at slightly higher energies, around 145 meV and 171 meV, with lower intensity.

For  $e$ -symmetry modes, the high-energy peak also shows functional-dependent variation: it is centered around 155 meV for the SCAN functionals, 150 meV for PBE, and 160 meV for HSE06. These trends indicate that PBE consistently predicts the lowest phonon energies for sharp features in the spectral function, HSE06 the highest, with the SCAN family yielding intermediate values.

The total electron–phonon coupling strengths are summarized in Table 2.4 in terms of partial HR factors  $S_{a_1}$  and  $S_e$ , associated with  $a_1$ - and  $e$ -symmetry vibrational modes, respectively, and their sum,  $S_{\text{tot}} = S_{a_1} + S_e$  [Eq. (1.105)]. Both symmetry types contribute to luminescence, with  $a_1$ -symmetry modes playing a dominant role. The experimental estimate  $S_{\text{tot}} \approx 3.49$  [Eq. (1.107)] is taken from Ref. [108].

Among the tested functionals, PBE underestimates  $S_{\text{tot}}$  by 0.59 (−16.9%), while HSE06 slightly overestimates it by 0.27 (+7.7%). The SCAN family of functionals provides intermediate values:

- SCAN:  $S_{\text{tot}} = 3.15$ , an underestimation of 0.34 (−9.7%).
- rSCAN:  $S_{\text{tot}} = 3.23$ , an underestimation of 0.26 (−7.4%).

**Table 2.4.** Calculated partial ( $S_{a_1}$  and  $S_e$ ) and total ( $S_{\text{tot}}$ ) Huang–Rhys factors for the luminescence of the  $\text{NV}^-$  center in diamond. The approximate experimental value is taken from Ref. [108]. Values in parentheses indicate the relative deviations from the experimental reference.

	$S_{a_1}$	$S_e$	$S_{\text{tot}}$	
PBE	2.39	0.51	2.90	(−16.9%)
SCAN	2.55	0.60	3.15	(−9.7%)
rSCAN	2.67	0.56	3.23	(−7.4%)
r <sup>2</sup> SCAN	2.62	0.54	3.17	(−9.2%)
HSE06	3.20	0.56	3.76	(+7.7%)
Expt.	–	–	3.49	

- r<sup>2</sup>SCAN:  $S_{\text{tot}} = 3.17$ , an underestimation of 0.32 (−9.2%).

These findings demonstrate that the SCAN functionals significantly improve upon PBE in describing electron–phonon coupling. Among them, rSCAN provides the most accurate result, even slightly surpassing HSE06. However, as discussed in Sec. 1.6.1, caution is required when comparing the theoretical  $S_{\text{tot}}$  with the experimentally derived  $\tilde{S}_{\text{tot}}$ , since the latter is obtained using an approximate relation given by Eq. (1.107).

### 2.3.5. Luminescence lineshape

Finally, the calculated luminescence lineshapes, derived from the spectral functions discussed above, are shown in Fig. 2.5 alongside the experimental low-temperature photoluminescence spectrum from Ref. [108]. All theoretical spectra reproduce the main features observed experimentally: a sharp ZPL with a DWF in the range of approximately 3% to 6%, and a broad PSB extending to lower energies.

It is important to note that, aside from the ZPL energy  $E_{\text{ZPL}}$ , the ZPL linewidth (modeled using a broadening parameter  $\gamma = 0.3$  meV), and the smoothing parameters applied to  $S(\hbar\omega)$ , no empirical parameters were introduced. This highlights the predictive capability of modern first-principles methods for reproducing experimental luminescence spectra.

As shown in Fig. 2.5, HSE06 underestimates the intensities of the first two phonon peaks at around 65 meV and 125 meV below the ZPL, while PBE overestimates them. In contrast, the SCAN functionals yield intermediate results and exhibit the best agreement with experiment, accurately reproducing both the fine structure of the PSB and the relative peak intensities.

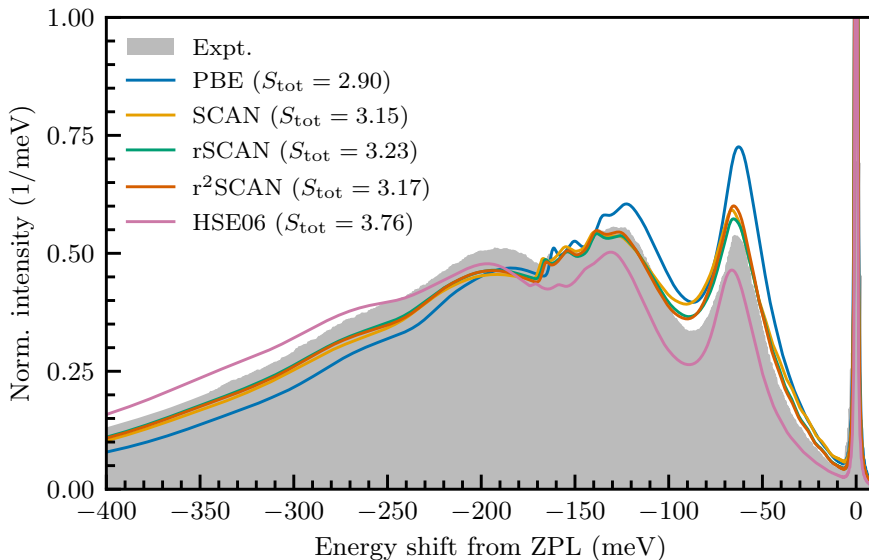


**Figure 2.5.** Calculated normalized luminescence lineshapes of the  $\text{NV}^-$  center in diamond, obtained using multiple functionals. Energies are plotted relative to the experimental ZPL energy. Experimental low-temperature data are taken from Ref. [108].

## Convergence of the luminescence lineshape

Achieving accurate optical lineshapes requires overcoming the computational limitations imposed by the size of directly accessible supercells, such as the  $4 \times 4 \times 4$  supercell employed in this study. While such supercells are adequate for capturing the overall spectral structure, they lack the accuracy necessary for reliable quantitative predictions. To evaluate the effect of the embedding methodology on the quality of the results, additional embedding calculations were performed for supercells of size  $N \times N \times N$ , with  $N \in \{8, 14, 16, 18\}$ .

Figure 2.6 presents the calculated spectral functions (left column) and the resulting normalized luminescence lineshapes (right column) as a function of supercell size  $N$ , using the  $\text{r}^2\text{SCAN}$  functional. Vertical lines in the left column represent the partial HR factors  $S_k$  for each phonon mode  $k$ , as defined in Eq. (1.108). Smoothing and broadening parameters were applied as described in Sec. 2.2.

While the luminescence lineshape appears well-converged for the  $14 \times 14 \times 14$  supercell, the description of the acoustic phonon region continues to improve with increasing size. This is due to the greater number of vibrational modes and the inclusion of lower-frequency acoustic modes, made possible by the larger real-space extent. This trend is

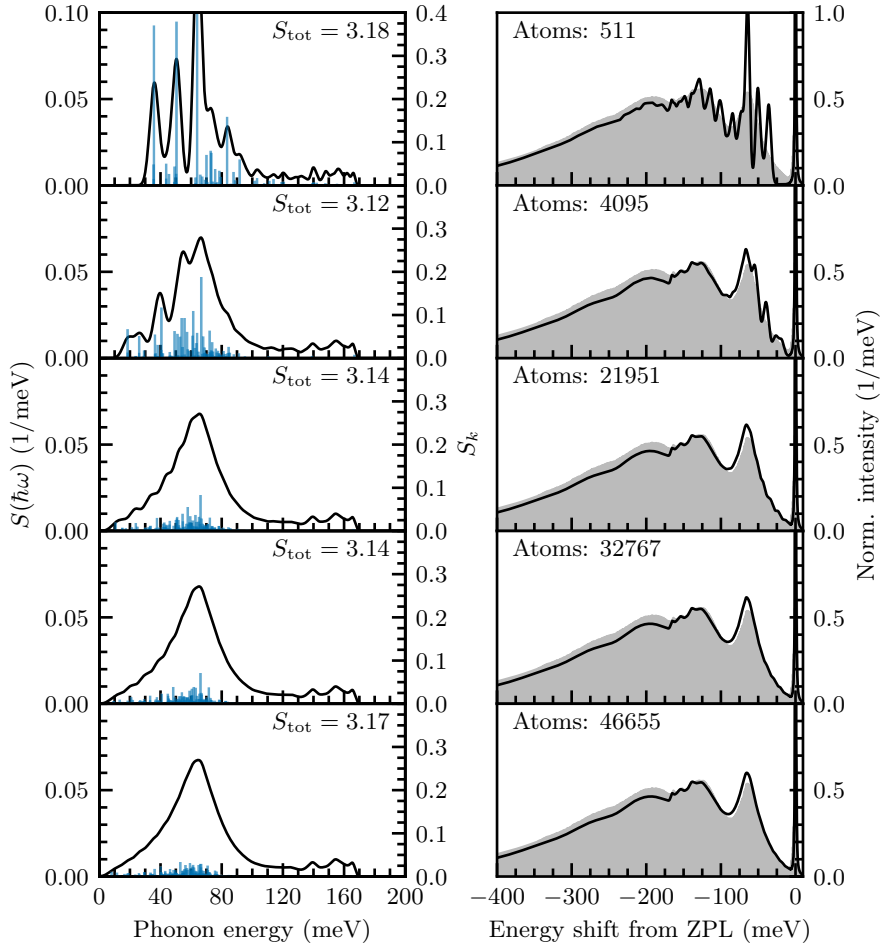


**Figure 2.6.** Convergence of the calculated spectral function of electron–phonon coupling  $S(\hbar\omega)$  (left column) and the normalized luminescence lineshape (right column) with respect to supercell size for the  $\text{NV}^-$  center in diamond. The vertical lines in the left column indicate the partial HR factors  $S_k$ . Supercells range in size from  $4 \times 4 \times 4$  (512 atomic sites) to  $18 \times 18 \times 18$  (46 656 atomic sites). The results correspond to calculations performed using the  $r^2\text{SCAN}$  functional, with smoothing and broadening parameters defined in Sec. 2.2. Experimental low-temperature data are taken from Ref. [108].

clearly reflected in the spectral function: the vertical lines, representing the contributions of individual phonon modes through the partial HR factors  $S_k$ , become denser and more uniformly distributed. In smaller supercells, such as  $4 \times 4 \times 4$  and  $8 \times 8 \times 8$ , these contributions are more sparsely distributed and exhibit greater variation in magnitude. As the supercell size increases, the phonon spectrum becomes smoother and more continuous, yielding a more accurate and converged representation of both the spectral function and the corresponding luminescence lineshape.

This convergence study also confirms the quasi-localized nature of the 65 meV feature [39, 71]. At larger supercells, the single peak resolves into many closely spaced phonon modes, each contributing less individually. Such behavior is characteristic of vibrational resonances arising from the defect-induced perturbation of the host-lattice phonon spectrum.

## 2.4. Summary and conclusions

This chapter presented a comparative analysis of several exchange–correlation functionals, such as PBE, SCAN, rSCAN, r<sup>2</sup>SCAN, and HSE06, for describing the structural, vibrational, and optical properties of diamond and the negatively charged nitrogen-vacancy (NV<sup>-</sup>) center. The key findings are summarized below:

1. All tested functionals yield lattice constants in good agreement with the zero-point–corrected experimental value. The SCAN family provides the closest match, offering slightly higher structural accuracy than both PBE and HSE06.
2. For the band gap, HSE06 remains the most accurate; however, the SCAN functionals significantly improve upon PBE. Within the SCAN family, SCAN itself shows the best agreement with experiment.
3. In terms of phonon frequencies, the SCAN functionals reproduce experimental data most accurately. PBE systematically underestimates, while HSE06 overestimates vibrational energies. Among them, r<sup>2</sup>SCAN provides the closest overall match to the experimental phonon spectrum.
4. For the zero-phonon line energy of the NV<sup>-</sup> center, HSE06 gives the most accurate value, as expected. Nevertheless, the SCAN functionals yield comparable results while markedly outperforming PBE.
5. Regarding the total electron–phonon coupling strength  $S_{\text{tot}}$ , the SCAN family offers a substantial improvement over PBE, achieving an optimal balance between computational cost and accuracy. Among them, rSCAN provides the best agreement with experimental data, even surpassing the more computationally demanding HSE06 functional.
6. For the luminescence lineshape, the SCAN functionals produce the closest match to experiment, accurately capturing both the fine structure of the phonon sideband and the relative spectral intensities.



# 3. Correlated electronic states: G-center in silicon

## 3.1. Introduction

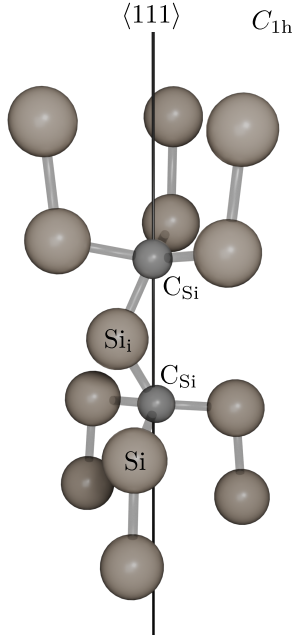
Silicon, a cornerstone of modern electronics, is also an emerging platform for quantum technologies owing to its compatibility with large-scale semiconductor fabrication and the presence of optically active point defects. Because of its relatively narrow band gap of approximately 1.1 eV, such defects emit in the technologically important near-infrared spectral region [13–20]. The formation and behavior of these centers are strongly influenced by the presence of common impurities in silicon, particularly carbon and oxygen.

Carbon impurities, introduced either during growth or post-processing, readily occupy substitutional lattice sites. Under irradiation, fast-diffusing silicon interstitials ( $\text{Si}_i$ ) can be trapped by substitutional carbon ( $\text{C}_{\text{Si}}$ ) atoms, forming mobile carbon interstitials ( $\text{C}_i$ ) [109]. These interstitials remain mobile even at room temperature [110, 111] and can interact with other impurities or additional  $\text{C}_{\text{Si}}$  atoms to form more complex defect structures. Through this sequence of reactions, the G-center structure can be stabilized as a thermodynamically favorable complex [112].

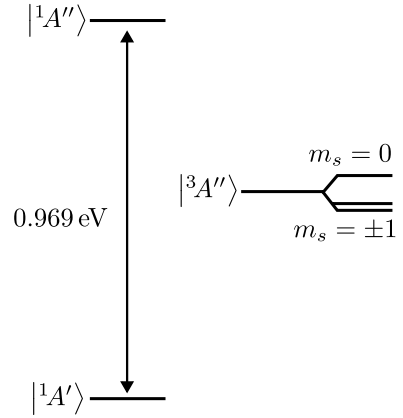
Structurally, the G-center is a neutral defect complex consisting of two  $\text{C}_{\text{Si}}$  atoms aligned along the  $\langle 111 \rangle$  crystallographic direction and a  $\text{Si}_i$  atom positioned between them, forming the  $\text{C}_{\text{Si}}\text{Si}_i\text{C}_{\text{Si}}$  configuration illustrated in Fig. 3.1a. This structure exhibits  $C_{1h}$  point group symmetry [113–116], with the symmetry plane defined by the three atoms.

Originally discovered in the 1960s as a product of irradiation damage caused by high-energy electrons, ions, or  $\gamma$ -rays [117], the G-center is now recognized as a promising optically active single-photon emitter. It features a sharp zero-phonon line (ZPL) at 0.969 eV (1279 nm) [14–16, 112, 118, 119] and a Debye–Waller factor (DWF) of approximately 20% [15, 16, 120, 121] at low temperature, making it an attractive candidate for telecom-band quantum light sources.

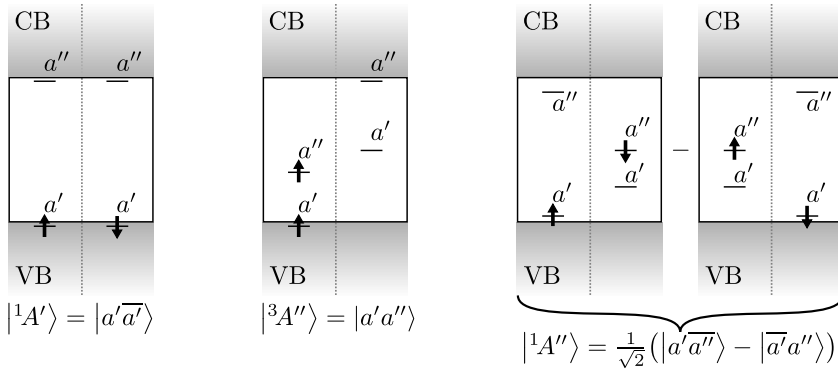
Because the  $\text{Si}_i$  atom is only twofold coordinated, the G-center is not a rigid structure. The interstitial silicon can rotate about the  $\langle 111 \rangle$  axis through six equivalent configurations, giving rise to six PES minima in both ground and excited states [122, 123]. The reorientation occurs in two nearly coplanar, threefold-symmetric planes, resulting in a six-fold PES. Nudged elastic band calculations [124, 125] yield rotational



(a) Atomic structure representation



(b) Energy-level diagram



(c) Representations of the Kohn–Sham electronic configurations of the spin-singlet ground state  $|{}^1A'\rangle$ , the metastable spin-triplet excited state  $|{}^3A''\rangle$ , and the spin-singlet excited state  $|{}^1A''\rangle$

**Figure 3.1.** The G-center in silicon

barriers of approximately 89 meV for the ground state and 40 meV for the triplet excited state, while fitting to the experimental data gives 33 meV for the singlet excited state [122]. Owing to these relatively small barriers, the interstitial atom undergoes tunneling and thermally activated hopping between minima, leading to athermal reorientation at cryogenic temperatures and thermal averaging to  $C_{3v}$  symmetry in the triplet excited state at elevated temperatures [122, 123]. Consequently, the PES exhibits pronounced anharmonicity along specific ionic degrees of freedom associated with the interstitial silicon atom. This indicates that a more advanced treatment accounting for the rotational degree of freedom of the interstitial silicon atom and its coupling to electronic states could be important for achieving a fully accurate description of the fine structure and optical lineshapes [122, 123].

The electronic structure of the G-center can be qualitatively described using a molecular orbital model. Each  $C_{Si}$  atom forms four  $sp^3$ -like bonds with neighboring silicon atoms, while the  $Si_i$  atom establishes two directional  $p$ -type bonds with the carbon atoms. This bonding arrangement leaves two electrons occupying highly strained  $sp$ -like orbitals localized on the interstitial atom. First-principles studies confirm that the ground state contains a fully occupied mirror-symmetric  $a'$  orbital resonant with the valence band maximum (VBM) and an unoccupied mirror-antisymmetric  $a''$  orbital located within the band gap [122], as illustrated in Fig. 3.1c. This configuration gives rise to a spin-singlet ground state  $|^1A'\rangle$ , well described by a non-correlated single-determinant wave function, and a spin-singlet excited state  $|^1A''\rangle$  with a correlated two-determinant character (Fig. 3.1c). Together, these states account for the observed optical transition shown in the energy-level diagram in Fig. 3.1b. A metastable spin-triplet excited state  $|^3A''\rangle$  has also been reported [126], with theoretical estimates placing it about 0.7 eV above the ground state [122].

In this chapter, the SCAN family of functionals [28–30] is benchmarked for its ability to describe the structural, vibrational, and electronic properties of bulk silicon and of the G-center defect. Following the procedure established in Chapter 2, the SCAN functionals are compared with PBE and HSE06 in terms of lattice constant, band gap, and phonon spectrum. Subsequently, the ZPL, vibrational properties, electron–phonon coupling strength, and luminescence lineshape of the G-center are investigated using the SCAN functional. Because the singlet excited state exhibits static electron correlation, three different approximations are employed to model it.

Unlike the benchmarking study presented for the  $NV^-$  center in Chapter 2, the results in this chapter are unpublished at the time of writing. Accurate modeling of the optical spectra of G-center is challenging

not only because the singlet excited state  $|^1A''\rangle$  has a multi-determinant electronic character, requiring methodological corrections to capture its open-shell singlet nature [33, 127], but also because the G-center possesses anharmonicity in both ground and excited states. Since a fully consistent treatment of anharmonic nuclear motion is complex and only certain ionic degrees of freedom are likely to exhibit anharmonicity, the defect is modeled here using a harmonic approximation around a representative equilibrium configuration. This provides a baseline for evaluating the influence of anharmonic effects on the observed optical response.

### 3.2. Computational details

The computations presented in this chapter follow the general methodology outlined in Sec. 1.8. The properties of silicon and the G-center were modeled using a 512-site cubic supercell, constructed by replicating the conventional cubic unit cell of silicon (containing eight atoms) in a  $4 \times 4 \times 4$  arrangement. A plane-wave energy cutoff of 500 eV was employed, and  $\Gamma$ -point sampling was used for Brillouin-zone sampling. For bulk silicon, five exchange–correlation functionals were tested: PBE [31], SCAN [28], rSCAN [29], r2SCAN [30], and HSE06 [32]. All defect-related calculations were carried out using the SCAN functional.

The spin-singlet ground state of the neutral G-center is a closed-shell system described by a single-determinant state,  $|S_0\rangle \equiv |^1A'\rangle = |a'\bar{a}'\rangle$ , in which both outermost electrons occupy the defect-induced  $a'$  orbital resonant with the VBM and localized on the silicon self-interstitial atom [122]. Promotion of one electron from the occupied  $a'$  orbital to the unoccupied  $a''$  orbital within the same spin channel, performed using the  $\Delta$ SCF method [46, 89, 90], yields a spin-triplet excited state  $|T\rangle \equiv |^3A''\rangle = |a'a''\rangle$ , expressed as a singlet determinant corresponding to the  $m_s = 1$  projection. In contrast, the spin-singlet excited state  $|S_1\rangle \equiv |^1A''\rangle = \frac{1}{\sqrt{2}}(|a'a''\rangle - |\bar{a}'a''\rangle)$ , exhibits static correlation and requires a two-determinant description, which cannot be represented within the single-determinant Kohn–Sham framework. The Kohn–Sham configurations of all three electronic states are illustrated in Fig. 3.1c.

Accurately describing the  $|S_1\rangle$  excited state necessitates methods capable of capturing its multi-determinant character [33, 127], which were not employed here. Instead, three approximate strategies were used to model this state:

1. Triplet approximation: The spin-triplet excited state  $|T\rangle = |a'a''\rangle$  was utilized as a structural proxy for the target singlet excited state  $|S_1\rangle$ . This approximation is physically motivated by the fact

that both the triplet and the singlet excited states arise from the same electronic transition: the promotion of an electron from the  $a'$  orbital to the  $a''$  orbital. Because they share an identical orbital configuration, it is assumed that their potential energy surfaces and resulting equilibrium geometries are sufficiently similar to represent the lattice relaxation of the singlet manifold. From a computational standpoint, the triplet state is advantageous because it is well-defined by a single Slater determinant, making it straightforward to calculate accurately within standard spin-polarized DFT.

2. Spin-contaminated approximation: This approach utilizes a single-determinant configuration as a simplified model for the correlated excited state  $|S_1\rangle$ . Within the  $\Delta$ SCF methodology, the state is represented by the configuration  $|M\rangle = |a'\overline{a''}\rangle$ . Formally, the “true” spin-singlet excited state is an entangled multi-determinant state:

$$|S_1\rangle = \frac{1}{\sqrt{2}}(|a'\overline{a''}\rangle - |\overline{a'}a''\rangle).$$

Since standard DFT is inherently a single-particle theory restricted to single Slater determinants, it cannot capture this entanglement directly. The mixed state  $|M\rangle$  serves as a practical approximation representing a formal 50/50 mixture of the singlet and triplet components:

$$|M\rangle = (|S_1\rangle + |T\rangle)/\sqrt{2}.$$

While this method accounts for the specific orbital occupations, it remains a single-determinant “spin-contaminated” state.

3. Approximate spin projection method: A modified spin-purification scheme [33, 127] was applied at the level of atomic forces. At each geometry optimization step, two self-consistent calculations were performed: one for the triplet state  $|T\rangle$  and one for the mixed-spin state  $|M\rangle$ . The atomic forces were then combined using the following expression:

$$\mathbf{F}(|S_1\rangle) \approx 2\mathbf{F}(|M\rangle) - \mathbf{F}(|T\rangle), \quad (3.1)$$

which is analogous to the spin-purified energy expression [128, 129]

$$E(|S_1\rangle) \approx 2E(|M\rangle) - E(|T\rangle). \quad (3.2)$$

The corresponding force-based minimization procedure was implemented as a separate post-processing code interfaced with the underlying electronic-structure calculations. Energy was calculated using the spin-purified energy expression. The resulting effective “state”, denoted as  $|F\rangle$ , was used to approximate the geometry and energy of the  $|S_1\rangle$  state.

**Table 3.1.** Calculated lattice constants  $a$  (in Å) and band gaps  $E_g$  (in eV) of bulk silicon, obtained using multiple density functionals. Experimental low-temperature values are taken from Refs. [130, 131]. For comparison, the zero-point-corrected experimental lattice constant reported in Ref. [104] is also included. Values in parentheses indicate the relative deviations from the experimental reference.

	$a$	$E_g$
PBE	5.469 (+0.87 %)	0.61 (−48 %)
SCAN	5.428 (+0.11 %)	0.83 (−29 %)
rSCAN	5.435 (+0.24 %)	0.78 (−33 %)
r <sup>2</sup> SCAN	5.440 (+0.33 %)	0.78 (−33 %)
HSE06	5.433 (+0.20 %)	1.15 (−2 %)
Expt.	5.430 <sup>a</sup> 5.422 <sup>b</sup>	1.17 <sup>c</sup>

<sup>a</sup>Ref. [130]   <sup>b</sup>Ref. [104]   <sup>c</sup>Ref. [131]

Phonon dispersion relations for bulk silicon and the vibrational properties of the G-center were computed using the finite-displacement method [87, 88] with atomic displacements of 0.02 Å.

The vibrational structure and the luminescence lineshape of the G-center were obtained using the embedding methodology [39, 71] described in Sec. 1.7, corresponding to an effective supercell size of  $18 \times 18 \times 18$  (46 656 atomic sites). To generate smooth electron-phonon coupling spectra and luminescence lineshapes, the Dirac  $\delta$ -functions in Eq. (1.111) were replaced by Gaussians with linearly varying standard deviations  $\sigma$ , decreasing from 3.5 meV near the ZPL to 1.5 meV toward the low-energy tail. Selected high-energy localized modes were additionally broadened using Lorentzian profiles with a HWHM of 0.3 meV, while the ZPL broadening in the luminescence spectrum was modeled using  $\gamma = 0.2$  meV, as defined in Eq. (1.103).

### 3.3. Results and discussion

#### 3.3.1. Lattice parameters of silicon

The lattice constant  $a$  and band gap  $E_g$  of bulk silicon were calculated using the XC functionals introduced earlier. The results, compared with low-temperature experimental values from Refs. [130, 131], are summarized in Table 3.1. As in the case of diamond (Sec. 2.3.1), a lattice constant corrected for the zero-point vibrations was also considered, following Ref. [104].

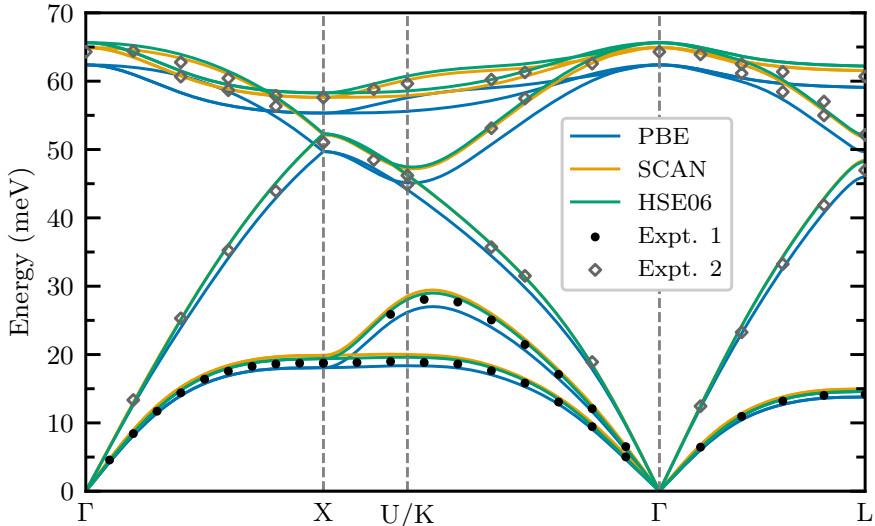


**Figure 3.2.** Calculated phonon dispersion relations of bulk silicon using PBE, SCAN, and HSE06 functionals. Experimental room-temperature values are taken from Ref. [132].

The SCAN functional provides the closest agreement with the zero-point-corrected experimental lattice constant value of  $a = 5.422 \text{ \AA}$  [104], predicting  $a = 5.428 \text{ \AA}$ , a deviation of  $+0.006 \text{ \AA}$  ( $+0.11 \%$ ). HSE06 performs comparably, yielding  $a = 5.433 \text{ \AA}$  ( $+0.011 \text{ \AA}$ ,  $+0.20 \%$ ). By contrast, PBE significantly overestimates the lattice constant, predicting  $a = 5.469 \text{ \AA}$  ( $+0.047 \text{ \AA}$ ,  $+0.87 \%$ ). The rSCAN and r<sup>2</sup>SCAN functionals produce intermediate values of  $5.435 \text{ \AA}$  ( $+0.013 \text{ \AA}$ ,  $+0.24 \%$ ) and  $5.440 \text{ \AA}$  ( $+0.018 \text{ \AA}$ ,  $+0.33 \%$ ), respectively.

For the band gap, HSE06 delivers the best performance, giving  $E_g = 1.15 \text{ eV}$  ( $-0.02 \text{ eV}$ ,  $-2 \%$ ), in close agreement with the experimental value of  $E_g = 1.17 \text{ eV}$  [131]. PBE, by contrast, severely underestimates the band gap at  $0.61 \text{ eV}$  ( $-0.56 \text{ eV}$ ,  $-48 \%$ ). SCAN improves upon this result, predicting  $0.83 \text{ eV}$  ( $-0.34 \text{ eV}$ ,  $-29 \%$ ), while rSCAN and r<sup>2</sup>SCAN both yield  $0.78 \text{ eV}$  ( $0.39 \text{ eV}$ ,  $-33 \%$ ).

### 3.3.2. Vibrational properties of silicon

Next, the lattice dynamics of bulk silicon were examined. The calculated phonon dispersion relations, obtained using PBE, SCAN, and HSE06 functionals, are shown in Fig. 3.2 alongside experimental room-temperature data from Ref. [132]. Complementary results for longitudinal optical (LO) phonon frequencies at selected high-symmetry points are listed in Table 3.2.

**Table 3.2.** Calculated longitudinal optical (LO) phonon frequencies  $\omega$  (in meV) at high-symmetry points in the Brillouin zone of the reciprocal lattice of bulk silicon, obtained using multiple density functionals. Experimental room-temperature values are taken from Ref. [132]. Only the frequencies of the highest-lying LO branches are reported. Values in parentheses indicate the relative deviations from the experimental reference.

	$\omega(\Gamma)$	$\omega(X)$	$\omega(L)$
PBE	62.4 (−2.95 %)	55.3 (−3.99 %)	59.1 (−2.64 %)
SCAN	64.9 (+0.93 %)	57.6 (0.00 %)	61.6 (+1.48 %)
rSCAN	64.3 (0.00 %)	57.1 (−0.87 %)	61.0 (+0.49 %)
r <sup>2</sup> SCAN	64.4 (+0.16 %)	57.2 (−0.69 %)	61.1 (+0.66 %)
HSE06	65.6 (+2.02 %)	58.3 (+1.22 %)	62.3 (+2.64 %)
Expt.	64.3	57.6	60.7

All functionals reproduce the qualitative shape of the phonon dispersion but differ in their quantitative accuracy. PBE systematically underestimates phonon frequencies, whereas HSE06 slightly overestimates them—an effect most evident in the optical branches. The SCAN, rSCAN, and r<sup>2</sup>SCAN functionals yield improved agreement with experimental data, producing nearly identical results across the family. For clarity, the SCAN functional is the only member of this family explicitly shown in Fig. 3.2.

As noted in the case of diamond (Sec. 2.3.2), the 0 K theoretical results are compared directly with room-temperature experimental data reported in Ref. [132]. Although silicon has a lower Debye temperature than diamond ( $T_D \approx 645$  K), room temperature still represents a regime where the anharmonic frequency shifts are relatively small [133]. Consequently, the discrepancies between 0 K theory and room-temperature experiment remain secondary to the systematic differences between the exchange–correlation functionals themselves.

In summary, as with diamond, the SCAN functionals provide an intermediate and accurate description. While PBE predicts a “softer” lattice with a larger lattice constant and lower phonon frequencies, HSE06 predicts a slightly “stiffer” lattice with a smaller lattice constant and higher frequencies. Notably, for silicon, the discrepancy between the SCAN family and HSE06 in the higher-lying optical branches is visibly smaller than that observed for diamond.

### 3.3.3. Zero-phonon line energy

Building on the bulk-property benchmarks, the ZPL of the G-center was computed for the optical transitions  $|S_0\rangle \leftrightarrow \{|T\rangle, |M\rangle, |F\rangle\}$ . The

**Table 3.3.** Calculated ZPL energies  $E_{\text{ZPL}}$  (in eV) for optical transitions between the  $|S_0\rangle$  state and the  $|T\rangle$ ,  $|M\rangle$ ,  $|F\rangle$  states of the G-center in silicon, obtained using the PBE and SCAN density functionals. The experimental reference value for the  $|S_0\rangle \leftrightarrow |S_1\rangle$  transition is 0.969 eV [119]. Values in parentheses indicate the relative deviations from the experimental reference for the  $|S_0\rangle \leftrightarrow \{|M\rangle, |F\rangle\}$  transitions.

$E_{\text{ZPL}}$	$ T\rangle$	$ M\rangle$	$ F\rangle$
PBE	0.565	0.655 (−32.4 %)	0.709 (−26.8 %)
SCAN	0.510	0.715 (−26.2 %)	0.901 (−7.0 %)

calculated ZPL energies, summarized in Table 3.3, were obtained using the PBE and SCAN functionals. Because the  $\text{Si}_i$  atom can occupy six degenerate orientations separated by low barriers and the  $\Delta\text{SCF}$  method samples only one of the equivalent minima, the associated anharmonicity of the PES contributes additional uncertainty to the calculated ZPL energies.

In the case of ZPL calculations, only the  $|M\rangle$  and  $|F\rangle$  states are used as approximations to the excited state  $|S_1\rangle$ , while the triplet state  $|T\rangle$  serves solely as a structural proxy for  $|S_1\rangle$  and is not intended to represent the target excitation.

Theoretical values are compared with the experimental ZPL value of 0.969 eV [119]. The best agreement is achieved using the approximate spin projection method (state  $|F\rangle$ ), which yields ZPLs of 0.901 eV with SCAN and 0.709 eV with PBE, with deviations of  $-0.068$  eV (−7.0 %) and  $-0.260$  eV (−26.8 %). The mixed-spin state  $|M\rangle$  leads to reduced agreement, with deviations of  $-0.314$  eV (−32.4 %) for SCAN and  $-0.254$  eV (−26.2 %) for PBE. The triplet configuration  $|T\rangle$ , which is not intended to represent the target excitation, yields ZPL energies of 0.510 eV (SCAN) and 0.565 eV (PBE).

### 3.3.4. Vibrational structure

The calculated vibrational structure of the ground state  $|S_0\rangle$  of the G-center is shown in Fig. 3.3, represented by the localization ratios  $\beta_k$  [Eq. (1.71)] for vibrational modes of  $a'$  symmetry. These results, obtained using the SCAN functional and the embedding methodology [39, 71] (Sec. 1.7), correspond to an effective supercell size of  $18 \times 18 \times 18$  (46 656 atomic sites). Theoretical results are compared with the low-temperature spectrum from Ref. [134].

As introduced in Sec. 1.4.5, larger  $\beta_k$  values indicate stronger vibrational localization near the defect. Because the ground state is non-degenerate, only symmetry-preserving  $a'$  modes contribute to first-

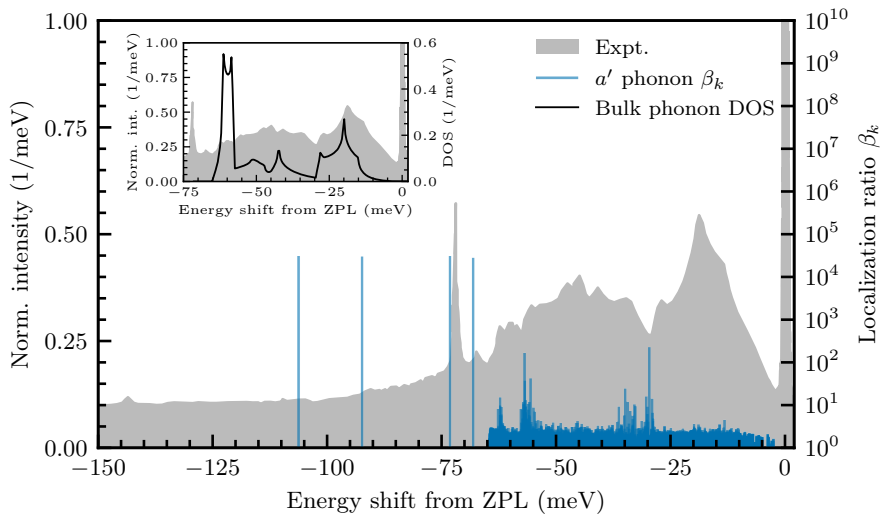


**Figure 3.3.** Calculated vibrational structure of the ground state of the G-center in silicon. Energies are plotted relative to the experimental ZPL energy. Vertical lines indicate the localization ratios ( $\beta_k$ ) of vibrational modes with  $a'$  symmetry, computed for an  $18 \times 18 \times 18$  supercell (46 656 atomic sites) using the SCAN functional. The inset shows the phonon DOS for pristine silicon, calculated using a  $4 \times 4 \times 4$  supercell (512 atomic sites). Experimental low-temperature luminescence data are taken from Ref. [134].

order electron–phonon coupling, in accordance with the Wigner–Eckart theorem [135]. The inset of Fig. 3.3 displays the phonon DOS for pristine silicon, obtained from a  $4 \times 4 \times 4$  supercell (512 atomic sites), overlaid with the experimental luminescence spectrum for reference.

Several highly localized  $a'$  modes ( $\beta_k > 1000$ ) are identified with energies of 68.6 meV, 72.6 meV, 92.2 meV and 105.8 meV. The localized modes at 68.6 meV and 72.6 meV correspond closely to prominent peaks in the experimental phonon sideband (PSB), albeit with a slight offset. In contrast, the absence of experimental features at 92.2 meV and 105.8 meV below the ZPL indicates that high localization alone does not guarantee strong coupling, as vibrational modes must also project effectively onto the structural relaxation vector  $\Delta\mathbf{R}$ , defined in Eq. (1.110). The existence of six equivalent minima in the PES implies that the  $\text{Si}_i$  atom can reorient among these configurations, which slightly modifies local force constants and introduces anharmonic effects. This dynamic behavior may contribute to the observed energy shifts of localized peaks in the experimental spectrum.<sup>17</sup>

<sup>17</sup>As demonstrated in the next chapter, applying the same methodology yields near-perfect agreement with the experimental vibrational frequencies of the C-center in silicon, where anharmonic effects are absent.

Beyond these localized modes, several clusters of quasi-localized resonances appear around 30 meV, 35 meV, 57 meV and 63 meV relative to the ZPL, characterized by moderate localization ( $\beta_k \approx 10$ ) and weak correspondence with features in the experimental spectrum.

Finally, bulk-like modes with low localization ( $\beta_k \approx 1$ ) extend up to about 65 meV from the ZPL, matching the upper phonon band-edge limit of pristine silicon. Their presence reflects extended lattice vibrations intrinsic to the host crystal. A comparison of the bulk phonon density of states (DOS) with the experimental photoluminescence spectrum in the inset of Fig. 3.3 shows that the first broad peak in the PSB follows the bulk density of states in the 10 meV to 30 meV range, indicating the involvement of delocalized bulk phonons in the electron–phonon interaction of the G-center.

### 3.3.5. Electron–phonon interaction and luminescence lineshape

Finally, Fig. 3.4 presents the calculated electron–phonon coupling spectra (inset) and the resulting luminescence lineshapes (main panel) of the G-center for the  $|S_1\rangle \rightarrow |S_0\rangle$  transition. The excited state  $|S_1\rangle$  was approximated using three distinct approaches described in Sec. 3.2. Because of symmetry restrictions, phonons of  $a''$  symmetry do not contribute to first-order coupling; thus, the spectral function  $S(\hbar\omega)$  contains only  $a'$  phonons. All calculations employed the SCAN functional, an  $18 \times 18 \times 18$  (46 656 atomic sites) supercell, and the embedding methodology [39, 71] (Sec. 1.7) to approximate the dilute-defect limit. The broadening parameters used to generate smooth spectral functions and lineshapes were used as specified in Sec. 3.2.

The transition involving state  $|T\rangle$  exhibits the strongest electron–phonon coupling ( $S_{\text{tot}} = 3.33$ ) and thus the lowest DWF ( $w_{\text{ZPL}} \approx 5\%$ ). The  $|M\rangle$  and  $|F\rangle$  states yield weaker couplings,  $S_{\text{tot}} = 1.83$  and  $S_{\text{tot}} = 2.01$ , with corresponding DWFs of  $w_{\text{ZPL}} \approx 17\%$  and  $w_{\text{ZPL}} \approx 15\%$ , respectively. The values of  $S_{\text{tot}}$  indicate that on average about two or three phonons are emitted per optical transition.

All three approximations predict a distinct low-energy peak about 15 meV below the ZPL that approximately aligns with the experimental peak. Because of the stronger electron–phonon coupling in the  $|T\rangle$ -state approximation, the PSB shifts toward lower energies, resulting in a lower intensity of the first peak and worse match with the experimental lineshape. At higher energies, several localized modes identified in Sec. 3.3.4, particularly those at 72.6 meV, 92.2 meV and 105.8 meV, manifest as features in the theoretical spectra. Of these, the 72.6 meV mode produces a strongly pronounced peak that aligns closely with the experimental data. The 92.2 meV mode appears most clearly in the lineshapes associated

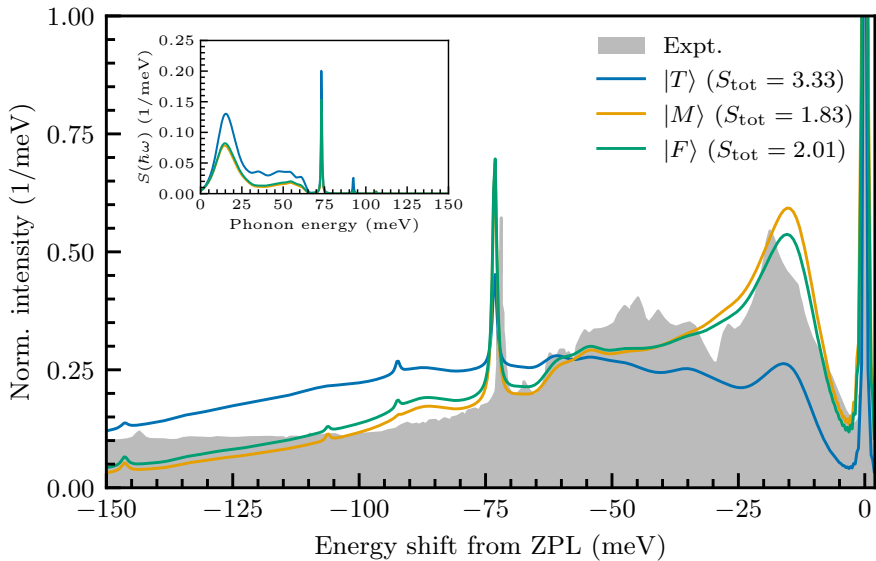


**Figure 3.4.** Calculated normalized luminescence lineshapes of the G-center in silicon for three different approximations to the excited state  $|S_1\rangle$ . Energies are plotted relative to the experimental ZPL energy. The inset shows the calculated spectral functions of electron–phonon coupling  $S(\hbar\omega)$  for the luminescence. The results correspond to calculations performed using an  $18 \times 18 \times 18$  supercell (46 656 atomic sites) and the SCAN functional. Experimental low-temperature data are taken from Ref. [134].

with the  $|T\rangle$  and  $|F\rangle$  states, while the 105.8 meV mode emerges more subtly in the spectra derived from the  $|M\rangle$  and  $|F\rangle$  approximations. A faint peak near 150 meV likely represents a two-phonon replica of the 72.6 meV mode. However, none of the approximations capture the broad feature between 30 meV to 60 meV.

The luminescence lineshapes derived from the  $|M\rangle$  and  $|F\rangle$  states show the best agreement with experiment, particularly in reproducing the PSB intensity distribution. However, none of the models fully capture the fine structure or exact peak positions, underscoring the sensitivity of the optical spectrum to an accurate description of the geometries of both electronic states involved in the transition. These discrepancies likely arise from the multi-determinant character of the singlet excited state and the anharmonic nature of the PESs of both ground and excited states of the G-center. This behavior highlights the limitations of methodologies that are otherwise well established for many defect systems, demonstrating that standard harmonic and single-determinant treatments are inadequate for the G-center. Consequently, the G-center emerges as a benchmark system for the development of advanced theoretical approaches capable of describing anharmonic electron–phonon interactions and correlated excited states.

### 3.4. Summary and conclusions

In this chapter, the performance of the SCAN family of functionals was benchmarked for modeling the bulk properties of silicon and compared with the widely used PBE and HSE06 functionals. Furthermore, the SCAN functional was employed to investigate the G-center in silicon, focusing on its luminescence lineshape and employing three different approximations to the statically correlated excited state. The key findings are summarized below:

1. All tested functionals yield lattice constants in good agreement with the zero-point-corrected experimental value, with the SCAN family providing the closest match.
2. For the band gap, the SCAN functionals substantially improve upon PBE, reducing the deviation from experiment, although HSE06 remains the most accurate overall. Within the SCAN family, the SCAN functional provides the best quantitative agreement.
3. In terms of phonon frequencies, the SCAN functionals reproduce experimental phonon frequencies most accurately. PBE systematically underestimates vibrational energies, while HSE06 tends to overestimate them.
4. For the zero-phonon line energy of the G-center, among the two approximations to the excited state, the best agreement with experiment is obtained using the approximate spin projection method.
5. For the electron-phonon interaction and resulting luminescence lineshape, the approximations based on the  $|M\rangle$  and  $|F\rangle$  states reproduce the experimental data more accurately than the  $|T\rangle$ -based model. While these approaches successfully capture the relative intensities within the phonon sideband, they do not recover its fine structure or the exact energies of the localized vibrational modes.

#### **Thesis statement (I)**

The luminescence lineshape of the G-center defect in silicon could only be partially reproduced using the approximate spin projection method to model the multi-Slater-determinant nature of the excited state. Differences between theory and experiment may arise from either a limited approximation of static correlation in the excited state or from anharmonic effects in the ionic potential that are not captured by the harmonic framework.

## 4. Weakly bound exciton-like electronic states: C-center in silicon

### 4.1. Introduction

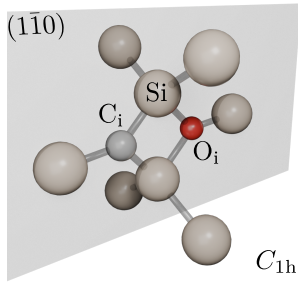
Another optically active defect in silicon is the C-center, which, like the G-center discussed in Chapter 3, was first identified in the 1960s as a byproduct of irradiation with high-energy particles [117]. The C-center exhibits an emission line (ZPL) at 1570 nm (0.790 eV) [136–139] and a Debye–Waller factor (DWF) of approximately 12% [140] at low temperature. Because its emission lies within the telecommunication band, the C-center is a promising candidate for fiber-compatible single-photon sources.

As described in Sec. 3.1, both carbon and oxygen impurities are commonly present in silicon. Following high-energy irradiation, interactions between substitutional carbon ( $C_{Si}$ ) and self-interstitial silicon ( $Si_i$ ) defects can lead to the formation of mobile carbon interstitials ( $C_i$ ) [109]. Because  $C_i$  atoms remain mobile even at room temperature [110, 111], they can subsequently bind with oxygen interstitials ( $O_i$ ) to form a neutral carbon-oxygen interstitial pair ( $C_iO_i$ ) [112], commonly known as the C-center.

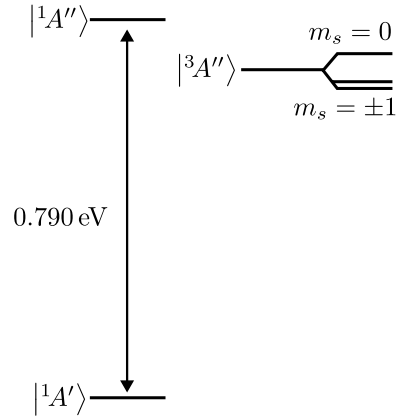
Structurally, the defect adopts a square-like ring configuration within the  $(1\bar{1}0)$  crystallographic plane, consisting of two silicon atoms and the two interstitial species [141, 142]. The resulting structure exhibits  $C_{1h}$  point group symmetry [137], as illustrated in Fig. 4.1a.

The electronic structure of the neutral C-center can be described using molecular orbital theory and partially resembles that of the G-center in silicon (Chapter 3). Both  $C_i$  and  $O_i$  form three  $sp^2$ -like hybridized bonds with neighboring silicon atoms, leaving four electrons to occupy two  $p$ -type orbitals. Previous theoretical studies have shown that the only defect-induced in-gap level, denoted  $a''$ , corresponds to a  $p$ -type orbital localized mainly on the carbon atom [140], while the oxygen-related orbital is resonant with the bulk states. The closed shell occupation of the  $a''$  orbital results in a spin-singlet ground state  $|^1A'\rangle$ .

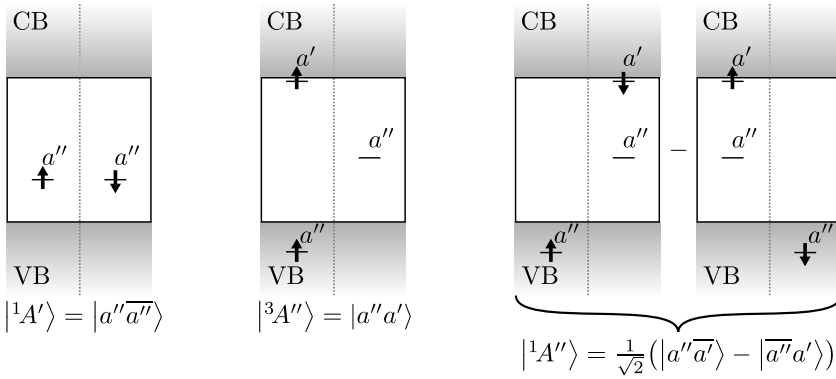
Although this one-orbital electronic structure might suggest the absence of intradefect optical transitions, photoluminescence excitation measurements reveal a series of bound exciton states [136, 137]. These states arise from the Coulomb interaction between the charged defect and a bound carrier, forming weakly-bound, hydrogen-like excitons. The lowest excitonic orbital is expected to be predominantly  $s$ -like and thus



(a) Atomic structure representation



(b) Energy-level diagram



(c) Representations of the Kohn–Sham electronic configurations of the spin-singlet ground state  $|^1A'\rangle$ , the metastable spin-triplet excited state  $|^3A''\rangle$ , and the spin-singlet excited state  $|^1A''\rangle$

**Figure 4.1.** The C-center in silicon

transforms as the totally symmetric  $a'$  representation; when combined with the underlying defect configuration, this results in a many-electron excitonic state  $|^1A''\rangle$ . A metastable spin-triplet excited state  $|^3A''\rangle$  is also predicted to exist, lying approximately 3 meV below the  $|^1A''\rangle$  state according to several studies [138, 140, 143]. These states are summarized in the energy-level diagram in Fig. 4.1b.

The optical transition from the triplet excited state  $|^3A''\rangle$  to the singlet ground state  $|^1A'\rangle$  possesses a finite electric dipole moment, making the triplet state observable in luminescence spectra [138]. However, the dominant contribution to the optical signal arises from the singlet-to-singlet transition  $|^3A''\rangle \rightarrow |^1A'\rangle$ , which forms the focus of this chapter.

This chapter investigates the thermodynamic stability, vibrational properties, and optical activity of the C-center. First, thermodynamic quantities are computed, including the formation energies of the most stable configurations of  $C_i$ ,  $O_i$ , and  $C_iO_i$  (C-center) in various charge states, the binding energy of the neutral complex, and the charge-state transition levels (CTLs) of the individual and combined defects. Vibrational analysis identifies localized, bulk-like, and resonant vibrational modes that explain features observed in the low-temperature experimental spectrum. The luminescence and absorption lineshapes are then computed, showing excellent agreement between the theoretical emission spectrum and experimental measurements, further supporting the attribution of the 0.790 eV emission to the  $C_iO_i$  complex. Finally, it is demonstrated that luminescence involving weakly bound exciton-like excited states can be modeled accurately using a practical approximation in which the excited-state geometry of the neutral defect is replaced by the relaxed geometry of the corresponding positively charged system.

The results presented in this chapter are based on the study by Silkinis *et al.* [144], in which the author of this thesis was the primary contributor.

## 4.2. Computational details

The calculations presented in this chapter follow the general methodology outlined in Sec. 1.8. The C-center was modeled using a 512-site cubic supercell, obtained by repeating the conventional silicon unit cell (containing eight atoms) in a  $4 \times 4 \times 4$  arrangement. A plane-wave energy cutoff of 500 eV was applied, and Brillouin-zone sampling was restricted to the  $\Gamma$ -point. DFT computations were performed using the PBE [31], SCAN [28], and HSE06 [32] functionals: phonon calculations were carried out with PBE and SCAN, while defect formation energies were obtained with HSE06. This choice leverages the strengths of each functional: SCAN offers an optimal balance between accuracy and

computational cost, making it suitable for structural and vibrational analyses [102], whereas HSE06, with its accurate description of the band gap, was employed to determine thermodynamic properties.

The neutral C-center is a closed-shell system whose ground state is represented by a single Slater determinant,  $|S_0\rangle \equiv |^1A'\rangle = |a''\bar{a}''\rangle$ , where both electrons occupy the in-gap molecular orbital  $a''$ . Excitation of an electron from this orbital to the conduction band gives rise to either a spin-triplet or spin-singlet excited state. The triplet excited state, similar to the ground state, can be expressed via a single determinant as  $|T\rangle \equiv |^3A''\rangle = |a''a'\rangle$ , where  $a'$  denotes a higher-lying orbital near the conduction band minimum (CBM). The singlet excited state, a multi-Slater-determinant state, given by  $|S_1\rangle \equiv |^1A''\rangle = \frac{1}{\sqrt{2}}(|a''\bar{a}'\rangle - |\bar{a}''a'\rangle)$ , exhibits static correlation and cannot be described exactly within standard single-determinant Kohn–Sham DFT. However, previous work [140] has shown that the  $|S_1\rangle$  state is dominated by one determinant, allowing it to be approximated within the  $\Delta$ SCF method using the spin-contaminated configuration  $|M\rangle = |a''\bar{a}'\rangle$ . The Kohn–Sham configurations of all three electronic states are illustrated in Fig. 4.1c.

The exciton-like character of the  $|S_1\rangle$  state presents an additional challenge, since the spatial extent of bound excitons can exceed the supercell size accessible in DFT ( $\sim 1000$  atoms). Assuming that the APES of the defect system is primarily determined by the localized orbital’s charge distribution, a simplified strategy is adopted: the geometry of  $|S_1\rangle$  state is approximated by relaxing the geometry of the positively charged ground state, denoted as  $|P\rangle$ . This approximation is justified *a posteriori* through comparison with experiment and is consistent with earlier studies of the  $C_i$  defect in silicon [145]. For reference, an additional approximation uses the geometry of the triplet excited state  $|T\rangle$ . Because the triplet and singlet excited states share the same orbital configuration and differ only by a small exchange splitting due to the electron delocalization, the geometry of the triplet excited state  $|T\rangle$  should closely mirror that of the singlet excited state  $|S_1\rangle$ .

Vibrational properties, as well as corresponding luminescence and absorption lineshapes, were calculated using the finite-displacement method [87, 88] with atomic displacements of 0.02 Å.

The embedding methodology [39, 71] from Sec. 1.7 was employed to construct an effective  $18 \times 18 \times 18$  supercell (46 656 atomic sites), enabling the simulation of the defect in the dilute limit. To obtain smooth electron–phonon coupling spectra, the Dirac  $\delta$ -functions in Eq. (1.111) were replaced with Gaussians whose standard deviation  $\sigma$  decreased linearly from 2.0 meV near the zero-phonon line (ZPL) to 1.0 meV toward the low-energy tail. For high-energy localized modes, Lorentzian broadening

with a HWHM of 0.8 meV was applied. The ZPL linewidth was modeled using phenomenological parameter  $\gamma = 0.15$  meV defined in Eq. (1.103).

#### 4.2.1. Thermodynamic quantities

The formation energy of a defect quantifies its thermodynamic stability with respect to the pristine crystal and external chemical reservoirs. It represents the energy required to create the defect under given atomic and electronic chemical potentials, and thus determines which defect configurations and charge states are thermodynamically favorable under specific growth or irradiation conditions. The formation energy of a defect  $X$  in charge state  $q$  is given by [146]

$$\Delta H_f^X(q) = E_{\text{tot}}^X(q) - E_{\text{bulk}} - \sum_i n_i \mu_i + q(E_{\text{VBM}} + E_{\text{F}}) + E_{\text{corr}}. \quad (4.1)$$

Here,  $E_{\text{tot}}^X(q)$  is the total energy of the defect-containing supercell, and  $E_{\text{bulk}}$  is that of the pristine crystal of the same size. The term  $n_i$  indicates the number of atoms of type  $i$  added ( $n_i > 0$ ) or removed ( $n_i < 0$ ), and  $\mu_i$  is the chemical potential of species  $i$ . The Fermi level  $E_{\text{F}}$ , referenced to the valence band maximum (VBM)  $E_{\text{VBM}}$ , accounts for the electronic chemical potential. The correction term  $E_{\text{corr}}$  compensates for spurious electrostatic interactions between charged defect images arising from periodic boundary conditions in finite supercells. In this work, a correction scheme described in Ref. [66] was applied.

For a defect complex  $AB$  composed of two defects  $A$  and  $B$ , the binding energy is defined by

$$E_{\text{b}}^{AB}(q) = \Delta H_f^A(q) + \Delta H_f^B(q) - \Delta H_f^{AB}(q). \quad (4.2)$$

A positive  $E_{\text{b}}^{AB}(q)$  indicates that the complex  $AB$  is energetically more favorable than the isolated constituents. However, a large positive binding energy does not necessarily imply a high equilibrium concentration of the complex, as configurational entropy tends to favor isolated defects [147].

Defects can exist in several charge states depending on the occupancy of in-gap states. The Fermi-level ranges in which specific charge states are thermodynamically stable are determined by the charge-state transition levels (CTLs), defined as [146]

$$\varepsilon(q/q') = \frac{\Delta H_f^X(q; E_{\text{F}} = 0) - \Delta H_f^X(q'; E_{\text{F}} = 0)}{q' - q}. \quad (4.3)$$

Here,  $\Delta H_f^X(q; E_{\text{F}} = 0)$  is the formation energy of the defect in charge state  $q$  with the Fermi level set to the VBM. For Fermi levels below

**Table 4.1.** Calculated formation energies  $\Delta H_f^X(0)$  (in eV) of neutral  $C_i$ ,  $O_i$ , and  $C_iO_i$  (C-center) defects in silicon, and the binding energy  $E_b^{C_iO_i}(0)$  (in eV) of the  $C_iO_i$  complex. Results are compared with available theoretical and experimental data. Note that the only available experimental reference value for defect formation energy is for the  $O_i$  defect.

	$\Delta H_f^{C_i}(0)$	$\Delta H_f^{O_i}(0)$	$\Delta H_f^{C_iO_i}(0)$	$E_b^{C_iO_i}(0)$
SCAN (this work)	3.49	1.79	3.75	1.53
HSE06 (this work)	3.70	1.81	3.95	1.56
	4.12 <sup>a</sup>	1.81 <sup>a</sup>	4.21 <sup>a</sup>	1.72 <sup>a</sup>
Prior	4.50 <sup>b</sup>	1.95 <sup>b</sup>	4.85 <sup>b</sup>	1.65 <sup>c</sup>
theory	3.74 <sup>c</sup>	1.56 <sup>d</sup>	3.63 <sup>c</sup>	1.64 <sup>h</sup>
	3.72 <sup>e,f</sup>	–	–	–
Expt.	–	$1.65 \pm 0.15^g$	–	–

<sup>a</sup>Ref. [149]    <sup>b</sup>Ref. [150]    <sup>c</sup>Ref. [151]    <sup>d</sup>Ref. [152]  
<sup>e</sup>Ref. [153]    <sup>f</sup>Ref. [145]    <sup>g</sup>Ref. [148]    <sup>h</sup>Ref. [154]

$\varepsilon(q/q')$ , charge state  $q$  is favored, while above it, the system transitions to charge state  $q'$ .

The ionization energy of a defect, the energy required to remove an electron, is obtained from the difference between the CTL and the CBM. Conversely, the energy required for electron capture from the valence band corresponds to the difference between the CTL and the VBM.

## 4.3. Results and discussion

### 4.3.1. Thermodynamic properties

To begin with, the thermodynamic stability of the neutral  $C_i$ ,  $O_i$ , and  $C_iO_i$  (C-center) defects was assessed by calculating their formation energies, as detailed in Sec. 4.2.1. The results are summarized in Table 4.1, together with literature data for comparison. Formation energies were computed using Eq. (4.1), where the chemical potentials for Si, C, and O were obtained from silicon, diamond, and  $\alpha$ -quartz ( $SiO_2$ ), respectively. Experimental reference values for defect formation energies are scarce, although a comparative value is available for the  $O_i$  defect from Ref. [148].

For the neutral  $C_i$  defect, three geometrical configurations were examined following Ref. [153]: the  $\langle 100 \rangle$   $C_i$  dumbbell, the  $\langle 110 \rangle$   $C_i$  dumbbell,

**Table 4.2.** Calculated CTLs (in eV) for the  $C_i$  and  $C_iO_i$  (C-center) defects in silicon using the HSE06 functional, compared with previously reported results. No CTL values were identified for the  $O_i$  defect.

	$C_i$	$C_iO_i$
HSE06 (this work)	$\varepsilon(+/0) = E_{VBM} + 0.32$ $\varepsilon(0/-) = E_{CBM} - 0.16$	$\varepsilon(+/0) = E_{VBM} + 0.39$
Prior theory	$\varepsilon(+/0) = E_{VBM} + 0.32^a$ $\varepsilon(0/-) = E_{CBM} - 0.19^a$	$\varepsilon(+/0) = E_{VBM} + 0.36^b$ $0.41^c$
Expt.	$\varepsilon(+/0) = E_{VBM} + 0.28^d$ $\varepsilon(0/-) = E_{CBM} - 0.10^d$	$\varepsilon(+/0) = E_{VBM} + 0.38^e$ $0.36^f$
	<sup>a</sup> Ref. [145] <sup>b</sup> Ref. [149]	<sup>c</sup> Ref. [140]
	<sup>d</sup> Ref. [157] <sup>e</sup> Ref. [158]	<sup>f</sup> Ref. [159]

and the bond-centered  $C_i$ . Consistent with previous studies [145, 153, 155, 156], the  $\langle 100 \rangle$  configuration is found to be the most stable. Its formation energies obtained with the SCAN and HSE06 functionals are 3.49 eV and 3.70 eV, respectively. The  $\langle 110 \rangle$  and bond-centered configurations are higher in energy by 0.55 eV (0.49 eV) and 0.70 eV (0.81 eV) within the SCAN (HSE06) framework.

For the neutral  $O_i$  defect, the computed formation energies are 1.79 eV (SCAN) and 1.81 eV (HSE06), both in good agreement with the experimental upper limit of  $(1.65 \pm 0.15)$  eV reported in Ref. [148].

Using Eq. (4.2) and the data in Table 4.1, the binding energy of the neutral C-center,  $E_b^{C_iO_i}(0)$ , is 1.53 eV (SCAN) and 1.56 eV (HSE06). These results align with earlier theoretical estimates [149, 151, 154], which placed the binding energy between 1.6 eV and 1.7 eV. Hence, both functionals correctly predict that formation of the C-center is energetically favorable relative to the isolated interstitials.

Figure 4.2 shows the formation energy diagram, plotting the formation energy as a function of Fermi level for lowest-energy charge state at each value of  $E_F$ . Dashed vertical lines indicate CTLs separating regions of stability; their numerical values are listed in Table 4.2. These levels can be related to ionization energies by taking the difference between the corresponding CTL and the CBM.

The calculations predict that the  $C_i$  defect can exist in the charge states  $\{1+, 0, 1-\}$ , the  $O_i$  defect only in the neutral state (no CTLs), and the C-center in the  $\{1+, 0\}$  states. These results are compared with previous theoretical work [140, 145, 149] and experimental data from Refs. [157–159].

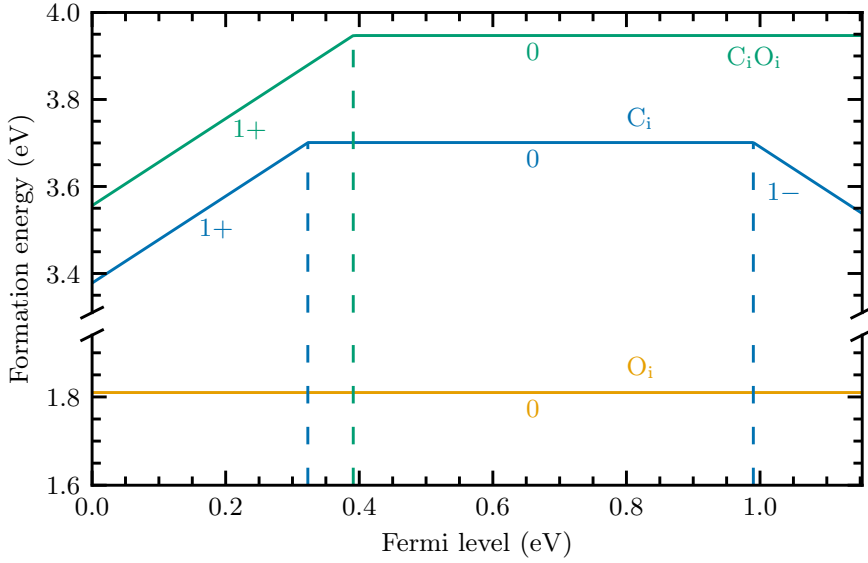


**Figure 4.2.** Calculated formation energies of the  $C_i$ ,  $O_i$ , and  $C_iO_i$  (C-center) defects in silicon as a function of the Fermi level, obtained using the HSE06 functional. The Fermi level is varied from 0 eV to the calculated band gap value of  $E_g = 1.15$  eV, as reported in Table 3.1.

For  $C_i$ , the HSE06 functional yields a donor level  $\varepsilon(+/0) = 0.32$  eV above the VBM, in close agreement with the experimental value of 0.28 eV [157]. The acceptor level  $\varepsilon(0/-)$  is found 0.16 eV below the CBM, consistent with the experimental estimate of 0.10 eV [157].

For the C-center, HSE06 gives a donor transition level  $\varepsilon(+/0) = 0.39$  eV above the VBM, in excellent agreement with experimental values of 0.38 eV and 0.36 eV reported in Refs. [158, 159]. This is also consistent with earlier theoretical predictions [140, 149], which place the level at 0.41 eV and 0.36 eV, respectively.

Using the HSE06 band gap value from Table 3.1, the ionization threshold energy is  $E_g - \varepsilon(+/0) = 0.76$  eV. This energy provides a theoretical upper bound for the ZPL. According to theoretical estimates in Ref. [137], the binding energy of the lowest bound exciton is approximately 40 meV, leading to a predicted ZPL energy of 0.72 eV. This value is in reasonably good agreement with the experimentally measured ZPL energy of 0.790 eV.

#### 4.3.2. Vibrational structure

The investigation of the vibrational properties of the C-center were carried out next, using the SCAN functional and an effective supercell of

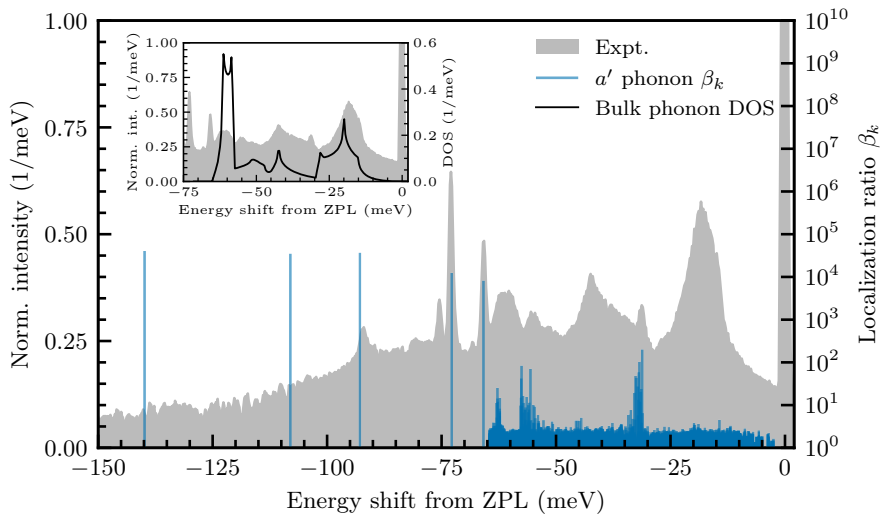


**Figure 4.3.** Calculated vibrational structure of the ground state of the C-center in silicon. Energies are plotted relative to the experimental ZPL energy. Vertical lines indicate the localization ratios ( $\beta_k$ ) of vibrational modes with  $a'$  symmetry, computed for an  $18 \times 18 \times 18$  supercell (46 656 atomic sites) using the SCAN functional. The inset shows the phonon DOS for pristine silicon, calculated using a  $4 \times 4 \times 4$  supercell (512 atomic sites). Experimental low-temperature luminescence data are taken from Ref. [139].

size  $18 \times 18 \times 18$  (46 656 atomic sites), obtained through the embedding methodology [39, 71] described in Sec. 1.7. Figure 4.3 shows the calculated localization ratios  $\beta_k$  of the  $a'$ -symmetry vibrational modes in the ground state  $|S_0\rangle$ , plotted alongside the normalized experimental luminescence spectrum from Ref. [139].

A higher  $\beta_k$  value corresponds to a mode that is more localized around the defect, as defined in Sec. 1.4.5. Because the ground state is non-degenerate, only symmetric  $a'$  modes participate in first-order electron-phonon coupling, in accordance with the Wigner-Eckart theorem [135], as also discussed for the G-center in Chapter 3. The inset of Fig. 4.3 shows the phonon DOS of pristine silicon, computed using a  $4 \times 4 \times 4$  supercell (512 atomic sites), overlaid with the experimental luminescence spectrum for reference.

Several highly localized vibrational modes ( $\beta_k > 1000$ ) are identified with energies of 65.8 meV, 72.8 meV, 92.7 meV, 107.9 meV and 139.7 meV. The corresponding atomic displacement patterns of these modes, restricted to nearest-neighbor atoms, are illustrated in Figs. 4.4(a)–(e). The modes at 65.8 meV, 72.8 meV and 92.7 meV [Figs. 4.4(a)–(c)] correlate closely with prominent phonon sideband (PSB) features in the experimental luminescence spectrum. By contrast, the absence of peaks

at 107.9 meV and 139.7 meV below the ZPL indicates that a high localization ratio alone does not guarantee strong electron–phonon coupling. Effective coupling requires significant overlap between the vibrational eigenvector and the structural relaxation vector  $\Delta\mathbf{R}$  following optical excitation, as described by Eqs. (1.109) and (1.110). The relaxation displacement, representing the geometry change from the ground state to the positively charged configuration (used to approximate the singlet excited state  $|S_1\rangle$ ), is visualized in Fig. 4.4(f).

The vibrational modes contributing to the luminescence spectrum, particularly the 65.8 meV, 72.8 meV and 92.7 meV phonons, exhibit strong vibrational amplitudes on the oxygen atom and its nearest-neighbor silicon atoms [Figs. 4.4(a)–(c)]. Although the oxygen atom itself moves only slightly during the optical relaxation [Fig. 4.4(f)], the surrounding silicon atoms undergo substantial displacements. These motions align closely with the eigenvectors of the 65.8 meV and 72.8 meV modes, and more weakly with the 92.7 meV mode. In contrast, the higher-energy modes at 107.9 meV and 139.7 meV [Figs. 4.4(d)–4.4(e)] are dominated by motion of the carbon atom, which experiences negligible displacement during the electronic transition. Consequently, these modes couple weakly to the electronic degrees of freedom, explaining the absence of corresponding spectral features in experiment.

In addition to localized vibrations, Fig. 4.3 reveals vibrational resonances, collections of quasi-localized modes centered near 32 meV, 54 meV and 62 meV relative to the ZPL. These exhibit intermediate localization ( $\beta_k \approx 10$ ) and can be tentatively associated with PSB structures observed in the luminescence spectrum, suggesting their participation in the optical response.

Lastly, bulk-like modes characterized by low localization ratios ( $\beta_k \approx 5$ ) extend up to approximately 65 meV from the ZPL, coinciding with the upper limit of the silicon phonon band. These extended lattice vibrations are present in both the pristine and defected lattices. Prominent features near 20 meV and 42 meV coincide with maxima in the phonon DOS and correspond to the low-energy side peaks of the experimental spectrum [inset of Fig. 4.3], confirming their bulk origin.

Similarly to Fig. 4.3 for the ground state, the vibrational frequencies and localization ratios  $\beta_k$  for the positively charged defect (state  $|P\rangle$ ), used as an approximation to the singlet excited state  $|S_1\rangle$ , are shown in Fig. 4.5. Relative to the ground state, the localized mode frequencies decrease markedly upon excitation. In particular, the 65.8 meV mode shifts below the bulk phonon band maximum, transforming into a vibrational resonance. Meanwhile, the quasi-localized modes at 32 meV, 54 meV and 62 meV remain nearly unchanged. The pronounced softening of the localized modes indicates the presence of quadratic electron–phonon coupling

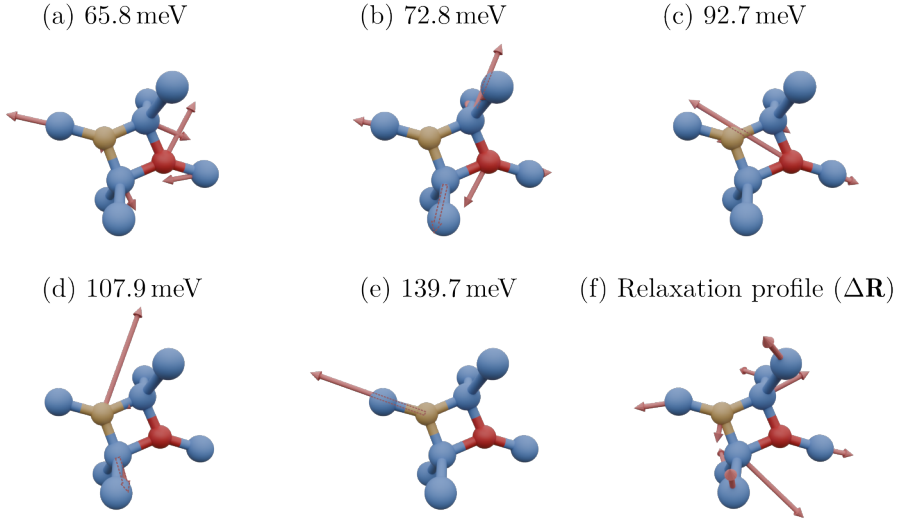


**Figure 4.4.** Illustrations of localized vibrational modes of  $a'$  symmetry in the ground state of the C-center defect in silicon, taken from Ref. [144]. Blue spheres represent silicon atoms, while yellow and red spheres denote carbon and oxygen interstitials, respectively. Arrows indicate the atomic displacements of nearest neighbors surrounding the defect's ring structure. The vibrational frequency of each mode (in meV) is labeled above the corresponding illustration. Panel (f) shows the calculated structural relaxation following optical excitation.

effects, which lie beyond linear approximation employed in this work.

### 4.3.3. Electron–phonon interaction

Next, the electron–phonon coupling strength and the resulting optical luminescence lineshape were evaluated using the vibrational modes described in Sec. 4.3.2. The spectral function of electron–phonon coupling,  $S(\hbar\omega)$ , shown in the inset of Fig. 4.6, quantifies the contribution of phonons with energy  $\hbar\omega$  to the optical transition. As noted earlier, only phonons of  $a'$  symmetry contribute to the first-order electron–phonon interaction. Smooth spectral functions were obtained using the Gaussian and Lorentzian broadening parameters specified in Sec. 4.2.

The total Huang–Rhys (HR) factor,  $S_{\text{tot}} = 1.79$ , indicates that on average fewer than two phonons are emitted per optical transition. Analysis of the partial HR factors [Eq. (1.108)] and the spectral function shows significant contributions from the localized vibrational modes at 65.8 meV, 72.8 meV and 92.7 meV [Figs. 4.4(a)–(c)], with respective partial HR factors of 0.126, 0.167 and 0.042. By contrast, modes dominated by the motion of the carbon atom exhibit much weaker electron–phonon coupling. Specifically, the 107.9 meV mode has an HR factor of 0.002,

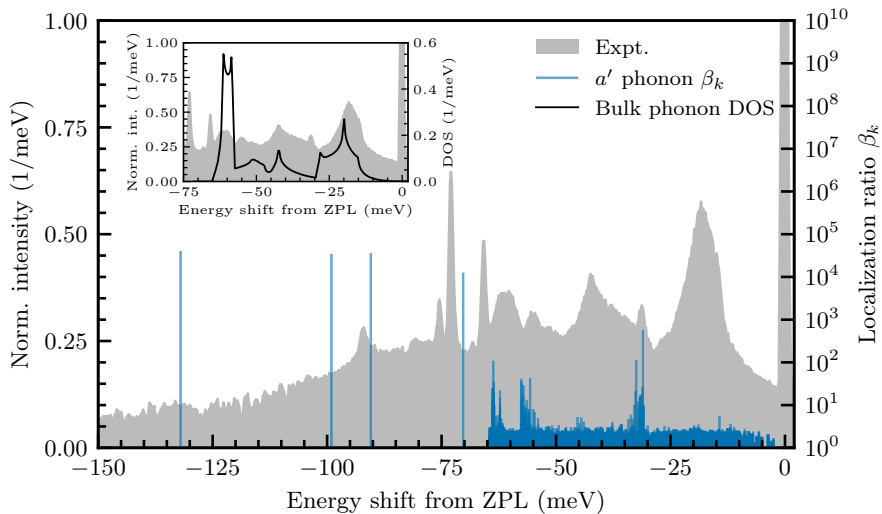


**Figure 4.5.** Calculated vibrational structure of the positively charged state  $|P\rangle$  of the C-center in silicon. Energies are plotted relative to the experimental ZPL energy. Vertical lines indicate the localization ratios ( $\beta_k$ ) of vibrational modes with  $a'$  symmetry, computed for an  $18 \times 18 \times 18$  supercell (46 656 atomic sites) using the SCAN functional. The inset shows the phonon DOS for pristine silicon, calculated using a  $4 \times 4 \times 4$  supercell (512 atomic sites). Experimental low-temperature luminescence data are taken from Ref. [139].

while the 139.7 meV mode yields a modest value of 0.011.

The spectral function further exhibits five distinct peaks below 65 meV, corresponding to resonant and bulk-like phonons. Features near 20 meV and 42 meV arise from regions of vibrational density in the bulk phonons DOS, whereas peaks at 32 meV, 54 meV and 62 meV correspond to quasi-localized vibrational resonances identified in Sec. 4.3.2. These results confirm that both localized and extended phonons contribute to the luminescence sideband of the C-center, with the strongest coupling associated with oxygen-related localized modes.

#### 4.3.4. Optical lineshapes

##### Luminescence spectrum

Finally, Fig. 4.6 shows the calculated luminescence lineshape, with the excited state taken to be  $|P\rangle$ , compared with normalized low-temperature experimental data from Ref. [139]. Overall, the calculated spectrum reproduces the experimental luminescence with high fidelity in both peak positions and relative intensities, yielding a DWF of approximately 19%. Distinct spectral features originating from localized vibrational modes at 65.8 meV, 72.8 meV and 92.7 meV, as well as from quasi-localized

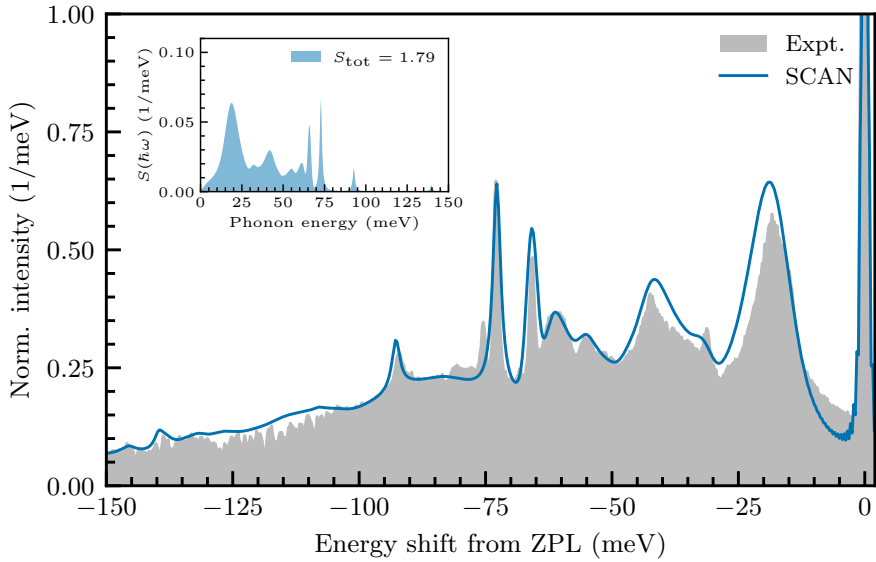


**Figure 4.6.** Calculated normalized luminescence lineshape of the C-center in silicon, with the excited state taken to be  $|P\rangle$ . Energies are plotted relative to the experimental ZPL energy. The inset shows the calculated spectral function of electron–phonon coupling  $S(\hbar\omega)$  for the luminescence. The results correspond to calculations performed using an  $18 \times 18 \times 18$  supercell (46 656 atomic sites) and the SCAN functional. Experimental low-temperature luminescence data are taken from Ref. [139].

resonances near 32 meV, 54 meV and 62 meV, are clearly visible and correspond closely to experimental sideband peaks. Broader structures around 20 meV and 42 meV below the ZPL arise from bulk-like phonons of the silicon host.

Despite the overall agreement, some discrepancies remain. The most notable is the missing sharp peak and shoulder at approximately 76 meV from the ZPL in the theoretical spectrum, whose origin in experiment remains unclear and may involve higher-order coupling effects.

### Convergence of luminescence spectrum

To illustrate the effectiveness of the embedding methodology (as was done for the  $\text{NV}^-$  center in diamond in Sec. 2.3.5), additional embedding calculations were performed for supercells of size  $N \times N \times N$  with  $N \in \{8, 12, 16, 18\}$ , while the  $4 \times 4 \times 4$  supercell (512 atomic sites) result is shown without embedding for comparison.

Figure 4.7 illustrates the evolution of the electron–phonon coupling spectral function (left column) and the corresponding normalized luminescence lineshapes (right column) as a function of supercell size  $N$ , using the SCAN functional. Vertical lines in the left column mark the partial HR factors  $S_k$  for each mode  $k$  [Eq. (1.108)]. Smoothing and broadening parameters were applied as described in Sec. 4.2.

The results clearly demonstrate that, for the chosen smoothing parameters, both the spectral function and the lineshape appear to be well converged for the  $12 \times 12 \times 12$  supercell. As observed previously for the  $\text{NV}^-$  center in diamond (Sec. 2.3.5), the description of the acoustic-phonon region continues to improve with increasing supercell: the discrete phonon contributions merge into a smooth, continuous distribution.

A key difference here is the strongly localized nature of the modes at 65.8 meV, 72.8 meV, 92.7 meV and 139.7 meV. Their partial HR factors  $S_k$  remain constant with increasing supercell size, confirming their localized character. In contrast, the HR factors of extended and quasi-localized modes decrease as the supercell grows, as expected for delocalized vibrations. Small supercells reproduce the main localized features qualitatively but yield artificial sharp peaks due to insufficient sampling of extended modes. These results emphasize the necessity of using sufficiently large supercells for quantitatively accurate luminescence spectra.

### Comparison of PBE and SCAN functionals

Additionally, Fig. 4.8 compares the luminescence spectra associated with the excited state  $|P\rangle$ , calculated with the SCAN and PBE functionals against experimental data [139]. All calculations were performed using an

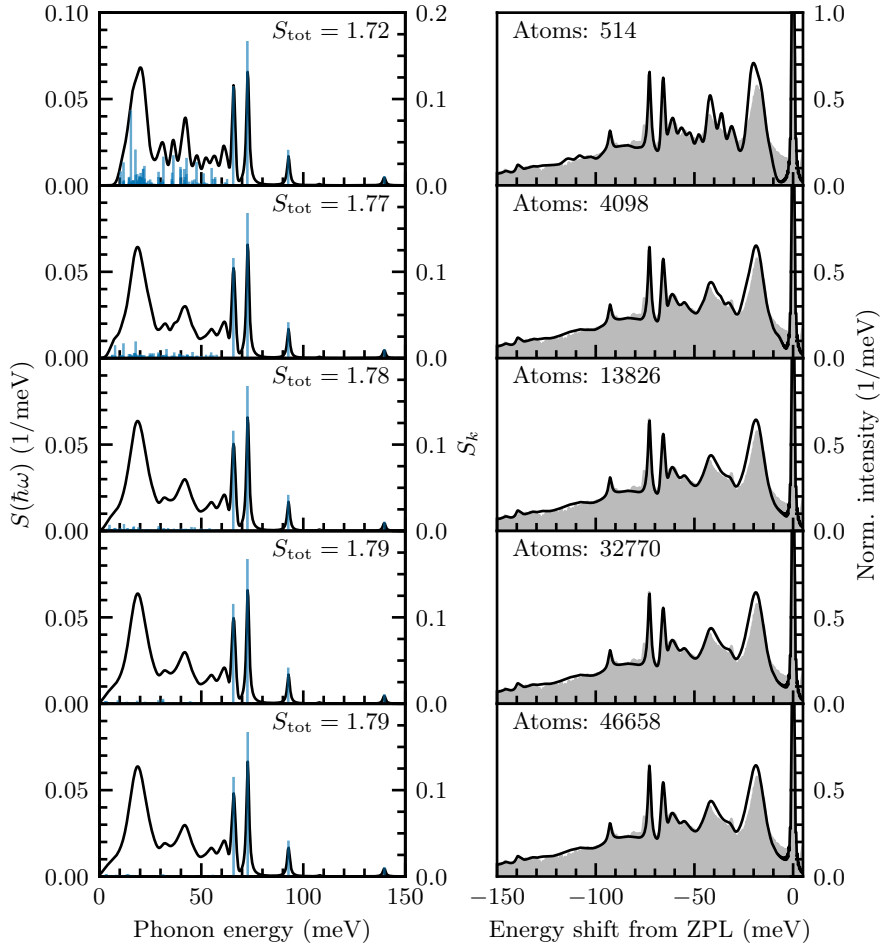


**Figure 4.7.** Convergence of the calculated spectral function of electron–phonon coupling (left column) and the normalized luminescence lineshape (right column) with respect to supercell size for the C-center in silicon, with the excited state taken to be  $|P\rangle$ . The vertical lines in the left column indicate the partial HR factors  $S_k$ . Supercells range in size from  $4 \times 4 \times 4$  (512 atomic sites) to  $18 \times 18 \times 18$  (46 656 atomic sites). The results correspond to calculations performed using the SCAN functional, with smoothing and broadening parameters defined in Sec. 4.2. Experimental low-temperature data are taken from Ref. [139].

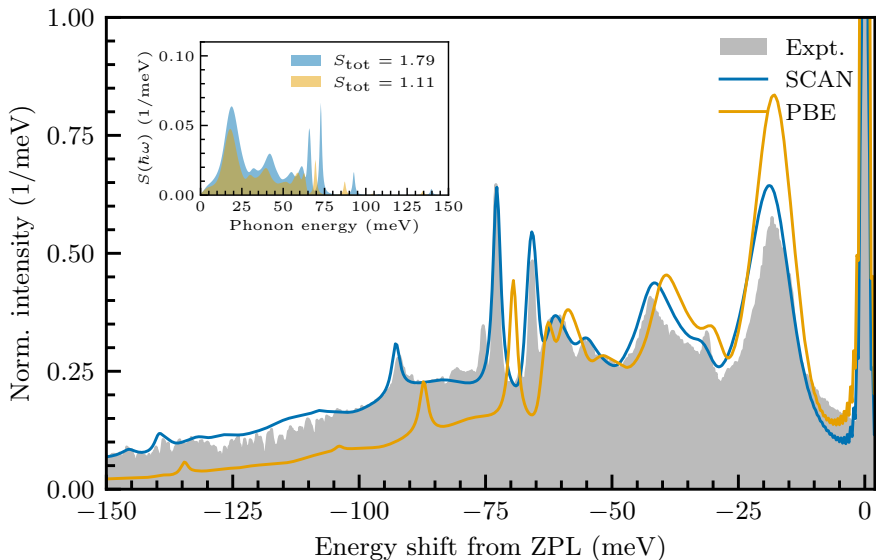


**Figure 4.8.** Comparison of the calculated normalized luminescence lineshapes, obtained using SCAN and PBE functionals, with the excited state taken to be  $|P\rangle$ . Energies are plotted relative to the experimental ZPL energy. The results correspond to calculations performed using an  $18 \times 18 \times 18$  supercell (46 656 atomic sites). Experimental low-temperature luminescence data are taken from Ref. [139].

$18 \times 18 \times 18$  supercell (46 656 atomic sites), with the plane-wave energy cutoff, Brillouin zone sampling, and the smoothing and broadening parameters identical to those used in the lineshape calculation shown in Fig. 4.6.

The SCAN functional reproduces both the energies of the localized vibrational modes and the relative spectral intensities across the sideband more accurately than PBE. The latter functional systematically underestimates the energies of localized modes and overestimates contributions from low-energy acoustic phonons, yielding a total HR factor  $S_{\text{tot}} = 1.11$  and a DWF of approximately 35%. In contrast, SCAN gives  $S_{\text{tot}} = 1.79$  and DWF of about 19%, in much better agreement with experiment.

### Comparison of excited state modeling approaches

As described in Sec. 4.2, the excited state geometry used in the luminescence calculations can be modeled in several ways. Figure 4.9 compares the luminescence lineshape obtained by using the geometry of the positively charged ground state  $|P\rangle$  with that derived from the  $\Delta$ SCF triplet state  $|T\rangle$ , while Fig. 4.10 contrasts results from  $|P\rangle$  and the

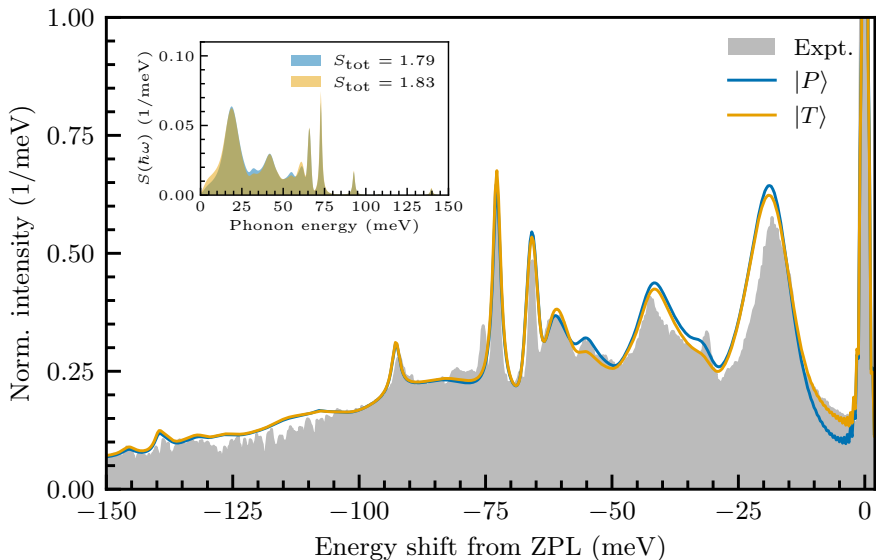


**Figure 4.9.** Comparison of the calculated normalized luminescence lineshape using two methodologies. The first methodology (from Fig. 4.6) models the structural properties of the excited state  $|S_1\rangle$  using a positively charged defect in its ground state, denoted as  $|P\rangle$ . The second methodology uses the  $\Delta$ SCF approach, approximating the excited state  $|S_1\rangle$  as a triplet state  $|T\rangle$ . Energies are plotted relative to the experimental ZPL energy. The results correspond to calculations performed using an  $18 \times 18 \times 18$  supercell (46 656 atomic sites) and the SCAN functional. Experimental low-temperature luminescence data are taken from Ref. [139].

spin-contaminated excited configuration  $|M\rangle$ . In both cases, theoretical spectra are shown alongside the experimental data [139].

All three approximations yield nearly indistinguishable spectra, each showing excellent agreement with experiment. The lineshapes calculated using  $|T\rangle$  and  $|M\rangle$  are virtually identical. Minor differences appear only near the ZPL, where  $|T\rangle$  and  $|M\rangle$  provide a slightly improved description of low-energy acoustic phonons, and near 32 meV and 54 meV below the ZPL, where  $|P\rangle$  better reproduces experimental features. None of the methods captures the unresolved sharp peak and shoulder at approximately 76 meV from the ZPL.

### Absorption spectrum

The theoretical framework of Sec. 1.6 applies equally to optical absorption. As a last addition, Fig. 4.11 compares the calculated absorption lineshape (orange) with the luminescence lineshape (blue) from Fig. 4.6, where the latter is plotted inverted about the ZPL energy. The inset shows

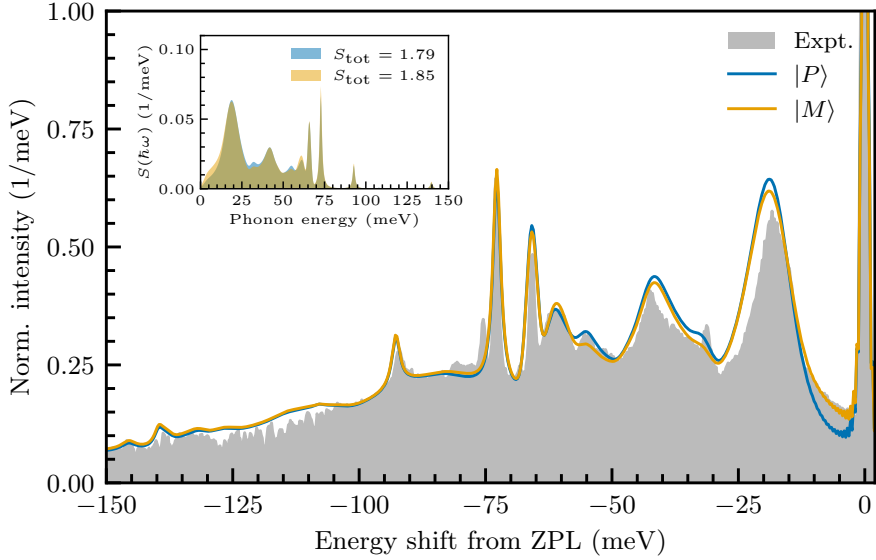


**Figure 4.10.** Comparison of the calculated normalized luminescence lineshape using two methodologies. The first methodology (from Fig. 4.6) models the structural properties of the excited state  $|S_1\rangle$  using a positively charged defect in its ground state, denoted as  $|P\rangle$ . The second methodology uses the  $\Delta$ SCF approach, approximating the excited state  $|S_1\rangle$  as a spin-contaminated state  $|M\rangle$ . Energies are plotted relative to the experimental ZPL energy. The results correspond to calculations performed using an  $18 \times 18 \times 18$  supercell (46 656 atomic sites) and the SCAN functional. Experimental low-temperature luminescence data are taken from Ref. [139].

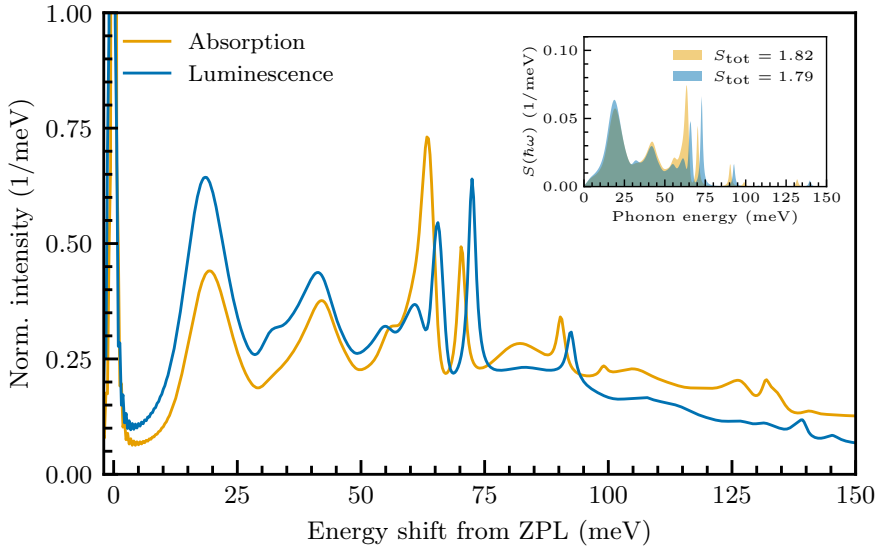


**Figure 4.11.** Calculated normalized absorption (orange) and luminescence (blue, from Fig. 4.6) lineshapes of the C-center in silicon, with the excited state taken to be  $|P\rangle$ . The luminescence lineshape is inverted with respect to the ZPL for comparison. The inset displays the calculated spectral functions of electron–phonon coupling  $S(\hbar\omega)$  for the luminescence and absorption. The results correspond to calculations performed using an  $18 \times 18 \times 18$  supercell (46 656 atomic sites) and the SCAN functional.

the corresponding spectral functions  $S(\hbar\omega)$  for both processes. The absorption lineshape was computed using the same supercell size and functional as in Fig. 4.6, but employing the vibrational modes of the positively charged state  $|P\rangle$  that approximates the singlet excited state  $|S_1\rangle$ , whereas luminescence used the ground-state modes.

The absorption and luminescence lineshapes are remarkably similar within approximately 60 meV below the ZPL. At higher energies, absorptions peaks, particularly those associated with localized modes, shift slightly to lower energy relative to luminescence. Notably, modes near 70.3 meV, 90.4 meV, 99.0 meV and 131.8 meV contribute significantly to the absorption process. The total HR factor for absorption,  $S_{\text{tot}} = 1.82$ , closely matches that for luminescence (1.79), indicating that the vibrational structures of the ground and excited states are well aligned in terms of phonon energies and their character.

The asymmetry between the two spectra arises from the  $\omega^\kappa$  prefactor in Eq. (1.101): for luminescence ( $\kappa = 3$ ), the factor amplifies the intensity near the ZPL more strongly than in absorption ( $\kappa = 1$ ). Consequently, the absorption spectrum appears slightly shifted and redistributed, although

the underlying spectral functions remain nearly symmetric.

Finally, it should be noted that the calculated absorption lineshape describes a bound-to-bound transition. In bulk silicon, the experimental absorption spectrum may also include contributions from photoionization into the conduction band continuum. The ionization threshold, estimated to lie approximately 38 meV above the ZPL [137], implies that the measured absorption signal is likely a convolution of bound-to-bound and ionization processes. Nevertheless, the distinct features predicted here should be experimentally observable in high-resolution absorption spectroscopy.

## 4.4. Summary and conclusions

This chapter presented a computational investigation of the thermodynamic stability, vibrational structure, and optical properties of the C-center defect in silicon. The primary objective was to model the luminescence lineshape using the SCAN functional and to compare the theoretical results with experimental observations. The key findings are summarized below:

1. The thermodynamic properties of  $C_i$  and  $O_i$  interstitials, as well as the C-center, were computed, showing good agreement with experimental data and previous theoretical studies.
2. The vibrational properties of the C-center were accurately described using an advanced embedding methodology, which allows reliable modeling of phonon spectra in the dilute limit. This analysis revealed a rich vibrational structure comprising localized, quasi-localized (resonant), and bulk-like phonon modes. The results provided detailed insight into the nature of the electron–phonon interaction in this defect system.
3. The calculated luminescence lineshape using the SCAN functional reproduces the experimental low-temperature spectrum with high accuracy, capturing nearly all observed spectral features in both position and relative intensity. This strong agreement further supports the assignment of the 790 meV emission line to the  $C_iO_i$  complex.
4. It was demonstrated that optical transitions involving weakly bound exciton-like states can be effectively modeled by approximating the excited-state geometry of the neutral defect with that of the corresponding positively charged configuration. This practical approach effectively captures the essential structural relaxation associated with exciton binding while neglecting the weak contribution of the delocalized electron.

### Thesis statement (II)

The experimental luminescence lineshape of the C-center defect in silicon, arising from an optical transition involving an exciton-like excited state, is accurately reproduced by approximating the ionic potential energy surface of the neutral excitonic configuration with that of the positively charged (ionized) defect.



# 5. Electronic degeneracy: $\text{NiV}^-$ center in diamond

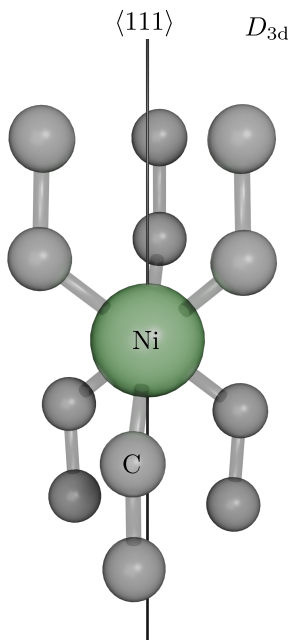
## 5.1. Introduction

Nickel is a common impurity in diamonds formed under high-pressure, high-temperature growth conditions. It gives rise to a range of distinct spectral features that can be detected through optical and magnetic spectroscopy techniques [160, 161]. Among these, a characteristic emission line at 1.40 eV (886 nm) is attributed to the negatively charged split nickel-vacancy center ( $\text{NiV}^-$ ) defect [162].

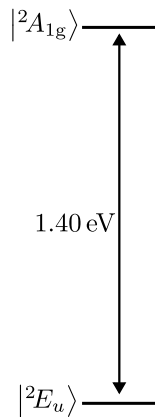
This chapter examines the paramagnetic  $\text{NiV}^-$  center in diamond, in which the nickel impurity is located at the inversion center between two adjacent vacancies [161]. Such configuration produces a structure of  $D_{3d}$  point group symmetry [162], with the symmetry axis oriented along the  $\langle 111 \rangle$  crystallographic direction, as illustrated in Fig. 5.1a. In contrast to the non-degenerate defect systems discussed in previous chapters, the  $\text{NiV}^-$  center exhibits pronounced Jahn–Teller (JT) activity, which strongly affects its electron–phonon coupling and consequently its luminescence lineshape.

The electronic structure of the  $\text{NiV}^-$  center can be understood within a molecular orbital framework. The negatively charged nickel atom contributes five  $3d$  atomic orbitals, while each of the six neighboring carbon atoms provides a dangling bond, yielding an 11-orbital basis [162]. In the ground state, seven of these orbitals form closed-shell configurations deep within the valence band, with the highest occupied orbital possessing  $a_{1g}$  symmetry, as illustrated in Fig. 5.1c. The remaining four orbitals form two degenerate doublets of  $e_u$  and  $e_g$  symmetry located within the band gap. The  $e_u$  orbitals accommodate three electrons, giving rise to an orbital doublet ground state of  $E_u$  symmetry, which can be described using a single Slater determinant. This  $|{}^2E_u\rangle$  ground state constitutes a dynamical Jahn–Teller (DJT) system of the form  $E_u \otimes (e_g \oplus e_g \oplus \dots)$ , in which vibrational modes of  $e_g$  symmetry couple the degenerate components  $|{}^2E_{ux}\rangle$  and  $|{}^2E_{uy}\rangle$  of the electronic manifold. This coupling gives rise to a complex vibronic structure, where the electronic and vibrational degrees of freedom are strongly entangled.

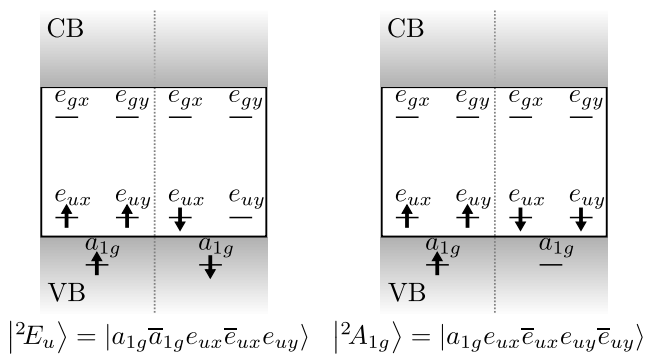
A proper description of such systems is challenging because it requires going beyond the adiabatic approximation, as discussed in Sec. 1.5. Studies addressing the JT effect in color centers remain scarce, and a fully *ab initio* reproduction of the resulting optical features has only been



(a) Atomic structure representation



(b) Energy-level diagram



(c) Representations of the Kohn-Sham electronic configurations of the spin-doublet ground state  $|^2E_u\rangle$  and the spin-doublet excited state  $|^2A_{1g}\rangle$

**Figure 5.1.** The  $\text{NiV}^-$  center in diamond

demonstrated for the absorption lineshape of the  $\text{NV}^-$  center in Ref. [39]. In that case, the JT interaction was relatively weak and manifested merely as a redistribution of the spectral intensity. In contrast, the  $\text{NiV}^-$  center exhibits a much stronger coupling, and the goal of this chapter is to assess whether modern theoretical methods can quantitatively reproduce its optical characteristics.

Unlike the ground state, the excited state is a non-degenerate orbital singlet of  $A_{1g}$  symmetry, formed by promoting a spin-minority electron from the  $a_{1g}$  orbital to one of the  $e_u$  orbitals. This configuration yields the single-determinant state  $|^2A_{1g}\rangle$ , also illustrated in Fig. 5.1c.

To describe the vibrationally resolved optical lineshape of the  $|^2A_{1g}\rangle \rightarrow |^2E_u\rangle$  transition, both the symmetry-preserving  $a_{1g}$  modes and the JT-active, symmetry-breaking  $e_g$  modes must be taken into account. Because the  $a_{1g}$  modes, by symmetry, do not couple the degenerate electronic components of the  $|^2E_u\rangle$  electronic state, their contribution to the luminescence spectrum can be accurately modeled within the adiabatic Huang–Rhys (HR) framework (Sec. 1.6.1), as employed in the previous chapters. In contrast, the  $e_g$  modes induce vibronic coupling between the  $|^2E_{ux}\rangle$  and  $|^2E_{uy}\rangle$  components, necessitating an explicit treatment of the DJT effect. This requires first solving the DJT problem for the ground-state manifold to obtain the vibronic eigenstates and then computing the overlaps between the initial and final vibronic wave functions (Sec. 1.5). In this way, two separate optical spectral functions are obtained: one corresponding to the symmetry-preserving  $a_{1g}$  modes and another to the JT-active  $e_g$  subsystem. The total luminescence lineshape is then obtained as a convolution of these two contributions (Sec. 1.6.2).

The results presented in this chapter are based on the study by Silkinis *et al.* [163], in which the author of this thesis was the primary contributor.

## 5.2. Computational details

The computations presented in this chapter follow the general methodology outlined in Sec. 1.8. The  $\text{NiV}^-$  defect was modeled using a 512-atom cubic supercell, obtained by repeating the conventional cubic diamond unit cell (containing eight atoms) in a  $4 \times 4 \times 4$  arrangement. A plane-wave energy cutoff of 600 eV was employed, and Brillouin-zone sampling was restricted to the  $\Gamma$ -point. All defect DFT calculations were performed using the  $r^2\text{SCAN}$  functional [30].

The spin-doublet excited state  $|^2A_{1g}\rangle$  was modeled using the  $\Delta\text{SCF}$  approach [46, 89, 90], in which an electron in the spin-minority channel is promoted from the occupied, localized  $a_{1g}$  orbital to one of the unoccupied, degenerate  $e_u$  orbitals. This configuration corresponds to

$a_{1g}e_{ux}\bar{e}_{ux}e_{uy}\bar{e}_{uy}$ , where overbars denote spin-down orbitals. The resulting Kohn–Sham orbital occupations for the ground  $|{}^2E_u\rangle$  (configuration  $a_{1g}\bar{a}_{1g}e_{ux}\bar{e}_{ux}e_{uy}$ ) and the excited state  $|{}^2A_{1g}\rangle$  are illustrated in Fig. 2.1c.

To describe the vibrational structure of the degenerate ground state  $|{}^2E_u\rangle$ , the parameters of the zero-order Hamiltonian [Eq. (1.75)], in which all JT interactions are suppressed, were first determined. To achieve this, the electronic configuration of the  $|{}^2E_u\rangle$  state was constrained to fractional orbital occupations, assigning half an electron to each of the two degenerate orbitals:

$$a_{1g}\bar{a}_{1g}e_{ux}\bar{e}_{ux}^{0.5}e_{uy}\bar{e}_{uy}^{0.5}.$$

This configuration represents an ensemble average over the two degenerate components, thereby effectively suppressing JT interactions and preserving the  $D_{3d}$  symmetry (Sec. 1.5.3). Within this high-symmetry configuration, the vibrational modes entering Hamiltonian (1.75) were computed using the finite-displacement method [87, 88] with atomic displacements of 0.01 Å. Because the symmetry was retained, the resulting normal modes could be classified according to the irreducible representations of the  $D_{3d}$  point group. To obtain the vibrational structure in the dilute-defect limit, the embedding methodology [39, 71] described in Sec. 1.7 was employed, yielding an effective supercell size of  $18 \times 18 \times 18$  (46 656 atomic sites).

To characterize the JT interaction in the  $E_u \otimes (e_g \oplus e_g \oplus \dots)$  system, the dimensionless vibronic coupling constants  $K_k$  [Eq. (1.90)] were computed for each pair of vibrational modes of  $e_g$  symmetry, following the methodology outlined in Sec. 1.5.3. These coupling constants were derived from the JT PES associated with  $e_g$ -symmetry distortions, as defined in Eq. (1.96). In practice, the symmetry-lowering distortion describing this surface was obtained by removing the fractional occupation constraint described above and allowing the system to relax to its statically distorted JT minimum. The resulting distortion was then projected onto each  $k$ -th pair of degenerate vibrational eigenmodes, from which the corresponding dimensionless vibronic coupling constants  $K_k$  were determined according to Eq. (1.98).

Smooth representations of the electron–phonon coupling spectral functions  $S_{a_{1g}}(\hbar\omega)$  and  $K^2(\hbar\omega)$ , and of the resulting luminescence spectrum, were obtained by approximating the Dirac  $\delta$ -functions in Eqs. (1.111) and (1.99) with Gaussians whose standard deviation  $\sigma$  decreased linearly from 3.5 meV near the zero-phonon line (ZPL) to 1.5 meV at the low-energy tail. The ZPL linewidth was modeled using  $\gamma = 0.35$  meV, as introduced in Eq. (1.103).

Although the obtained vibrational frequencies and vibronic coupling constants fully define the vibronic Hamiltonian, the direct diagonalization

of Eq. (1.89) is prohibitively demanding due to the large number of vibrational modes. To overcome this issue, a few-mode approximation was employed [39], as introduced in Sec. 1.5.4, in which the full symmetry-breaking phonon spectrum is represented by a reduced set of effective modes. For the NiV<sup>-</sup> center, it was determined that  $N_{\text{eff}} = 18$  effective modes provide sufficient spectral resolution. The phonon basis was truncated to allow a maximum of  $N_{\text{ex}} = 5$  excited phonons. To generate a smooth effective linear JT coupling spectral density  $K_{\text{eff}}^2(\hbar\omega)$ , the Dirac  $\delta$ -functions in Eq. (1.100) were approximated by Gaussians with a fixed standard deviation of  $\sigma = 4.6$  meV.

## 5.3. Results and discussion

### 5.3.1. Spectral functions of electron–phonon interaction

First, the calculated spectral functions of electron–phonon coupling for the luminescence of the NiV<sup>-</sup> center are shown in Fig. 5.2. Panel (a) presents the HR spectral density  $S_{a_{1g}}(\hbar\omega)$ , arising from coupling to symmetry-preserving  $a_{1g}$  vibrational modes, while panel (b) shows the linear JT coupling spectral density  $K^2(\hbar\omega)$ , associated with symmetry-breaking  $e_g$  modes. Both panels also display the cumulative coupling measures, the total HR factor  $S_{\text{tot}} = \sum_k S_{a_{1g},k}$  and the total JT coupling strength  $K_{\text{tot}}^2 = \sum_k K_k^2$ . All calculations were performed using the r<sup>2</sup>SCAN functional and an embedded supercell of  $18 \times 18 \times 18$  (46 656 atomic sites), following the methodology in Sec. 1.7 [39, 71]. The smoothing parameters used to construct the spectral functions are those defined in Sec. 5.2.

The resulting cumulative coupling values are  $S_{\text{tot}} = 0.29$  and  $K_{\text{tot}}^2 = 0.96$ , showing that the contribution from JT-active  $e_g$  modes is more than three times larger than that from the  $a_{1g}$  modes. These values quantify the distortion of the APES during the optical transition and are directly related to the relaxation energies.

The relaxation energy along the symmetry-preserving  $a_{1g}$  coordinate during the vertical transition  $|^2A_{1g}\rangle \rightarrow |^2E_u\rangle$  is

$$\Delta E_{a_{1g}} = \sum_k \hbar\omega_k S_{a_{1g},k},$$

while the JT relaxation energy along the  $e_g$  direction is

$$\Delta E_{\text{JT}} = \sum_k \hbar\omega_k K_k^2.$$

The latter represents the energy lowering that accompanies the structural relaxation of the ground-state electronic manifold from the high-symmetry

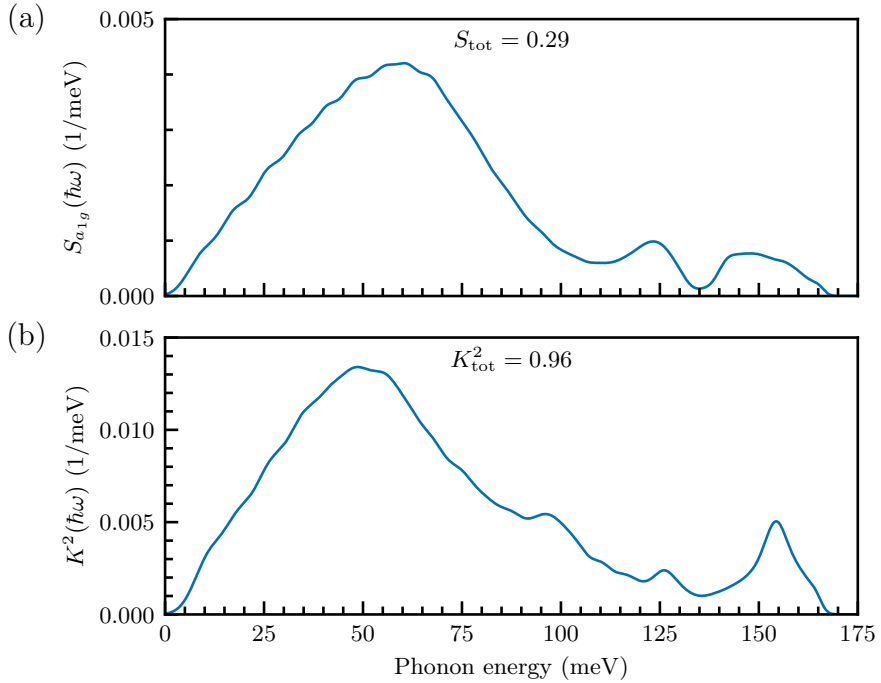


**Figure 5.2.** Calculated spectral functions of electron–phonon coupling for the luminescence of the  $\text{NiV}^-$  center in diamond. Panel (a) shows the HR spectral density  $S_{a_{1g}}(\hbar\omega)$  associated with  $a_{1g}$ -symmetry modes, while panel (b) presents the linear JT coupling spectral density  $K^2(\hbar\omega)$ , stemming from  $e_g$ -symmetry modes. Both panels also include the cumulative coupling parameters  $S_{\text{tot}}$  and  $K_{\text{tot}}^2$ . The results correspond to calculations performed using an  $18 \times 18 \times 18$  supercell (46 656 atomic sites) and the  $r^2\text{SCAN}$  functional.

$D_{3d}$  geometry (enforced using fractional orbital occupations) to the distorted low-symmetry  $C_{2h}$  configuration. The calculated values are  $\Delta E_{a_{1g}} = 18.8 \text{ meV}$  and  $\Delta E_{JT} = 63.5 \text{ meV}$ , confirming the dominant role of JT-active modes in the total electron–phonon coupling for the luminescence of the  $\text{NiV}^-$  center.

To assess the accuracy of the few-mode approximation used to diagonalize the vibronic Hamiltonian (Sec. 1.5.4), the effective linear JT coupling spectral density  $K_{\text{eff}}^2(\hbar\omega)$  was calculated for different numbers of effective modes  $N_{\text{eff}}$  and compared with the full  $K^2(\hbar\omega)$ . The convergence behavior, shown in Fig. 5.3 for  $N_{\text{eff}} \in \{4, 12, 18\}$ , demonstrates rapid improvement with increasing mode number. The Dirac  $\delta$ -functions in  $K_{\text{eff}}^2(\hbar\omega)$  were broadened using Gaussians with standard deviations  $\sigma = 17.7 \text{ meV}$  ( $N_{\text{eff}} = 4$ ),  $\sigma = 6.0 \text{ meV}$  ( $N_{\text{eff}} = 12$ ), and  $\sigma = 4.6 \text{ meV}$  ( $N_{\text{eff}} = 18$ ). All calculations employed the r<sup>2</sup>SCAN functional and a vibronic basis with  $N_{\text{ex}} = 5$  phonons excitations.

### 5.3.2. Optical spectral functions

In JT-active systems, the optical spectral function that determines the luminescence lineshape [Eq. (1.101)] can be expressed as a convolution of two independent spectral functions:

$$A(\hbar\omega) = \int A_{a_{1g}}(\hbar\omega - \hbar\omega') A_{e_g}(\hbar\omega') d\hbar\omega',$$

as introduced in Sec. 1.6.2. The function  $A_{a_{1g}}(\hbar\omega)$  describes coupling to  $a_{1g}$ -symmetry modes and is treated within the adiabatic HR framework. In contrast,  $A_{e_g}(\hbar\omega)$  accounts for coupling to JT-active  $e_g$  modes.

For the computation of  $A_e(\hbar\omega)$ , two distinct methodologies were employed. In the first approach, based on HR theory, the  $e_g$  modes were treated analogously to  $a_{1g}$  modes. In contrast, the second approach employs a full dynamical JT treatment, involving explicit diagonalization of the vibronic Hamiltonian using  $N_{\text{eff}} = 18$  effective modes identified in Fig. 5.3. The spectral function is then calculated evaluating overlaps between ionic components of vibronic eigenstates of the dynamical JT Hamiltonian and vibrational wave functions of the adiabatic  $|^2A_{1g}\rangle$  electronic state [Eq. (1.114)].

The calculated optical spectral functions are presented in Fig. 5.4. The function  $A_a(\hbar\omega)$  [Fig. 5.4(a)] decays rapidly and becomes negligible beyond approximately 170 meV below the ZPL, indicating that  $a_{1g}$  modes alone cannot account for the broad experimental phonon sideband (PSB) extending to about 300 meV. In contrast, the  $A_e(\hbar\omega)$  spectrum [Fig. 5.4(b)] shows a pronounced tail extending well beyond 300 meV

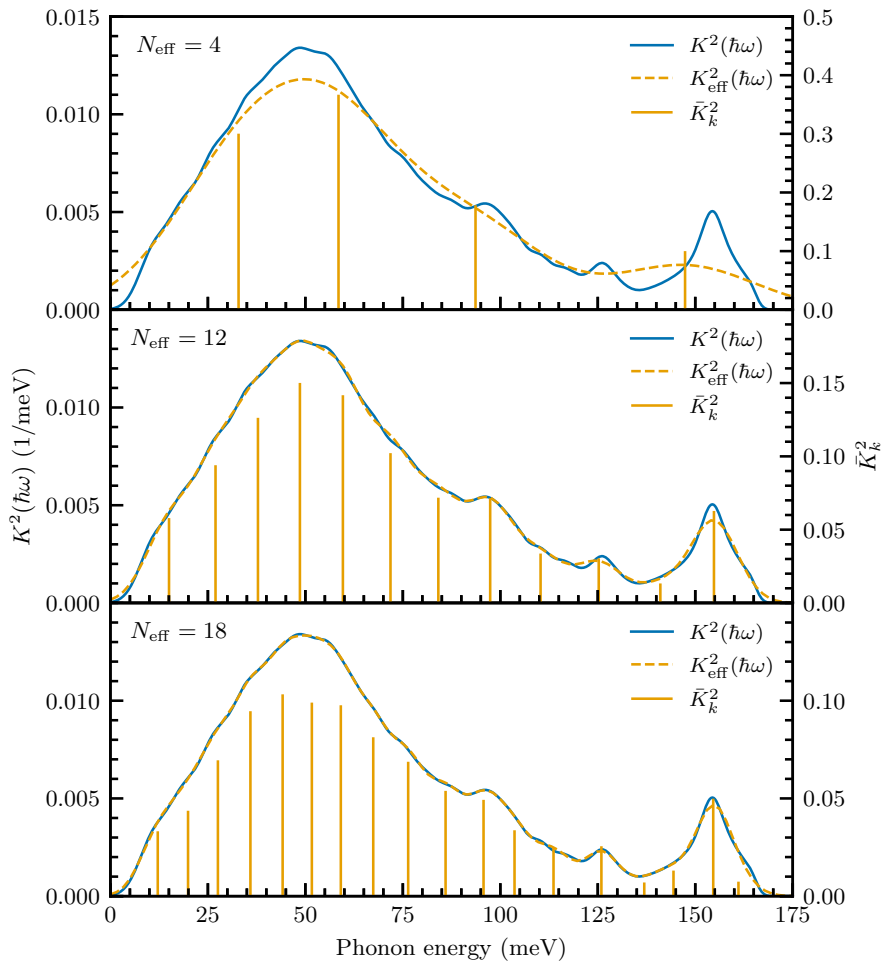


**Figure 5.3.** Convergence of the calculated effective linear JT coupling spectral density  $K_{\text{eff}}^2(\hbar\omega)$  for the luminescence of the  $\text{NiV}^-$  center in diamond with respect to the number of effective modes  $N_{\text{eff}}$ . Orange vertical lines indicate the individual effective modes, with their respective energies  $\hbar\omega_k$  and coupling strengths  $\bar{K}_k^2$ . The results correspond to calculations performed using an  $18 \times 18 \times 18$  supercell (46 656 atomic sites) and the r<sup>2</sup>SCAN functional.

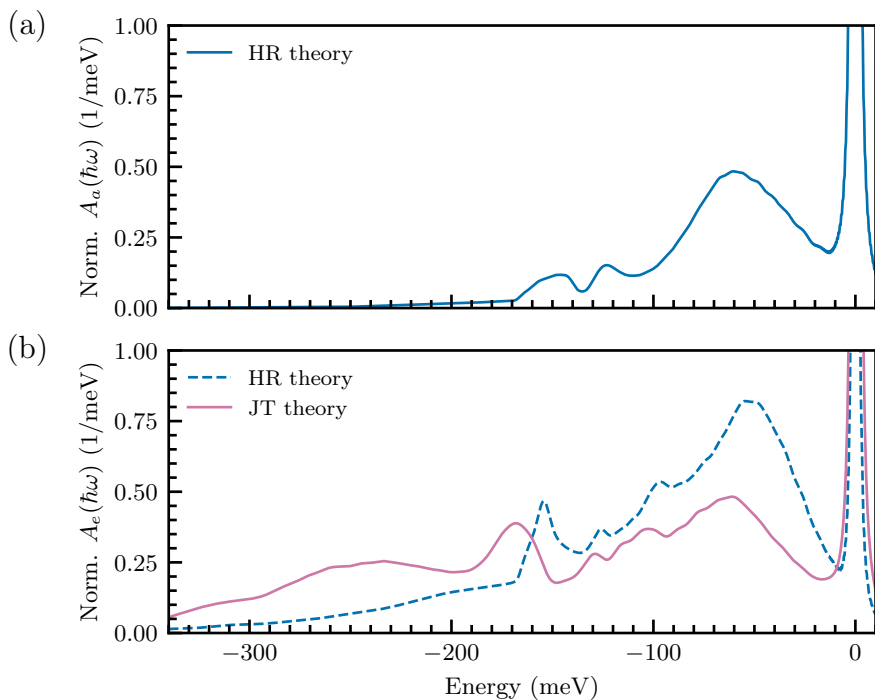


**Figure 5.4.** Calculated optical spectral functions for the luminescence of the  $\text{NiV}^-$  center in diamond. Panel (a) shows the spectral function  $A_a(\hbar\omega)$  for  $a_{1g}$ -symmetry modes, while panel (b) presents the spectral function  $A_e(\hbar\omega)$  for  $e_g$ -symmetry modes, computed using both the dynamical JT theory (solid purple line) and the HR theory (dashed blue line). Energies are plotted relative to the experimental ZPL energy. The results correspond to calculations performed using an  $18 \times 18 \times 18$  supercell (46 656 atomic sites) and the r<sup>2</sup>SCAN functional.

below the ZPL, consistent with the experimental luminescence spectrum (Fig. 5.5).

As seen in Fig. 5.4(b), the dynamical JT spectral function differs markedly from the HR result. While the HR approach produces distinct peaks up to 170 meV below the ZPL and decays sharply thereafter, the JT-derived spectrum extends continuously to 300 meV below the ZPL. This extended PSB and modified intensity distribution highlight the necessity of a dynamical JT framework to reproduce the full spectral extent observed experimentally.

### 5.3.3. Luminescence lineshape

Finally, Fig. 5.5 compares the calculated luminescence lineshapes, derived from the optical spectral functions  $A_a(\hbar\omega)$  and  $A_e(\hbar\omega)$ , with normalized low-temperature experimental data from Ref. [160]. The lineshape obtained within the HR theory agrees with previous theoretical results [162] but fails to reproduce the experimental trend, underscoring the limitations of the adiabatic HR approach in JT-active systems.

In contrast, the multimode dynamical JT model yields excellent agreement with experiment, reproducing both the detailed spectral features and overall intensity distribution. The calculated Debye–Waller factor (DWF) is approximately 35 % in the HR framework and 41 % in the dynamical JT model. The latter predicts a more intense ZPL and a more extended PSB, in close correspondence with experimental observations. These results confirm that incorporating dynamical JT effects is essential for a realistic description of the luminescence of JT-active defects such as  $\text{NiV}^-$  center in diamond.

The sensitivity of the calculated lineshape to the vibronic-basis parameters is illustrated in Fig. 5.6. Panel (a) displays the convergence behavior with respect to the number of effective modes,  $N_{\text{eff}}$ , while panel (b) shows the convergence relative to the phonon basis size,  $N_{\text{ex}}$ . The results indicate that as  $N_{\text{eff}}$  and  $N_{\text{ex}}$  are increased, the calculated spectral features and relative intensities systematically converge towards the experimental data. Specifically, the configuration with  $N_{\text{eff}} = 18$  and  $N_{\text{ex}} = 5$  provides a representation that closely aligns with the measured spectrum, effectively recovering the essential vibronic characteristics of the system.

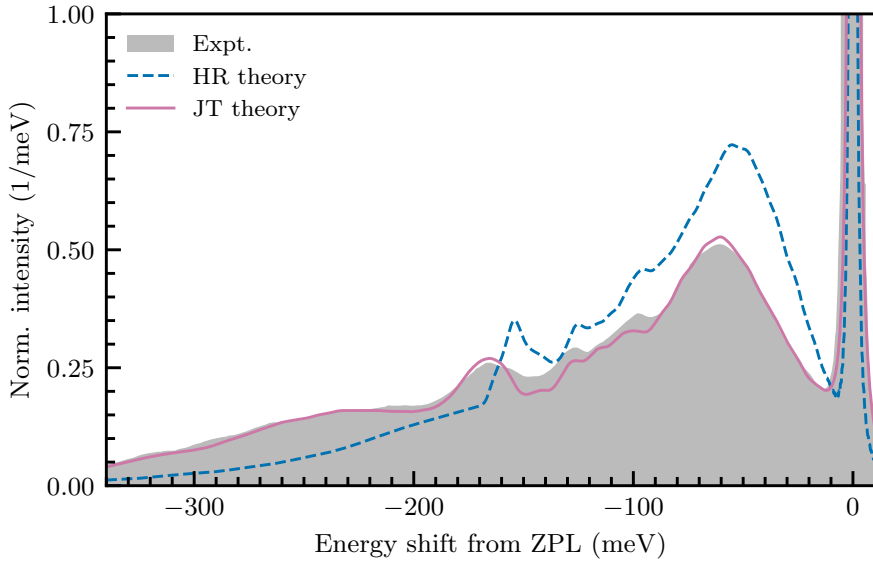


**Figure 5.5.** Calculated normalized luminescence lineshapes of the  $\text{NiV}^-$  center in diamond obtained using HR theory (dashed blue line) and dynamical JT theory (solid purple line). Energies are plotted relative to the experimental ZPL energy. The results correspond to calculations performed using an  $18 \times 18 \times 18$  supercell (46 656 atomic sites) and the  $r^2\text{SCAN}$  functional. Experimental low-temperature luminescence data are taken from Ref. [160].

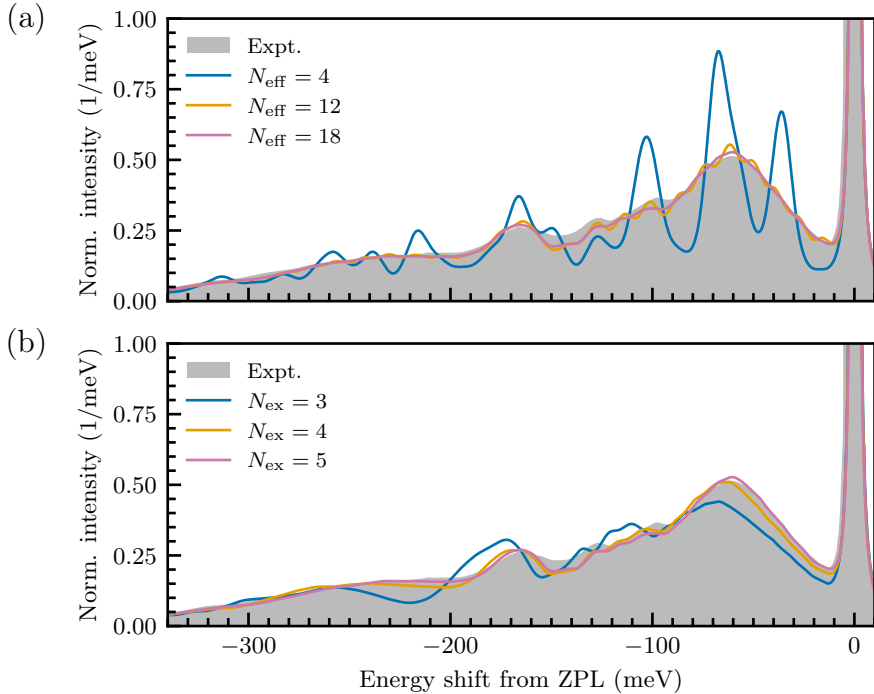


**Figure 5.6.** Convergence of the calculated normalized luminescence lineshape of the NiV<sup>-</sup> in diamond. Panel (a) shows the convergence with respect to the number of effective modes  $N_{\text{eff}}$ , with the size of the phonon basis fixed at  $N_{\text{ex}} = 5$ . Panel (b) presents the convergence with respect to  $N_{\text{ex}}$ , keeping  $N_{\text{eff}} = 18$  fixed. Energies are plotted relative to the experimental ZPL energy. The results correspond to calculations performed using an  $18 \times 18 \times 18$  supercell (46 656 atomic sites) and the r<sup>2</sup>SCAN functional. Experimental low-temperature luminescence data are taken from Ref. [160].

## 5.4. Summary and conclusions

This chapter addressed the problem of accurately modeling the luminescence lineshape of a Jahn–Teller-active defect system, focusing on the negatively charged nickel–vacancy ( $\text{NiV}^-$ ) complex in diamond. The combination of electron–phonon coupling analysis and multimode vibronic modeling provided insight into the role of dynamical Jahn–Teller effects in shaping optical spectra. The key findings are summarized below:

1. The calculated luminescence lineshape shows excellent agreement with low-temperature experimental data, accurately reproducing both the spectral features and their relative intensities.
2. The results demonstrate that a multimode dynamical Jahn–Teller approach is essential for reliably modeling optical lineshapes in systems exhibiting strong vibronic coupling. In particular, it captures the extended phonon sideband and its features that cannot be reproduced within the adiabatic Huang–Rhys approximation.

### **Thesis statement (III)**

The close agreement between the luminescence lineshape predicted from dynamical Jahn–Teller theory and the experimental spectrum provides strong evidence that the 1.40 eV center in diamond originates from the negatively charged split nickel–vacancy defect. This result underscores the decisive role of Jahn–Teller-active vibrational modes in determining the optical lineshape and demonstrates the effectiveness of advanced computational approaches for modeling optical properties in complex systems with multiple Jahn–Teller-active frequencies.



# References

- [1] U. K. Mishra, P. Parikh, and Y.-F. Wu, “AlGaN/GaN HEMTs—An overview of device operation and applications,” *Proc. IEEE* **90**, 1022–1031 (2002).
- [2] C. H. Henry and D. V. Lang, “Nonradiative capture and recombination by multiphonon emission in GaAs and GaP,” *Phys. Rev. B* **15**, 989–1016 (1977).
- [3] M. W. Doherty, N. B. Manson, P. Delaney, F. Jelezko, J. Wrachtrup, and L. C. L. Hollenberg, “The nitrogen-vacancy colour centre in diamond,” *Phys. Rep.* **528**, 1–45 (2013).
- [4] P. C. Maurer, G. Kucsko, C. Latta, L. Jiang, N. Y. Yao, S. D. Bennett, F. Pastawski, D. Hunger, N. Chisholm, M. Markham, D. J. Twitchen, J. I. Cirac, and M. D. Lukin, “Room-temperature quantum bit memory exceeding one second,” *Science* **336**, 1283–1286 (2012).
- [5] N. Bar-Gill, L. M. Pham, A. Jarmola, D. Budker, and R. L. Walsworth, “Solid-state electronic spin coherence time approaching one second,” *Nat. Commun.* **4**, 1743 (2013).
- [6] E. D. Herbschleb, H. Kato, Y. Maruyama, T. Danjo, T. Makino, S. Yamasaki, I. Ohki, K. Hayashi, H. Morishita, M. Fujiwara, and N. Mizuochi, “Ultra-long coherence times amongst room-temperature solid-state spins,” *Nat. Commun.* **10**, 3766 (2019).
- [7] C. L. Degen, F. Reinhard, and P. Cappellaro, “Quantum sensing,” *Rev. Mod. Phys.* **89**, 035002 (2017).
- [8] J. M. Taylor, P. Cappellaro, L. Childress, L. Jiang, D. Budker, P. R. Hemmer, A. Yacoby, R. Walsworth, and M. D. Lukin, “High-sensitivity diamond magnetometer with nanoscale resolution,” *Nat. Phys.* **4**, 810–816 (2008).
- [9] D. Le Sage, K. Arai, D. R. Glenn, S. J. DeVience, L. M. Pham, L. Rahn-Lee, M. D. Lukin, A. Yacoby, A. Komeili, and R. L. Walsworth, “Optical magnetic imaging of living cells,” *Nature* **496**, 486–489 (2013).
- [10] L. Rondin, J.-P. Tetienne, T. Hingant, J.-F. Roch, P. Maletinsky, and V. Jacques, “Magnetometry with nitrogen-vacancy defects in diamond,” *Rep. Prog. Phys.* **77**, 056503 (2014).

- [11] B. Vindolet, M.-P. Adam, L. Toraille, M. Chipaux, A. Hilberer, G. Dupuy, L. Razinkovas, A. Alkauskas, G. Thiering, A. Gali, M. De Feudis, M. W. Ngandeu Ngambou, J. Achard, A. Tallaire, M. Schmidt, C. Becher, and J.-F. Roch, “Optical properties of SiV and GeV color centers in nanodiamonds under hydrostatic pressures up to 180 GPa,” *Phys. Rev. B* **106**, 214109 (2022).
- [12] B. Bürgler, T. F. Sjolander, O. Brinza, A. Tallaire, J. Achard, and P. Maletinsky, “All-optical nuclear quantum sensing using nitrogen-vacancy centers in diamond,” *npj Quantum Inf.* **9**, 56 (2023).
- [13] C. Chartrand, L. Bergeron, K. J. Morse, H. Riemann, N. V. Abrosimov, P. Becker, H.-J. Pohl, S. Simmons, and M. L. W. Thewalt, “Highly enriched  $^{28}\text{Si}$  reveals remarkable optical linewidths and fine structure for well-known damage centers,” *Phys. Rev. B* **98**, 195201 (2018).
- [14] M. Hollenbach, Y. Berencén, U. Kentsch, M. Helm, and G. V. Astakhov, “Engineering telecom single-photon emitters in silicon for scalable quantum photonics,” *Opt. Express* **28**, 26111–26121 (2020).
- [15] W. Redjem, A. Durand, T. Herzig, A. Benali, S. Pezzagna, J. Meijer, A. Y. Kuznetsov, H. S. Nguyen, S. Cuffe, J.-M. Gérard, I. Robert-Philip, B. Gil, D. Caliste, P. Pochet, M. Abbarchi, V. Jacques, A. Dréau, and G. Cassabois, “Single artificial atoms in silicon emitting at telecom wavelengths,” *Nat. Electron.* **3**, 738–743 (2020).
- [16] A. Durand, Y. Baron, W. Redjem, T. Herzig, A. Benali, S. Pezzagna, J. Meijer, A. Y. Kuznetsov, J.-M. Gérard, I. Robert-Philip, M. Abbarchi, V. Jacques, G. Cassabois, and A. Dréau, “Broad diversity of near-infrared single-photon emitters in silicon,” *Phys. Rev. Lett.* **126**, 083602 (2021).
- [17] S. M. Buckley, A. N. Tait, G. Moody, B. Primavera, S. Olson, J. Herman, K. L. Silverman, S. Papa Rao, S. Woo Nam, R. P. Mirin, and J. M. Shainline, “Optimization of photoluminescence from W centers in silicon-on-insulator,” *Opt. Express* **28**, 16057–16072 (2020).
- [18] Y. Baron, A. Durand, P. Udvarhelyi, T. Herzig, M. Khoury, S. Pezzagna, J. Meijer, I. Robert-Philip, M. Abbarchi, J.-M. Hartmann, V. Mazzocchi, J.-M. Gérard, A. Gali, V. Jacques, G. Cassabois, and A. Dréau, “Detection of single W-centers in silicon,” *ACS Photonics* **9**, 2337–2345 (2022).

- [19] D. Dhaliya, Y. Xiong, A. Sipahigil, S. M. Griffin, and G. Hautier, “First-principles study of the T center in silicon,” *Phys. Rev. Materials* **6**, L053201 (2022).
- [20] C. Clear, S. Hosseini, A.-H. Alizadeh-Khaleidi, N. Brunelle, A. Woolverton, J. Kanaganayagam, M. Kazemi, C. Chartrand, M. Keshavarz, Y. Xiong, L. Alaerts, Ö. O. Soykal, G. Hautier, V. Karasiouk, M. Thewalt, D. Higginbottom, and S. Simmons, “Optical-transition parameters of the silicon T center,” *Phys. Rev. Appl.* **22**, 064014 (2024).
- [21] N. Gisin and R. Thew, “Quantum communication,” *Nat. Photonics* **1**, 165–171 (2007).
- [22] B. E. Kane, “A silicon-based nuclear spin quantum computer,” *Nature* **393**, 133–137 (1998).
- [23] T. D. Ladd, F. Jelezko, R. Laflamme, Y. Nakamura, C. Monroe, and J. L. O’Brien, “Quantum computers,” *Nature* **464**, 45–53 (2010).
- [24] J. R. Weber, W. F. Koehl, J. B. Varley, A. Janotti, B. B. Buckley, C. G. Van de Walle, and D. D. Awschalom, “Quantum computing with defects,” *Proc. Natl. Acad. Sci. U.S.A.* **107**, 8513–8518 (2010).
- [25] L. C. Bassett, A. Alkauskas, A. L. Exarhos, and K.-M. C. Fu, “Quantum defects by design,” *Nanophotonics* **8**, 1867–1888 (2019).
- [26] P. Hohenberg and W. Kohn, “Inhomogeneous electron gas,” *Phys. Rev.* **136**, B864–B871 (1964).
- [27] W. Kohn and L. J. Sham, “Self-consistent equations including exchange and correlation effects,” *Phys. Rev.* **140**, A1133–A1138 (1965).
- [28] J. Sun, A. Ruzsinszky, and J. P. Perdew, “Strongly constrained and appropriately normed semilocal density functional,” *Phys. Rev. Lett.* **115**, 036402 (2015).
- [29] A. P. Bartók and J. R. Yates, “Regularized SCAN functional,” *J. Chem. Phys.* **150**, 161101 (2019).
- [30] J. W. Furness, A. D. Kaplan, J. Ning, J. P. Perdew, and J. Sun, “Accurate and numerically efficient  $r^2$ SCAN meta-generalized gradient approximation,” *J. Phys. Chem. Lett.* **11**, 8208–8215 (2020).
- [31] J. P. Perdew, K. Burke, and M. Ernzerhof, “Generalized gradient approximation made simple,” *Phys. Rev. Lett.* **77**, 3865–3868 (1996).

- [32] J. Heyd, G. E. Scuseria, and M. Ernzerhof, “Hybrid functionals based on a screened Coulomb potential,” *J. Chem. Phys.* **118**, 8207–8215 (2003).
- [33] U. von Barth, “Local-density theory of multiplet structure,” *Phys. Rev. A* **20**, 1693–1703 (1979).
- [34] J. Lischner, J. Deslippe, M. Jain, and S. G. Louie, “First-principles calculations of quasiparticle excitations of open-shell condensed matter systems,” *Phys. Rev. Lett.* **109**, 036406 (2012).
- [35] L. Muechler, D. I. Badrtdinov, A. Hampel, J. Cano, M. Rösner, and C. E. Dreyer, “Quantum embedding methods for correlated excited states of point defects: Case studies and challenges,” *Phys. Rev. B* **105**, 235104 (2022).
- [36] Z.-H. Zhang, P. Stevenson, G. Thiering, B. C. Rose, D. Huang, A. M. Edmonds, M. L. Markham, S. A. Lyon, A. Gali, and N. P. De Leon, “Optically detected magnetic resonance in neutral silicon vacancy centers in diamond via bound exciton states,” *Phys. Rev. Lett.* **125**, 237402 (2020).
- [37] A. Zywietz, J. Furthmüller, and F. Bechstedt, “Spin state of vacancies: From magnetic Jahn–Teller distortions to multiplets,” *Phys. Rev. B* **62**, 6854–6857 (2000).
- [38] M. Etzelmüller Bathen, A. Galeckas, R. Karsthof, A. Delteil, V. Sallet, A. Y. Kuznetsov, and L. Vines, “Resolving Jahn–Teller induced vibronic fine structure of silicon vacancy quantum emission in silicon carbide,” *Phys. Rev. B* **104**, 045120 (2021).
- [39] L. Razinkovas, M. W. Doherty, N. B. Manson, C. G. Van de Walle, and A. Alkauskas, “Vibrational and vibronic structure of isolated point defects: The nitrogen-vacancy center in diamond,” *Phys. Rev. B* **104**, 045303 (2021).
- [40] T. Azumi and K. Matsuzaki, “What does the term ”vibronic coupling” mean?” *Photochem. Photobiol.* **25**, 315–326 (1977).
- [41] M. Levy, “Universal variational functionals of electron densities, first-order density matrices, and natural spin-orbitals and solution of the  $v$ -representability problem,” *Proc. Natl. Acad. Sci. U.S.A.* **76**, 6062–6065 (1979).
- [42] G. Vignale and M. Rasolt, “Density-functional theory in strong magnetic fields,” *Phys. Rev. Lett.* **59**, 2360–2363 (1987).
- [43] C. J. Grayce and R. A. Harris, “Magnetic-field density-functional theory,” *Phys. Rev. A* **50**, 3089–3095 (1994).

- [44] J. P. Perdew and K. Schmidt, “Jacob’s ladder of density functional approximations for the exchange-correlation energy,” in AIP Conf. Proc. Vol. 577, 1 (2001), pp. 1–20.
- [45] J. P. Perdew and M. Levy, “Physical content of the exact Kohn–Sham orbital energies: Band gaps and derivative discontinuities,” Phys. Rev. Lett. **51**, 1884–1887 (1983).
- [46] R. O. Jones and O. Gunnarsson, “The density functional formalism, its applications and prospects,” Rev. Mod. Phys. **61**, 689–746 (1989).
- [47] D. C. Langreth and M. J. Mehl, “Beyond the local-density approximation in calculations of ground-state electronic properties,” Phys. Rev. B **28**, 1809–1834 (1983).
- [48] A. D. Becke, “Density-functional exchange-energy approximation with correct asymptotic behavior,” Phys. Rev. A **38**, 3098–3100 (1988).
- [49] J. P. Perdew, S. Kurth, A. Zupan, and P. Blaha, “Accurate density functional with correct formal properties: A step beyond the generalized gradient approximation,” Phys. Rev. Lett. **82**, 2544–2547 (1999).
- [50] J. Tao, J. P. Perdew, V. N. Staroverov, and G. E. Scuseria, “Climbing the density functional ladder: Nonempirical meta-generalized gradient approximation designed for molecules and solids,” Phys. Rev. Lett. **91**, 146401 (2003).
- [51] F. Tran, J. Stelzl, and P. Blaha, “Rungs 1 to 4 of DFT Jacob’s ladder: Extensive test on the lattice constant, bulk modulus, and cohesive energy of solids,” J. Chem. Phys. **144**, 204120 (2016).
- [52] D. Mejía-Rodríguez and S. B. Trickey, “Comment on “Regularized SCAN functional” [J. Chem. Phys. 150, 161101 (2019)],” J. Chem. Phys. **151**, 207101 (2019).
- [53] A. D. Becke, “A new mixing of Hartree–Fock and local density-functional theories,” J. Chem. Phys. **98**, 1372–1377 (1993).
- [54] J. P. Perdew, M. Ernzerhof, and K. Burke, “Rationale for mixing exact exchange with density functional approximations,” J. Chem. Phys. **105**, 9982–9985 (1996).
- [55] G. Kresse and J. Furthmüller, “Efficient iterative schemes for *ab initio* total-energy calculations using a plane-wave basis set,” Phys. Rev. B **54**, 11169–11186 (1996).

- [56] G. Kresse and D. Joubert, “From ultrasoft pseudopotentials to the projector augmented-wave method,” *Phys. Rev. B* **59**, 1758–1775 (1999).
- [57] P. Giannozzi, S. Baroni, N. Bonini, M. Calandra, R. Car, C. Cavazzoni, D. Ceresoli, G. L. Chiarotti, M. Cococcioni, I. Dabo, A. Dal Corso, S. de Gironcoli, S. Fabris, G. Fratesi, R. Gebauer, U. Gerstmann, C. Gougoussis, A. Kokalj, M. Lazzeri, L. Martin-Samos, N. Marzari, F. Mauri, R. Mazzarello, S. Paolini, A. Pasquarello, L. Paulatto, C. Sbraccia, S. Scandolo, G. Sclauzero, A. P. Seitsonen, A. Smogunov, P. Umari, and R. M. Wentzcovitch, “QUANTUM ESPRESSO: A modular and open-source software project for quantum simulations of materials,” *J. Phys. Condens. Matter* **21**, 395502 (2009).
- [58] P. Giannozzi, O. Andreussi, T. Brumme, O. Bunau, M. Buongiorno Nardelli, M. Calandra, R. Car, C. Cavazzoni, D. Ceresoli, M. Cococcioni, N. Colonna, I. Carnimeo, A. Dal Corso, S. de Gironcoli, P. Delugas, R. A. DiStasio, A. Ferretti, A. Floris, G. Fratesi, G. Fugallo, R. Gebauer, U. Gerstmann, F. Giustino, T. Gorni, J. Jia, M. Kawamura, H.-Y. Ko, A. Kokalj, E. Küçükbenli, M. Lazzeri, M. Marsili, N. Marzari, F. Mauri, N. L. Nguyen, H.-V. Nguyen, A. Otero-de-la-Roza, L. Paulatto, S. Poncé, D. Rocca, R. Sabatini, B. Santra, M. Schlipf, A. P. Seitsonen, A. Smogunov, I. Timrov, T. Thonhauser, P. Umari, N. Vast, X. Wu, and S. Baroni, “Advanced capabilities for materials modelling with Quantum ESPRESSO,” *J. Phys. Condens. Matter* **29**, 465901 (2017).
- [59] X. Gonze, J.-M. Beuken, R. Caracas, F. Detraux, M. Fuchs, G.-M. Rignanese, L. Sindic, M. Verstraete, G. Zerah, F. Jollet, M. Torrent, A. Roy, M. Mikami, P. Ghosez, J.-Y. Raty, and D. C. Allan, “First-principles computation of material properties: The ABINIT software project,” *Comput. Mater. Sci.* **25**, 478–492 (2002).
- [60] S. J. Clark, M. D. Segall, C. J. Pickard, P. J. Hasnip, M. I. J. Probert, K. Refson, and M. C. Payne, “First principles methods using CASTEP,” *Zeitschrift für Kristallographie - Crystalline Materials* **220**, 567–570 (2005).
- [61] C. Kittel, *Introduction to solid state physics*, 8th ed. (John Wiley and Sons, 2004), 700 pp.
- [62] H. J. Monkhorst and J. D. Pack, “Special points for Brillouin-zone integrations,” *Phys. Rev. B* **13**, 5188–5192 (1976).
- [63] D. R. Hamann, M. Schlüter, and C. Chiang, “Norm-conserving pseudopotentials,” *Phys. Rev. Lett.* **43**, 1494–1497 (1979).

- [64] D. Vanderbilt, “Soft self-consistent pseudopotentials in a generalized eigenvalue formalism,” *Phys. Rev. B* **41**, 7892–7895 (1990).
- [65] P. E. Blöchl, “Projector augmented-wave method,” *Phys. Rev. B* **50**, 17953–17979 (1994).
- [66] C. Freysoldt, J. Neugebauer, and C. G. Van de Walle, “Fully *ab initio* finite-size corrections for charged-defect supercell calculations,” *Phys. Rev. Lett.* **102**, 016402 (2009).
- [67] R. P. Feynman, “Forces in molecules,” *Phys. Rev.* **56**, 340–343 (1939).
- [68] V. Karpus, *Kristalinis būvis. Kietųjų kūnų fizika* (Ciklonas, 2002), 256 pp.
- [69] M. Born and K. Huang, *Dynamical theory of crystal lattices*, International series of monographs on physics (Oxford University Press, 1954), 432 pp.
- [70] R. J. Bell, P. Dean, and D. C. Hibbins-Butler, “Localization of normal modes in vitreous silica, germania and beryllium fluoride,” *J. Phys. C: Solid State Phys.* **3**, 2111–2118 (1970).
- [71] A. Alkauskas, B. B. Buckley, D. D. Awschalom, and C. G. Van de Walle, “First-principles theory of the luminescence lineshape for the triplet transition in diamond NV centres,” *New J. Phys.* **16**, 073026 (2014).
- [72] H. A. Jahn and E. Teller, “Stability of polyatomic molecules in degenerate electronic states. I—Orbital degeneracy,” *Proc. R. Soc. Lond. A* **161**, 220–235 (1937).
- [73] U. Öpik and M. H. L. Pryce, “Studies of the Jahn–Teller effect. I. A survey of the static problem,” *Proc. R. Soc. Lond. A* **238**, 425–447 (1957).
- [74] H. C. Longuet-Higgins, U. Öpik, M. H. L. Pryce, and R. A. Sack, “Studies of the Jahn–Teller effect. II. The dynamical problem,” *Proc. R. Soc. Lond. A* **244**, 1–16 (1958).
- [75] I. B. Bersuker and V. Z. Polinger, eds., *Vibronic interactions in molecules and crystals*, Vol. 49, Springer series in chemical physics (Springer-Verlag Berlin Heidelberg, 1989), 434 pp.
- [76] F. S. Ham, “Dynamical Jahn–Teller effect in paramagnetic resonance spectra: Orbital reduction factors and partial quenching of spin-orbit interaction,” *Phys. Rev.* **138**, A1727–A1740 (1965).
- [77] F. S. Ham, “Effect of linear Jahn–Teller coupling on paramagnetic resonance in a  ${}^2E$  state,” *Phys. Rev.* **166**, 307–321 (1968).

- [78] M. C. M. O'Brien, "The dynamic Jahn–Teller effect with many frequencies: A simple approach to a complicated problem," *J. Phys. C: Solid State Phys.* **5**, 2045–2063 (1972).
- [79] M. C. M. O'Brien and S. N. Evangelou, "The calculation of absorption band shapes in dynamic Jahn–Teller systems by the use of the Lanczos algorithm," *J. Phys. C: Solid State Phys.* **13**, 611–623 (1980).
- [80] O. Gunnarsson, H. Handschuh, P. S. Bechthold, B. Kessler, G. Ganteför, and W. Eberhardt, "Photoemission spectra of  $C_{60}^-$ : Electron–phonon coupling, Jahn–Teller effect, and superconductivity in the fullerenes," *Phys. Rev. Lett.* **74**, 1875–1878 (1995).
- [81] N. Iwahara, T. Sato, K. Tanaka, and L. F. Chibotaru, "Vibronic coupling in  $C_{60}^-$  anion revisited: Derivations from photoelectron spectra and DFT calculations," *Phys. Rev. B* **82**, 245409 (2010).
- [82] L. Razinkovas, "Vibrational properties and photoionization of color centers in diamond: Theory and *ab initio* calculations," PhD thesis (Vilnius University, Lithuania, 2021), 212 pp.
- [83] J. J. Markham, "Interaction of normal modes with electron traps," *Rev. Mod. Phys.* **31**, 956–989 (1959).
- [84] M. Lax, "The Franck–Condon principle and its application to crystals," *J. Chem. Phys.* **20**, 1752–1760 (1952).
- [85] R. Kubo and Y. Toyozawa, "Application of the method of generating function to radiative and non-radiative transitions of a trapped electron in a crystal," *Prog. Theor. Phys.* **13**, 160–182 (1955).
- [86] K. Huang and A. Rhys, "Theory of light absorption and non-radiative transitions in  $F$ -centres," *Proc. R. Soc. Lond. A* **204**, 406–423 (1950).
- [87] A. Togo, "First-principles phonon calculations with phonopy and phono3py," *J. Phys. Soc. Jpn.* **92**, 012001 (2023).
- [88] A. Togo, L. Chaput, T. Tadano, and I. Tanaka, "Implementation strategies in phonopy and phono3py," *J. Phys. Condens. Matter* **35**, 353001 (2023).
- [89] A. Hellman, B. Razaznejad, and B. I. Lundqvist, "Potential-energy surfaces for excited states in extended systems," *J. Chem. Phys.* **120**, 4593–4602 (2004).
- [90] T. Kowalczyk, S. R. Yost, and T. V. Voorhis, "Assessment of the  $\Delta$ SCF density functional theory approach for electronic excitations in organic dyes," *J. Chem. Phys.* **134**, 054128 (2011).

- [91] L. du Preez, “Electron paramagnetic resonance and optical investigations of defect centres in diamond,” PhD thesis (University of the Witwatersrand, Johannesburg, Republic of South Africa, 1965), 309 pp.
- [92] J. Meijer, B. Burchard, M. Domhan, C. Wittmann, T. Gaebel, I. Popa, F. Jelezko, and J. Wrachtrup, “Generation of single color centers by focused nitrogen implantation,” *Appl. Phys. Lett.* **87**, 261909 (2005).
- [93] J. H. N. Loubser and J. A. van Wyk, “Electron spin resonance in the study of diamond,” *Rep. Prog. Phys.* **41**, 1201–1248 (1978).
- [94] C. D. Clark and C. A. Norris, “Photoluminescence associated with the 1.673, 1.944 and 2.498 eV centres in diamond,” *J. Phys. C: Solid State Phys.* **4**, 2223–2229 (1971).
- [95] G. Davies and M. F. Hamer, “Optical studies of the 1.945 eV vibronic band in diamond,” *Proc. R. Soc. Lond. A* **348**, 285–298 (1976).
- [96] N. R. S. Reddy, N. B. Manson, and E. R. Krausz, “Two-laser spectral hole burning in a colour centre in diamond,” *J. Lumin.* **38**, 46–47 (1987).
- [97] E. van Oort, N. B. Manson, and M. Glasbeek, “Optically detected spin coherence of the diamond N-V centre in its triplet ground state,” *J. Phys. C: Solid State Phys.* **21**, 4385–4391 (1988).
- [98] K. Holliday, N. B. Manson, M. Glasbeek, and E. van Oort, “Optical hole-bleaching by level anti-crossing and cross relaxation in the N-V centre in diamond,” *J. Phys.: Condens. Matter* **1**, 7093–7102 (1989).
- [99] D. A. Redman, S. Brown, R. H. Sands, and S. C. Rand, “Spin dynamics and electronic states of N-V centers in diamond by EPR and four-wave-mixing spectroscopy,” *Phys. Rev. Lett.* **67**, 3420–3423 (1991).
- [100] L. J. Rogers, S. Armstrong, M. J. Sellars, and N. B. Manson, “Infrared emission of the NV centre in diamond: Zeeman and uniaxial stress studies,” *New J. Phys.* **10**, 103024 (2008).
- [101] J. Harrison, M. J. Sellars, and N. B. Manson, “Measurement of the optically induced spin polarisation of N-V centres in diamond,” *Diam. Relat. Mater.* **15**, 586–588 (2006).
- [102] M. Maciaszek, V. Žalandauskas, R. Silkinis, A. Alkauskas, and L. Razinkovas, “The application of the SCAN density functional to color centers in diamond,” *J. Chem. Phys.* **159**, 084708 (2023).

- [103] O. Madelung, ed., *Semiconductors, Group IV elements and III-V compounds*, Data in science and technology (Springer-Verlag Berlin Heidelberg, 1991), 170 pp.
- [104] P. Hao, Y. Fang, J. Sun, G. I. Csonka, P. H. T. Philipsen, and J. P. Perdew, “Lattice constants from semilocal density functionals with zero-point phonon correction,” *Phys. Rev. B* **85**, 014111 (2012).
- [105] J. Kulda, H. Kainzmaier, D. Strauch, B. Dorner, M. Lorenzen, and M. Krisch, “Overbending of the longitudinal optical phonon branch in diamond as evidenced by inelastic neutron and X-ray scattering,” *Phys. Rev. B* **66**, 241202 (2002).
- [106] A. A. Maradudin and A. E. Fein, “Scattering of neutrons by an anharmonic crystal,” *Phys. Rev.* **128**, 2589–2608 (1962).
- [107] G. Lang, K. Karch, M. Schmitt, P. Pavone, A. P. Mayer, R. K. Wehner, and D. Strauch, “Anharmonic line shift and linewidth of the Raman mode in covalent semiconductors,” *Phys. Rev. B* **59**, 6182–6188 (1999).
- [108] P. Kehayias, M. W. Doherty, D. English, R. Fischer, A. Jarmola, K. Jensen, N. Leefer, P. Hemmer, N. B. Manson, and D. Budker, “Infrared absorption band and vibronic structure of the nitrogen-vacancy center in diamond,” *Phys. Rev. B* **88**, 165202 (2013).
- [109] S. Zhao, A. M. Agarwal, J. L. Benton, G. H. Gilmer, and L. C. Kimerling, “Interstitial defect reactions in silicon,” *MRS Proc.* **442**, 231–236 (1996).
- [110] J. R. Noonan, C. G. Kirkpatrick, and B. G. Streetman, “Photoluminescence from Si irradiated with 1.5-MeV electrons at 100°K,” *J. Appl. Phys.* **47**, 3010–3015 (1976).
- [111] L. C. Kimerling, M. T. Asom, J. L. Benton, P. J. Drevinsky, and C. E. Cafer, “Interstitial defect reactions in silicon,” *Mater. Sci. Forum* **38–41**, 141–150 (1989).
- [112] G. Davies, “The optical properties of luminescence centres in silicon,” *Phys. Rep.* **176**, 83–188 (1989).
- [113] C. P. Foy, M. C. do Carmo, G. Davies, and E. C. Lightowers, “Uniaxial stress measurements on the 0.97 eV line in irradiated silicon,” *J. Phys. C: Solid State Phys.* **14**, L7–L12 (1981).
- [114] K. Thonke, H. Klemisch, J. Weber, and R. Sauer, “New model of the irradiation-induced 0.97-eV (*G*) line in silicon: A  $C_S-Si^*$  complex,” *Phys. Rev. B* **24**, 5874–5886 (1981).

- [115] K. P. O'Donnell, K. M. Lee, and G. D. Watkins, "Origin of the 0.97 eV luminescence in irradiated silicon," *Physica B+C* **116**, 258–263 (1983).
- [116] R. B. Capaz, A. Dal Pino Jr., and J. D. Joannopoulos, "Theory of carbon-carbon pairs in silicon," *Phys. Rev. B* **58**, 9845–9850 (1998).
- [117] R. J. Spry and W. D. Compton, "Recombination luminescence in irradiated silicon," *Phys. Rev.* **175**, 1010–1020 (1968).
- [118] G. Davies, E. C. Lightowers, R. C. Newman, and A. S. Oates, "A model for radiation damage effects in carbon-doped crystalline silicon," *Semicond. Sci. Technol.* **2**, 524–532 (1987).
- [119] Y. Baron, A. Durand, T. Herzig, M. Khoury, S. Pezzagna, J. Meijer, I. Robert-Philip, M. Abbarchi, J.-M. Hartmann, S. Reboh, J.-M. Gérard, V. Jacques, G. Cassabois, and A. Dréau, "Single G centers in silicon fabricated by co-implantation with carbon and proton," *Appl. Phys. Lett.* **121**, 084003 (2022).
- [120] C. Beaufiles, W. Redjem, E. Rousseau, V. Jacques, A. Y. Kuznetsov, C. Raynaud, C. Voisin, A. Benali, T. Herzig, S. Pezzagna, J. Meijer, M. Abbarchi, and G. Cassabois, "Optical properties of an ensemble of G-centers in silicon," *Phys. Rev. B* **97**, 035303 (2018).
- [121] M. Hollenbach, N. Klingner, N. S. Jagtap, L. Bischoff, C. Fowley, U. Kentsch, G. Hlawacek, A. Erbe, N. V. Abrosimov, M. Helm, Y. Berencén, and G. V. Astakhov, "Wafer-scale nanofabrication of telecom single-photon emitters in silicon," *Nat. Commun.* **13**, 7683 (2022).
- [122] P. Udvarhelyi, B. Somogyi, G. Thiering, and A. Gali, "Identification of a telecom wavelength single photon emitter in silicon," *Phys. Rev. Lett.* **127**, 196402 (2021).
- [123] A. Durand, Y. Baron, P. Udvarhelyi, F. Cache, K. V. R., T. Herzig, M. Khoury, S. Pezzagna, J. Meijer, J.-M. Hartmann, S. Reboh, M. Abbarchi, I. Robert-Philip, A. Gali, J.-M. Gérard, V. Jacques, G. Cassabois, and A. Dréau, "Hopping of the center-of-mass of single G centers in silicon-on-insulator," *Phys. Rev. X* **14**, 041071 (2024).
- [124] G. Henkelman, B. P. Uberuaga, and H. Jónsson, "A climbing image nudged elastic band method for finding saddle points and minimum energy paths," *J. Chem. Phys.* **113**, 9901–9904 (2000).
- [125] G. Henkelman and H. Jónsson, "Improved tangent estimate in the nudged elastic band method for finding minimum energy paths and saddle points," *J. Chem. Phys.* **113**, 9978–9985 (2000).

- [126] K. M. Lee, K. P. O'Donnell, J. Weber, B. C. Cavenett, and G. D. Watkins, "Optical detection of magnetic resonance for a deep-level defect in silicon," *Phys. Rev. Lett.* **48**, 37–40 (1982).
- [127] T. Ziegler, A. Rauk, and E. J. Baerends, "On the calculation of multiplet energies by the Hartree–Fock–Slater method," *Theoret. Chim. Acta* **43**, 261–271 (1977).
- [128] M. Mackoit-Sinkevičienė, M. Maciaszek, C. G. Van de Walle, and A. Alkauskas, "Carbon dimer defect as a source of the 4.1 eV luminescence in hexagonal boron nitride," *Appl. Phys. Lett.* **115**, 212101 (2019).
- [129] M. Maciaszek and L. Razinkovas, "Blue quantum emitter in hexagonal boron nitride and a carbon chain tetramer: A first-principles study," *ACS Appl. Nano Mater.* **7**, 18979–18985 (2024).
- [130] D. N. Batchelder and R. O. Simmons, "Lattice constants and thermal expansivities of silicon and of calcium fluoride between 6° and 322°K," *J. Chem. Phys.* **41**, 2324–2329 (1964).
- [131] W. Bludau, A. Onton, and W. Heinke, "Temperature dependence of the band gap of silicon," *J. Appl. Phys.* **45**, 1846–1848 (1974).
- [132] M. Holt, Z. Wu, H. Hong, P. Zschack, P. Jemian, J. Tischler, H. Chen, and T.-C. Chiang, "Determination of phonon dispersions from X-ray transmission scattering: The example of silicon," *Phys. Rev. Lett.* **83**, 3317–3319 (1999).
- [133] D. S. Kim, H. L. Smith, J. L. Niedziela, C. W. Li, D. L. Abernathy, and B. Fultz, "Phonon anharmonicity in silicon from 100 to 1500 K," *Phys. Rev. B* **91**, 014307 (2015).
- [134] W. Redjem, "Spectroscopie optique des centres G dans le silicium: des ensembles au centre unique," French, PhD thesis (Université de Montpellier, France, 2019), 152 pp.
- [135] M. Tinkham, *Group theory and quantum mechanics*, Dover books on chemistry (Dover Publications, 2003), 352 pp.
- [136] J. Wagner, K. Thonke, and R. Sauer, "Excitation spectroscopy on the 0.79-eV (*C*) line defect in irradiated silicon," *Phys. Rev. B* **29**, 7051–7053 (1984).
- [137] K. Thonke, A. Hangleiter, J. Wagner, and R. Sauer, "0.79 eV (*C* line) defect in irradiated oxygen-rich silicon: Excited state structure, internal strain and luminescence decay time," *J. Phys. C: Solid State Phys.* **18**, L795–L801 (1985).

- [138] T. Ishikawa, K. Koga, T. Itahashi, K. M. Itoh, and L. S. Vlasenko, “Optical properties of triplet states of excitons bound to interstitial-carbon interstitial-oxygen defects in silicon,” *Phys. Rev. B* **84**, 115204 (2011).
- [139] M. Tajima, S. Asahara, Y. Satake, and A. Ogura, “Free-to-bound emission from interstitial carbon and oxygen defects ( $C_iO_i$ ) in electron-irradiated Si,” *Appl. Phys. Express* **14**, 011006 (2021).
- [140] P. Udvarhelyi, A. Pershin, P. Deák, and A. Gali, “An L-band emitter with quantum memory in silicon,” *npj Comput. Mater.* **8**, 262 (2022).
- [141] J. M. Trombetta and G. D. Watkins, “Identification of an interstitial carbon - interstitial oxygen complex in silicon,” *MRS Proc.* **104**, 93–98 (1987).
- [142] R. Jones and S. Öberg, “Oxygen frustration and the interstitial carbon-oxygen complex in Si,” *Phys. Rev. Lett.* **68**, 86–89 (1992).
- [143] G. Bohnert, K. Weronek, and A. Hangleiter, “Transient characteristics of isoelectronic bound excitons at hole-attractive defects in silicon: The C(0.79 eV), P(0.767 eV), and H(0.926 eV) lines,” *Phys. Rev. B* **48**, 14973–14981 (1993).
- [144] R. Silkinis, M. Maciaszek, V. Žalandauskas, M. Etzelmüller Batten, L. Vines, A. Alkauskas, and L. Razinkovas, “Optical line-shapes of the C center in silicon from *ab initio* calculations: Interplay of localized modes and bulk phonons,” *Phys. Rev. B* **111**, 125136 (2025).
- [145] P. Deák, S. Li, and A. Gali, “Quantum bit with telecom wavelength emission from a simple defect in Si,” *Commun. Phys.* **7**, 337 (2024).
- [146] C. Freysoldt, B. Grabowski, T. Hickel, J. Neugebauer, G. Kresse, A. Janotti, and C. G. Van de Walle, “First-principles calculations for point defects in solids,” *Rev. Mod. Phys.* **86**, 253–305 (2014).
- [147] C. G. Van de Walle and J. Neugebauer, “First-principles calculations for defects and impurities: Applications to III-nitrides,” *J. Appl. Phys.* **95**, 3851–3879 (2004).
- [148] A. R. Bean and R. C. Newman, “The solubility of carbon in pulled silicon crystals,” *J. Phys. Chem. Solids* **32**, 1211–1219 (1971).
- [149] J. Coutinho, R. Jones, P. R. Briddon, S. Öberg, L. I. Murin, V. P. Markevich, and J. L. Lindström, “Interstitial carbon-oxygen center and hydrogen related shallow thermal donors in Si,” *Phys. Rev. B* **65**, 014109 (2001).

- [150] H. Wang, A. Chroneos, C. A. Londos, E. N. Sgourou, and U. Schwingenschlögl, “Carbon related defects in irradiated silicon revisited,” *Sci. Rep.* **4**, 4909 (2014).
- [151] S. Hao, L. Kantorovich, and G. Davies, “The interstitial  $C_iO_i$  defect in bulk Si and  $Si_{1-x}Ge_x$ ,” *J. Phys.: Condens. Matter* **16**, 8545–8555 (2004).
- [152] S. Hao, L. Kantorovich, and G. Davies, “Interstitial oxygen in Si and  $Si_{1-x}Ge_x$ ,” *Phys. Rev. B* **69**, 155204 (2004).
- [153] F. Zirkelbach, B. Stritzker, K. Nordlund, J. K. N. Lindner, W. G. Schmidt, and E. Rauls, “Combined *ab initio* and classical potential simulation study on silicon carbide precipitation in silicon,” *Phys. Rev. B* **84**, 064126 (2011).
- [154] D. J. Backlund and S. K. Estreicher, “C4 defect and its precursors in Si: First-principles theory,” *Phys. Rev. B* **77**, 205205 (2008).
- [155] G. D. Watkins and K. L. Brower, “EPR observation of the isolated interstitial carbon atom in silicon,” *Phys. Rev. Lett.* **36**, 1329–1332 (1976).
- [156] L. W. Song and G. D. Watkins, “EPR identification of the single-acceptor state of interstitial carbon in silicon,” *Phys. Rev. B* **42**, 5759–5764 (1990).
- [157] L. W. Song, X. D. Zhan, B. W. Benson, and G. D. Watkins, “Bistable interstitial-carbon–substitutional-carbon pair in silicon,” *Phys. Rev. B* **42**, 5765–5783 (1990).
- [158] P. M. Mooney, L. J. Cheng, M. Süli, J. D. Gerson, and J. W. Corbett, “Defect energy levels in boron-doped silicon irradiated with 1-MeV electrons,” *Phys. Rev. B* **15**, 3836–3843 (1977).
- [159] H. M. Ayedh, A. A. Grigorev, A. Galeckas, B. G. Svensson, and E. V. Monakhov, “Annealing kinetics of the interstitial carbon–dioxxygen complex in silicon,” *Phys. Status Solidi A* **216**, 1800986 (2019).
- [160] A. T. Collins and P. M. Spear, “The 1.40 eV and 2.56 eV centres in synthetic diamond,” *J. Phys. C: Solid State Phys.* **16**, 963–973 (1983).
- [161] V. Nadolinny, A. Komarovskikh, and Y. Palyanov, “Incorporation of large impurity atoms into the diamond crystal lattice: EPR of split-vacancy defects in diamond,” *Crystals* **7**, 237 (2017).
- [162] G. Thiering and A. Gali, “Magneto-optical spectra of the split nickel-vacancy defect in diamond,” *Phys. Rev. Res.* **3**, 043052 (2021).

- [163] R. Silkinis, V. Žalandauskas, G. Thiering, A. Gali, C. G. Van de Walle, A. Alkauskas, and L. Razinkovas, “Optical lineshapes for orbital singlet to doublet transitions in a dynamical Jahn–Teller system: The NiV<sup>−</sup> center in diamond,” *Phys. Rev. B* **110**, 075303 (2024).



# Santrauka

## Įvadas

Taškiniai defektai puslaidininkiuose, tokie kaip vakansijos ar priemaišos, yra įvairūs kristalinės gardelės periodiškumo sutrikdymai. Šie defektai įprastai skirstomi į dvi klases: sekliuosius ir giliuosius defektus. Sekliosios priemaišos (angl. *shallow impurities*) gali būti termiškai jonizuojamos ir naudojamos puslaidininkių elektrinėms ir optinėms savybėms kontroliuoti. Priešingai, gilieji defektai (angl. *deep-level defects*), pasižymintys aukštomis jonizacijos energijomis, tradiciškai buvo laikomi nepageidaujamais dėl krūvininkų pagavos [1] ir nespindulinės rekombinacijos [2].

Tačiau per pastaruosius kelis dešimtmečius kai kurie gilieji taškiniai defektai (angl. *deep-level point defects*) tapo perspektyviomis sistemomis, tinkamomis kietakūnėms kvantinėms technologijoms realizuoti. Lokalizotos elektroninės būsenos, atsirandančios giliai medžiagos draustinėje juostoje, lemia spektroskopiškai stabilius ir siaurus optinius šuolius, kurie sudaro sąlygas pavienių fotonų emisijai. Tokie defektai taip pat gali turėti kontroliuojamas sukinio būsenas su ilgomis koherencijos trukmėmis net esant įprastoms aplinkos sąlygoms. Šių savybių visuma sudaro pagrindą įvairiems taikymams kvantinės komunikacijos, jutiklių ir informacijos apdorojimo srityse.

Klasikinis taškinio defekto, pasižyminčio kvantinėms technologijoms palankiomis savybėmis, pavyzdys yra neigiamai įkrautas azoto-vakansijos ( $NV^-$ ) centras deimante [3]. Šio defekto sukinio koherencijos trukmės viršija milisekundes esant kambario temperatūrai [4–6], dėl ko jis laikomas pavyzdine sistema kuriant kvantinius jutiklius [7–12]. Žinoma, svarbūs defektai randami ir kitose medžiagose. Pavyzdžiui, silicije įvairūs defektai spinduliuoja telekomunikacijų bangų ruože [13–20], todėl yra suderinami su jau išvystyta šviesolaidine infrastruktūra. Tai padaro siliciję perspektyvia medžiaga kuriant pavienių fotonų šaltinius kvantinės komunikacijos reikmėms [21]. Šie ir kiti taškiniai defektai įvairiose medžiagose yra aktyviai tiriami taikymams ir kvantinės kompiuterijos srityje [22–24].

Defektų, turinčių pageidaujamas savybes kvantinėms technologijoms, paieška reikalauja itin plačios įvairių medžiagų ir jose egzistuoti galinčių defektų kombinacijų analizės [25]. Norint spręsti šį uždavinį, būtina gebėti patikimai nustatyti elektronines, vibronines, magnetines ir optines kiekvienos sistemos savybes, nes būtent jos ir nulemia tokių sistemų potencialų panaudojimą kuriant kvantines technologijas. Nors eksperimentiniai tyrimai yra nepakeičiami, jie dažnai nesuteikia visapusiškos informacijos apie defektinių sistemų atominę struktūrą ar jų optoelektro-

nines savybes. Šiuo požiūriu *ab initio*<sup>18</sup> skaičiavimo metodai, tokie kaip tankio funkcionalo teorija (angl. *density functional theory*, DFT), suteikia galimybes tirti defektų savybes, kurias sunku stebėti eksperimentiniais metodais.

Tankio funkcionalo teorija leidžia atlikti daugelio elektronų sistemos modeliavimą ir prognozuoti molekulinės sistemos struktūrinės, virpesinės ir elektroninės savybes. Ši teorija performuluoja daugiaelektronės Schrödinger lygties sprendimo uždavinį į pagrindinės būsenos elektronų tankio, iš kurio galima apskaičiuoti kitas svarbias sistemos savybes [26, 27], nustatymo uždavinį. Performulavimas atliekamas naudojant funkcionalus – matematinius objektus, kurių įvestis yra funkcija, o išvestis – skaliarinis dydis. Tankio funkcionalo teorijos kontekste funkcionalo įvestis priklauso nuo sistemos elektronų tankio, jo aukštesnės eilės skleidimo narių ir neretai nuo dar kitų parametrų, o išvestis yra skaliarinis dydis, pavyzdžiui, bendra sistemos energija.

Nepaisant didelio pasisekimo, tankio funkcionalo teorija nėra visiškai tiksli ir turi tam tikrų apribojimų. Tiksliai pakaitos ir koreliacijos (angl. *exchange–correlation*, XC) funkcionalo forma – esminė teorijos, apibrėžiančios elektron–elektroninę sąveiką, sudedamoji dalis – yra nežinoma. Šioje disertacijoje taškinių defektų sistemoms modeliuoti naudojama moderni SCAN funkcionalų [28–30] klasė dėl jos gebėjimo užtikrinti skaičiavimų spartą ir tikslumą. Pastarųjų funkcionalų efektyvumas vertinamas analizuojant  $NV^-$  centrą deimante ir gautus rezultatus lyginant su eksperimentiniais duomenimis ir skaičiavimais, atliktais naudojant kitus funkcionalus: PBE [31] ir daugiau skaičiavimo išteklių reikalaujantį hibridinį funkcionalą HSE06 [32]. Pastarasis dažnai laikomas „auksiniu standartu“ taškinių defektų skaičiavimuose.

Taškiniai defektai puslaidininkiuose pasižymi įvairiomis elektroninėmis ir vibroninėmis savybėmis, kurios neaprašomos standartine tankio funkcionalo teorija. Daugelis savybių yra nulemtos sužadintų elektroninių būsenų ir jų sąveikos su gardelės virpesiais. Kai kuriais atvejais sužadintos būsenos yra statiškai koreliuotos ir negali būti aprašytos naudojant suvidurkinto lauko (angl. *mean-field*) metodus, todėl reikia apytikrių ar pažangesnių būdų norint suprasti jų energetiką ir elektron–fononinę sąveiką [33–35]. Kitose sistemose optinis sužadinimas gali sukurti silpnai susietas eksitonines sužadintas būsenas [36], kurių elektrono ir skylės poros sąveika nėra patikimai aprašoma tankio funkcionalo teorijos kontekste. Be to, daugelyje svarbių defektinių sistemų pasireiškia sudėtingi neadiabatiniai reiškiniai, tokie kaip dinaminis Jahn-Teller efektas, kuriuose elektroninės būsenos dinamiškai sąveikauja su gardelės virpesiais [37–39].

---

<sup>18</sup>Lotynų kalba *ab initio* reiškia „nuo pradžios“. Moksliniame kontekste, tai reiškia skaičiavimus, pagrįstus vien tik pagrindiniais fizikos dėsniais, nenaudojant empirinių parametrų.

Šiame darbe derinami *ab initio* tankio funkcionalo teorijos skaičiavimai ir apytikriai sužadintų būsenų, eksitoninių ir neadiabatinių reiškinių modeliavimo metodai. Naudojant virpesinių modų analizę ir optinių linijų skaičiavimo įrankius, šis darbas siekia suteikti daugiau įžvalgų į pasirinktų defektinių sistemų optinį elgesį technologiniu požiūriu svarbiose medžiagose – deimante ir silicyje.

## Darbo tikslas

Pagrindinis šio darbo tikslas – ištirti ir tobulinti tankio funkcionalo teorijos metodų taikymą modeliuojant giliųjų taškinių defektų puslaidininkuose elektron-fononines sąveikas ir optines linijas. Ypatingas dėmesys skiriamas sudėtingiems atvejams, įskaitant:

- koreliuotas sužadintas būsenas,
- silpnai susietas eksitonines sužadintas būsenas ir
- sistemas, kurios pasižymi reikšmingo stiprumo neadiabatinėmis Jahn-Teller sąveikomis.

## Darbo uždaviniai

Siekiant įgyvendinti darbo tikslą, buvo išskelti šie uždaviniai:

- (1) Įvertinti SCAN funkcionalų šeimos efektyvumą aprašant deimanto ir silicio taškinių defektų struktūrines ir virpesines savybes.
- (2) Įvertinti harmoninės aproksimacijos ir apytikrių metodų, taikomų koreliuotoms sužadintoms būsenoms modeliuoti, efektyvumą atkuriant G-centro defekto silicyje liuminescencijos liniją.
- (3) Ištirti apytikres optinių linijų modeliavimo strategijas C-centro defektui silicyje, kur optiniai šuoliai susiję su silpnai susietomis eksitoninėmis sužadintomis būsenomis.
- (4) Sumodeliuoti neigiamai įkrauto nikelio-vakansijos defekto deimante, pasižyminčio reikšmingo stiprumo neadiabatinėmis Jahn-Teller sąveikomis, liuminescencijos liniją naudojant naujovišką daugelio Jahn-Teller modų skaičiavimo metodologiją.

## Darbo aktualumas ir naujumas

Šioje disertacijoje nagrinėjama tema, esanti skaičiuojamosios medžiagotyros ir sparčiai besivystančios kvantinių technologijų srities sankirtoje. Toliau pateikiamas šio darbo aktualumas ir naujumas.

### Aktualumas

Didėjantis susidomėjimas kurti patikimas kvantinės komunikacijos, jutiklių ir kompiuterijos architektūras lėmė tai, kad gilieji taškiniai defektai puslaidininkiuose tapo viena iš perspektyvių terpių šioms technologijoms įgyvendinti. Atsižvelgiant į milžinišką galimų defektų ir medžiagų konfigūracijų įvairovę, šių sistemų identifikavimas ir apibūdinimas yra sudėtingas uždavinys, kurio sprendimui būtini patikimi *ab initio* metodai. Šiuo darbu prisidedama prie teorinių modelių, skirtų tokių taškinių defektų optinėms charakteristikoms nustatyti, kūrimo ir taikymo.

### Naujumas

- Vienas pagrindinių šio darbo naujumų yra pažangios įterpimo metodologijos (angl. *embedding methodology*) taikymas tiriant kelis spalvinius centrus. Modeliuojant sistemas, talpinančias dešimtis tūkstančių atomų, ši metodika leidžia sumodeliuoti aukštos skiriamosios gebos optines linijas.
- Šiame tyrime taikomos ir vertinamos skaičiavimo strategijos, skirtos elektroninėms konfigūracijoms, kurių modeliavimas išlieka sudėtingu uždaviniu standartinei tankio funkcionalo teorijai. Konkrečiai nagrinėjama statinė elektronų koreliacija ir silpnai susietos eksitoninės būsenos.
- Šioje disertacijoje pateikiamas pirmasis dinaminis Jahn-Teller efektu pasižymintio spalvinio centro ( $NiV^-$  centras deimante) spektroskopinio signalo modeliavimas naudojant pažangią *ab initio* daugelio Jahn-Teller modų skaičiavimo metodologiją. Tiesiogiai išsprendus vibroninį Hamiltonianą, šiuo metodu pavyko tiksliai atkurti plačią fononų pajuostę, kurios standartinė adiabatinė teorija nepajėgia aprašyti.

## Ginamieji teiginiai

- (I) Liuminescencijos optinė linija, susijusi su G-centro defektu silicyje, galėjo būti tik iš dalies atkurta naudojant apytikslės sukinio projekcijos metodiką, kuria buvo siekiama sumodeliuoti sužadintą būseną, aprašomą keliais Slater determinantais. Skirtumai tarp teorijos ir eksperimento gali kilti dėl riboto statinės elektronų koreliacijos sužadintoje būsenoje įskaitymo arba dėl galimai anharmoninio joninio potencialo.
- (II) Eksperimentinė C-centro defekto silicyje liuminescencijos linija, atsirandanti dėl optinio šuolio, susijusio su silpnai susieta eksitonine sužadinta būsena, yra tiksliai atkuriami neutralios būsenos joninių potencinės energijos paviršių aproksimuojant teigiamai įkrauto (jonizuoto) defekto kuriamu joniniu potencialu.
- (III) Artimas sutapimas tarp liuminescencijos linijos, nustatytos naudojant dinaminę Jahn-Teller teoriją, ir eksperimentinio spektro yra svarus įrodymas, kad 1.40 eV centras deimante yra neigiamai įkrautas nikelio-vakansijos defektas. Šis rezultatas pabrėžia Jahn-Teller efekto svarbą formuojant optinę liniją ir parodo pažangių skaičiavimo metodų, skirtų sudėtingų sistemų optinėms savybėms modeliuoti, efektyvumą.

## Darbo struktūra

Disertacija sudaryta iš penkių pagrindinių skyrių. Pirmame skyriuje pateikiama teorinė medžiaga ir metodologinis pagrindas, įskaitant trumpą tankio funkcionalo teorijos apžvalgą, gardelės virpesių dinamikos aprašymą, elektron-fononinę sąveiką, Jahn-Teller efektą ir taikytus skaičiavimo metodus. Antrame–penktame skyriuose pateikiami keturių taškinių defektų sistemų tyrimų rezultatai. Antrame skyriuje nagrinėjamas  $NV^-$  centras deimante ir lyginami skirtingi tankio funkcionalai. Trečiame skyriuje analizuojamas G-centras silicyje, kurio sužadinta būsena pasižymi reikšminga statine elektronų koreliacija. Ketvirtame skyriuje tiriamas C-centras silicyje, kuriam būdinga liuminescencija, kylanti iš silpnai susietos eksitoninės sužadintos būsenos. Galiausiai, penktame skyriuje nagrinėjamas Jahn-Teller efektu pasižymintis  $NiV^-$  centras deimante, kurio emisijos savybės modeliuojamos derinant adiabatinių ir vibroninių artinius.

## Autoriaus indėlis

Doktorantūros studijų laikotarpiu autorius prisidėjo prie keturių mokslinių publikacijų ir pristatė aštuonis pranešimus konferencijose (iš jų penkios buvo tarptautinės), apimančius du žodinius ir šešis standinius. Toliau pateiktas autoriaus indėlis į publikacijas:

- Publikacija (P1): autorius atliko  $NV^-$  centro deimante optinių linijų skaičiavimus, naudodamas įvairius tankio funkcionalus, ir vykdė vertikalios sužadavimo energijos skaičiavimus visiems tyrime nagrinėtiems spalviniams centrams. Be to, autorius prisidėjo prie publikacijos rankraščio redagavimo. Šios publikacijos rezultatai sudaro antrojo skyriaus pagrindą.
- Publikacija (P2): autorius buvo pagrindinis šios publikacijos vykdytojas. Jis atliko didžiąją dalį deimanto ir  $NiV^-$  centro skaičiavimų. Taikydamas daugelio Jahn-Teller modų skaičiavimo metodologiją, autorius išanalizavo gautus duomenis ir pateikė išvadas. Be to, bendradarbiaujant su darbo vadovu, autorius buvo pagrindinis publikacijos rankraščio rengimo ir redakcijos vykdytojas. Šios publikacijos rezultatai sudaro penktojo skyriaus pagrindą.
- Publikacija (P3): autorius buvo pagrindinis šios publikacijos vykdytojas, atlikęs didžiąją dalį silicio, įskaitant įvairius defektus jame, skaičiavimų. Išanalizavęs gautus duomenis, autorius pateikė išvadas. Jis taip pat buvo pagrindinis publikacijos rankraščio rengimo ir redakcijos vykdytojas. Šios publikacijos rezultatai sudaro ketvirtojo skyriaus pagrindą.
- Publikacija (P4): autorius atliko dviejų divakansijos silicio karbide konfigūracijų emisijos linijų skaičiavimus ir dalyvavo publikacijos rankraščio redagavimo procese. Šios publikacijos rezultatai į disertaciją neįtraukti.

## Publikacijos

- (P1) M. Maciaszek, V. Žalandauskas, R. Silkinis, A. Alkauskas ir L. Razinkovas, *The application of the SCAN density functional to color centers in diamond*, J. Chem. Phys. **159**, 084708 (2023).
- (P2) R. Silkinis, V. Žalandauskas, G. Thiering, A. Gali, C. G. Van de Walle, A. Alkauskas ir L. Razinkovas, *Optical lineshapes for orbital singlet to doublet transitions in a dynamical Jahn–Teller system: The  $NiV^-$  center in diamond*, Phys. Rev. B **110**, 075303 (2024).

- (P3) R. Silkinis, M. Maciaszek, V. Žalandauskas, M. E. Bathen, L. Vines, A. Alkauskas ir L. Razinkovas, *Optical lineshapes of the C-center in silicon from ab initio calculations: Interplay of localized modes and bulk phonons*, Phys. Rev. B **111**, 125136 (2025).
- (P4) V. Žalandauskas, R. Silkinis, L. Vines, L. Razinkovas ir M. E. Bathen, *Theory of the divacancy in 4H-SiC: Impact of Jahn–Teller effect on optical properties*, npj Comput. Mater. **11**, 155 (2025).

## Konferencijos

- (C1) R. Silkinis, L. Razinkovas ir A. Alkauskas, *Modeling semiconductor alloys using special quasi-random structures*, 10-oji FTMC doktorantų ir jaunųjų mokslininkų konferencija „FizTeCh2020”, 2020-10-23, Vilnius, Lietuva. Stendinis pranešimas.
- (C2) R. Silkinis, L. Razinkovas ir A. Alkauskas, *Theoretical modeling of luminescence lineshape in silicon due to a carbon-carbon pair complex*, 65-oji tarptautinė studentų ir jaunųjų mokslininkų konferencija „Open Readings 2022”, 2022-03-15, Vilnius, Lietuva. Stendinis pranešimas.
- (C3) R. Silkinis, L. Razinkovas ir A. Alkauskas, *Theoretical modeling of luminescence lineshape in silicon due to a carbon-carbon pair complex*, Tarptautinė konferencija „Defects in solids for quantum technologies” (DSQT), 2022-06-15, Stokholmas, Švedija. Stendinis pranešimas.
- (C4) R. Silkinis, L. Razinkovas, V. Žalandauskas ir A. Alkauskas, *Luminescence lineshape of the G-center in silicon from ab-initio calculations*, 12-oji FTMC doktorantų ir jaunųjų mokslininkų konferencija „FizTeCh2022”, 2022-10-19, Vilnius, Lietuva. Žodinis pranešimas.
- (C5) R. Silkinis, M. E. Bathen, A. Alkauskas ir L. Razinkovas, *Theoretical modeling of vibrationally resolved optical lineshapes of a carbon-oxygen pair defect in silicon*, Tarptautinė konferencija „Humboldt Kolleg on Synthetic Quantum Matter”, 2023-07-03, Vilnius, Lietuva. Stendinis pranešimas.
- (C6) R. Silkinis, M. E. Bathen, A. Alkauskas ir L. Razinkovas, *Theoretical modeling of vibrationally resolved optical lineshapes of a carbon-oxygen pair defect in silicon*, 32-oji tarptautinė defektų puslaidininkiuose konferencija (ICDS), 2023-09-11, Rehoboth Beach, Delaveras, JAV. Stendinis pranešimas.

- (C7) R. Silkinis, M. Maciaszek, V. Žalandauskas, M. E. Bathen, L. Vines, A. Alkauskas ir L. Razinkovas, *Theoretical modeling of vibrationally resolved optical lineshapes of a carbon-oxygen pair defect in silicon*, 13-oji FTMC doktorantų ir jaunųjų mokslininkų konferencija „Fiz-TeCh2023”, 2023-10-19, Vilnius, Lietuva. Žodinis pranešimas.
- (C8) R. Silkinis, M. Maciaszek, V. Žalandauskas, M. E. Bathen, L. Vines, A. Alkauskas ir L. Razinkovas, *Theoretical modeling of vibrationally resolved optical lineshapes of a carbon-oxygen pair defect in silicon*, Tarptautinė konferencija „Defects in solids for quantum technologies” (DSQT), 2024-06-11, Budapeštas, Vengrija. Stendinis pranešimas.

# 1. Teorinis ir metodologinis pagrindas

## 1.1. Daugiadalelis uždavinys

Medžiagos savybės aprašomos kvantinės mechanikos principais. Izo-  
liuotų, nereliatyvistinių sistemų analizės atskaitos taškas yra nuo laiko  
nepriklausanti Schrödinger lygtis:

$$\hat{H}|\Psi\rangle = E|\Psi\rangle, \quad (1)$$

čia  $\hat{H}$  yra sistemos hamiltonianas,  $|\Psi\rangle$  yra būsenos vektorius, o  $E$  yra  
bendra sistemos energija. Molekulinėse sistemose, sudarytose iš sąveikau-  
jančių elektronų ir jonų, hamiltonianas priklauso tiek nuo elektronų ( $\mathbf{r}$ ),  
tiek nuo jonų ( $\mathbf{R}$ ) laisvės laipsnių:

$$\hat{H}(\mathbf{r}, \mathbf{R}) = \hat{T}_e + \hat{T}_n + \hat{V}_{ee}(\mathbf{r}) + \hat{V}_{en}(\mathbf{r}, \mathbf{R}) + \hat{V}_{nn}(\mathbf{R}), \quad (2)$$

čia  $\hat{T}_e$  ir  $\hat{T}_n$  žymi elektronų ir jonų kinetinės energijos operatorius, o trys  
potencinės energijos nariai aprašo elektron-elektroninę ( $\hat{V}_{ee}(\mathbf{r})$ ), elektron-  
joninę ( $\hat{V}_{en}(\mathbf{r})$ ) ir jon-joninę ( $\hat{V}_{nn}(\mathbf{r})$ ) sąveikas.

Kadangi sistemos būsenos vektorius  $|\Psi\rangle$  priklauso nuo visų elekt-  
ronų ir jonų koordinacių, tiesioginis jo radimas sprendžiant (1) lygtį  
yra neįmanomas realaus dydžio sistemoms. Šio uždavinio sprendimui  
būtina pasitelkti fizikiškai pagrįstas aproksimacijas, leidžiančias atskirti  
elektronines ir jonines posistemes.

## 1.2. Adiabatinė aproksimacija

Bendras potencialas, veikiantis elektronus, yra

$$\hat{V}_e(\mathbf{r}, \mathbf{R}) = \hat{V}_{ee}(\mathbf{r}) + \hat{V}_{en}(\mathbf{r}, \mathbf{R}), \quad (3)$$

kurią galima išskleisti aplink pusiausvyrinę jonų (kurių yra  $N_n$ ) konfigūra-  
ciją  $\mathbf{R}^{(0)} \equiv \{\mathbf{R}_1^{(0)}, \mathbf{R}_2^{(0)}, \dots, \mathbf{R}_{N_n}^{(0)}\}$ :

$$\begin{aligned} \hat{V}_e(\mathbf{r}, \mathbf{R}) &= \hat{V}_e(\mathbf{r}; \mathbf{R}^{(0)}) \\ &+ \sum_{\alpha}^{N_n} \sum_{i \in \{x, y, z\}} \left( \frac{\partial \hat{V}_e}{\partial R_{\alpha_i}} \right)_{\mathbf{R}^{(0)}} u_{\alpha_i} \\ &+ \frac{1}{2} \sum_{\alpha, \beta}^{N_n} \sum_{i, j \in \{x, y, z\}} u_{\alpha_i} \left( \frac{\partial^2 \hat{V}_e}{\partial R_{\alpha_i} \partial R_{\beta_j}} \right)_{\mathbf{R}^{(0)}} u_{\beta_j} \\ &+ O(\mathbf{u}^3), \end{aligned} \quad (4)$$

čia  $\mathbf{u}_\alpha = \mathbf{R}_\alpha - \mathbf{R}_\alpha^{(0)}$  yra jono  $\alpha$  nuokrypis nuo pusiausvyrinės padėties  $\mathbf{R}_\alpha^{(0)}$ , o  $\mathbf{u} \equiv \{\mathbf{u}_1, \mathbf{u}_2, \dots, \mathbf{u}_{N_n}\}$ .

Išskaitant tik pirmąjį pastarojo skleidinio narį, gaunama *statinė adiabatinė aproksimacija* (angl. *crude adiabatic approximation*) [40], kurioje *elektroninis* hamiltonianas  $\hat{H}_e(\mathbf{r}; \mathbf{R}^{(0)})$  yra „iššaldytas“ pusiausvyrinėje geometrijoje,

$$\hat{H}_e(\mathbf{r}; \mathbf{R}^{(0)}) = \hat{T}_e + \hat{V}_e(\mathbf{r}; \mathbf{R}^{(0)}), \quad (5)$$

o atitinkamas elektroninės posistemės tikrinių verčių uždavinys

$$\left[ \hat{T}_e + \hat{V}_e(\mathbf{r}; \mathbf{R}^{(0)}) \right] \psi_s(\mathbf{r}; \mathbf{R}^{(0)}) = \varepsilon_s(\mathbf{R}^{(0)}) \psi_s(\mathbf{r}; \mathbf{R}^{(0)}) \quad (6)$$

*elektroninėms* banginėms funkcijoms  $\psi_s(\mathbf{r}; \mathbf{R}^{(0)})$  yra sprendžiama esant fiksuotoms jonų koordinatėms. Tuomet sistemos pilnutinę *vibroninę* banginę funkciją galima užrašyti adiabatinėje formoje:

$$\Psi_{st}(\mathbf{r}, \mathbf{R}) = \psi_s(\mathbf{r}; \mathbf{R}^{(0)}) \chi_{st}(\mathbf{R}), \quad (7)$$

čia  $\chi_{kt}(\mathbf{R})$  yra *virpesinės* banginės funkcijos, tenkinančios *joninę* Schrödinger lygtį:

$$\begin{aligned} & \left[ \hat{T}_n + \hat{V}_{nn}(\mathbf{R}) + \left\langle \psi_s(\mathbf{r}; \mathbf{R}^{(0)}) \left| \Delta \hat{V}_e(\mathbf{r}, \mathbf{R}) \right| \psi_s(\mathbf{r}; \mathbf{R}^{(0)}) \right\rangle_{\mathbf{r}} \right] \chi_{st}(\mathbf{R}) \\ & = \left[ E_{st} - \varepsilon_s(\mathbf{R}^{(0)}) \right] \chi_{st}(\mathbf{R}), \end{aligned} \quad (8)$$

čia

$$\langle y | \hat{A} | x \rangle_{\mathbf{r}} \equiv \int y^* \hat{A} x \, d\mathbf{r}_1 \dots d\mathbf{r}_{N_e}, \quad \mathbf{r} \equiv \{\mathbf{r}_1, \mathbf{r}_2, \dots, \mathbf{r}_{N_e}\}.$$

### 1.3. Tankio funkcionalo teorija

Atskyrus elektroninius ir joninius laisvės laipsnius, pagrindinis uždavinys suvedamas į daugiaelektronio hamiltoniano

$$\hat{H}_e(\mathbf{r}; \mathbf{R}^{(0)}) = \hat{T}_e + \hat{V}_{ee}(\mathbf{r}) + \sum_i^{N_e} v(\mathbf{r}_i; \mathbf{R}^{(0)}) \quad (9)$$

diagonalizavimą su išoriniu potencialu<sup>19</sup>

$$v(\mathbf{r}_i; \mathbf{R}^{(0)}) = - \sum_{\alpha}^{N_n} \frac{Z_{\alpha}}{|\mathbf{r}_i - \mathbf{R}_{\alpha}^{(0)}|}, \quad (10)$$

<sup>19</sup>Formulėse naudojami Hartree atominiai vienetai:  $\hbar = m_e = e = 4\pi\epsilon_0 = 1$ .

kurį jaučia kiekvienas iš  $N_e$  elektronų. Deja, bet tiesioginis hamiltoniano (9) tikrinių funkcijų radimas yra nepraktiškas. Viena iš šios problemos sprendimo alternatyvų yra tankio funkcionalo teorija (angl. *density functional theory*, DFT), kuri performuluoja uždavinį per elektronų tankį

$$\rho(\bar{\mathbf{r}}) = N_e \int |\psi(\bar{\mathbf{r}}, \mathbf{r}_2, \dots, \mathbf{r}_{N_e})|^2 d^3\mathbf{r}_2 \dots d^3\mathbf{r}_{N_e}, \quad (11)$$

priklausantį ne nuo  $3N_e$  erdvinių laisvės laipsnių, bet nuo trijų komponentų erdvinio vektoriaus  $\bar{\mathbf{r}} = (x, y, z)$ .

Centrinė DFT įžvalga yra tai, kad visus pagrindinės būsenos stebinius (angl. *observables*) galima išreikšti naudojant funkcionalus, priklausančius nuo pagrindinės būsenos elektronų tankio  $\rho_0(\bar{\mathbf{r}})$ , taip apeinant poreikį skaičiuoti daugiaelektronę banginę funkciją  $\psi$ . Šios įžvalgos pamatas yra dvi teoremos, 1964 metais suformuluotos Pierre Hohenberg ir Walter Kohn [26].

Hohenberg-Kohn (HK) teoremos nustato, kad (1) išorinis potencialas  $v(\bar{\mathbf{r}})$ , o tuo pačiu ir visas hamiltonianas, yra unikalūs pagrindinės būsenos elektronų tankio  $\rho_0(\bar{\mathbf{r}})$  funkcionalas ir (2) energijos funkcionalas  $E[\rho]$  įgyja minimumą tik su pagrindinės būsenos elektronų tankiu  $\rho_0(\bar{\mathbf{r}})$ . Problema ta, kad tiksli šio energijos funkcionalo forma nėra žinoma.

Nors HK teoremos nustato, kad pagrindinės būsenos elektronų tankis unikaliai nulemia visas daugiaelektronės sistemos pagrindinės būsenos savybes, jos nepateikia praktinio būdo šio tankio apskaičiavimui. Šiai problemai 1965 metais sprendimą pasiūlė Walter Kohn ir Le Jeu Sham, įvedę nesąveikaujančių elektronų sistemos modelį, kuris tiksliai atkuria tikrosios, daugiaelektronės sistemos pagrindinės būsenos elektronų tankį [27]. Šiame formalizme elektronų tankis konstruojamas iš nesąveikaujančių viendalelių orbitalių  $\{\phi_i^{\text{KS}}(\mathbf{r}_i)\}$ , tenkinančių Kohn-Sham (KS) lygtis:

$$\left[ -\frac{1}{2} \frac{\partial^2}{\partial \bar{\mathbf{r}}^2} + v_{\text{eff}}(\bar{\mathbf{r}}) \right] \phi_i^{\text{KS}}(\bar{\mathbf{r}}) = \varepsilon_i^{\text{KS}} \phi_i^{\text{KS}}(\bar{\mathbf{r}}), \quad i = 1, \dots, N_e, \quad (12)$$

čia

$$v_{\text{eff}}(\bar{\mathbf{r}}) = v(\bar{\mathbf{r}}) + \int \frac{\rho(\bar{\mathbf{r}}')}{|\bar{\mathbf{r}} - \bar{\mathbf{r}}'|} d^3\bar{\mathbf{r}}' + v_{\text{XC}}(\bar{\mathbf{r}}) \quad (13)$$

yra efektinis KS potencialas. Pakaitos ir koreliacijos potencialas  $v_{\text{XC}}(\bar{\mathbf{r}}) = \delta E_{\text{XC}}[\rho] / \delta \rho(\bar{\mathbf{r}})$  apima visas neklasikines sąveikas ir pataisas, atsirandančias dėl nesąveikaujančių dalelių modelio naudojimo. Šioje išraiškoje esantis pakaitos ir koreliacijos energijos funkcionalas  $E_{\text{XC}}[\rho]$  yra vienintelė dalis, kurios tiksli forma nežinoma, todėl jos aprašymui pasitelkiamos įvairios aproksimacijos.

Verta pabrėžti, kad tankio funkcionalo teorija yra formaliai tiksli, jei būtų žinoma tiksli funkcionalo  $E_{\text{XC}}[\rho]$  forma. Realybėje skaičiavimų

kokybė priklauso nuo šiam funkcionalui taikomos aproksimacijos, keletas kurių toliau trumpai aptariamos:

- Lokalaus tankio aproksimacija (angl. *local-density approximation*, LDA) [27] – paprasčiausias pakaitos ir koreliacijos energijos funkcionalo artinys, paremtas vienalyčių elektronų dujų modeliu. Daroma prielaida, kad pakaitos ir koreliacijos energija bet kuriame taške priklauso tik nuo elektronų tankio tame taške. Ši aproksimacija pakankamai tiksliai aprašo sistemų su lėtai kintančiu elektronų tankiu struktūrinės savybes, bet netiksliai įvertina sąveikos energijas, cheminių reakcijų barjerus ir draustinės juostos tarpus [45, 46].
- Apibendrinto gradiento aproksimacija (angl. *generalized gradient approximation*, GGA) [47, 48], lyginant su LDA, papildomai įskaito elektronų tankio gradientą, leidžiantį geriau įvertinti tankio pokyčius. Kietakūnių sistemų modeliavimui dažniausiai naudojamas GGA funkcionalas yra Perdew–Burke–Ernzerhof (PBE) [31].
- Meta-GGA funkcionalai [49, 50] dar įtraukia kinetinės energijos tankį, kas leidžia geriau įvertinti įvairius nelokalius efektus. Plačiausiai naudojamas meta-GGA funkcionalo pavyzdys yra SCAN (angl. *strongly constrained and appropriately normed*) [28], ir iš jo vėliau kilę reguliarizuoti variantai, rSCAN [29] ir r<sup>2</sup>SCAN [30].
- Hibridiniai funkcionalai [53] į XC funkcionalą papildomai įtraukia dalį nelokalios Hartree-Fock pakaitos energijos. Šie funkcionalai žymiai tiksliau įvertina draustinių juostų tarpus ir elektroninių lygmenų energijas. Pagrindinis jų trūkumas – žymiai padidėjusios skaičiavimų sąnaudos. Hibridinių funkcionalų tarpe HSE06 [32] variantas yra vienas iš dažniausiai naudojamų modeliuojant kietakūnes sistemas.

Praktiniuose kietakūnių sistemų skaičiavimuose, be pasirinktos tankio funkcionalo aproksimacijos, lemiamą vaidmenį atlieka ir keli techniniai aspektai:

- Bazės pasirinkimas. Modeliuojant periodines sistemas paprasčiausias sprendimas yra naudoti plokščiųjų bangų bazę [61], nes ji leidžia patogiai kontroliuoti rezultatų konvergavimą.
- Elektronų įskaitymas. Netoli atomų branduolių esančių elektronų orbitalėms tiksliai aprašyti reikalinga itin didelė plokščiųjų bangų bazė, todėl tiesioginis visų elektronų įskaitymas būtų per daug brangus skaitiškai. Šiai problemai spręsti naudojami pseudopotencialai [63–65], kurie eliminuoja tikslų giliųjų elektronų (angl. *core*

*electrons*) įskaitymą ir dėmesį skiria chemiškai aktyvių valentinių elektronų aprašymui.

- Sistemos dydis ir kraštinės sąlygos. Defektų modeliavime dažniausiai naudojamas supergardelės metodas: sukonstruojama pakankamai didelė sistema (iki maždaug 1000 atomų) su jame įterptu pavieniu defektu taikant periodines kraštines sąlygas.

#### 1.4. Kietųjų kūnų virpesinės savybės

Iki čia buvo aptarinėjamas elektroninės posistemės [formulė (9)] sprendimo uždavinys, laikant, kad sistemos jonai yra „užšaldyti“. Tačiau realybėje šie jonai nėra stacionarūs ir jų judėjimas nulemia įvairias kietakūnių sistemų savybes.

Joninės sistemos potencinė energija, priklausanti nuo jonų padėčių  $\mathbf{R}$  šalia pusiausvyros padėties  $\mathbf{R}^{(0)}$ , apibūdina sistemos adiabatinių potencinės energijos paviršių (angl. *adiabatic potential energy surface*, APES):

$$E_{\text{APES}}(\mathbf{R}) = \varepsilon_s(\mathbf{R}) + \hat{V}_{\text{nn}}(\mathbf{R}), \quad (14)$$

čia  $\varepsilon_s(\mathbf{R})$  yra elektroninės būsenos  $\psi_s(\mathbf{r}; \mathbf{R})$  energija [formulė (9)], o  $\hat{V}_{\text{nn}}(\mathbf{R})$  yra jon-joninės sąveikos narys [formulė (2)]. Naudojantis šia energijos išraiška ir Hellmann-Feynman teorema [67], joną  $\alpha$  veikianti jėga yra

$$\mathbf{F}_\alpha(\mathbf{R}) = - \int \rho(\bar{\mathbf{r}}) \frac{\partial \hat{V}_{\text{en}}(\bar{\mathbf{r}}; \mathbf{R})}{\partial \mathbf{R}_\alpha} d^3\bar{\mathbf{r}} - \frac{\partial \hat{V}_{\text{nn}}(\mathbf{R})}{\partial \mathbf{R}_\alpha}, \quad (15)$$

čia

$$\frac{\partial}{\partial \mathbf{a}} \equiv \begin{bmatrix} \frac{\partial}{\partial a_1} \\ \frac{\partial}{\partial a_2} \\ \vdots \\ \frac{\partial}{\partial a_n} \end{bmatrix}.$$

Taigi, jonus veikiančios jėgos priklauso nuo elektronų tankio  $\rho(\bar{\mathbf{r}})$ , kuris yra tiesiogiai prieinamas tankio funkcionalo teorijoje.

Išskleidus APES pusiausvyros padėties  $\mathbf{R}^{(0)}$  aplinkoje (naudojant nuokrypius  $\mathbf{u}_\alpha = \mathbf{R}_\alpha - \mathbf{R}_\alpha^{(0)}$ ) ir pritaikius harmoninę aproksimaciją, gaunama ši potencinės energijos paviršiaus išraiška:

$$E_{\text{APES}}(\mathbf{R}) \approx \frac{1}{2} \sum_{\alpha, \beta}^{N_n} \sum_{i, j \in \{x, y, z\}} \Phi_{\alpha_i \beta_j} u_{\alpha_i} u_{\beta_j}, \quad (16)$$

čia  $\Phi_{\alpha_i\beta_j}$  yra jėgos konstantų matricos (hesiano)  $\Phi$  elementas:

$$\Phi_{\alpha_i\beta_j} \equiv \left( \frac{\partial^2 E_{\text{APES}}}{\partial \mathbf{R}_{\alpha_i} \partial \mathbf{R}_{\beta_j}} \right)_{\mathbf{R}^{(0)}}, \quad (17)$$

$$\Phi_{\alpha\beta} \equiv \begin{pmatrix} \Phi_{\alpha_x\beta_x} & \Phi_{\alpha_x\beta_y} & \Phi_{\alpha_x\beta_z} \\ \Phi_{\alpha_y\beta_x} & \Phi_{\alpha_y\beta_y} & \Phi_{\alpha_y\beta_z} \\ \Phi_{\alpha_z\beta_x} & \Phi_{\alpha_z\beta_y} & \Phi_{\alpha_z\beta_z} \end{pmatrix}. \quad (18)$$

Taigi, harmoninės aproksimacijos kontekste joninę posistemę [formulė (8)] aprašantis hamiltonianas yra

$$\hat{H}_n(\mathbf{R}) = \hat{T}_n + \frac{1}{2} \sum_{\alpha,\beta}^{N_n} \mathbf{u}_\alpha^\top \Phi_{\alpha\beta} \mathbf{u}_\beta, \quad (19)$$

čia

$$\mathbf{u}_\alpha^\top = [u_{\alpha_x} \quad u_{\alpha_y} \quad u_{\alpha_z}].$$

Kaip matyti, hamiltonianas (19) apibūdina *sukabintų* harmoninių osciliatorių sistemą. Galima parodyti [61, 68, 69], kad egzistuoja apibendrintųjų koordinačių bazė  $\mathbf{Q} \equiv \{Q_k\}$ , kurioje kristalinės sistemos harmoninis hamiltonianas įgyja diagonalią formą:

$$\hat{H}_n = \frac{1}{2} \sum_{\mathbf{q}}^{N_{\text{cells}}} \sum_{\lambda}^{3\sigma} [\dot{Q}_k^2(t) + \omega_k^2 Q_k^2(t)]. \quad (20)$$

Čia  $Q_k$  žymi (mase pasvertas) apibendrintąsias koordinates,  $\omega_k$  yra svyravimo  $k \equiv (\mathbf{q}, \lambda)$  kampinis dažnis,  $\mathbf{q}$  yra svyravimo banginis vektorius,  $\lambda$  indeksuoja svyravimų spektro šakas,  $N_{\text{cells}}$  yra kristale esančių primityvių narvelių skaičius, o  $\sigma$  žymi kiekviename primityviame narvelyje esančių jonų skaičių.

Kiekvienas iš  $3\sigma N_{\text{cells}} = 3N_n$  „naujųjų“ laisvės laipsnių  $Q_k$  apibrėžia *nepriklausomą* harmoninį osciliatorių, dėl ko bendrą joninės posistemės banginę funkciją  $\chi$  galima išreikšti kaip sandaugą pavienių virpesinių banginių funkcijų:

$$\chi(\mathbf{Q}) = \prod_k^{3N_n} \chi_k(Q_k), \quad m_k \in \{0, 1, 2, \dots\}, \quad (21)$$

čia  $m_k$  yra virpesinis kvantinis skaičius, žymintis  $k$ -tojo harmoninio osciliatoriaus sužadavimo lygmenį ir jo energiją:

$$\epsilon_k = \omega_k \left( m_k + \frac{1}{2} \right), \quad m_k \in \{0, 1, 2, \dots\}. \quad (22)$$

Energijos  $\omega_k$  kvantas, susijęs su  $k$ -tuoju harmoniniu osciliatoriumi, yra vadinamas *fononu* – kristalo gardelės virpesinės energijos kvantu. Kai osciliatorius, aprašomas  $Q_k$  apibendrintąja koordinate, yra  $m_k$ -ame sužadintame lygmenyje, tai sakoma, kad sistemoje yra  $m_k$  virpesinės modos  $k$  fononų.

Į idealų, periodiškai atsikartojantį kristalą įterpus taškinį defektą yra sutrikdoma translacinė gardelės simetrija. Nors toks defektas yra sąlyginai lokali kristalo perturbacija, jis gali smarkiai pakeisti visos sistemos virpesines savybes. Bendru atveju yra išskiriamos trys virpesinių modų kategorijos [70, 71]:

- Erdvėje išplitusios modos (angl. *bulk-like modes*), primenančios idealaus kristalo virpesius.
- Lokalizotos modos (angl. *localized modes*) – virpesiai, kurių amplitudės smarkiai lokalizuotos defekto aplinkoje.
- Rezonansinės modos (angl. *resonant modes*) – hibridinės modos, atsirandančios dėl sąveikos tarp idealaus kristalo virpesių ir defekto sukeltų gardelės sutrikdymų.

Kiekybiniam virpesinės modos  $k$  lokalizacijos įvertinimui naudojama atvirkštinio dalyvavimo santykio (angl. *inverse participation ratio*, IPR) sąvoka [70, 71]:

$$\text{IPR}_k = \frac{\left[ \sum_{\alpha}^{N_n} w_{\alpha}(k) \right]^2}{\sum_{\alpha}^{N_n} [w_{\alpha}(k)]^2}, \quad w_{\alpha}(k) = M_{\alpha} |e_{\alpha}(k)|^2, \quad (23)$$

čia  $M_{\alpha}$  yra jono  $\alpha$  masė, o  $e_{\alpha}(k)$  yra  $k$ -tosios modos poliarizacijos vektorius, aprašantis santykinį jono  $\alpha$  judėjimą primityviame kristalo narvelyje.

$\text{IPR}_k$  vertė nusako efektyvų skaičių jonų, dalyvaujančių  $k$ -tajame virpėjime. Jei iš esmės juda tik vienas jonas,  $\text{IPR}_k = 1$ . Jei visi  $N_n$  jonai virpa panašiomis amplitudėmis,  $\text{IPR}_k = N_n$ . Kuomet efektyviai virpa  $P < N_n$  jonų,  $\text{IPR}_k \approx P$ .

Atliekant defektinių sistemų skaičiavimus su tankio funkcionalo teorijos įrankiais, yra naudojamas anksčiau minėtas supergardelės metodas. Tai reiškia, kad IPR reikšmės priklauso nuo jonų skaičiaus sistemoje. Šiek tiek patogesnė ir nuo sistemos dydžio nepriklausanti bedimensė metrika yra lokalizacijos santykis (angl. *localization ratio*) [71]:

$$\beta_k = \frac{N_n}{\text{IPR}_k}. \quad (24)$$

Kuo didesnis  $\beta_k$ , tuo labiau erdvėje yra lokalizuota virpesinė moda  $k$ .

## 1.5. Elektroninis išsigimimas ir vibroninės sąveikos

Elektroninis išsigimimas yra dažnas taškinių defektų, esančių aukštos simetrijos aplinkose, reiškinys. Sąveika tarp išsigimusių elektroninių būsenų ir sistemos simetriją mažinančių virpesinių modų neleidžia taikyti vieno adiabatinio potencinės energijos paviršiaus vaizdinio, nes toks jonų judėjimas sumaišo elektroninio multipletto komponentes ir iš esmės pakeičia potencinės energijos paviršiaus struktūrą. Šis neadiabatinis reiškinys žinomas kaip Jahn-Teller (JT) efektas [72–75], kuriam būdinga neatsiejama elektroninių būsenų ir joninių laisvės laipsnių sąveika. Dinaminio JT (DJT) efekto režime [74, 76], esant silpnai arba vidutinei elektronų ir fononų sąveikai, sistema vidutiniškai išlaiko aukštą simetriją, tačiau jos vibroninės būsenos iš esmės skiriasi nuo tų, kurios gaunamos taikant adiabatinį modelį.

Kanoninis JT sistemos pavyzdys yra  $E \otimes e$  uždavinys, kuomet dvigubai išsigimusi elektroninė būsena  $|E\rangle$  sąveikauja su dvigubai išsigimusia  $e$  simetrijos virpesine moda [74]. Esant stipriai sąveikai, dažnai pakanka vienos efektyvios modos modelio [78, 79], tačiau silpnos ar vidutinės sąveikos atveju būtina taikyti kelių modų aprašymą [39, 80, 81].

Kaip buvo pristatyta anksčiau [formulė (7)], nesant elektroninio išsigimimo, bendrą būsenos vibroninę banginę funkciją galima išskaidyti į elektroninės ir virpesinės komponentių sandaugą:

$$\Psi_{pr}(\mathbf{r}, \mathbf{R}) = \chi_p^a(\mathbf{Q}_a) \chi_r^e(\mathbf{Q}_e) \psi_A(\mathbf{r}; \mathbf{R}^{(0)}), \quad (25)$$

čia  $\psi_A(\mathbf{r}; \mathbf{R}^{(0)})$  yra elektroninė banginė funkcija [formulė (6)], o  $\chi_p^a(\mathbf{Q}_a)$  ir  $\chi_r^e(\mathbf{Q}_e)$  žymi virpesines bangines funkcijas, susijusias su simetriją išlaikančiomis ( $a$ ) ir simetriją griaunančiomis ( $e$ ) apibendrintosiomis koordinatėmis  $\mathbf{Q}_a$  ir  $\mathbf{Q}_e$ . Išsigimusio elektroninio dubletto  $E = \{|E_x\rangle, |E_y\rangle\}$  atveju, bendra vibroninė banginė funkcija atrodo taip [75]:

$$\Psi_{st}(\mathbf{r}, \mathbf{R}) = \chi_s^a(\mathbf{Q}_a) \left[ \chi_t^{e_x}(\mathbf{Q}_e) \psi_{E_x}(\mathbf{r}; \mathbf{R}^{(0)}) + \chi_t^{e_y}(\mathbf{Q}_e) \psi_{E_y}(\mathbf{r}; \mathbf{R}^{(0)}) \right], \quad (26)$$

čia  $\chi_t^{e\gamma}(\mathbf{Q}_e)$  ( $\gamma \in \{x, y\}$ ) yra virpesiniai koeficientai, gaunami išsprendus JT uždavinį.

Tiesinį vibroninį apibendrintos sistemos  $E \otimes (e \oplus e \oplus \dots)$  hamiltonianą galima užrašyti kaip [75]

$$\hat{H} = \hat{H}_0 + \hat{H}_{JT}, \quad (27)$$

čia nulinės eilės narys

$$\begin{aligned}\hat{H}_0 &= \frac{1}{2} \sum_k^{N_e} \sum_{\gamma \in \{x,y\}} (P_{k\gamma}^2 + \omega_k^2 Q_{k\gamma}^2) \hat{I} \\ &= \sum_k^{N_e} \sum_{\gamma \in \{x,y\}} \omega_k \left( \hat{a}_{k\gamma}^\dagger \hat{a}_{k\gamma} + \frac{1}{2} \right) \hat{I}\end{aligned}\quad (28)$$

aprašo harmoninius virpesius [formulė (20)]. Čia  $P_{k\gamma} = -i \partial / \partial Q_{k\gamma}$  yra apibendrintosios koordinatės  $Q_{k\gamma}$  jungtinis judesio kiekis,  $\hat{I}$  yra dvimatis vienetinis operatorius, veikiantis orbitiniame poerdvyje, o indeksas  $k$  žymi visas  $N_e$  išsigimusių  $e$  simetrijos virpesių poras. Fononų kūrimo ir naikimo operatoriai apibrėžiami taip:

$$\hat{a}_{k\gamma}^\dagger = \sqrt{\frac{\omega_k}{2}} \left( Q_{k\gamma} - i \frac{P_{k\gamma}}{\omega_k} \right), \quad \hat{a}_{k\gamma} = \sqrt{\frac{\omega_k}{2}} \left( Q_{k\gamma} + i \frac{P_{k\gamma}}{\omega_k} \right). \quad (29)$$

Tiesinis JT sąveikos hamiltonianas,  $\hat{H}_{JT}$ , „sumaišo“ išsigimusias būsenas  $|E_x\rangle$  ir  $|E_y\rangle$  per jonų judėjimą [39, 75, 77, 79]:

$$\begin{aligned}\hat{H}_{JT} &= \sum_k^{N_e} \sum_{\gamma \in \{x,y\}} V_k Q_{k\gamma} \hat{C}_{E_\gamma} \\ &= \sum_k^{N_e} \sum_{\gamma \in \{x,y\}} \frac{V_k}{\sqrt{2\omega_k}} \left( \hat{a}_{k\gamma}^\dagger + \hat{a}_{k\gamma} \right) \hat{C}_{E_\gamma},\end{aligned}\quad (30)$$

čia  $V_k$  yra *vibroninės sąveikos koeficientai*, o  $\hat{C}_{E_\gamma}$  žymi Clebsch-Gordan koeficientų matricas:

$$\hat{C}_{E_x} = \frac{1}{\sqrt{2}} \begin{pmatrix} 0 & 1 \\ 1 & 0 \end{pmatrix}, \quad \hat{C}_{E_y} = \frac{1}{\sqrt{2}} \begin{pmatrix} 1 & 0 \\ 0 & -1 \end{pmatrix}. \quad (31)$$

Tiesioginis bendrojo hamiltoniano (27) diagonalizavimas tampa skaitiškai brangus didėjant  $e$  simetrijos virpesinių modų porų skaičiui. Vis dėlto,  $\hat{H}_{JT}$  pasižymi tam tikromis simetrijos savybėmis, leidžiančiomis reikšmingai supaprastinti skaičiavimus [39, 74, 79].

Įvedus posūkių generatorius orbitiniame ir virpesiniame poerdviuose,

$$\hat{J}_{el} = \frac{1}{2} \hat{\sigma}_y = \frac{i}{2} \begin{pmatrix} 0 & -1 \\ 1 & 0 \end{pmatrix}, \quad \hat{J}_{ph} = \sum_k^{N_e} \hat{L}_{z,k} \hat{I}, \quad (32)$$

čia

$$\hat{L}_{z,k} = Q_{kx} P_{ky} - Q_{ky} P_{kx} = -i \left( \hat{a}_{kx}^\dagger \hat{a}_{ky} - \hat{a}_{ky}^\dagger \hat{a}_{kx} \right) \quad (33)$$

yra virpesinio dubleto  $\{Q_{kx}, Q_{ky}\}$  judesio kiekio momento operatorius, galima pastebėti, kad  $\hat{H}_0$  komutuoja su  $\hat{J}_{\text{el}}$  ir  $\hat{J}_{\text{ph}}$ , o  $\hat{H}_{\text{JT}}$  komutuoja su jų suma [74]

$$\hat{J} = \hat{J}_{\text{el}} + \hat{J}_{\text{ph}}. \quad (34)$$

Toliau ieškomos būsenos, kurios būtų tuo pačiu metu  $\hat{H}_0$ ,  $\hat{J}_{\text{el}}$  ir  $\hat{J}_{\text{ph}}$  tikrinės būsenos. Operatoriaus  $\hat{J}_{\text{el}}$ , taigi ir  $\hat{H}_0$ , tikrinės būsenos yra

$$|E_{\pm}\rangle = \frac{1}{\sqrt{2}}(|E_x\rangle \pm i|E_y\rangle), \quad (35)$$

su tikrinėmis vertėmis  $J_{\text{el}} = j_{\text{el}} = \pm\frac{1}{2}$ .

Operatoriaus  $\hat{J}_{\text{ph}}$  tikrinės būsenos yra chiraliniai fononai, antrinio kvantavimo formalizme aprašomi per operatorius [39]

$$\hat{a}_{k\pm} = \frac{1}{\sqrt{2}}(\hat{a}_{kx} \mp i\hat{a}_{ky}), \quad \hat{n}_{k\pm} = \hat{a}_{k\pm}^\dagger \hat{a}_{k\pm}, \quad (36)$$

kuriais naudojantis turime

$$\hat{H}_0 = \sum_k^{N_e} \omega_k (\hat{n}_{k+} + \hat{n}_{k-} + 1) \hat{I}, \quad \hat{J}_{\text{ph}} = \sum_k^{N_e} (\hat{n}_{k+} - \hat{n}_{k-}) \hat{I}. \quad (37)$$

Taigi, operatorių  $\hat{H}_0$ ,  $\hat{J}_{\text{el}}$  ir  $\hat{J}_{\text{ph}}$  tikrines funkcijas galima žymėti kaip  $|n_1 l_1 \dots n_{N_e} l_{N_e}; E_+\rangle$  ir  $|n_1 l_1 \dots n_{N_e} l_{N_e}; E_-\rangle$ , kur:

- $n_k = n_{k+} + n_{k-}$  yra  $k$ -tojo fonono skaičius,
- $l_k = n_{k+} - n_{k-}$  yra  $k$ -tojo fonono judesio kiekio momento kvantinis skaičius.

Kadangi šios būsenos kartu yra ir  $\hat{J} = \hat{J}_{\text{el}} + \hat{J}_{\text{ph}}$  tikrinės būsenos, kiekvieną jų galima pažymėti kvantiniu skaičiumi

$$j = j_{\text{el}} + \sum_k^{N_e} l_k. \quad (38)$$

Esminis šio atvaizdavimo privalumas yra tas, kad  $\hat{H}_{\text{JT}}$  matrica gali būti konstruojama ir diagonalizuojama kiekvienam  $j$  atskirai, taip suskaidant pirminę didžiąją erdvę į kelis, daug mažesnius, tarpusavyje nesimaišančius poerdvius.

Galima parodyti, kad naujai įvestoje tikrinių funkcijų bazėje nulinės eilės hamiltoniano  $\hat{H}_0$  matriciniai elementai atrodo taip [39]:

$$\begin{aligned} & \langle n_1 l_1, \dots, n_{N_e} l_{N_e}; E_{\pm} | \hat{H}_0 | n_1 l_1, \dots, n_{N_e} l_{N_e}; E_{\pm} \rangle \\ &= \sum_k^{N_e} \omega_k (n_k + 1), \end{aligned} \quad (39)$$

o tiesinio JT sąveikos hamiltoniano  $\hat{H}_{\text{JT}}$  matriciniai elementai atrodo taip [39]:

$$\begin{aligned} & \langle n'_1 l'_1, \dots, n'_{N_e} l'_{N_e}; E_- | \hat{H}_{\text{JT}} | n'_1 l'_1, \dots, n'_{N_e} l'_{N_e}; E_+ \rangle \\ &= \sqrt{2} \sum_k^{N_e} K_k \omega_k \delta_{l'_k, l_k + 1} \left[ \prod_{j \neq k} \delta_{n'_j, n_j} \delta_{l'_j, l_j} \right] \\ & \times \left[ \sqrt{\frac{n_k - l_k}{2}} \delta_{n'_k, n_k - 1} + \sqrt{\frac{n_k + l_k + 2}{2}} \delta_{n'_k, n_k + 1} \right], \end{aligned} \quad (40)$$

čia

$$K_k = \frac{V_k}{\sqrt{2\omega_k^3}} \quad (41)$$

yra  $k$ -tosios išsigimusių  $e$  simetrijos fononų poros *bedimensė vibroninės sąveikos konstanta*. Šias konstantas galima suskaičiuoti tankio funkcionalo teorijos kontekste naudojantis tokia priklausomybe [39, 75]:

$$K_k^2 = \frac{\omega_k (\Delta Q_k)^2}{2}, \quad (42)$$

čia  $\Delta Q_{k\gamma}$  žymi  $k$ -tosios fononų poros  $\gamma \in \{x, y\}$  komponentės projekciją į geometrijų skirtumą tarp išsigimusių multipletų ansamblių modeliuojančios (aukštos simetrijos) ir pilnai relaksuotos (žemos simetrijos) sistemų.

Kadangi realiuose kietakūnių sistemų taškiniuose defektuose dažniausiai pasireiškia didelis skaičius  $e$  simetrijos virpesinių modų porų, tiesioginis visų jų įtraukimas į skaičiavimus tampa nepraktiškas. Todėl taikoma kelių efektyvių modų aproksimacija [39], leidžianti žymiai sumažinti skaičiavimų sudėtingumą. Šiame metode JT sąveikos spektrinis tankis

$$K^2(\omega) = \sum_k^{N_e} K_k^2 \delta(\omega - \omega_k), \quad (43)$$

sukonstruotas iš baigtinio skaičiaus ( $N_e$ )  $e$  simetrijos fononų porų, yra aproksimuojamas naudojant gerokai mažesni skaičių efektyvių modų porų  $N_{\text{eff}} \ll N_e$ .

Apibendrinant,  $E \otimes (e \oplus e \oplus \dots)$  JT uždavinio sprendimas susideda iš kelių pagrindinių etapų:

1. Pirmiausia apskaičiuojamos nulinės eilės hamiltonianą  $\hat{H}_0$  [formulė (28)] atitinkančios harmoninės virpesinės būsenos. Praktiniuose tankio funkcionalo teorijos skaičiavimuose neadiabatinės sąveikos šiame žingsnyje yra nuslopinamos modeliuojant išsigimusių elektroninių multipletų būsenų ansamblių [39].

2. Naudojantis gautąja virpesinių būsenų baze ir apribojant maksimalų fononų sužadinių skaičių iki  $N_{\text{ex}}$ , apskaičiuojami tiesinės JT sąveikos hamiltoniano  $\hat{H}_{\text{JT}}$  [formulė (28)] matriciniai elementai.
3. Galiausiai diagonalizuojamas pilnas vibroninis hamiltonianas  $\hat{H}$  [formulė (27)] ir gaunamas vibroninių būsenų spektras.

## 1.6. Optiniai spektrai

Optiniai šuoliai taškiniuose defektuose yra susiję su elektroniniais sužadimais arba relaksavimais, kuriuos sukelia fotonų absorbcija arba emisija, ir su tuo susijusiu joninių koordinačių persitvarkymu. Tokie perėjimai vyksta tarp skirtingų potencinės energijos paviršių ir todėl yra neatskiriamai susiję su kristalinės gardelės virpesiais. Gautą optinį spektrą sudaro befononinė linija (angl. *zero-phonon line*, ZPL), atitinkanti grynai elektroninį perėjimą, ir fononų pajuostė (angl. *phonon sideband*, PSB), atsirandanti dėl fononų dalyvavimo optinio šuolio metu. Optinio spektro virpesinė struktūra suteikia tiesioginės informacijos apie elektronų ir fononų sąveikos pobūdį ir stiprumą.

Remiantis adiabatine aproksimacija ir esant nulinei temperatūrai, normalizuota liuminescencijos arba absorbcijos linijos forma yra aprašoma išraiška [39, 71]

$$L(\omega) = C\omega^\kappa A(\omega), \quad (44)$$

čia  $C$  yra normavimo konstanta, parametras  $\kappa = 3$  atitinka liuminescencijos atvejį, o  $\kappa = 1$  – absorbcijos. Funkcija  $A(\omega)$  žymi optinę spektrinę funkciją, kurioje sutelkta visa informacija apie virpesines sanklotas tarp pradinės ir galutinės elektroninių būsenų.

Perėjimams tarp neišsigimusių elektroninių būsenų optinė spektrinė funkcija išreiškiama taip [71]:

$$A(\omega) = \sum_m |\langle \chi_{0,i} | \chi_{m,f} \rangle|^2 \delta(E_{\text{ZPL}} \mp [\epsilon_{m,f} - \epsilon_{0,f}] - \omega), \quad (45)$$

čia  $E_{\text{ZPL}}$  yra nagrinėjamo optinio šuolio befononinės linijos energija, o  $|\chi_{0,i}\rangle$  ir  $|\chi_{m,f}\rangle$  atitinkamai žymi pradinės ir galutinės elektroninių būsenų virpesines tikrines funkcijas. Dydis  $\epsilon_{m,f}$  nusako galutinės elektroninės būsenos  $m$ -tojo virpesinio lygmens energiją. Minuso ir pliuso ženklai atitinkamai žymi liuminescencijos ir absorbcijos procesus.

Tiesiogiai apskaičiuoti formulėje (45) pateiktus virpesinius sanklotos integralus realioms sistemoms, turinčioms daug virpesinių modų, praktiškai neįmanoma. Šiam uždaviniui spręsti taikoma tapačiųjų modų aproksimacija (angl. *equal-mode approximation*) [39, 83], kuria remiantis teigiama, kad abiejų elektroninių būsenų virpesinės modos sutampa. Pagal šią aproksimaciją optinė spektrinė funkcija gali būti apskaičiuojama

taikant generuojančios funkcijos metodą [84, 85]:

$$A(\omega) = \frac{1}{2\pi} \int_{-\infty}^{\infty} G(t) \exp[-i(E_{\text{ZPL}} - \omega)t] \exp(-\gamma|t|) dt, \quad (46)$$

čia  $\gamma$  yra fenomenologinis ZPL išplitimo parametras. Šiuo atveju generuojanti funkcija turi formą [82]

$$G(t) = \exp \left[ - \sum_k^{3N_n} S_k (1 - \exp(\pm i\omega_k t)) \right], \quad (47)$$

čia pliuso (minuso) ženklas atitinka liuminescencijos (absorbcijos) procesą.

Dydis  $S_k$  žymi dalinį Huang-Rhys (HR) faktorių, apibrėžtą  $k$ -tajai virpesinei modai su kampiniu dažniu  $\omega_k$ . Jis nusako vidutinį  $k$ -tojo fonono, dalyvaujančio optinio šuolio metu, skaičių [86]:

$$S_k = \frac{\omega_k (\Delta Q_k)^2}{2}. \quad (48)$$

Čia  $\Delta Q_k$  yra  $k$ -tojo fonono projekcija į masę pasvertą poslinkį tarp pradinės ir galutinės elektroninių būsenų pusiausvyrųjų geometrijų.

Bendras HR faktorius

$$S_{\text{tot}} = \sum_k^{3N_n} S_k \quad (49)$$

kiekybiškai apibūdina bendrą elektron-fononinės sąveikos stiprumą ir tiesiogiai nusako santykinį ZPL intensyvumą optiniame spektre.

Skaičiavimuose virpesinė sąveika aprašoma pasitelkiant elektron-fononinės sąveikos spektrinę funkciją [71]:

$$S(\omega) \equiv \sum_k^{3N_n} S_k \delta(\omega_k - \omega). \quad (50)$$

Praktikoje, turint didelį, bet baigtinį virpesinių modų skaičių, Dirac  $\delta$ -funkcijos pakeičiamos baigtinio pločio išplitusiomis funkcijomis, kurių tipas parenkamas pagal atitinkamų modų lokalizacijos savybes.

Kuomet galutinė elektroninė būseną yra išsigimusi, pavyzdžiui  $A \rightarrow E$  tipo optiniams šuoliams, prie simetriją išlaikančių  $a$ -tipo virpesinių modų prisideda ir simetriją griauančios  $e$ -tipo virpesinės modos. Tokiu atveju optinė spektrinė funkcija įgyja konvoliucinę formą [39]:

$$A(\omega) = \int A_a(\omega - \omega') A_e(\omega') d\omega', \quad (51)$$

čia  $A_a(\omega)$  žymi standartinę adiabatinę  $a$  simetrijos fononų dedamąją, o  $A_e(\omega)$  aprašo simetriją griauančių  $e$  fononų įtaką optiniam šuoliui. Pastaroji kontribucija išreiškiama taip [82]:

$$A_e(\omega) = \sum_m \left[ \left| \langle \chi_{0,i}^e | \chi_{m,f}^{e_x} \rangle \right|^2 + \left| \langle \chi_{0,i}^e | \chi_{m,f}^{e_y} \rangle \right|^2 \right] \times \delta(\mp[\epsilon_{m,f}^e - \epsilon_{0,f}^e] - \omega), \quad (52)$$

čia  $|\chi_{m,f}^{e_x}\rangle$  ir  $|\chi_{m,f}^{e_y}\rangle$  yra virpesinės tikrinės būsenos, susijusios su išsigimusio elektroninio dublto komponentėmis  $\{|E_x\rangle, |E_y\rangle\}$ . Minuso ir pliuso ženklai atitinkamai nusako liuminescencijos ir absorbcijos procesus.

## 1.7. Įterpimo metodologija

Periodinėmis kraštinėmis sąlygomis apibrėžtose supergardenėse apskaičiuotoms taškinių defektų virpesinėms ir elektron-fononinės sąveikos savybėms didelę įtaką daro įvairūs baigtinio dydžio efektai (angl. *finite-size effects*), tokie kaip dirbtinė defekto atvaizdų tarpusavio sąveika, ribotas ilgo bangos ilgio (akustinių) fononų įskaitymas ir netolydus virpesinis spektras. Siekiant sumažinti šių efektų įtaką, taikoma jėgos konstantų įterpimo metodologija (angl. *embedding methodology*) [39, 71], kurios metu, remiantis tarpatominių jėgų trumpaveikiškumo savybe, iš tiesiogiai prieinamų skaičiavimų duomenų sukonstruojamas didelis efektyvus jėgos konstantų hesianas, kurį diagonalizuojant gaunama gerokai didesnės sistemos virpesinė struktūra.

## 1.8. Skaičiavimų detalės

Visi skaičiavimai buvo atlikti naudojant tankio funkcionalo teoriją su programiniu paketu VASP (**V**ienna **A**b **i**nicio **S**imulation **P**ackage) [55, 56]. Visuose defektų skaičiavimuose buvo įskaityta sukinių poliarizacija, o sąveika tarp valentinių elektronų ir atomų branduolių aprašyta taikant PAW (angl. *projector-augmented wave*) formalizmą [65]. Virpesinės savybės buvo apskaičiuotos naudojant baigtinių poslinkių (angl. *finite-displacement*) metodą, realizuotą phonopy programiniame pakeite [87, 88].

Darbe buvo naudojami keli pakaitos ir koreliacijos funkcionalai, įskaitant PBE [31], SCAN [28], rSCAN [29], r<sup>2</sup>SCAN [30] ir HSE06 [32]. Sužadintos elektroninės būsenos buvo modeliuojamos taikant  $\Delta$  suderintinio lauko (angl.  $\Delta$  *self-consistent field*,  $\Delta$ SCF) schemą [46, 89, 90].

Virpesinės struktūros buvo apskaičiuotos naudojant anksčiau trumpai aptartą įterpimo metodologiją [39, 71]. Liuminescencijos atveju buvo naudojami pagrindinės būsenos fononai, o absorbcijos spektrai buvo skaičiuojami remiantis sužadintos būsenos virpesinėmis charakteristikomis.

Visi teoriniai spektrai atvaizduoti eksperimentinės befoninės linijos (ZPL) atžvilgiu, o eksperimentiniai duomenys buvo normuojami pagal poreikį.

## 2. Skirtingų tankio funkcionalų taikymas: $NV^-$ centras deimante

Deimantas yra plačiajuostis puslaidininkis, pasižymintis optiniu aktyvumu dėl jame esančių taškinių defektų. Iš jų labiausiai ištirtas yra neigiamai įkrautas azoto-vakansijos ( $NV^-$ ) centras [3]. Jis sudarytas iš pakaitinio azoto atomo ir gretimos anglies vakansijos komplekso, pasižymi  $C_{3v}$  taškinės grupės simetrija [94, 95], orientuota išilgai  $\langle 111 \rangle$  kristalografinės krypties (žr. 2.1a pav.), ir yra paramagnetinis defektas [93]. Technologiniu požiūriu viena svarbiausių šio centro savybių yra milisekundžių eilės sukinio koherencijos trukmės esant kambario temperatūrai [4–6].

Ryškesniausia  $NV^-$  centro optinė savybė yra 1.945 eV (637 nm) befononinė linija, susijusi su spinduliniu šuoliu tarp sužadintos  $|^3E\rangle$  ir pagrindinės  $|^3A_2\rangle$  elektroninių būsenų [93, 96–99], kaip parodyta energijos lygmenų diagramoje 2.1b pav. Ši šuolių lydi plati fononų pajuostė, atspindinti vidutinio stiprumo elektron-fononinę sąveiką liuminescencijos proceso metu. Dėl sąlyginai ilgų sukinio koherencijos trukmių ir nuo sukinio priklausančios fluorescencijos  $NV^-$  centras yra viena iš svarbiausių taškinių defektų sistemų kuriant kvantinius jutiklius.

Šiame skyriuje SCAN šeimos tankio funkcionalai yra lyginami su PBE ir HSE06 funkcionalais, nagrinėjant tiek gryno deimanto, tiek  $NV^-$  centro struktūrines, virpesines ir optines savybes. Pagrindinis tikslas – įvertinti šių funkcionalų patikimumą skaičiuojant virpesines ir elektron-fononinės sąveikos charakteristikas, kurios yra esminės modeliuojant defektų optines savybes.

### 2.1. Rezultatai

Naudojant PBE, SCAN, rSCAN, r<sup>2</sup>SCAN ir HSE06 funkcionalus iš pradžių buvo apskaičiuota deimanto gardelės konstanta  $a$  ir draustinės juostos tarpas  $E_g$ . Skaičiavimų rezultatai pateikti S1 lentelėje, iš kurių matyti, kad gardelės konstantos vertės svyruoja nuo 3.546 Å (HSE06) iki 3.572 Å (PBE), o draustinės juostos tarpo vertės kinta nuo 4.12 eV (PBE) iki 5.34 eV (HSE06). Abiejų parametru atvejais SCAN šeimos funkcionalai generuoja tarpines vertes.

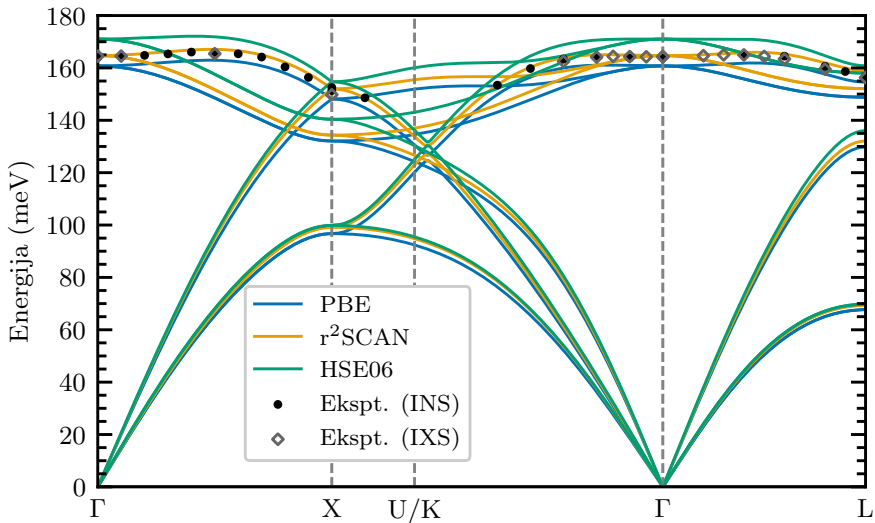
Siekiant įvertinti skirtingų funkcionalų gebėjimą aprašyti gardelės dinamiką, toliau buvo apskaičiuotos deimanto fononų dispersijos kreivės, pateiktos S1 pav. ir S2 lentelėje. Rezultatai rodo, kad naudojant SCAN šeimos funkcionalus gaunamos fononų dažnių vertės, kurios yra tarp PBE ir HSE06 rezultatų bei geriausiai atitinka eksperimentinius duomenis.

$NV^-$  centro  $|^3A_2\rangle \leftrightarrow |^3E\rangle$  optinio šuolio ZPL energija  $E_{ZPL}$  buvo apskaičiuota naudojant visus penkis funkcionalus, kurių rezultatai pateikti

**S1 lentelė.** Suskaičiuotos deimanto gardelės konstantos  $a$  (Å) ir draustinės juostos tarpai  $E_g$  (eV) naudojant skirtingus tankio funkcionalus. Skliaustuose nurodytos vertės rodo santykinius nuokrypius nuo eksperimentinių verčių.

	$a$	$E_g$
PBE	3.572 (+0.48 %)	4.12 (−25 %)
SCAN	3.554 (−0.03 %)	4.56 (−17 %)
rSCAN	3.556 (+0.03 %)	4.38 (−20 %)
r <sup>2</sup> SCAN	3.561 (+0.17 %)	4.33 (−21 %)
HSE06	3.546 (−0.25 %)	5.34 (−3 %)
Ekspt.	3.555 <sup>a</sup>	5.48 <sup>b</sup>

<sup>a</sup>[104]    <sup>b</sup>[103]



**S1 pav.** Suskaičiuotos deimanto fononų dispersijos kreivės naudojant PBE, r<sup>2</sup>SCAN ir HSE06 funkcionalus. Eksperimentinės kambario temperatūros vertės paimtos iš šaltinio [105].

**S2 lentelė.** Suskaičiuoti deimanto išilginių optinių fononų dažniai  $\omega$  (meV) aukštos simetrijos atvirkštinės gardelės taškuose naudojant skirtingus tankio funkcionalus. Lentelėje nurodyti tik aukščiausių išilginių optinių fononų šakų dažniai. Skliaustuose nurodytos vertės rodo santykinius nuokrypius nuo eksperimentinių verčių, paimtų iš šaltinio [105].

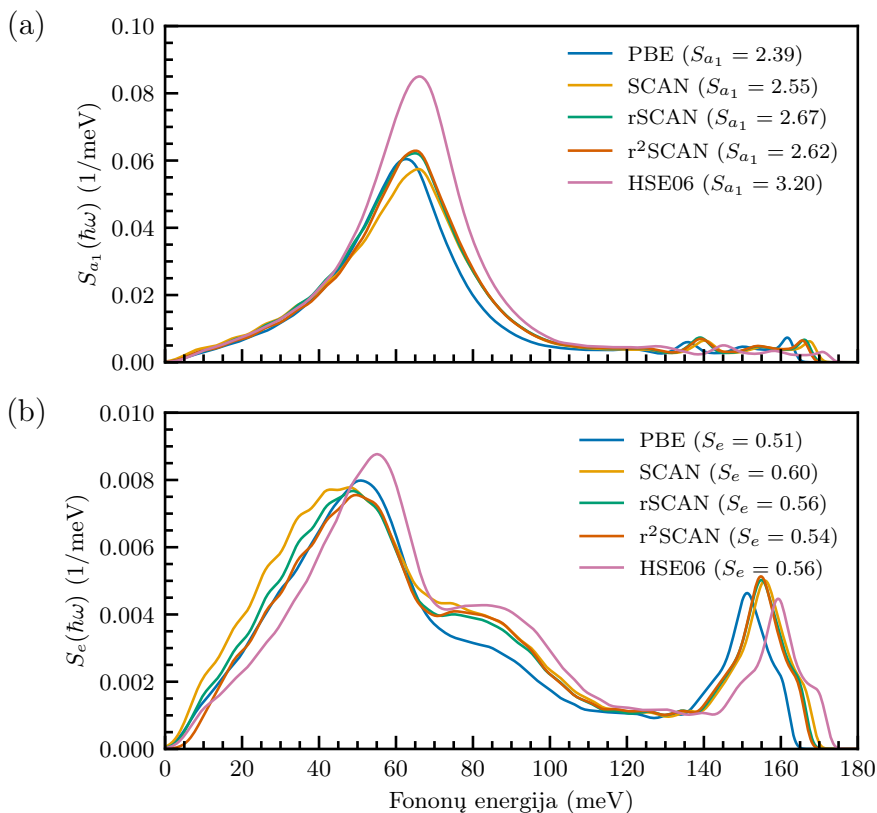
	$\omega(\Gamma)$	$\omega(X)$	$\omega(L)$
PBE	160.7 (−2.01 %) (−2.31 %)	148.1 (−2.12 %) (−1.13 %)	154.6 (−1.53 %) (−1.09 %)
SCAN	167.0 (+1.83 %) (+1.52 %)	153.2 (+1.26 %) (+2.27 %)	160.4 (+2.17 %) (+2.62 %)
rSCAN	165.0 (+0.61 %) (+0.30 %)	152.5 (+0.79 %) (+1.80 %)	159.6 (+1.66 %) (+2.11 %)
r <sup>2</sup> SCAN	164.7 (+0.43 %) (+0.12 %)	152.0 (+0.46 %) (+1.47 %)	159.0 (+1.27 %) (+1.73 %)
HSE06	171.0 (+4.27 %) (+3.95 %)	154.7 (+2.25 %) (+3.27 %)	160.8 (+2.42 %) (+2.88 %)
Ekspt. (INS)	164.0	151.3	157.0
Ekspt. (IXS)	164.5	149.8	156.3

S3 lentelėje. Iš duomenų matyti, kad meta-GGA ir hibridiniai funkcionalai ženkliai pagerina NV<sup>−</sup> centro ZPL energijos aprašymą, palyginti su pusiau lokaliu PBE funkcionalu. Geriausią sutapimą su eksperimentine 1.945 eV verte duoda HSE06 funkcionalas – 2.002 eV.

NV<sup>−</sup> centro elektron-fononinė sąveika buvo apskaičiuota taikant adiabatinę schemą su įterpimo metodologija, aprašyta 1.7 sekcijoje. Dalinės spektrinės funkcijos, atitinkančios  $a_1$  ir  $e$  simetrijos virpesines modas, parodytos S2 pav., o pilna spektrinė funkcija – S3 pav. Atitinkami Huang-

**S3 lentelė.** Suskaičiuotos NV<sup>−</sup> centro deimante befononinės linijos energijos  $E_{ZPL}$  (eV) vertės  $|^3A_2\rangle \leftrightarrow |^3E\rangle$  optiniam šuoliui naudojant skirtingus tankio funkcionalus. Skliaustuose nurodytos vertės rodo santykinius nuokrypius nuo eksperimentinės vertės, paimtos iš šaltinio [3].

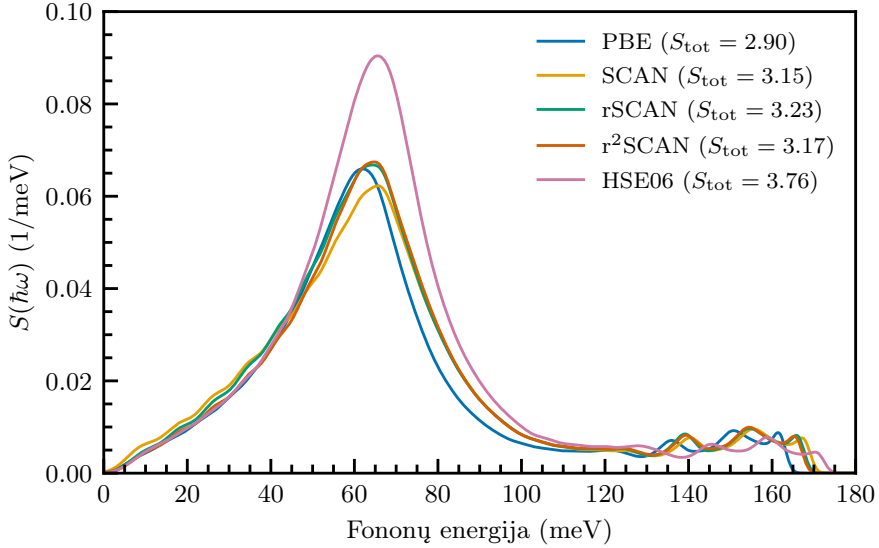
	$E_{ZPL}$
PBE	1.692 (−13.0 %)
SCAN	1.867 (−4.0 %)
rSCAN	1.812 (−6.8 %)
r <sup>2</sup> SCAN	1.806 (−7.1 %)
HSE06	2.002 (+2.9 %)
Ekspt.	1.945



**S2 pav.** Suskaičiuotos NV<sup>-</sup> centro deimante liuminescencijos proceso elektron-fononinės sąveikos dalinės spektrinės funkcijos  $S_{a_1}(\hbar\omega)$  ir  $S_e(\hbar\omega)$  naudojant skirtingus tankio funkcionalus

Rhys faktoriai pateikti S4 lentelėje. Apskaičiuotos elektron-fononinės sąveikos stiprumo vertės  $S_{\text{tot}}$  yra 2.90 (PBE), 3.15 (SCAN), 3.23 (rSCAN), 3.17 (r<sup>2</sup>SCAN) ir 3.76 (HSE06), palyginti su eksperimentiniu įverčiu  $S_{\text{tot}} \approx 3.49$  [108]. Visais atvejais dominuojantį indėlį sudaro  $a_1$  simetrijos modos, tuo tarpu  $e$  simetrijos modos prisideda mažiau.

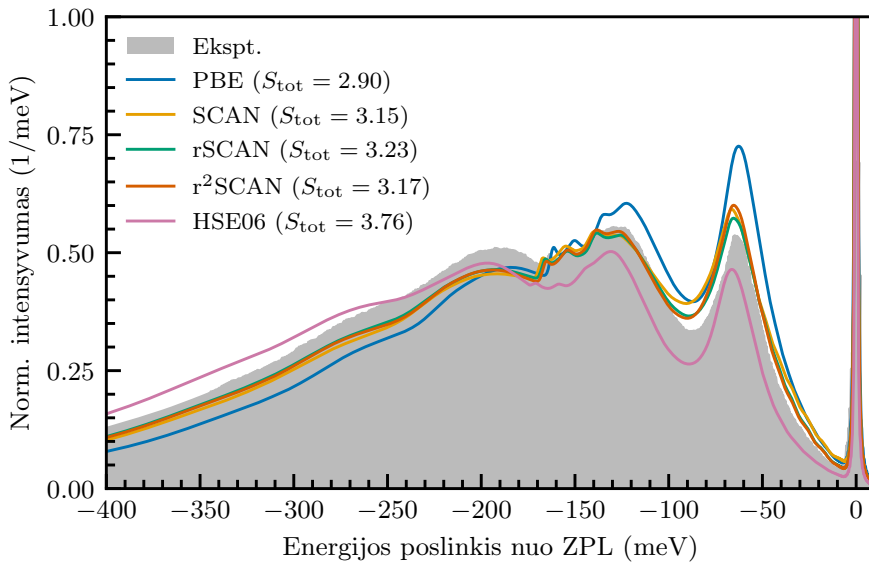
Galiausiai, suskaičiuotos normalizuotos NV<sup>-</sup> centro liuminescencijos linijos pateiktos S4 pav., kartu su eksperimentiniais žemos temperatūros fotoluminescencijos duomenimis. Kaip matyti, visi teoriniai spektrai atkuria pagrindines eksperimentiškai stebimas savybes: ryškią befononinę liniją ir plačią fononų pajuostę, besitęsiančią į žemesnių energijų sritį. Iš visų naudotų tankio funkcionalų SCAN šeimos rezultatai yra tarpiniai ir geriausiai atitinka eksperimentinius duomenis, nes sąlyginai tiksliai atkuria tiek fononų pajuostės smulkiają struktūrą, tiek santykinę linijos intensyvumo pasiskirstymą.



**S3 pav.** Suskaičiuota  $NV^-$  centro deimante liuminescencijos proceso elektron-fononinės sąveikos spektrinė funkcija  $S(\hbar\omega)$  naudojant skirtingus tankio funkcionalus

**S4 lentelė.** Suskaičiuoti  $NV^-$  centro deimante liuminescencijos proceso daliniai ( $S_{a_1}$  ir  $S_e$ ) ir pilnas ( $S_{tot}$ ) Huang-Rhys faktoriai. Skliaustuose nurodytos vertės rodo santykinius nuokrypius nuo apytikrės vertės, paimtos iš šaltinio [108].

	$S_{a_1}$	$S_e$	$S_{tot}$	
PBE	2.39	0.51	2.90	(−16.9%)
SCAN	2.55	0.60	3.15	(−9.7%)
rSCAN	2.67	0.56	3.23	(−7.4%)
r <sup>2</sup> SCAN	2.62	0.54	3.17	(−9.2%)
HSE06	3.20	0.56	3.76	(+7.7%)
Ekspt.	–	–	3.49	



**S4 pav.** Suskaičiuota normalizuota  $NV^-$  centro deimante luminescencijos linija naudojant įvairius tankio funkcionalus. Energijos atidėtos eksperimentinės befononinės linijos atžvilgiu. Eksperimentinis žemos temperatūros spektras paimtas iš šaltinio [108].

### 3. Koreliuotos elektroninės būsenos: G-centras silicyje

Silicis, nepaisant pakankamai siauro draustinės juostos tarpo (apie 1.1 eV), vertinamas kaip perspektyvi kvantinių technologijų medžiaga, pasižyminti technologiniu brandumu ir suderinamumu su puslaidininkų gamybos procesais. Optiškai aktyvūs taškiniai defektai silicyje spinduliuoja artimųjų infraraudonųjų spindulių srityje, todėl yra ypač patrauklūs taikymams kvantinės telekomunikacijos srityje [13–20].

Vienas iš tokių defektų yra G-centras – struktūriškai neutralus,  $C_{1h}$  taškinės grupės simetrijos kompleksas [113–116], sudarytas iš dviejų pakaitinių anglies atomų, išsidėsčiusių išilgai  $\langle 111 \rangle$  kristalografinės krypties, ir tarp jų esančio įterptinio silicio atomo (žr. 3.1a pav.). Šis defektas pasižymi ryškia 0.969 eV (1279 nm) befononine linija [14–16, 112, 118, 119] ir apie 20% Debye-Waller faktoriumi [15, 16, 120, 121], todėl yra laikomas perspektyviu pavienių fotonų šaltiniu kvantinės telekomunikacijos technologijoms.

Įterptinis silicio atomas suformuoja tik dvi jungtis su gretimais anglies atomais, dėl ko G-centras turi šešias ekvivalenčias minimumo konfigūracijas, atskirtas pakankamai mažais energijos barjeriais: 89 meV pagrindinėje singuletinėje būsenoje, 40 meV sužadintoje tripletinėje būsenoje ir 33 meV sužadintoje singuletinėje būsenoje [122, 123].

Elektroninė G-centro struktūra sudaryta iš pagrindinės singuletinės būsenos  $|S_0\rangle \equiv |^1A'\rangle$ , kuri gerai aprašoma vienu Slater determinantu, ir koreliuotos sužadintos singuletinės būsenos  $|S_1\rangle \equiv |^1A''\rangle$ , reikalaujančios daugiadeterminantinio aprašymo (žr. 3.1c pav.). Taip pat egzistuoja metastabili sužadinta tripletinė būseną,  $|T\rangle \equiv |^3A''\rangle$ , esanti maždaug 0.7 eV virš pagrindinės būsenos [122, 126].

Sužadinta singuletinė būseną  $|S_1\rangle$  buvo modeliuojama taikant tris schemas:

1. tripletinę aproksimaciję  $|T\rangle$ ,
2. sumaišyto sukini (angl. *spin-contaminated*) aproksimaciją  $|M\rangle$ ,
3. apytikslės sukini projekcijos (angl. *approximate spin projection*) aproksimaciją [33, 127] jėgoms [formulė (3.1)].

Šiame skyriuje SCAN šeimos tankio funkcionalai lyginami su PBE ir HSE06 funkcionalais nagrinėjant gryną silicį ir G-centro virpesines bei optines savybes.

#### 3.1. Rezultatai

Naudojant PBE, SCAN, rSCAN, r<sup>2</sup>SCAN ir HSE06 funkcionalus buvo apskaičiuotos silicio gardelės konstanta  $a$  ir draustinės juostos

**S5 lentelė.** Suskaičiuotos silicio gardelės konstantos  $a$  (Å) ir draustinės juostos tarpai  $E_g$  (eV) naudojant skirtingus tankio funkcionalus. Skliaustuose nurodytos vertės rodo santykinius nuokrypius nuo eksperimentinių verčių.

	$a$	$E_g$
PBE	5.469 (+0.87 %)	0.61 (−48 %)
SCAN	5.428 (+0.11 %)	0.83 (−29 %)
rSCAN	5.435 (+0.24 %)	0.78 (−33 %)
r <sup>2</sup> SCAN	5.440 (+0.33 %)	0.78 (−33 %)
HSE06	5.433 (+0.20 %)	1.15 (−2 %)
Ekspt.	5.422 <sup>a</sup>	1.17 <sup>b</sup>

<sup>a</sup>[104]    <sup>b</sup>[131]

**S6 lentelė.** Suskaičiuoti deimanto išilginių optinių fononų dažniai  $\omega$  (meV) aukštos simetrijos atvirkštinės gardelės taškuose naudojant skirtingus tankio funkcionalus. Lentelėje nurodyti tik aukščiausių išilginių optinių fononų šakų dažniai. Skliaustuose nurodytos vertės rodo santykinius nuokrypius nuo eksperimentinių verčių, paimtų iš šaltinio [132].

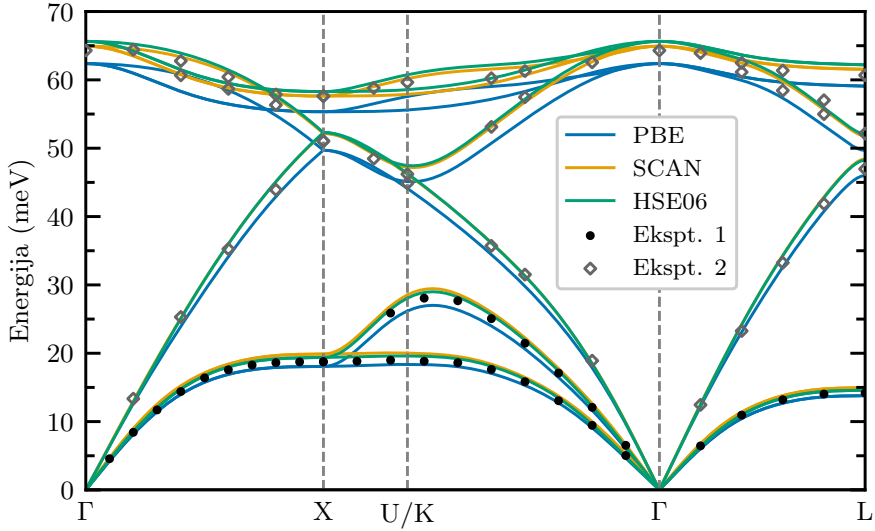
	$\omega(\Gamma)$	$\omega(X)$	$\omega(L)$
PBE	62.4 (−2.95 %)	55.3 (−3.99 %)	59.1 (−2.64 %)
SCAN	64.9 (+0.93 %)	57.6 (0.00 %)	61.6 (+1.48 %)
rSCAN	64.3 (0.00 %)	57.1 (−0.87 %)	61.0 (+0.49 %)
r <sup>2</sup> SCAN	64.4 (+0.16 %)	57.2 (−0.69 %)	61.1 (+0.66 %)
HSE06	65.6 (+2.02 %)	58.3 (+1.22 %)	62.3 (+2.64 %)
Ekspt.	64.3	57.6	60.7

tarpas  $E_g$ . Iš rezultatų, pateiktų S5 lentelėje, matyti, kad tiksliausią gardelės konstantą rezultatai prognozuoja SCAN funkcionalas (5.428 Å), o draustinės juostos tarpą – HSE06 funkcionalas (1.15 eV).

Silicio fononų dispersijos kreivių skaičiavimo rezultatai pateikti S5 pav. ir S6 lentelėje. Kitaip nei deimanto atveju, silicyje skirtumas tarp SCAN ir HSE06 funkcionalų rezultatų yra nedidelis – abu metodai duoda panašias dažnių vertes, tačiau SCAN funkcionalas geriau dera su eksperimentiniais duomenimis, ypač aukštesnėse optinių fononų šakose.

G-centro optinių šuolių energijos vertės iš pagrindinės būsenos  $|S_0\rangle$  į sužadintos singuletinės būsenos  $|S_1\rangle$  aproksimacijas pateiktos S7 lentelėje. Iš nagrinėtų artinių geriausia atitikimą su eksperimentu (0.969 eV) suteikia apytikslės sukinio projekcijos aproksimacija  $|F\rangle$  su SCAN funkcionalu (0.901 eV).

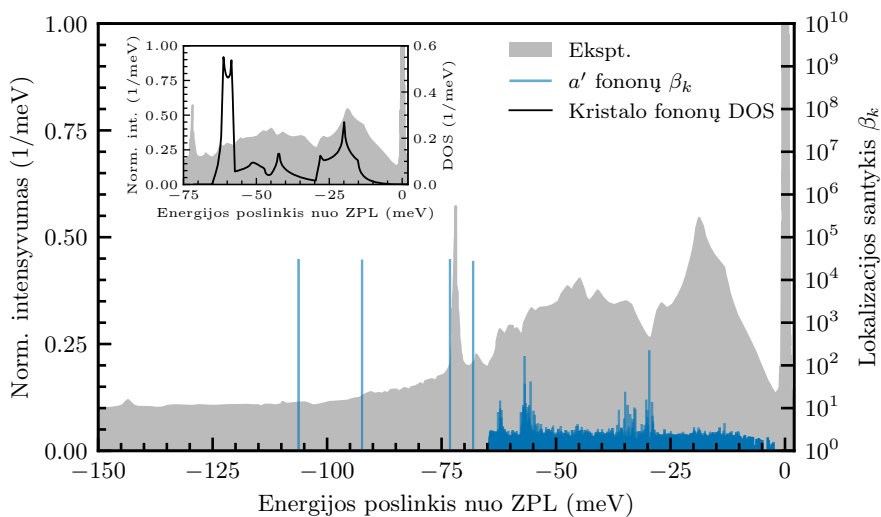
Pagrindinei būsenai  $|S_0\rangle$  suskaičiuota virpesinė struktūra pavaizduota S6 pav., naudojant  $a'$  simetrijos modų lokalizacijos santykius  $\beta_k$ . Iden-



**S5 pav.** Suskaičiuotos silicio fononų dispersijos kreivės naudojant PBE, SCAN ir HSE06 funkcionalus. Eksperimentinės kambario temperatūros vertės paimtos iš šaltinio [132].

**S7 lentelė.** Suskaičiuotos G-centro silicyje befononinės linijos energijos  $E_{ZPL}$  (eV) vertės optiniams šuoliams tarp  $|S_0\rangle$  ir  $|T\rangle$ ,  $|M\rangle$ ,  $|F\rangle$  būsenų naudojant PBE ir SCAN funkcionalus. Skliaustuose nurodytos vertės rodo santykinius nuokrypius nuo eksperimentinės  $|S_0\rangle \leftrightarrow |S_1\rangle$  optinio šuolio vertės 0.969 eV [119].

$E_{ZPL}$	$ T\rangle$	$ M\rangle$	$ F\rangle$
PBE	0.565	0.655 (-32.4 %)	0.709 (-26.8 %)
SCAN	0.510	0.715 (-26.2 %)	0.901 (-7.0 %)

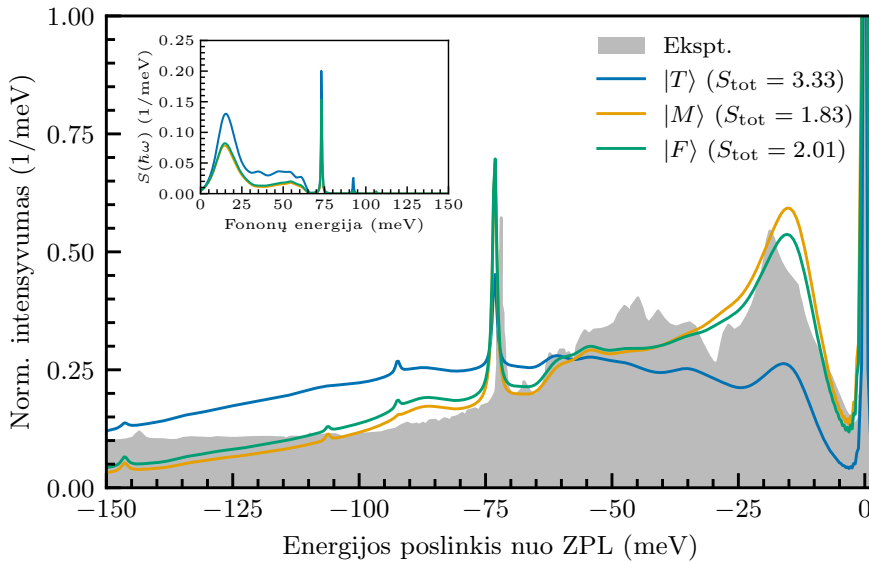


**S6 pav.** Suskaičiuota G-centro silicyje pagrindinės būsenos virpesinė struktūra. Energijos atidėtos eksperimentinės befononinės linijos atžvilgiu. Vertikalios linijos žymi  $a'$  simetrijos virpesinių modų lokalizacijos santykius ( $\beta_k$ ), apskaičiuotus su  $18 \times 18 \times 18$  supergardele (46 656 atominiai mazgai) naudojant SCAN funkcionalą. Vidiniame paveiksliuke pavaizduota silicio fononų būsenų tankio funkcija (DOS), suskaičiuota su  $4 \times 4 \times 4$  supergardele (512 atominių mazgų). Eksperimentinis žemos temperatūros spektras paimtas iš šaltinio [134].

tifikuotos kelios stipriai lokalizuotos modos su energijomis 68.6 meV, 72.6 meV, 92.2 meV ir 105.8 meV, iš kurių pirmosios dvi atitinka ryškias smailes eksperimentinėje fononų pajuostėje. Taip pat stebimi modų rezonansai 30 meV–65 meV intervale ir erdvėje išplitusios modos iki silicio fononų juostos krašto.

Galiausiai, elektron-fononinės sąveikos spektrinės funkcijos ir atitinkamos luminescencijos linijos, gautos trims sužadintos singuletinės būsenos  $|S_1\rangle$  aproksimacijoms, pateiktos S7 pav. Bendrieji Huang-Rhys faktoriai yra  $S_{\text{tot}} = 3.33$  ( $|T\rangle$ ), 1.83 ( $|M\rangle$ ) ir 2.01 ( $|F\rangle$ ), atitinkantys maždaug 5 %, 17 % ir 15 % Debye-Waller faktorius.

Visos aproksimacijos atkuria žemos energijos smaile apie 15 meV žemiau befononinės linijos ( $|T\rangle$  būsenos santykinis sutapimas prasčiausias) bei aukštesnių energijų intervale esančias smailes, susijusias su lokalizuotomis modos, ypač 72.6 meV virpesiu. Geriausią bendrą atitikimą su eksperimentiniais duomenimis atkuria  $|M\rangle$  ir  $|F\rangle$  būsenos. Likę neatitikimai siejami su koreliuotu (daugiadeterminantiniu) sužadintos būsenos pobūdžiu ir galimai anharmoniniais tiek pagrindinės, tiek sužadintos būsenos potencinės energijos paviršiais.



**S7 pav.** Suskaičiuotos normalizuotos G-centro silicyje liuminescencijos linijos naudojant tris skirtingas sužadintos būsenos  $|S_1\rangle$  aproksimacijas. Energijos atidėtos eksperimentinės befononinės linijos atžvilgiu. Vidiniame paveiksliuke pavaizduotos elektron-fononinės sąveikos spektrinės funkcijos  $S(\hbar\omega)$  liuminescencijos procesui. Skaičiavimai atlikti naudojant  $18 \times 18 \times 18$  supergardele (46 656 atominiai mazgai) ir SCAN funkcionalą. Eksperimentinis žemos temperatūros spektras paimtas iš šaltinio [134].

## 4. Silpnai susietos eksitoninės sužadintos elektroninės būsenos: C-centras silicyje

Kitas artimųjų infraraudonųjų spindulių srityje spinduliuojantis defektas silicyje yra C-centras. Jis pasižymi 1570 nm (0.790 eV) befononine linija [136–139] ir apie 12 % Debye-Waller faktoriumi [140], todėl taip pat laikomas kvantinės telekomunikacijos sričiai patraukliu pavienių fotonų šaltiniu.

Struktūriškai šis defektas yra neutralus  $C_iO_i$  kompleksas, susiformuojantis, kai mobilūs anglies įterptiniai ( $C_i$ ) atomai susijungia su deguonies įterptiniais ( $O_i$ ) atomais [109–112]. Gauta konfigūracija sudaro kvadratą primenantį žiedą ( $1\bar{1}0$ ) kristalografinėje plokštumoje (žr. 4.1a pav.) ir pasižymi  $C_{1h}$  taškinės grupės simetrija [137].

C-centro pagrindinė būsena  $|S_0\rangle \equiv |^1A'\rangle$  yra singuletinė dėl draustinės juostos tarpe pilnai užpildytos defekto indukuotos  $a''$  orbitalės. Nors tokia elektroninė struktūra iš pirmo žvilgsnio suponuoja, kad intradefektiniai optiniai šuoliai neturėtų vykti, fotoluminescencijos matavimai atskleidžia eksitoninių sužadintų būsenų seką [136, 137]. Žemiausioji iš jų yra  $|S_1\rangle \equiv |^1A''\rangle$ . Taip pat yra indikacijų apie metastabilią tripletinę būsena  $|T\rangle \equiv |^3A''\rangle$ , esančią maždaug 3 meV žemiau  $|S_1\rangle$  būsenos [138, 140, 143].

Šiame skyriuje nagrinėjamos C-centro termodinaminės savybės, virpesinė struktūra, elektron-fononinė sąveika ir optinės linijos, sužadintą singuletinę būseną aproksimuojant teigiamai įkrautu defektu.

### 4.1. Rezultatai

Neutralaus krūvio  $C_i$ ,  $O_i$  ir  $C_iO_i$  (C-centras) defektų formavimosi energijos bei  $C_iO_i$  komplekso surišimo energijos vertės pateiktos S8 lentelėje. Kaip matyti, tiek SCAN, tiek HSE06 funkcionalais gauti termodinaminiai įverčiai paklaidų ribose pakankamai gerai sutampa su literatūroje randamais duomenimis.

Krūvio būsenų perėjimo lygmenys (angl. *charge-state transition levels*, CTLs), apskaičiuoti HSE06 funkcionalu  $C_i$  ir C-centro defektams, pateikti S9 lentelėje. Šiuo atveju gautieji rezultatai yra ypač artimi literatūroje nurodytoms vertėms.

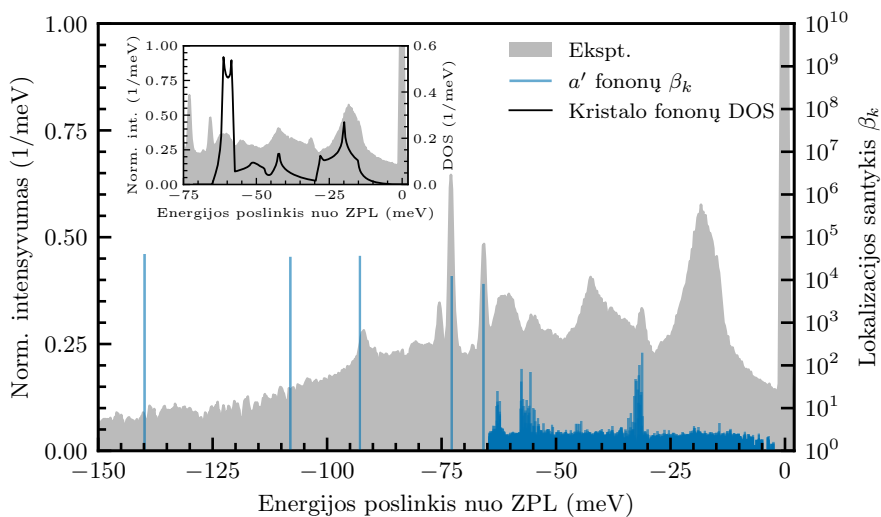
Naudojant SCAN funkcionalą, pagrindinės būsenos  $|S_0\rangle$  virpesinė struktūra vaizduojama S8 pav. Lokalizacijos santykiai  $\beta_k$  identifikuoja kelias stipriai lokalizuotas  $a'$  simetrijos modas su energijomis 65.8 meV, 72.8 meV, 92.7 meV, 107.9 meV ir 139.7 meV. Pirmosios trys aiškiai matomos eksperimentinėje fononų pajuostėje [139], o dvi aukščiausios energijos modos spektre iš esmės nestebimos. Be lokalizuotų modų stebimi ir rezonansai ties 32 meV, 54 meV ir 62 meV, taip pat erdvėje išplitusios modos iki silicio fononų juostos krašto. Apibendrinant, stebima gera atitiktis

**S8 lentelė.** Suskaičiuotos neutralių  $C_i$ ,  $O_i$  ir  $C_iO_i$  (C-centras) defektų silicyje formavimosi energijos  $\Delta H_f^X(0)$  (eV) ir  $C_iO_i$  komplekso surišimo energija  $E_b^{C_iO_i}(0)$  (eV) naudojant SCAN ir HSE06 funkcionalus. Rezultatai palyginti su literatūroje prieinamais teoriniais ir eksperimentiniais duomenimis.

	$\Delta H_f^{C_i}(0)$	$\Delta H_f^{O_i}(0)$	$\Delta H_f^{C_iO_i}(0)$	$E_b^{C_iO_i}(0)$
SCAN (šis darbas)	3.49	1.79	3.75	1.53
HSE06 (šis darbas)	3.70	1.81	3.95	1.56
Teorija	4.12 <sup>a</sup>	1.81 <sup>a</sup>	4.21 <sup>a</sup>	1.72 <sup>a</sup>
	4.50 <sup>b</sup>	1.95 <sup>b</sup>	4.85 <sup>b</sup>	1.65 <sup>c</sup>
	3.74 <sup>c</sup>	1.56 <sup>d</sup>	3.63 <sup>c</sup>	1.64 <sup>h</sup>
	3.72 <sup>e,f</sup>	–	–	–
Ekspt.	–	1.65 ± 0.15 <sup>g</sup>	–	–
	<sup>a</sup> [149] <sup>e</sup> [153]	<sup>b</sup> [150] <sup>f</sup> [145]	<sup>c</sup> [151] <sup>g</sup> [148]	<sup>d</sup> [152] <sup>h</sup> [154]

**S9 lentelė.** Suskaičiuoti  $C_i$  ir C-centro defektų silicyje krūvio būsenų perėjimo lygmenys (eV) naudojant HSE06 funkcionalą. Rezultatai palyginti su literatūroje prieinamais teoriniais ir eksperimentiniais duomenimis.

	$C_i$	$C_iO_i$
HSE06 (šis darbas)	$\varepsilon(+/0) = E_{VBM} + 0.32$ $\varepsilon(0/-) = E_{CBM} - 0.16$	$\varepsilon(+/0) = E_{VBM} + 0.39$
Teorija	$\varepsilon(+/0) = E_{VBM} + 0.32^a$ $\varepsilon(0/-) = E_{CBM} - 0.19^a$	$\varepsilon(+/0) = E_{VBM} + 0.36^b$ $0.41^c$
Ekspt.	$\varepsilon(+/0) = E_{VBM} + 0.28^d$ $\varepsilon(0/-) = E_{CBM} - 0.10^d$	$\varepsilon(+/0) = E_{VBM} + 0.38^e$ $0.36^f$
	<sup>a</sup> [145] <sup>d</sup> [157]	<sup>b</sup> [149] <sup>e</sup> [158]
	<sup>c</sup> [140] <sup>f</sup> [159]	

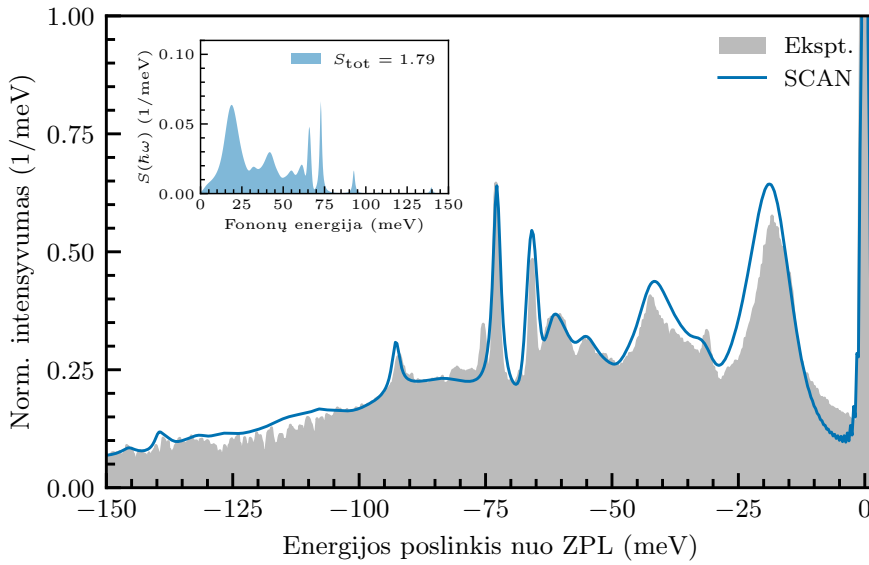


**S8 pav.** Suskaičiuota C-centro silicyje pagrindinės būsenos virpesinė struktūra. Energijos atidėtos eksperimentinės befononinės linijos atžvilgiu. Vertikalios linijos žymi  $a'$  simetrijos virpesinių modų lokalizacijos santykius ( $\beta_k$ ), apskaičiuotus su  $18 \times 18 \times 18$  supergardele (46 656 atominiai mazgai) naudojant SCAN funkcionalą. Vidiniame paveiksluke pavaizduota silicio fononų būsenų tankio funkcija (DOS), suskaičiuota su  $4 \times 4 \times 4$  supergardele (512 atominių mazgų). Eksperimentinis žemos temperatūros spektras paimtas iš šaltinio [139].

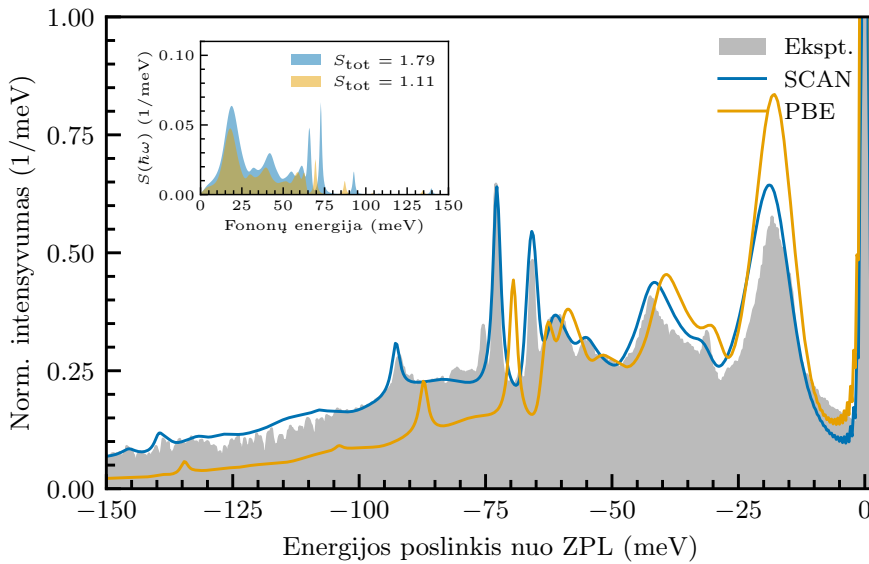
tarp teoriškai suskaičiuotų ir eksperimente stebimų pajuostės smailių.

Apskaičiuota luminescencijos linija (S9 pav.) gerai sutampa su žemos temperatūros eksperimentiniu spektru [139], įskaitant fononų pajuostės smailes ir bendrą intensyvumo pasiskirstymą. Lokalizuotų ir rezonansinių modų indėlis tiksliai atkuriamas tiek energijų, tiek santykinų intensyvumų požiūriu. Platesnės struktūros ties 20 meV ir 42 meV, kurios atsiranda dėl virpesių grynajame silicyje, taip pat atkuriamos pakankamai geru tikslumu.

Galiausiai, S10 pav. palyginamos luminescencijos linijos, apskaičiuotos naudojant PBE ir SCAN funkcionalus. PBE funkcionalas per stipriai įskaito akustinių virpesių ir per silpnai – aukštesnės energijos modų indėlių, todėl gaunamas Huang-Rhys faktorius  $S_{\text{tot}} = 1.11$ . Tuo tarpu SCAN prognozuoja  $S_{\text{tot}} = 1.79$ , daug geriau atkartodamas fononinės pajuostės struktūrą.



**S9 pav.** Suskaičiuota normalizuota C-centro silicyje liuminescencijos linija. Energijos atidėtos eksperimentinės befononinės linijos atžvilgiu. Vidiniame paveiksliuke pavaizduota elektron-fononinės sąveikos spektrinė funkcija  $S(\hbar\omega)$  liuminescencijos procesui. Skaičiavimai atlikti naudojant  $18 \times 18 \times 18$  supergardele (46 656 atominiai mazgai) ir SCAN funkcionalą. Eksperimentinis žemos temperatūros spektras paimtas iš šaltinio [139].



**S10 pav.** Suskaičiuotų normalizuotų C-centro silicyje liuminescencijos linijų, naudojant PBE ir SCAN funkcionalus, palyginimas. Energijos atidėtos eksperimentinės befononinės linijos atžvilgiu. Vidiniame paveiksliuke pavaizduotos elektron-fononinės sąveikos spektrinės funkcijos  $S(\hbar\omega)$  liuminescencijos procesui. Skaičiavimai atlikti naudojant  $18 \times 18 \times 18$  supergirdelę (46 656 atominiai mazgai). Eksperimentinis žemos temperatūros spektras paimtas iš šaltinio [139].

## 5. Elektroninis išsigimimas: $\text{NiV}^-$ centras deimante

Nikelis yra įprasta deimanto, susidarančio aukšto slėgio ir temperatūros sąlygomis, priemaiša ir pasižymi įvairiomis spektrinėmis savybėmis [160, 161]. Tarp jų ryškiausia yra 1.40 eV (886 nm) emisijos linija, priskiriama neigiamai įkrautam nikelio-vakansijos ( $\text{NiV}^-$ ) centrai [162]. Šiame paramagnetiniame defekte priemaišinis nikelio atomas lokalizuotas inversijos centre tarp dviejų anglies vakansijų ir sudaro  $D_{3d}$  taškinės grupės simetriją [162], orientuotą išilgai  $\langle 111 \rangle$  kristalografinės krypties (žr. 5.1a pav.).

$\text{NiV}^-$  centro pagrindinė būseną  $|^2E_u\rangle$  yra orbitiškai išsigimusi (žr. 5.1c pav.) ir sudaro dinaminį Jahn-Teller (DJT) efektu pasižyminčią  $E_u \otimes (e_g \oplus e_g \oplus \dots)$  sistemą, kurioje  $e_g$  simetrijos virpesinės modos „suriša“ išsigimusias elektroninio multipletto komponentes  $|^2E_{ux}\rangle$  ir  $|^2E_{uy}\rangle$ . Priešingai, sužadinta būseną  $|^2A_{1g}\rangle$  yra orbitinis singuletas, aprašomas vienu Slater determinantu.

Kadangi optinio šuolio  $|^2A_{1g}\rangle \rightarrow |^2E_u\rangle$  metu dalyvauja tiek simetriją išlaikančios  $a_{1g}$ , tiek simetriją griaunančios  $e_g$  virpesinės modos, tiksliam liuminescencijos linijos modeliavimui būtina derinti adiabatinių (žr. 1.2) ir neadiabatinių (žr. 1.5) formalizmus. Bendra optinė spektrinė funkcija gaunama atliekant šių dviejų dedamųjų konvoliuciją [formulė (51)].

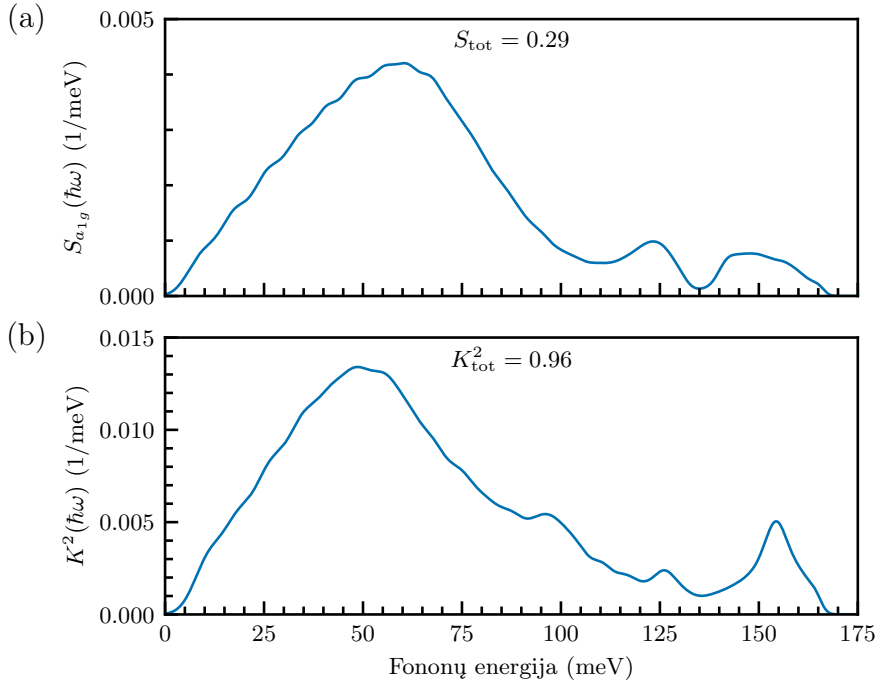
Šiame skyriuje nagrinėjamas  $\text{NiV}^-$  defekto, pasižyminčio neadiabatiniėmis sąveikomis, liuminescencijos linijos modeliavimas.

### 5.1. Rezultatai

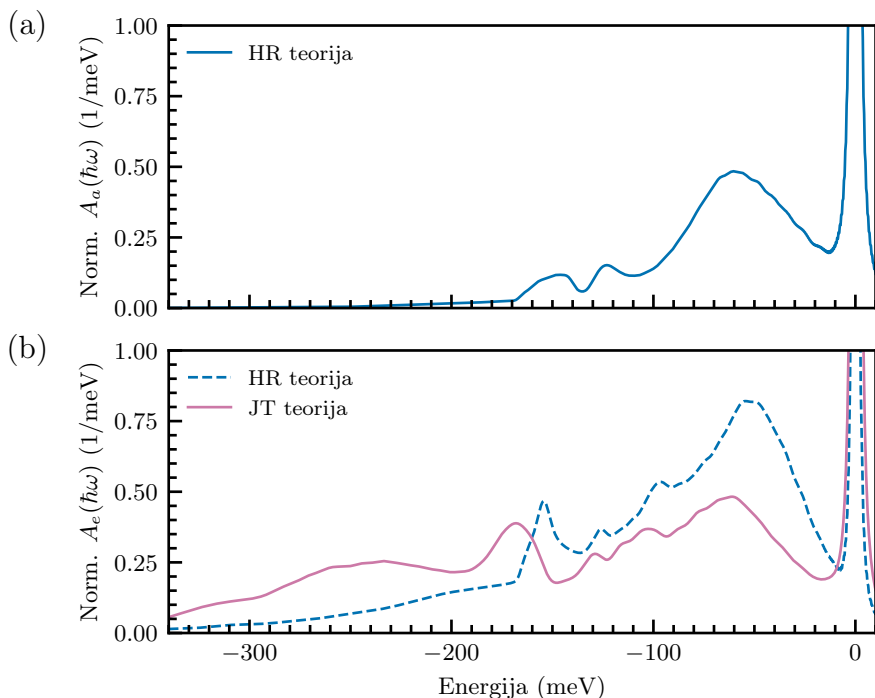
Apskaičiuotos liuminescencijos proceso elektron-fononinės sąveikos spektrinės funkcijos pateiktos S11 pav. Kaip matyti,  $a_{1g}$  modų indėlis ( $S_{\text{tot}} = 0.29$ ) yra maždaug tris kartus mažesnis už simetriją griaunančių  $e_g$  modų indėlį ( $K_{\text{tot}}^2 = 0.96$ ).

Optinių spektrinių funkcijų rezultatai pateikti S12 pav. Funkcija  $A_a(\hbar\omega)$ , atitinkanti  $a_{1g}$  modų indėlį, greitai išnyksta ties maždaug 170 meV žemiau befononinės linijos ir negali paaiškinti plačios fononų pajuostės, besitęsiančios iki maždaug 300 meV. Tuo tarpu  $A_e(\hbar\omega)$ , atitinkanti JT-aktyvius  $e_g$  modas, formuoja žymiai platesnę fononų pajuostę ir aiškiai skiriasi nuo adiabatinio formalizmo rezultato.

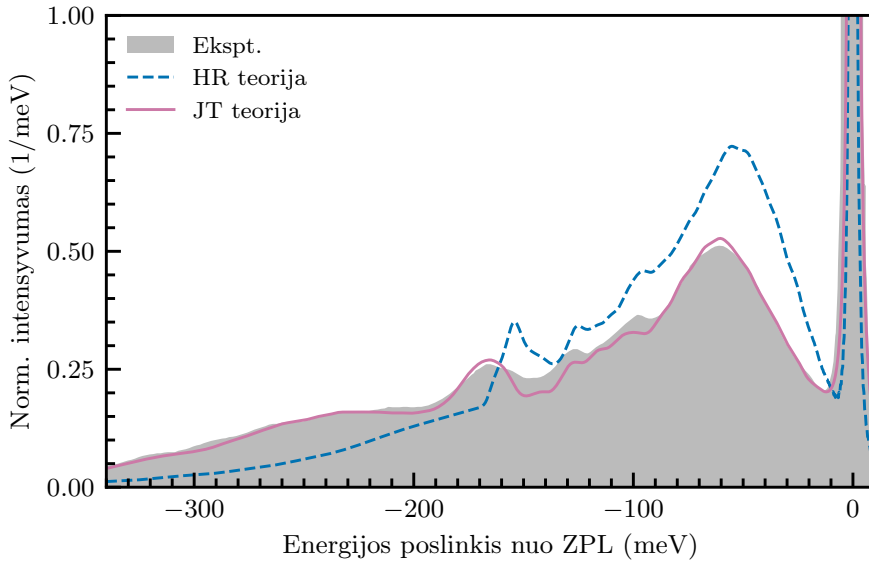
Galiausiai, liuminescencijos linijų palyginimas, pateiktas S13 pav., rodo, kad adiabatinė (HR) teorija spektrą atkuria tik iš dalies ir nesugeba tiksliai atkartoti fononų pajuostės formos. Priešingai, iš neadiabatio (DJT) daugelio modų formalizmo kylantis spektras puikiai sutampa su eksperimentiniais duomenimis [160] ir tiksliai atkuria tiek fononų pajuostės smailių padėtis, tiek jų intensyvumo pasiskirstymą. Šie rezultatai rodo, kad tikslus  $\text{NiV}^-$  centro liuminescencijos spektro modeliavimas reikalauja



**S11 pav.** Suskaičiuotos  $\text{NiV}^-$  centro deimante liuminescencijos proceso elektron-fononinės sąveikos spektrinės funkcijos. Viršutiniame (a) pav. pateikiama adiabatinė spektrinė funkcija  $S_{a_{1g}}(\hbar\omega)$ , susijusi su  $a_{1g}$  simetrijos virpesinėmis modomis, o apatiniame (b) pav. pateikiama tiesinės nediabatinės sąveikos spektrinė funkcija  $K^2(\hbar\omega)$ , kylanti dėl  $e_g$  simetrijos modų. Skaičiavimai atlikti naudojant  $18 \times 18 \times 18$  dydžio supergardelę (46 656 atominiai mazgai) ir  $r^2\text{SCAN}$  funkcionalą.



**S12 pav.** Suskaičiuotos  $\text{NiV}^-$  centro deimante liuminescencijos proceso optinės spektrinės funkcijos. Viršutiniame (a) pav. pateikiama  $A_a(\hbar\omega)$  funkcija, apibūdinanti  $a_{1g}$  simetrijos modų indėlių, o apatiniame (b) pav. pateikiama  $A_e(\hbar\omega)$  funkcija, atsirandanti dėl  $e_g$  simetrijos modų, suskaičiuota naudojant adiabatinį (HR) ir neadiabatinį (JT) formalizmus. Energijos atidėtos eksperimentinės befononinės linijos atžvilgiu. Skaičiavimai atlikti naudojant  $18 \times 18 \times 18$  dydžio supergardele (46 656 atominiai mazgai) ir  $r^2\text{SCAN}$  funkcionalą.



**S13 pav.** Suskaičiuotų  $\text{NiV}^-$  centro deimante liuminescencijos linijų, gautų taikant adiabatinių (HR) ir neadiabatinių (JT) formalizmus, palyginimas. Energijos atidėtos eksperimentinės befoninės linijos atžvilgiu. Skaičiavimai atlikti naudojant  $18 \times 18 \times 18$  dydžio supergardele (46 656 atominiai mazgai) ir  $r^2\text{SCAN}$  funkcionalą. Eksperimentinis žemos temperatūros spektras paimtas iš šaltinio [160].

neadiabatinių sąveikų įskaitymo, nes vien adiabatinis formalizmas yra nepakankamas JT-aktyvių sistemų analizei.



# Curriculum vitae

**Given name:** Rokas  
**Family name:** Silkinis  
Place of birth: Kaunas, Lithuania

## Education:

2020 – 2025 Center for Physical Sciences and Technology (FTMC)  
Department of Fundamental Research  
*PhD studies*

2018 – 2020 Vilnius University  
Faculty of Physics  
*Master of Physical Sciences*

2014 – 2018 Kaunas University of Technology  
Faculty of Mathematics and Natural Sciences  
*Bachelor of Materials Technology and Mathematics*

2011 – 2014 Kaunas Jonas Basanavičius Gymnasium

2010 – 2011 Kaunas Milikonys Secondary School

## Work experience:

2023-10 – 2026 Center for Physical Sciences and Technology (FTMC)  
Department of Fundamental Research  
*Junior Researcher*

2023-02 – 2023-10 Center for Physical Sciences and Technology (FTMC)  
Department of Fundamental Research  
*Senior Engineer*

2018-10 – 2023-02 Center for Physical Sciences and Technology (FTMC)  
Department of Fundamental Research  
*Engineer*

# Gyvenimo aprašymas

**Vardas:** Rokas  
**Pavardė:** Silkinis  
**Gimimo vieta:** Kaunas, Lietuva

## Išsilavinimas:

2020 – 2025 Fizinių ir technologijos mokslų centras (FTMC)  
Fundamentinių tyrimų skyrius  
*Doktorantūros studijos*

2018 – 2020 Vilniaus universitetas  
Fizikos fakultetas  
*Fizinių mokslų magistras*

2014 – 2018 Kauno technologijos universitetas  
Matematikos ir gamtos mokslų fakultetas  
*Medžiagų technologijų ir matematikos bakalauras*

2011 – 2014 Kauno Jono Basanavičiaus gimnazija

2010 – 2011 Kauno Milikonių vidurinė mokykla

## Profesinė veikla:

2023-10 – 2026 Fizinių ir technologijos mokslų centras (FTMC)  
Fundamentinių tyrimų skyrius  
*Jaunesnysis mokslo darbuotojas*

2023-02 – 2023-10 Fizinių ir technologijos mokslų centras (FTMC)  
Fundamentinių tyrimų skyrius  
*Vyresnysis inžinierius*

2018-10 – 2023-02 Fizinių ir technologijos mokslų centras (FTMC)  
Fundamentinių tyrimų skyrius  
*Inžinierius*

# Notes

# Notes

# Notes

Vilnius University Press  
Saulėtekio al. 9, LT-10222 Vilnius, Lithuania  
E-mail: [info@leidykla.vu.lt](mailto:info@leidykla.vu.lt), [www.leidykla.vu.lt](http://www.leidykla.vu.lt)  
[bookshop.vu.lt](http://bookshop.vu.lt), [journals.vu.lt](http://journals.vu.lt)  
Print run copies 15